Alma Mater Studiorum - Università di Bologna

DOTTORATO DI RICERCA IN CHIMICA

Ciclo XXIX

Settore Concorsuale di afferenza: 03/A2
Settore Scientifico disciplinare: CHIM/02

MODELING CHARGE AND ENERGY TRANSFER IN ORGANIC MOLECULAR MATERIALS

Presentata da: Sofia Canola

Coordinatore Dottorato:
Prof. Aldo Roda

Relatore:
Prof. Fabrizia Negri

Esame Finale anno 2017

"... quelle emozioni fondamentali che sono il misurarsi con la materia (che è un giudice imparziale, impassibile ma durissimo: se sbagli ti punisce senza pietà), il vincere, il rimanere sconfitti."

— Primo Levi, *L'altrui mestiere*

Contents

Abstract

The understanding of nanoscale physics, chemistry and biology still poses unanswered questions such as how the optical and electrical properties of materials evolve from those of individual molecules. Organic semiconductors fall in this class of materials and have received increasing attention in both academic and industrial fields as an alternative to inorganic semiconductors. They are characterized by appealing properties, such as for example flexibility, versatility, and the ease of tuning optoelectronic properties through the design of new active molecules and their interactions in the condensed phase. The main processes occurring in such systems are both charge and energy transfer and they are responsible for the practical operation of electronic devices, like solar cells, thin film transistors, LEDS and others. In particular, small-molecule materials are attractive from the experimental point of view, because they can be efficiently purified and they tend to form ordered structures that enable high charge mobilities. On the other hand, small-molecule materials have served as model systems for a variety of fundamental studies concerning energy transfer and charge dynamics. Therefore, an understanding at a fundamental level of the mechanism behind the device operation and the electronic properties of the involved molecules can help the optimization of each process, aiming to a better global performance of the material.

My three years PhD activity was developed along two major lines of research: charge and energy transport, both based on the computational investigation of intramolecular properties and intermolecular interactions. Strictly related to energy transport are the optical properties of condensed phase materials and how they evolve from those of isolated molecular components. The charge transport properties were investigated for several organic molecular crystals showing semiconducting behavior, whose experimental crystal structure and charge mobilities are available. As the same interactions that drive the transport of charge play also a role in determining the optical properties and the energy transport in molecular aggregates, in my research activity I investigated such processes as well. In this regard, I took into account a dimer of perylene-bisimide (PBI), with the aim of elucidating the role of charge transfer states and their effect on optoelectronic properties. Additionally, to assess the propagation of excited states in a molecular material a kinetic constant is required, similarly to charge transport, but the expression in this case includes the overlap between the absorption spectrum of the acceptor and the emission spectrum of the donor. To this end I also developed a code devoted to the simulation of linear absorption and emission spectra of an isolated molecule, starting from computed quantum mechanical properties.

Introduction

The understanding of nanoscale physics, chemistry and biology still poses unanswered questions such as how the optical and electrical properties of materials evolve from those of individual molecules. Organic semiconductors fall in the class of nanoscale materials and have received increasing attention in both academic and industrial fields as an alternative to inorganic semiconductors. They are characterized by appealing properties, such as for example flexibility, versatility, and the ease of tuning optoelectronic properties through the design of new active molecules and their interactions in the condensed phase.

The main processes occurring in such systems are both charge and energy transfer and they are responsible for the practical operation of electronic devices, like solar cells, thin film transistors, LEDS and others [1, 2]. In addition, such processes are very common also in nature: photosynthetic systems are the most relevant and striking examples [3, 4], and recently they have become source of inspiration for the design of bio-inspired energy conversion devices [4].

There are two major classes of organic semiconductors: small-molecule semiconductors and polymers with advanced optoelectronic properties. Small-molecule materials are attractive from the experimental point of view, because they can be efficiently purified and they tend to form ordered structures that enable high charge mobilities. On the other hand, small-molecule materials have served as model systems for a variety of fundamental studies concerning energy transfer and charge dynamics [5]. The interplay of charge and energy transport is particularly important in organic solar cells. Indeed in this type of devices, as a result of the absorption of photons, both energy and charge transfer processes occur: the photogenerated excited states, namely the exciton that is the particle responsible for the energy transport, migrates through the material toward the interface where the charge separation takes place [2, 6]. The formation of charge transfer complexes is a crucial intermediate step between exciton dissociation after transport and charge migration [7]: once the two charges (holes and electrons) are apart they move across the material to reach the electrodes [2, 6].

An understanding at a fundamental level of the mechanism behind the device operation and the electronic properties of the involved molecules can help the optimization of each process, aiming to a better global performance of the material. In this regard, theoretical and computational studies can help to understand the microscopic intra and intermolecular properties, in order to rationalize the macroscopic behavior and eventually provide suggestions for the design of new organic semiconductors with suitable properties [1, 2, 6].

My three years PhD activity was driven by the above questions and was developed along two major lines of research: charge and energy transport, both based on the computational investigation of intramolecular properties and intermolecular interactions. Strictly related to energy transport are the optical properties of condensed phase materials and how they evolve from those of isolated molecular components. My research activity included, on one side, the development of some parts of software to compute specific properties and, on the other side, application of well established procedures and in house developed programs.

Concerning the first topic, the charge transport properties were investigated for several organic molecular crystals showing semiconducting properties, by computing microscopic parameters that govern these phenomena. I have performed calculations of charge transport properties of several molecular organic semiconductors, whose experimental crystal structure and charge mobilities are available, as reported in the first part of this dissertation. The theoretical framework for these studies is proven to be the non-adiabatic hopping regime and, because of the non-negligible quantum nature of the molecular motions involved, the rate constants have been computed according to the Marcus-Levich-Jortner formulation [8]. The computational methodology involves an integrated approach. The parameters governing the process are computed with Quantum Mechanical (QM) calculations. The first one is the reorganization energy, which is the energy amount necessary to move from neutral to charged state and vice versa; the second one is the electron coupling, the intermolecular interaction between donor and acceptor of the charge carrier. This is computed assuming the monoelectronic approximation, that is between HOMOs orbitals for p-type semiconductors (hole mobility) or between LUMOs for n-type semiconductors (electron mobility). The availability of the crystal structure enables the analysis in terms of possible charge hopping pathways in the crystal. The computed rate constants are then the input for Kinetic Monte Carlo (KMC) simulations, a suitable approach to reproduce the stochastic nature of the transfer process: the charge is propagated in the crystal, either in the absence or in the presence of an external electric field. Finally Molecular Dynamics (MD) simulations combined with QM calculations of electronic couplings are carried out to investigate the effects (fluctuations) on the intermolecular electronic interactions due to thermally induced disorder. The final computed charge mobilities are then compared to experimental measures available in literature.

The same interactions that drive the charge transport play also a role in determining the optical properties and the energy transport in molecular aggregates. This has therefore naturally led my research activity to investigate such processes as well. Energy transfer is indeed governed by intermolecular interactions (electron and exciton couplings) and by the spectral features of donor and acceptor molecules. In recent years it has been shown that, beside the role of local excited states, the contribution from charge transfer states can be relevant since it may influence the efficiency of energy transfer in molecular materials [1, 6, 7]. For this reason, a careful analysis of the excited states that characterize molecular aggregates, must take into account also this peculiar contribution which has generally been overlooked in models. In this regard, during a 4 months stay in the group of Prof. Reinhold Fink at the Eberhard Karls Universität Tübingen, I investigated a simple aggregate: a dimer of perylene-bisimide (PBI), with the aim of elucidating the role of charge transfer states and their effect on optoelectronic properties. The results obtained for the PBI dimer enable the use of a relatively simple model that can be extended to more complex systems. In particular I have computed at different levels of theory the parameters that define a simple model Hamiltonian: their determination allows to decipher the role of locally excited and charge transfer contributions on the basis of interactions (electron and exciton couplings), whose magnitude can be rationalized as a function of the structure of the aggregate.
To investigate the propagation of excited states in a molecular material, similarly to charge transport, a kinetic constant is required. The expression in this case includes the overlap between the absorption spectrum of the acceptor and the emission spectrum of the donor. To this end I developed a code devoted to the simulation of linear absorption and emission spectra of an isolated molecule, starting from computed quantum mechanical properties. This code can be used to compare computed and experimental spectra including their vibronic structure and it has been tested also for the calculation of the spectral overlap that enters the kinetic constant expression. These studies are reported in the second part of this thesis.

Part I

Charge transport

CHAPTER 1

Introduction to charge transport

1.1 Charge transfer models and regimes

Organic semiconductors are π -conjugated molecular systems capable of transporting charges in their condensed phase. A semiconductor is "n-type" if transports negative charges (electrons) or "p-type" if positive charges (holes). Its most important experimental property is the charge mobility, namely the efficiency of the system in transporting the charge, that represents the macroscopic quantity simulations must compare with. Indeed charge mobility can be experimentally measured in thin film or crystal samples with various methodologies, as for example the Time-of-Flight (TOF) technique: a thin layer (few microns thick) is posed between two electrodes and charges are generated by irradiation with laser pulses at one electrode; the charges migrate across the material following the applied electric field (usually about $10^4 - 10^6$ V/cm) and the current is recorder at the second electrode as a function of time, providing the mobility [9]. The experimental mobilities obtained in this way or with other methodologies are strongly dependent on the sample under investigation: besides the chemical and energetic characteristics of the molecule, they also depend on the structure (crystal or amorphous), the degree of order, the purity and the presence of defects [9, 5]. In particular, the charge mobility is generally markedly temperature dependent with a very peculiar behavior. The experimental mobility for several organic conjugated molecules decreases with temperature according to a power law (T^{-n}), at very low temperatures (toward 0 K) [9]. A crystal at temperatures close to 0 K has a full translational order and the charge can be modeled as spread in the whole crystal. From a theoretical point of view its wave function is fully delocalized (crystal orbitals or bands) and the transport is defined as *band-like regime* with higher mobilities due to this almost "barrierless" type of transfer. However an increasing temperature excites low frequency lattice phonons

that break the translational order, causing a localization of the charge wave function and hence at higher temperature, a model in terms of band transport is generally not suitable anymore. Indeed, if the mobility measure is performed in a range of higher temperatures (around room temperature), the mobilities increase with T (at variance with the band mechanism), suggesting that a different transfer regime starts to occur (*hopping regime*): the more thermally disordered situation makes a description based on wave functions localized on the single molecular units in the crystal more appropriate. The charge tends to localize on the molecular units and hence each transfer consists of discrete jumps between pairs of molecules. Each jump can be visualized as a sort of "exchange reaction" (see below) that hence can be modeled as an Arrhenius-like activated process: higher temperatures improve the transport by providing the energy necessary to overcome the barrier. Additionally, this trend of mobility as function of temperature can be further enhanced by thermal disorder since it can trigger the creation of new transport paths, that would be statically forbidden (more details about this point in Section 1.4).

All these considerations highlight the fact that so far an unified theory, capable of describing the charge transport process in all conditions, has not been identified and the two regimes (bands and hopping) are described in the framework of two different models. The choice of the suitable model to describe a given system requires a preliminary estimate of appropriate system quantities: the balance between the energetic contributions tunes the equilibrium between localization and delocalization.

1.1.1 The polaron Hamiltonian

Generally the models are based on suitable Hamiltonians and the most common quantum-mechanical model employed to describe the molecular system of interest relies on a polaron Hamiltonian [9, 5, 10]:

$$\hat{H} = \hat{H}^e + \hat{H}^N + \hat{H}^{eN}. \tag{1.1}$$

It includes both an electronic ($\hat{H}^e$) and a vibrational/phonon ($\hat{H}^N$) term, plus an interaction among those degrees of freedom included in the $\hat{H}^{eN}$ term (electron-phonon coupling). In this model what is actually transported is a "polaron": to each transported charge it is associated a lattice distortion and the equilibrium geometry of a molecule is modified upon adding or removing a charge. The electronic part of the Hamiltonian includes :

$$\hat{H}^e = \sum_i \hat{H}_i + \sum_{i,j} \hat{V}_{ij} \tag{1.2}$$

where i and j run over all the molecules in the system; the first term represents the electronic energy of each isolated molecule and the second one represents the interaction between the electronic states of every pair of molecules, namely the intermolecular electronic coupling. Such an interaction is assumed to act only between nearest neighbors

molecules (tight-binding model) since it is demonstrated that it decays very fast with the distance. The nuclear Hamiltonian describes the nuclear motion of each molecular unit in the framework of the Harmonic approximation and in terms of the normal modes Q (neglecting the kinetic energy part):

$$\hat{H}^N = \sum_i \sum_k^{3N_a-6} \frac{1}{2}\hbar\omega_{i,k}Q_{i,k}^2. \tag{1.3}$$

summed over every molecule and over all the $3N_a - 6$ normal modes of each one (being N_a the number of atoms composing the molecule) and having each k-th mode of the i-th molecule $\omega_{i,k}$ frequency. However, in the framework of a polaron theory, the electronic and nuclear degrees of freedom are not fully independent and this is accounted for in the electron-phonon coupling term $\hat{H}^{eN}$. It encompasses a local and a non-local term: both describe the modulation of the electronic energy due to nuclear vibrations, but the former accounts for the intramolecular vibrations while the latter the intermolecular ones. Now for the purpose of this discussion only the intramolecular term is taken into account building an Holstein-like model, while the intermolecular is more exhaustively discussed in Section 1.4.

The complete Hamiltonian of Eq.(1.1) can be diagonalized providing the energy of a charge carrier on the i-th molecular unit [9, 11]:

$$E_i = \epsilon_i + \sum_k \hbar\omega_{i,k}\left(v_{i,k} + \frac{1}{2}\right) + \sum_j V_{ij}^{el} - \sum_j \sum_k^{3N_a-6} S_{ij,k}\hbar\omega_k. \tag{1.4}$$

The first and the third terms are the electronic part: ϵ is the energy of a given molecule (site energy) and V^{el} is the intermolecular coupling between the electronic states of each neighboring molecules. The second term represents the nuclear energy of i, summed over each k-th normal mode with ω_k frequency. The last one is local electron-phonon term including the S coupling, that expresses the extent to which the two types of degrees of freedom are interacting. It has a minus sign and is always a stabilizing term, named also polaron binding energy E_{pol} while half of its value is named intramolecular reorganization energy λ_{intra}. While the reason for the latter name is made clear in Section 1.3, the first one (local electron-phonon coupling) highlights how this term represents the stabilization of the charge on the site i due to geometry relaxation after getting charged (hence, after the transfer) [10].

As mentioned the two coupling terms describe two opposite tendencies: on one hand V^{el} is a measure of the extent to which the wave function (namely the charge) is delocalized while E_{pol} (and hence $\lambda_{intra}/2$) is the energy gain from the nuclear degrees of freedom upon localization. This fact can also be visualized through a representation of the potential energy surfaces of the *diabatic* initial state (before the exchange) and the final state (after the exchange) represented along a suitable coordinate to describe the transport process, Fig.(1.1). The intersection point represents a sort of transition state to be overcome for the system to go into the final state, i.e., for the charge to

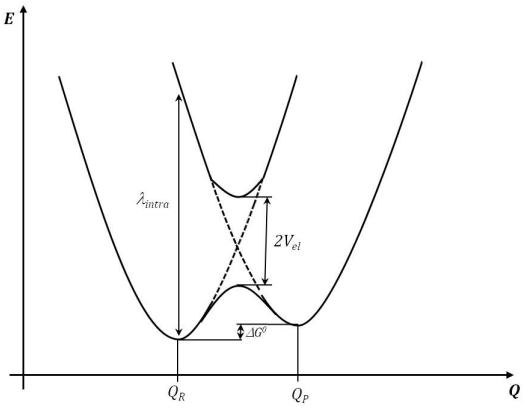

Figure 1.1: Potential energy surfaces along a reaction coordinate: diabatic (dashed) and adiabatic (solid) states (adapted from [10]).

be exchanged. The Hamiltonian matrix can be diagonalized providing the eigenvectors, namely the *adiabatic* wave functions. This basis is given by a mixing of the diabatic states with a splitting around the crossing point, determined by twice the V^{el} interaction value: the larger the interaction, the larger the splitting and hence the deeper the energy difference between the two eigenstates. On the other hand the reorganization energy λ_{intra} in this scheme is represented by the vertical transition energy between the two diabatic curves. The balance between V^{el} and λ_{intra} changes dramatically the PES profile. Furthermore the two terms are also related to the characteristic times of the processes through their inverse and hence determine the most appropriate regime to describe the charge transport: the inverse of squared V^{el} is related to the typical time of charge motion (t_{CT}) while the inverse of λ_{intra} to the vibrational motion (t_{vibr}). A simple classification of the transport regimes is then made [11]:

- $t_{el} \ll t_{vib} \rightarrow |V^{el}| \gg E_{pol} \equiv |V^{el}| \gg \lambda_{intra}/2$.
  The electron transfer occurs much faster than any nuclear geometric reorganization. On one hand the energy stabilization upon localization triggered by E_{pol} is poor, while on the other hand the intermolecular electronic interaction is large, hence the molecules are strongly coupled. Both aspects point to a proper description of the electron wave function through a delocalized wave function: the Hamiltonian in Eq.(1.1) must encompass all the system molecules, namely the crystal periodic wave functions (bands) having width equal to $4|V^{el}|$. A wave packet is coherently spread (*band-like* transport) and the mobility is defined from the effective mass of the particle. The motion is barrierless and proceeds on the lower adiabatic PES of Fig.(1.1) (*adiabatic transfer*) [11, 10]. As mentioned this model is usually successfully applicable at low temperatures.

- $t_{el} \gg t_{vib} \rightarrow |V^{el}| \ll E_{pol} \equiv |V^{el}| \ll \lambda_{intra}/2$.
  It corresponds to the opposite situation: the vibrational motion is much faster than the charge exchange and promotes a localization of the charge on a molecular unit. Hence the charge motion proceeds with a series of incoherent jumps between

the molecular units (*hopping* transport). The Hamiltonian in Eq.(1.1) includes only a pair of molecules (dimer) in which the jump occurs. In this case the PES in Fig.(1.1) has a double well potential with a barrier to be overcome, whose height is inversely proportional to the electron coupling V^{el}, and the transfer process has an activated nature (*nonadiabatic transfer*) [11].

The systems presented in this dissertation were mostly concerned with hopping transfer, since they satisfy the requirement that $V^{el} \ll \lambda_{intra}/2$. For this reason the following discussion will focus on the hopping model.

1.1.2 Hopping transport.

In this framework the transfer process can be modeled as a reaction between a pair of molecules (named a and b):

$$a^{-(+)} + b \rightarrow a + b^{-(+)}. \tag{1.5}$$

The reactant (on the left) and the product (on the right) states are described by the diabatic wave functions. This smaller system can be described by the polaron Hamiltonian of Eq.(1.1) but restricting the sum to the two molecular units; for this reason hereafter the electron coupling is referred as V_{el} removing the ij subscript. As for chemical reactions, an expression for the kinetic constant can be defined. Since the coupling between the electronic states is small, it is possible to carry out a perturbation treatment with respect to V_{el} where the diabatic states are the zeroth order functions. To the first order, the Fermi Golden Rule formulation provides an expression for the transfer rate that has been conveniently reshuffled from J. Jortner, obtaining the Marcus-Levich-Jortner kinetic constant equation of charge transfer process [12]:

$$k_{eT} = \left(\frac{4\pi}{h}\right) V_{el}^2 \left(\frac{1}{4\pi\lambda_{class} k_B T}\right)^{\frac{1}{2}} \sum_{\nu} exp(-S_{eff}) \frac{S_{\text{eff}}^{\nu}}{\nu!} exp\left(-\frac{(\Delta G^0 + \lambda_{class} + \nu\hbar\langle\omega_{eff}\rangle)^2}{4\lambda_{class} k_B T}\right). \tag{1.6}$$

Eq.(1.6) describes both the electronic and the phonon degrees of freedom involved in the transfer at a quantum-mechanical level, as a difference form the Marcus equation that was derived in a semiclassical framework, which is more suitable for electron transfer in solution [13]. Indeed the Marcus-Levich-Jortner formulation is more appropriate when studying molecular systems in condensed phase, since the frequencies of the involved phonons are quite high (intramolecular vibrations) and it is appropriate a quantum-mechanical treatment. All the terms on the left of the summation, in the framework of classical collision theory, can be interpreted as the frequency of the electron transfer in the absence of a barrier [8]. In particular, the transfer kinetics is triggered by the squared electron coupling V_{el}, namely the intermolecular parameter: the electron transfer occurs in case of a perturbation causing a mixing between the molecular electronic states and for a high exchange rate it must be maximized (keeping in the boundaries of the hopping

model, $|V_{el}| < \lambda_{intra}/2$). k_B is the Boltzmann constant, T the temperature and λ_{class} is the reorganization energy term gathering the contribution of low frequencies phonons that can be classically described. All the terms included in the summation of Eq.(1.6) represent what in the field of spectroscopy is called Franck-Condon factors, explained in more detail in the second part of this dissertation in relation to energy transport (Chapter 7): it gathers the vibrational contribution for each $0 \rightarrow v$ transition between the vibrational states of donor and acceptor (here assuming the donor in its ground vibrational state). λ_{intra}, the intramolecular nuclear contribution (included in the polaron Hamiltonian of Eq.(1.1)) here is developed into a sum running over the normal modes of an expression, encompassing a Poissonian and an exponential function over a single effective normal mode of ω_{eff} frequency and S_{eff} Huang-Rhys factor; its global effect is to modulate the electron coupling. The total reorganization energy term should be minimized for a more efficient transport. Finally ΔG^0 represents the free energy difference between "reactants" and "products" during the reaction ($\Delta G^0 = 0$ in case of self-exchange). Interestingly from this equation naturally emerges an Arrhenius-like exponential factor, similarly as for the kinetics of more conventional chemical reactions. Additionally it is retained also the description of the inverted region, in continuity with the semiclassical Marcus equation [13]. The thermal activated character of the process justifies the typical temperature dependence of the hopping, in contrast with the band regime [5]. However this equation includes, besides the classical strategy to overcome the barrier, also the tunneling, whose role gets more relevant based on the amount of vibrational overlap between initial and final states, included in the vibrational part of the expression [8].

For the studies carried out on real molecular semiconductors in their crystal form presented in the following, the hopping model proved to be the suitable framework for the calculation of the charge transport properties, aiming to obtain the charge mobility to be compared with experimental values available in literature. In the following sections the models and the methodologies to compute the single terms of the Hamiltonian in Eq.(1.1) are presented, focusing in particular on the couplings entering the Marcus-Levich-Jortner equation Eq.(1.6) . In Section 1.2 it is discussed the computational strategy to evaluate diagonal and off-diagonal elements of the model Hamiltonian discussed in Section 1.1.1: to obtain the site energies and the electron coupling, a standard methodology based on the isolated dimer along with a novel method recently developed in the group encompassing quantum-mechanically also the effect of the surrounding embedding is presented. Practical methods for the calculation of the local electron-phonon coupling are dealt with in Section 1.3, while the non-local electron-phonon term, neglected so far, is discussed in more detail in Section 1.4. With the kinetic constants of all the available jumps of the system in hand, it is possible to simulate the charge propagation in the incoherent hopping regime, in order to get the final estimate of the charge mobility to be compared with the experimental data; the propagation of the charge also

allows to rationalized the computed values, in terms of the intricate network of available paths. The simulation is based on the solution of the classical equations of motion for the charge through an algorithm based on a Kinetic Monte Carlo method presented in Section 1.5. Finally the application of the whole machinery to semiconducting molecular systems are presented in Chapters 2-5.

1.2 Site energies and electron coupling

The system undergoing the exchange "reaction", presented in Eq.(1.5), as previously mentioned, is composed of the a and b molecule. Now, the focus is on the electronic part of the polaron Hamiltonian, Eq.(1.2), here reported once again specializing the notation for a dimer:

$$\hat{H} = \hat{H}_a + \hat{H}_b + \hat{V}. \tag{1.7}$$

It comprises the isolated molecule Hamiltonians $\hat{H}_a$ and $\hat{H}_b$ plus the intermolecular interaction operator $\hat{V}$, representing the Coulomb term between all the pairs of i-th electron belonging to a and j-th electron belonging to b:

$$\hat{V} = \sum_{i \in a, j \in b} \frac{1}{|\boldsymbol{r}_i - \boldsymbol{r}_j|} \tag{1.8}$$

expressed in atomic units.

The reactants and products wave function can be written for the "reaction" in Eq.(1.5). For simplicity hereafter it is considered the case of an electron exchange (minus superscript) but the formalism can be identically applied to hole transfer. In this development only the electronic part is considered [9, 14]:

$$\Psi_i = \psi_a^0 \psi_b^- \qquad \Psi_f = \psi_a^- \psi_b^0 \tag{1.9}$$

where ψ_a, ψ_b are the electronic states of an isolated molecule, in the neutral ground state with the superscript 0 or in the charged state with the superscript -. Ψ_i, Ψ_f are the diabatic states representing the localized valence wave functions of reactants and products of the reaction Eq.(1.5), that are the PES represented in Fig.(1.1).

The Hamiltonian matrix built on the basis of the diabatic states in Eq.(1.9) is a 2×2 matrix of this form:

$$\boldsymbol{H}_{ab}^{diab} = \begin{bmatrix} H_{11} & H_{12} \\ H_{21} & H_{22} \end{bmatrix} \tag{1.10}$$

assuming orthogonalized wave functions, such that the overlap is null. The elements of

the matrix are:

$$\begin{aligned} H_{11} &= \langle \psi_a^0 \psi_b^- | \hat{H}_a | \psi_a^0 \psi_b^- \rangle + \langle \psi_a^0 \psi_b^- | \hat{H}_b | \psi_a^0 \psi_b^- \rangle + \langle \psi_a^0 \psi_b^- | \hat{V} | \psi_a^0 \psi_b^- \rangle \\ &= E_a^0 + E_b^- + V_{11} \equiv \epsilon_b \\ H_{22} &= \langle \psi_a^- \psi_b^0 | \hat{H}_a | \psi_a^- \psi_b^0 \rangle + \langle \psi_a^- \psi_b^0 | \hat{H}_b | \psi_a^- \psi_b^0 \rangle + \langle \psi_a^- \psi_b^0 | \hat{V} | \psi_a^- \psi_b^0 \rangle \\ &= E_a^- + E_b^0 + V_{22} \equiv \epsilon_a \\ H_{12} &= \langle \psi_a^0 \psi_b^- | \hat{H} | \psi_a^- \psi_b^0 \rangle \equiv V_{el}. \end{aligned} \tag{1.11}$$

where E_a, E_b are the electronic energies of the a and b molecules in their ground (E^0) or charged (E^-) electronic states and V_{11}, V_{22} are the intermolecular interaction integrals of the "reactant" and "product" wave functions. The terms H_{11} and H_{22} are also named "site energies": assuming the ground state energy equal to 0 (as a reference), the site energies represent the energy of the charged states of the isolated molecules in the dimer, hence including the interaction with the other molecule. This aspect is important, since generally the site energy of each molecule in the dimer is different from the isolated one; additionally the site energies of a and b in the dimer can be different. This is true not only in the general case of chemically different molecules but also for identical monomers not equivalent by symmetry, due to polarization effects, that are related to the intermolecular interactions included in the V_{11} and V_{22} integrals. Both monomers in the dimer feel the interaction with the neighboring, but each one experiences different Coulomb interactions: the influence of a on b may be different from the interaction of b on a [9, 15]. This fact is strictly related to the dimer symmetry [16]: this difference approaches zero when the reactants and products diabatic states are equivalent by symmetry, i.e., they are related by a symmetry operation that makes $V_{11} = V_{22}$. This consideration is important, especially when dealing with molecules in a crystal environment (as the molecular systems taken into account in Chapters 2-5): even if the difference between ϵ_a and ϵ_b are small they might be comparable to V_{el} when it is small as well. Consequently a calculation of V_{el} might provide overestimated values, especially if employing the ESD methodology (see below) [9, 16]. Finally in Eq.(1.11) the off-diagonal term is V_{el}, the electron interaction (or electron coupling or charge transfer interaction) entering the Marcus-Levich-Jortner kinetic equation. It represents the interaction between the reactant and products diabatic configurations, causing an energy splitting when moving to the adiabatic picture Section 1.1. The adiabatic wave functions are the dimer eigenstates from the diagonalization of the Hamiltonian in Eq.(1.10), i.e., the dimer electronic states, written as linear combinations of the diabatic configurations:

$$\Psi_{1,2}^D = c_{0-}^{D1,2} \psi_a^0 \psi_b^- \pm c_{-0}^{D1,2} \psi_a^- \psi_b^0 \tag{1.12}$$

where the coefficients c_{0-}^D,c_{-0}^D are generally different (and represent two different sets for the states 1 and 2) but, when the two molecules are identical and equivalent by symmetry, the coefficients are equal and set to $1/\sqrt{2}$ in order to ensure a normalized wave function. The Hamiltonian on the basis of the eigenstates has a diagonal form con-

taining the related eigenvalues that can be analytically computed from the determinant of the 2×2 Hamiltonian matrix (1.10) and are:

$$\begin{aligned} E^D_{1,2} &= \frac{1}{2}(H_{11} + H_{22}) \pm \frac{1}{2}\sqrt{(H_{11} - H_{22})^2 + 4|H_{12}|^2} \\ &= \frac{1}{2}(\epsilon_a + \epsilon_b) \pm \frac{1}{2}\sqrt{(\epsilon_a - \epsilon_b)^2 + 4|V_{el}|^2}. \end{aligned} \tag{1.13}$$

The energy difference between the adiabatic states is the energy splitting computed at the transition state:

$$\Delta E = |E^D_2 - E^D_1| = \sqrt{(\epsilon_b - \epsilon_a) + 4|V_{el}|^2}. \tag{1.14}$$

If the site energies are equal for the two molecules ($\epsilon_a = \epsilon_b$, as it is the case for symmetry equivalent molecules, see above) the energy splitting corresponds to twice the electron interaction. These considerations are the starting point of the ESD methodology for the V_{el} calculation (see below).

A further simplification is represented by the Koopmans' theorem, i.e., the monoelectronic approximation [9, 17]. The charge exchange is assumed to occur only between frontier orbitals, namely the HOMOs for holes exchange or LUMOs for electrons. This simplification, additionally, assumes that the addition or removal of a charge does not cause a significant change in the distribution of all the other electrons. As a consequence the electronic states can be identified only by the orbitals directly involved in the exchange and the elements of the 2×2 Hamiltonian matrix in Eq.(1.10) are computed on the basis of the molecular orbitals. Two matrices can be written for HOMOs and LUMOs orbitals:

$$\boldsymbol{H}^{diab}_{ab} \simeq \begin{bmatrix} \epsilon^H_a & V^H_{el} \\ V^H_{el} & \epsilon^H_b \end{bmatrix} \qquad \begin{bmatrix} \epsilon^L_a & V^L_{el} \\ V^L_{el} & \epsilon^L_b \end{bmatrix} \tag{1.15}$$

and the elements are computed as the integrals:

$$\begin{aligned} V_{el} &= \langle \varphi^a_i(\boldsymbol{r}) | \hat{H} | \varphi^b_j(\boldsymbol{r}) \rangle \\ \epsilon_a = \langle \varphi^a_i(\boldsymbol{r}) | \hat{H} | \varphi^a_i(\boldsymbol{r}) \rangle \qquad & \epsilon_b = \langle \varphi^b_j(\boldsymbol{r}) | \hat{H} | \varphi^b_j(\boldsymbol{r}) \rangle \,. \end{aligned} \tag{1.16}$$

φ^a_i, φ^b_j are molecular orbitals located on, respectively, a and b, and are specifically the HOMOs for p-type semiconductors or LUMOs for n-type. This approximation simplifies considerably the calculation of V_{el} that now represents the interaction between two degenerate molecular orbitals belonging to a and b, and is related to the energy of the delocalized dimer orbitals. V_{el} is therefore proportional to the overlap between the wave functions of the two orbitals, and hence displays an exponential decay with the intermolecular distance. When ϵ_a and ϵ_b now represent the energy of a molecular orbital (HOMO or LUMO) belonging to a and b, under the polarization effects from the other molecule of the dimer. In this case they are different, $\epsilon_a - \epsilon_b$ enters the free energy difference term ΔG^0 in the exponential part of the Marcus-Levich-Jortner, Eq.(1.6).

As mentioned, the Hamiltonian matrix in Eq.(1.11) (as well as the monoelectronic

equivalent in Eq.(1.15)), and hence also its element V_{el}, is expressed assuming orthonormal wave functions, and this assumption retains also in the approximation of the Koopmans' theorem. However, molecular orbitals belonging to different molecules are generally not orthonormal. Therefore to properly apply the formalism presented above, it is necessary to transform the nonorthogonal set of molecular orbitals of a and b ($\{\tilde{\varphi}_i^a\}$, $\{\tilde{\varphi}_i^b\}$) into orthogonal ones ($\{\varphi_i^a\}$, $\{\varphi_i^b\}$). The employed orthogonalization procedure is the Löwdin symmetric transformation, in order to preserve as much as possible the local character of the initial molecular orbital (further details about the orthogonalization procedure in Section 1.2.1). The basis set orthogonalization is equivalent to transform the site energies and the electron coupling computed on the non-orthogonal basis $\tilde{\epsilon}$, $\tilde{V_{el}}$:

$$\begin{aligned} \tilde{V}_{el} &= \langle \tilde{\varphi}_i^a(\boldsymbol{r}) | \hat{H} | \tilde{\varphi}_j^b(\boldsymbol{r}) \rangle \\ \tilde{\epsilon}_a = \langle \tilde{\varphi}_i^a(\boldsymbol{r}) | \hat{H} | \tilde{\varphi}_i^a(\boldsymbol{r}) \rangle \qquad & \tilde{\epsilon}_b = \langle \tilde{\varphi}_j^b(\boldsymbol{r}) | \hat{H} | \tilde{\varphi}_j^b(\boldsymbol{r}) \rangle \end{aligned} \tag{1.17}$$

into the orthogonalized ones ϵ, V_{el} (also called "effective" integrals) [16],

$$\begin{aligned} \epsilon_{a,b} = \frac{1}{2} \frac{(\tilde{\epsilon}_a + \tilde{\epsilon}_b) - 2\tilde{V}_{el} S_{ab} \pm (\tilde{\epsilon}_a - \tilde{\epsilon}_b)\sqrt{1 - S_{ab}^2}}{1 - S_{ab}^2} &\equiv \epsilon_{a,b}^{eff} \\ V_{el} = \frac{\tilde{V_{el}} - \frac{1}{2}(\tilde{\epsilon_a} + \tilde{\epsilon_b}) S_{ab}}{1 - S_{ab}^2} &\equiv V_{el}^{eff}. \end{aligned} \tag{1.18}$$

S_{ab} represents the spatial overlap between the non-orthogonalized molecular orbitals involved in the charge transfer:

$$S_{ab} = \langle \tilde{\varphi}_i^a(\boldsymbol{r}) | \tilde{\varphi}_j^b(\boldsymbol{r}) \rangle \,. \tag{1.19}$$

$\tilde{\epsilon}$, $\tilde{V_{el}}$ have the same physical meaning as the analogous elements on the orthonormalized basis set but the latter are more appropriate to be employed and in particular V_{el} ($\equiv V_{el}^{eff}$) is the integral employed in the Marcus-Levich-Jortner kinetic equation, Eq.(1.6).

To compute the electron couplings V_{el} between the two molecules of an isolated dimer, two methodologies can be employed: a direct and an indirect method. In calculations on molecular systems of Chapters 2-5, only the first has been employed, but the second is also presented for the sake of completeness.

V_{el} calculation : direct method. The calculation of V_{el} is directly performed by extracting the off-diagonal elements from the matrix in Eq.(1.10), with the method also named *fragment orbital approach* [18, 19]. To simplify the calculations, the matrix is computed for the dimer neutral state (both molecules have no charge) and the neutral state geometry is used, since the transition state calculation presents many complex aspects, but the result is not expected to be dramatically different. Additionally the Koopmans' theorem is applied and hence the Hamiltonian matrix, equivalent to Eq.(1.15), is built on the basis of the molecular orbitals. Since the molecular or dimers orbitals are obtained from quantum-mechanical calculations involving the com-

plete electronic structure, the matrix operations to extract the model Hamiltonian 2×2 are performed and defined on the complete orbital basis.
When the Hamiltonian matrix is built on the diabatic basis, i.e., on the monomers molecular orbitals $\boldsymbol{H}_{ab}^{diab}$, the diagonal terms represent the molecular orbitals energies and the off-diagonal term the coupling V_{el} between the various orbitals. On the other hand, from a standard calculation it is directly available only the diagonalized form of that matrix $\boldsymbol{E}_D$, including the dimer orbital energies, and the related eigenvectors $\boldsymbol{C}_D$, the dimer delocalized orbitals in the atomic orbital basis. Therefore the problem now reduces to transform the diagonal $\boldsymbol{E}_D$ into the localized $\boldsymbol{H}_{ab}$ matrix, from which the electron couplings and the site energies can be extracted. The employed procedure, as a first step, requires the knowledge of the molecular orbitals of a and b molecules: the eigenvalues in the diagonal $\boldsymbol{E}_a$ and $\boldsymbol{E}_b$ matrices and the eigenvectors arranged in columns in the $\boldsymbol{C}_a$ and $\boldsymbol{C}_b$ matrices (in the atomic orbital basis), that are obtained through standard monomer calculations.

As an initial guess for the dimer calculation it is built the block diagonal matrix $\boldsymbol{C}_{ab}$ and each block contains the molecular orbitals of one monomer (upper block for a MOs and lower block for b MOs). This matrix represents the localized basis set of the dimer, namely the diabatic states. The elements of the Fock (or Kohn-Sham) Hamiltonian are then constructed using these orbitals as a guess. A standard calculation is run with a single SCF cycle in order to diagonalize the Fock or Kohn-Sham matrix and build the dimer eigenvalues $\boldsymbol{E}_D$, eigenvectors $\boldsymbol{C}_D$ and overlap matrix $\boldsymbol{S}$ on the atomic orbitals, without further changing the wave function. Now, the diagonal dimer Hamiltonian is transformed in its non diagonal form $\boldsymbol{F}_D$ built on the atomic basis, corresponding to the dimer Fock or Kohn-Sham matrix:

$$\boldsymbol{F}_D = \boldsymbol{S} * \boldsymbol{C}_D * \boldsymbol{E}_D * \boldsymbol{C}_D^T * \boldsymbol{S}. \tag{1.20}$$

Now finally $\boldsymbol{F}_D$ is rotated into $\boldsymbol{H}_{ab}^{diab}$, on the basis of the molecular orbitals localized on a and b (diabatic basis) $\boldsymbol{C}_{ab}$:

$$\boldsymbol{H}_{ab}^{diab} = \boldsymbol{C}_{ab}^T * \boldsymbol{F}_D * \boldsymbol{C}_{ab}. \tag{1.21}$$

$\boldsymbol{H}_{ab}^{diab}$ corresponds to the dimer Hamiltonian in the diabatic basis, in the framework of the approximations above mentioned: the diagonal elements are the site energies, namely the energies of each molecular orbital including the effect of the dimer environment. The off-diagonal ones are the electron couplings between all the pairs of MOs and the desired V_{el} have to be picked out from this matrix to construct the model 2×2 Hamiltonian. However, either V_{el} or the site energies ϵ obtained so far are not built on the orthogonalized basis set, since the orbitals $\boldsymbol{C}_a$ and $\boldsymbol{C}_b$ used to construct the $\boldsymbol{C}_{ab}$ matrix (diabatic basis set) come from calculations on isolated molecules and are hence not orthogonal. As a consequence the quantities in $\boldsymbol{H}_{ab}^{diab}$ matrix correspond to those in Eq.(1.17) and the orthogonalization procedure of Eq.(1.2) is necessary to obtain the

corresponding effective required quantities.

In general, apart from some peculiar cases (as for example the system in Chapter 3), V_{el} is computed between degenerate orbitals and particularly for the frontier ones. For non degenerate orbitals these interactions are neglected, because they are small since in most cases the energy gap between the orbitals proves to be quite large and the larger it is, the smaller the effect of the interaction between the corresponding orbitals is. However, it has been verified that some molecular systems may have HOMO-1 or LUMO+1 very close to the frontier orbitals, as it is in the case for the thienoacene derivative in Chapter 3 whose HOMO and HOMO-1 are very close. In the contest of charge transport this aspect may become relevant since it means that it might be possible to generate both types of charge carriers. For such cases, this methodology to compute V_{el} can be also generalized to the calculation of the crossed electron couplings: they are V_{el} between different types of molecular orbitals belonging to a and b molecule. They are available in $\boldsymbol{H}_{ab}^{diab}$ matrix as off-diagonal elements between non degenerate molecular orbitals.

V_{el} calculation : indirect method. As mentioned the electron coupling represents the interaction between the "reactant" and "product" electronic states and hence is the cause of the degeneracy removal between the corresponding diabatic states at the transition state geometry, Fig.(1.1). The calculation of the energy of the adiabatic states corresponding to the avoided crossing would make it possible to determine V_{el} from the energy difference as in Eq.(1.14). As mentioned above, this calculation is generally performed by employing the geometry of the dimer ground neutral state (with both a and b with no charges) as a simplification, and its electronic structure and dimer orbitals φ^D are computed. Assuming that the molecular orbitals of the monomer are energetically well separated, a given φ_k^D is built as a linear combination two degenerate molecular orbitals localized on a (φ_i^a) and b (φ_i^b):

$$\varphi_k^D = c_i\varphi_i^a \pm c_j\varphi_j^b \tag{1.22}$$

weighted by appropriate coefficients. Since in the framework of the monoelectronic approximation the electron coupling represents the interaction between the frontier degenerate molecular orbitals Eq.(1.15), it provides the energy splitting of the dimer orbitals originating from the linear combinations of the monomers HOMOs or LUMOs. More specifically, the combinations of the molecular HOMOs generate the dimer HOMO-1 and HOMO, while the molecular LUMOs originate the dimer LUMO and LUMO+1. Consequently V_{el} can be extracted backwards from the energy difference between the dimer orbitals: ΔE between the dimer HOMO-1 and HOMO provides V_{el} between the monomers HOMOs (V_{el}^H), while ΔE between the dimer LUMO+1 and LUMO provides V_{el} between the monomers LUMOs (V_{el}^L). In this method the dimer orbitals (eigenvectors) are computed through a standard Hartree-Fock or Kohn-Sham calculation and then from the difference of their energies can be recovered the desired electron coupling

by rearranging Eq.(1.14):

$$V_{el}^{H} = \sqrt{(E_H^D - E_{H-1}^D)^2 - (\epsilon_a^H - \epsilon_b^H)^2} \qquad V_{el}^{L} = \sqrt{(E_{L+1}^D - E_L^D)^2 - (\epsilon_a^L - \epsilon_b^L)^2}. \quad (1.23)$$

where ϵ_a, ϵ_b are the MOs energies of the isolated monomers again from standard calculation. Notice that this coupling fully corresponds to the effective one, since the orthogonalization is naturally included in this development. If the molecular units are fully equivalent ($\epsilon_a = \epsilon_b$) the coupling reduces to half the energy splitting between the corresponding orbitals, but also small differences between ϵ_a and ϵ_b must be included since it is notorious that to neglect this contribution may cause severe overestimates of V_{el} final value [9, 16]. The only drawback of the methodology is the loss of information concerning the coupling sign, but on the other hand it is not necessary for the purpose of inserting it in the Marcus-Levich-Jortner equation since it has to be squared, see Eq.(1.6).

1.2.1 Cluster approach

Site energies and electronic couplings are generally evaluated in the standard dimer approach described above. The method computes the energy sites and electron couplings for isolated dimers, without taking into account the possible effect of the environment surrounding the dimer in a real molecular crystal. This is generally indicated as "embedding effect", a long-range interaction due to the inclusion of the molecules in the crystal packing that can modify both the single monomer properties and their mutual interactions [20]. In particular, the molecular orbitals experience a relaxation effect induced by the long-range Coulomb and short-range exchange interactions, that can modulate their energy. In the framework of the monoelectronic approximation, the frontier orbitals accommodate the exchanged charge and the influence of the embedding represents the "polarization effect" induced by the excess charge, namely the stabilization energy experienced by the charge due to the interaction with its electrostatic environment [20]. Clearly, this aspect might be of interest for studies on molecular crystal semiconductors, since the packing might have an influence on the quantum-mechanical parameters governing the charge transport.

To this end the standard dimer method has been generalized in the so called "*cluster approach*", that considers a central reference monomer surrounded by a large number of molecules described in a fully quantum-mechanical formalism. In this way, it is possible to gain an estimate of the embedding effect on the site energies, i.e., on the molecular orbitals energies; this contribution is included also in the standard dimer approach but only partially and asymmetrically, leading to an underestimate of the effect [21]. With the cluster approach also the intermolecular interactions V_{el} among all the pairs of molecules in the cluster are computed, including the influence of the surrounding interacting molecules in contrast with the dimer approach where the dimer is isolated. Other methods for the estimate of the environment effect on the site energies are available in

literature but mostly based on a classical description of the surrounding molecules, like QM/MM or QM/PCM techniques [22, 23, 24] and microelectrostatic calculations [25]. However also examples based on a generalized fragment molecular orbital procedure are reported in literature, for a better assessment of eventual degenerate orbitals energy mismatch due to the crystal embedding [21] or the site energies and electron couplings in a stack of few molecules [26]. The novelty of the method here described lies first in the full quantum-mechanical treatment of either the central molecule or the surrounding ones, and second in considering large clusters, in an attempt to mimic a portion of the real crystal.

The cluster method requires the extension of the fragment orbital approach adopted for the dimer to a suitable cluster of N_{clus} interacting molecules, as for example those represented in Fig.(1.2), to be included in the quantum-mechanical calculation. The procedure is basically the same but a central reference molecule is selected, for which the polarization effects are computed on orbitals and intermolecular interactions. First, it is required a quantum-mechanical calculation on each monomer of the cluster but taken as isolated, providing the eigenvalues (molecular orbitals energies) and the eigenvectors (molecular orbitals wave functions). Then an analogous calculation on all the molecules together (the whole cluster) provides the cluster eigenvalues in the diagonal matrix $\boldsymbol{E}_{clus}$ and the related eigenvectors, which are the columns of the $\boldsymbol{C}_{clus}$ matrix. Then the monomer eigenvectors are assembled into the $\boldsymbol{C}_{mon}$ matrix, composed of N_{clus} blocks arranged along the diagonal, each representing one monomer; the central reference monomer is located in the first block. This matrix represents the localized basis set which the cluster eigenvalues are rotated on. Indeed the E_{clus} matrix is back diagonalized and subsequently rotated on the molecular orbitals basis set, similarly to in Eq.(1.20) and (1.21) here summarized in a single step:

$$\boldsymbol{H}_{mon}^{diab} = \boldsymbol{C}_{mon}^{T} * \boldsymbol{S} * \boldsymbol{C}_{clus} * \boldsymbol{E}_{clus} * \boldsymbol{C}_{clus}^{T} * \boldsymbol{S} * \boldsymbol{C}_{mon} \tag{1.24}$$

where $\boldsymbol{S}$ is the overlap matrix between atomic orbitals. The site energies of the reference molecule are the first diagonal terms of the $\boldsymbol{H}_{mon}^{diab}$ matrix while the electron couplings among all the monomers appear as the sparse off-diagonal elements.

However, similarly to the 2×2 case, the localized basis set is not orthogonalized. Hence the Löwdin orthogonalization procedure is applied in its more general form [27, 28]. Indeed the equations employed in the standard dimer approach, Eq.(1.2) [16], belong to the same procedure specialized and developed for the 2×2 matrix [29]. A more general form requires the construction of the orthogonalized $\boldsymbol{C}_{mon}^{ortho}$ matrix to be employed in the transformation in Eq.(1.24) instead of $\boldsymbol{C}_{mon}$ as:

$$\boldsymbol{C}_{mon}^{ortho} = \boldsymbol{S}^{\frac{1}{2}} \boldsymbol{C}_{mon}. \tag{1.25}$$

This particular procedure is employed because, as already mentioned, among all the available orthogonalization techniques, it is the one that better keeps the natural sym-

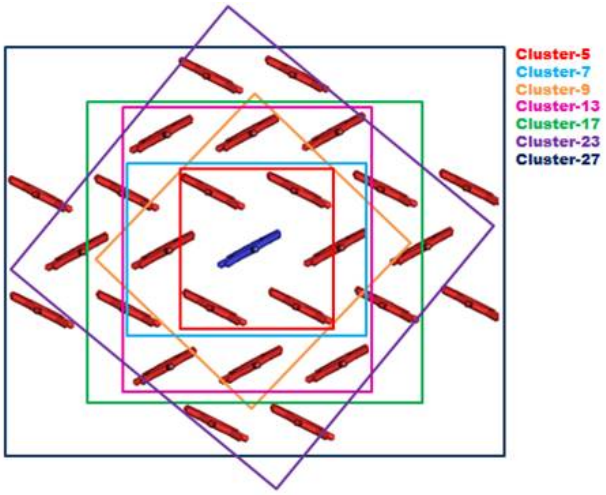

Figure 1.2: Example of cluster structure with DBTDT molecule of Chapter 3 [30].

metry of the non orthogonal basis set and hence conserves the "physical identity" of the monomers wave functions [27]. The basis set transformation of Eq.(1.25) is equivalent to directly compute the Hamiltonian matrix [29]:

$$\boldsymbol{H}_{mon}^{eff} = \boldsymbol{S}^{-\frac{1}{2}} \boldsymbol{H}_{mon}^{diab} \boldsymbol{S}^{-\frac{1}{2}}. \tag{1.26}$$

The elements in the $\boldsymbol{H}_{mon}^{eff}$ matrix are the "cluster" analogous of the effective quantities in Eq.(1.2). The $\boldsymbol{H}_{mon}^{diab}$ matrix has been either fully or partially orthogonalized: in the first case in the $\boldsymbol{S}$ matrix the overlaps between all the molecular wave functions of the basis set are included (full orthogonalization), while in the second only a subset of the molecular orbitals is included and in particular it is employed a sub-matrix formed by the HOMO or LUMO orbitals respectively for p- or n-type semiconductors (partial orthogonalization). Precisely, the exact correspondence with the dimer approach Eq.(1.2) can be recovered only with the partial orthogonalization, that lies in the framework of the same tight-binding approach with the monoelectronic approximation ("one molecule - one state" model). On the contrary, performing the full orthogonalization, is equivalent to describe each molecule with the full set of molecular orbitals and can be identified as a sort of modified tight-binding ("one molecule - many states" model).

This method has been applied to the thienoacene family members DBTDT and its derivative, in order to to estimate the solid phase embedding effect on the small HOMO/HOMO-1 energy difference and evaluate its influence on charge transport (Chapter 3 and 4). Additionally it has been used together with the standard dimer approach to study two different pentacene polymorphs and estimate the different influence of the packing (Chapter 5). The number of molecules included in a cluster is variable taking into account not only the nearest neighbors but also molecules further away from the reference one. In particular, the molecules number is set at increasing numbers of coordination spheres, as represented in Fig.(1.2): from 8 (1st sphere) up to 30 (3rd

sphere) molecules, representing intermolecular distances where Coulomb interactions are expected to decay. The computational procedure is analogous to that of the dimer approach (more practical details in Section 1.6), just extended on larger system: now the *Gaussian09* [31] calculations are run on a larger cluster of molecules instead of a dimer and the matrix manipulation according to Eq.(1.24) involves much larger arrays.

1.3 Reorganization energy (local electron-phonon coupling)

The reorganization energy λ represents the energetic contribution related to the geometry reorganization of the molecular backbone accompanying the charge transfer. This term includes not only the energy related to the nuclear arrangement of the molecule directly involved in the exchange, but also the effect on the surrounding ones in the crystal. Indeed in [32] it has been suggested that the total contribution of λ can be divided into a quanto-mechanical and a classic part:

$$\lambda = \lambda_{QM} + \lambda_{class} \equiv \lambda_{intra} + \lambda_{class}. \tag{1.27}$$

The classical contribution is usually way smaller than the quanto-mechanical one. On one hand, it includes an intramolecular contribution, ascribable to the effect of low frequency vibrational modes with an high anharmonic character and hence treated classically. On the other hand, for a molecule embedded in a crystal environment, it includes also the so called "outer sphere contribution": it is the reorganization of the surrounding medium and represents an intermolecular reorganization energy. Such a quantity is a small term difficult to compute, so in literature some estimates are available and suitable to be applied to different systems [33, 34]. This is the chosen approach for the studies presented in the following chapters. The quantum mechanical term includes only intramolecular contributions and hence hereafter is named λ_{intra}. It can be computed in two ways discussed in the following.

Adiabatic potentials method (AP). λ_{intra} is determined through the standard calculation of selected points on the potential energy surfaces (PES) of the neutral and charged states of the molecule. The electronic transitions are deemed vertical (Franck-Condon principle, exemplified by green and red arrows in Fig.(1.3)) and the total λ_{intra} is given by the sum of the neutral λ^n_{intra} and charged λ^c_{intra} contribution, see Fig.(1.3):

$$\lambda_{intra} = \lambda^n_{intra} + \lambda^c_{intra}. \tag{1.28}$$

The contribution of each state is simply given by the energy difference of the equilibrium point of the PES and the vertical point corresponding to the equilibrium geometry of the other state of interest, see Fig.(1.3).

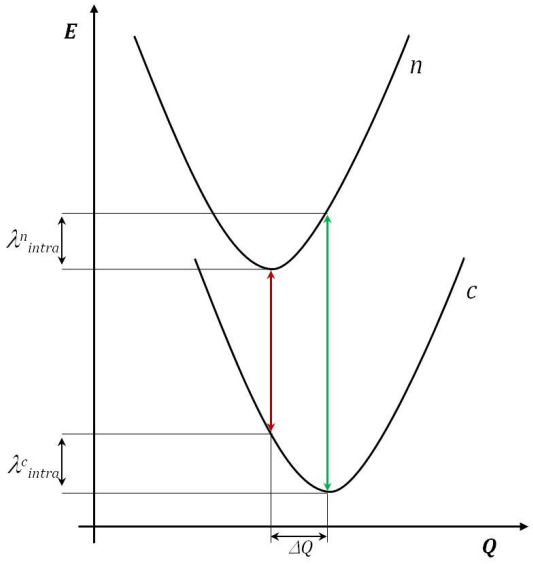

Figure 1.3: Adiabatic Potentials curves of the neutral (n) and charged (c) molecule.

Huang-Rhys factors (HR). The hypothesis which the Huang-Rhys factors (HR) method is based on is the harmonic approximation: the nuclear coordinates can be factorized into the normal coordinates that describe vibration modes independent one from the other (more details about normal modes in Chapter 7). An additional assumption is that the neutral and charged states have the same vibrational Hamiltonian, and thus the frequencies and vibration modes are similar. As a consequence the total intramolecular reorganization energy λ_{intra} can be divided into the sum of each normal mode k contribution [35]:

$$\lambda_{intra} = \sum_{k}^{3N_a-6} \lambda_k = \sum_{k}^{3N_a-6} \frac{1}{2} K_k \Delta Q_k^2. \tag{1.29}$$

The sum runs over the $3N_a-6$ vibrational modes (being N_a the number of atoms), K_k is the force constant of the normal mode k and ΔQ is the geometry difference between the equilibrium geometries of the neutral and charged electronic states. In other words it is the projection of the equilibrium geometry difference of the neutral Q^n_{k0} and charged Q^c_{k0} states on the k-th normal mode:

$$\Delta Q_k = Q^n_{k0} - Q^c_{k0}. \tag{1.30}$$

ΔQ_k can be computed from the linear transformation of the same difference in Cartesian coordinates:

$$\Delta Q_k = [\boldsymbol{R}^n_0 - \boldsymbol{R}^c_0]\boldsymbol{M}^{\frac{1}{2}}\boldsymbol{C}_k. \tag{1.31}$$

$\boldsymbol{R}^n_0$,$\boldsymbol{R}^c_0$ is the $3N_a$ dimensional vector of the Cartesian coordinates corresponding to the equilibrium geometry of, respectively, neutral and charged state; $\boldsymbol{M}$ is the diagonal matrix $3N_a \times 3N_a$ of the atomic masses and $\boldsymbol{C}_k$ is the $3N_a$ dimensional vector of the normal coordinates. In Eq.(1.29), the force constant K_k of the mode can be substituted

with its definition $K_k = \omega_k^2$ and rearranging the equation it becomes:

$$\lambda_{intra} = \sum_{k}^{3N_a-6} \hbar\omega_k^2 \frac{\Delta Q_k^2}{2\hbar} = \sum_{k}^{3N_a-6} \hbar\omega_k S_k. \tag{1.32}$$

In this way it is defined the Huang-Rhys factor of each mode k-th, S_k, a dimensionless quantity weighting the contribution of the energy quantum of each mode and according to the definition it is:

$$S_k = \frac{\omega_k \Delta Q_k^2}{2\hbar}. \tag{1.33}$$

The larger the geometry displacement between the charged and nuclear states along that normal coordinate, the larger its Huang-Rhys factor and consequently the larger the contribution to the whole reorganization energy. If $S_k = 0$, the geometry difference vectors projected along k-th normal mode are orthogonal. These HR are the same as those computed in the field of electronic molecular spectroscopy and governing the spectral intensities (more details in Chapter 7). In other words, S quantifies the vibro-electronic coupling of each normal mode: the larger the distortion associated to a certain mode due to charge exchange, the more relevant the contribution of that mode to the overall energy. This methodology provides additional information that can be associated with a specific normal mode, compared to the adiabatic potential method that provides only the cumulative λ_{intra}.

In general, the ionization (or neutralization) process does not affect the symmetry of the molecule that hence is conserved. Accordingly only the totalsymmetric (TS) normal modes have non zero Huang-Rhys factors. Indeed the TS vibrations determine a geometry distortion that do not break the molecular symmetry and therefore along the TS coordinates the neutral and charged equilibrium geometries of the PES are in different positions: $\Delta Q_{TS} \neq 0$. On the contrary, the same minima along NTS coordinates have the same position with $\Delta Q_{NTS} = 0$ as well as the corresponding Huang-Rhys factor $S = 0$. Indeed, the summation in Eq.(1.29) runs only over the TS modes, since the NTS ones provide zero contribution [35].

In the Marcus-Levich-Jortner equation Eq.(1.6), λ_{intra} appears as an "average" through the definition of a single effective mode of ω^{eff} frequency, given by the average of the single modes frequencies (ω_k) weighted on the corresponding Huang-Rhys factors S_k:

$$\omega^{eff} = \sum_{k}^{3N_a-6} \omega_k \frac{S_k}{\sum_l^{3N_a-6} S_l}. \tag{1.34}$$

It is similarly defined also the corresponding effective Huang-Rhys factor S^{eff} as a function of the total reorganization energy:

$$S^{eff} = \frac{\lambda_{intra}}{\hbar\omega^{eff}}. \tag{1.35}$$

1.4 Thermal disorder (non-local electron phonon coupling)

Calculations aiming to reproduce data as close as possible to real systems cannot avoid to tackle the effect of the temperature on charge transfer process. Recalling the explanations sketched in Section 1.1, the temperature activated lattice vibrations, with their uncorrelated motion [36], break the translational symmetry similarly as static disorder does; the consequence is the localization of the charge wave function with loss of coherence and, also for systems describable with delocalized wave function models, the band-like charge transport regime breaks down [36, 37]. For molecular systems described with the hopping model, as it is the interest in this work, the "dynamic localization" is not necessarily a factor depressing the mobility, since it increases the jump probability (being an activated process) and may even open transport paths forbidden at lower temperatures (see below). The thermally induced vibrations interact with the electron properties (electron-phonon coupling) and can affect both the intramolecular properties and the intermolecular interaction.

The local coupling (or diagonal or Holstein coupling) describes the modulation of the site energies, i.e., HOMO and LUMO molecular orbitals energies. This coincides with the intramolecular reorganization energy, namely the molecular energy change upon ionization, that in the framework of the monoelectronic approximation is identified by the site energy. The coupling is represented by the Huang-Rhys factor, Eq.(1.33), as described in Section 1.3. It was directly included as the E_{pol} (or λ_{intra}) term in the polaron model, Eq.(1.1), as described in Section 1.1.

The nonlocal coupling (or off-diagonal or Peierls coupling) refers to the modulation of the transfer integral V_{el} due to the oscillations of the molecular positions around their equilibrium distance while the lattice vibrates. Indeed V_{el} has an extreme sensitivity on reciprocal displacements and rotations of neighboring molecules in the dimer, since it is directly related to the wave functions overlap [37]. This mechanism represents a non-Condon effect since the variations of V_{el} are an explicit function of the vibrational coordinates. The non-local electron-phonon interaction appears when expanding up to the first order the electron coupling in power series of the lattice normal coordinates Q [38]:

$$V_{el} = V_{el}^0 + \sum_i \left(\frac{\partial V_{el}}{\partial Q_i} \right) Q_i + ... \tag{1.36}$$

V_{el}^0 is the coupling at the static equilibrium geometry and its first derivative with respect to Q represents the linear electron-phonon coupling. It is a measure of the extent to which each lattice mode i influences the electron coupling. Its role is similar to that of Huang-Rhys factors for the local coupling. On the contrary in this case from the point of view of the symmetry, contributions are given by both totally and non-totally symmetric lattice vibrations but their impact on V_{el} might be different: some distortions significantly affect the electron density pattern, namely the molecular orbital

pattern [38]. This has been clearly pointed out especially when considering molecules in translationally non equivalent lattice positions: while TS vibrations conserve the same V_{el} pattern, distortions along antisymmetric phonons may create an alternation ("Peierls type dimerization") of the intermolecular distances and a mirrored alternating variation of the electronic couplings ("antisymmetric non-local electron-phonon coupling") [38, 39].

The involved lattice vibrations are low frequency intermolecular modes and hence are usually included in the framework of semi-classic models [36]; for the same reasons they are also assumed decoupled from intramolecular vibrations, that can be hence neglected to exploit a rigid body model. Hence the evolution in time of $V_{el}(t)$ is governed by the classical motion of the molecular backbone and its only effect is to modulate the interaction magnitude. Each mode contributes independently to V_{el} fluctuations and, despite the small contribution of each one, the global effect can be very relevant for crystals containing many low frequency phonons. Additionally it has been demonstrated [36] how, to a good degree of approximation, the fluctuations of various V_{el} between different dimers can be considered uncorrelated and independent one from the other.

A typical approach to assess the role of lattice thermal fluctuations in the framework of a semiclassical approximation is employing Molecular Dynamics (MD). A trajectory is run for several picoseconds on a lattice portion and some snapshots are collected, in order to have several lattice geometries, with the molecules treated as rigid bodies oscillating around their equilibrium position. For each snapshot a QM calculation is run to evaluate the time evolution of V_{el}, presenting a characteristic oscillating behavior, as in the example represented in Fig.(1.4) left. The V_{el} values belong to a Gaussian distribution, see Fig.(1.4), right [38]:

$$f(V_{el}) = \frac{1}{\sqrt{2\pi}\sigma} exp\left[-\frac{\left(V_{el} - \langle V_{el}\rangle\right)^2}{2\sigma^2}\right], \tag{1.37}$$

whose variance represents a measure of its thermal fluctuations:

$$\sigma^2 = \left\langle \left[V_{el} - \langle V_{el}\rangle\right]^2 \right\rangle. \tag{1.38}$$

The higher the temperature, the wider the distribution. $\langle V_{el}\rangle$ represents the average value, namely the Gaussian center; its position should match the transfer integral computed at the static equilibrium geometry of the crystal, but actually it might be slightly shifted due to small changes of the crystal structure at the higher temperature set in the dynamic. However an important point is to check that this shift is not too large, since it may be a symptom of problems in the force field choice. If the $f(V_{el})$ distribution significantly deviates from a Gaussian shape, it means that the linear dependence of the electron couplings from the normal coordinates, as assumed in Eq.(1.36) is no longer suitable, and higher order terms in the expansion are required [37].

As suggested in [37], the impact of the lattice vibrations on the charge transport

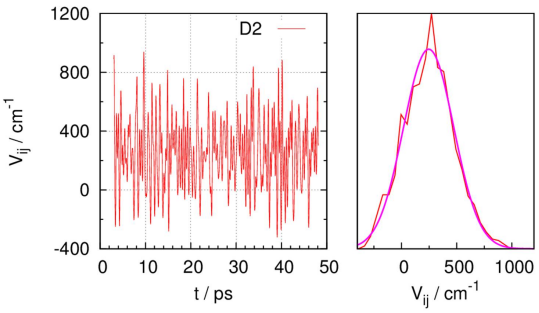

Figure 1.4: Example of thermally induced disorder effects (300K) on the distribution of V_{el} associated with the D2 pathway of FNDI (Chapter 2 and [40]): (left) fluctuation as a function of time and (right) Gaussian fitting (magenta) of the dispersion of computed couplings (red).

properties, with respect to that at the equilibrium geometry is evaluated considering the ratio η:

$$\eta = \left| \frac{\langle V_{el} \rangle}{\sigma} \right| \tag{1.39}$$

between the average value of V_{el} and the width of its distribution. On the basis of η several cases can be distinguished. As a first case, if η has a large value: the static V_{el} is large and the distribution width σ is small. In such a case the lattice dynamics perturbs only slightly the charge mobility properties and hence its impact is moderate or small. On the contrary, if η has a small value the transfer integral has a vanishingly small value, centering the Gaussian distribution around zero, with a finite width. In such a case the effect of the thermal vibrations can be determinant, since they may open new hopping paths along directions forbidden in the static crystal. Kinetic Monte Carlo simulations of charge propagation must take into account this aspect in the proper way (see below). Finally, the average $\langle V_{el} \rangle$ and the Gaussian distribution width might have similar values (η has intermediate values), and in that case the fluctuations impact should be carefully evaluated on a case by case basis.

The Fourier transform of the autocorrelation function of the electron couplings $\langle V_{el}(t = 0) V_{el}(t) \rangle$ allows to identify the frequencies of the lattice vibrations governing the coupling fluctuations. They can be plotted in a sort of a spectrum that, if properly simulated, may have some peaks in common with the Raman spectrum of the molecular crystal [36], see Fig.(2.12). It must be kept in mind that the basic assumption is a classical description of the vibrational modes, that is reliable if the involved vibrational frequencies are low enough, allowing the employment of classical Molecular Dynamics. However it is necessary a careful check on this aspect, in order to establish a correct procedure to include the thermal effects in the KMC simulations of charge transport, as explained in Section 1.5.

1.5 Charge propagation: Kinetic Monte Carlo

The problem to be tackled, namely charge transfer in the framework of the hopping approximation, can be conveniently represented as a stochastic process. Indeed the quantum effects on charges carriers can be assumed to be lost in the hopping regime, since it is an incoherent motion; consequently a wave function based model can be abandoned in favor of a classical description [11]. The system before and after a charge is exchanged represents the initial and the final state. The charge jumps define the transitions and they are modeled as independent and rare (or infrequent) events, assuming that each one occurs at a significantly longer time scale than the system vibrations (i.e., lattice phonons). Consequently, to a good approximation, the vibration time scales and the event time scales are assumed decoupled [41]: indeed, each state (i.e., each system condition in which the charge is localized on a molecular unit) is a local energy minimum and the long time between the transitions is due to the fact that the system must overcome an energy barrier [42], so the residence time of the system in a local minimum of the potential surface is several orders of magnitude larger than the vibrational times scales [41]. In this framework the sequence of charge jumps can be characterized as a Poisson process, whose formal mathematical description presents well known and convenient features [43]. Additionally, rare events that stay in a potential well for long times (in this case regarding the time of a vibration) are memoryless: all the history about how they got there is basically lost due to the vibrations between the two transitions [41]. This characteristic of hopping process allows to assume the system undergoing a Markovian process: the probability of occupying a generic i state depends only on P_{i-1} and not on the previous states. As a consequence a Markovian system is completely defined by an initial state and the related probability densities, providing a model considerably simplified [41]. The rate constants k are the parameters describing the probability to move from the state i to the state j. For the problem under discussion, namely the hopping charge transport, for each jump $i \rightarrow j$ the kinetic constant is provided by the Marcus-Levich-Jortner equation, Eq.(1.6), to be computed between each pair of molecules forming the system. The kinetic equations describing such kind of processes are the master equations, a set of coupled differential equations, defining the time evolution of the probability of the system to be at a given state j at a given time t [44]:

$$\frac{\partial P_j(t)}{\partial t} = \sum_{i \neq j} k_{ij} P_i(t) - k_{ji} P_j(t) \tag{1.40}$$

where k_{ij} is kinetic constant of the $i \rightarrow j$ transition and k_{ji} is the opposite. Globally the equation represents a gain-loss balance for the probabilities of populating i and j states and when taking into account all the system states, the differential equations system to be solved becomes very large. Kinetic Monte Carlo (KMC), in its dynamical interpretation [43], represents a convenient numerical way to solve the master equations, provided that the phenomenon under investigation is stochastic in nature. Hence the dynamical (or kinetic) Monte Carlo has been developed to describe systems dynamically

evolving from state to state, in a non equilibrium condition [42]. KMC treats directly the transitions between the states, making the method suitable to be adapted for different systems undergoing processes over different time scales: the total simulation time is strongly system dependent [42].

A Kinetic Monte Carlo algorithm is set up to properly propagate the system state. In each KMC trajectory a single charge carrier is let move in the crystal through hopping events occurring between pairs of near neighbors molecules (dimer). As a first step, the molecule of the crystal representing the starting point for charge propagation is randomly selected. The general probability P_j associated with the jump of the charge carrier to the j-th neighbor of a given molecule is:

$$P_j = \frac{k_j}{\sum_{n=0}^{N_{neigh}} k_n} \tag{1.41}$$

where k is the Marcus-Levich-Jortner kinetic constant and the sum over n runs over the possible paths for a charge on a giver molecular unit, i.e., the number N_{neigh} of nearest neighbors available for the jump. The transition probabilities are computed this way in order to guarantee the detailed balance condition in the simulation [43], namely the full reversibility of each step. Then the trajectory is advanced by choosing a random number Y uniformly distributed between 0 and 1. The target of the jump is the neighboring site j fulfilling the relation:

$$\sum_{n=0}^{j-1} P_n < Y \leq \sum_{n=0}^{j} P_n. \tag{1.42}$$

This method allows a random selection of the target sites, weighted on the exchange rates, that ensures the independence of events comprising the time sequence of the process: this is a criterion to be strictly fulfilled for a proper simulation of a Poisson process [43]. Now the selected jump to the j molecule is executed. The system configuration is modified by updating the charge carrier spatial position: the distance associated with the hopping is the distance between the centers of mass of the starting and arrival molecules. Also the simulation time is updated by adding the Δt of the jump. The time interval Δt associated with a single KMC event (namely the charge transfer) it is demonstrated to be [41]:

$$\Delta t_j = -\frac{\log X}{\sum_{n=0}^{N_{neigh}} k_n} \tag{1.43}$$

where X is a random number again uniformly distributed between 0 and 1 and the sum is over all the available jumps. In this way the time of each event is picked from an exponential distribution, again in relation with the features of Poisson processes [43]. Hence each event advances the simulation time of a slightly different time increment but the average time step is:

$$\Delta t_{ave} = \frac{1}{\sum_{n=0}^{N_{neigh}} k_n}. \tag{1.44}$$

the inverse of the sum of the rate constants. The procedure of choosing the time step increment according to Eq.(1.43) is demonstrated to ensure a direct relationship between Monte Carlo simulation time and real time [43]. Now, the new configuration becomes the starting point of a new jump and the whole procedure is iterated for a large number of points. A series of KMC trajectories is collected for a convenient averaging of the properties: since KMC is a stochastic method its results suffers from a statistical error, that can be lowered by exploiting a larger number of simulations.

Simulations run this way and with constant temperature describe the transport of a single charge carrier undergoing a Brownian motion, with a diffusive behavior, as the trajectories depicted as an example in Fig.(1.5) left. From the simulations it is collected the mean square displacement of the charge $\langle \Delta r^2 \rangle$ with respect to the initial position as a function of time: $\langle \Delta r^2 \rangle = \langle [r(t) - r(0)]^2 \rangle$. This quantity is important since it is related to the diffusion coefficient D through the Einstein equation [44]: at long time intervals, as shown in Fig.(1.5) right, the relation between time t and the mean square displacement becomes linear on the average and the slope represents the diffusion coefficient

$$D_{\alpha\beta} = \lim_{t\to\infty} \frac{\langle \Delta r_\alpha \Delta r_\beta \rangle}{6t}, \tag{1.45}$$

with $\alpha, \beta = x, y, z$. $\boldsymbol{D}$ is a 3×3 tensor and each term is provided by taking different Cartesian components of $\langle \Delta r \rangle$. The average diffusion coefficient D is a macroscopic quantity computed in the same way of Eq.(1.45) but employing $\langle \Delta r^2 \rangle$ instead of each Cartesian component. The diagonalization of the diffusion tensor allows to visualize the mobilities (its eigenvalues) along the crystallographic directions (its eigenvectors). The Einstein-Smoluchowski equation, finally, provides the elements of the mobility tensor $\mu_{\alpha\beta}$ [44]:

$$\mu_{\alpha\beta} = \frac{D_{\alpha\beta}}{k_B t} \tag{1.46}$$

and the average mobility μ is analogously the ratio between the average diffusion coefficient D and the "thermal quantum" $k_b T$, as in Eq.(1.46). The final mobility is obtained based on the distance traveled by a charge carrier, which is basically provided by a sum of random variables. As a consequence μ is affected from a statistical error that can be estimated as half of the difference between the minimum and the maximum mobility values [45]:

$$error = \frac{\mu_{max} - \mu_{min}}{2}. \tag{1.47}$$

The error is demonstrated to converge towards low values by increasing the number of simulations trajectories included in the averages. An alternative formulation of the diffusion tensor reported in literature is the "isotropic approximation" [46]:

$$D = \frac{1}{6} \sum_i r_i^2 k_i P_i \tag{1.48}$$

where the square of the intermolecular distance associated with the jump to the i-th site, r_i, times the associated kinetic constant k_i are weighted for the jump probability. This

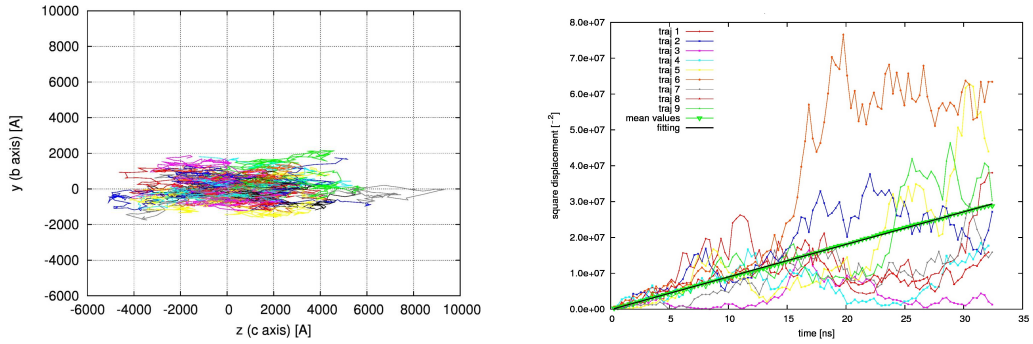

Figure 1.5: (left) Plot with an example collecting several Brownian trajectories of FNDI (Chapter 2 and [40]) in the $y(\equiv b)z$ plane and (right) as a function of time, highlighting the average linear behavior.

expression is way more approximated of the Einstein equation in Eq.(1.45) providing values usually severely underestimated. This is due to the basic assumption of an isotropic medium in which the charges can jump and so its deviation from the more correct value of Eq.(1.45) can provide a measure of the degree of anisotropy of the transport process.

However in the experiments measuring charge mobility, as for example TOF (Section 1.1), an electric field $\boldsymbol{E}$ along a precise direction is applied. It represents a driving force guiding the charge movements and adds an additional energy gradient, perturbing the site energies that must be taken into account in the Marcus-Levich-Jortner kinetic constants expression, Eq.(1.6), with an additional free energy term $\Delta G_E^0 = -e\boldsymbol{r}_j \cdot \boldsymbol{E}$, with e the unit charge, r_j the jump distance to the j-th molecule and E the field modulus. The KMC simulations performed under the influence of an electric field, are of the "time of flight" type (TOF), aimed to mimic more closely the experimental conditions. The "crystal" in which the simulation runs has a fixed dimension d resembling the experimental device thickness (TOF measurements are performed on thin films, Section 1.1). Now the trajectory propagates under the effect of $\boldsymbol{E}$, until the charge has traveled the distance d and providing the time employed by the charge τ. The TOF mobility can be estimated as [45]:

$$\mu_{TOF} = \frac{d}{\tau E}. \tag{1.49}$$

τ is computed as the sum of the jumps time steps, Eq.(1.43). In principle a single trajectory would be sufficient for the evaluation of μ_{TOF}, since in this case the motion is no longer diffusive but more of a ballistic character, however for a better statistics it is averaged over several trajectories. The TOF mobility is very important since it is the quantity that can be directly compared with the experimental charge mobility values. Including $\boldsymbol{E}$ oriented along different directions, μ_{TOF} takes different values, because the charge motion is differently affected. Collecting the μ_{TOF} values for different $\boldsymbol{E}$ directions provides the mobility anisotropy along different directions of the system under investigation.

The impact of the thermal effects (Section 1.4) on the charge mobilities can be

assessed by running proper KMC simulations. To this end, it is necessary a preliminary careful comparison between the vibrational frequencies and the charge transfer rates. Typically charge transfer happens with times of the order of fs, hence with rates of about $10^{13} - 10^{15}$ s^{-1}. Frequencies below 10^{12} s^{-1} correspond to vibration energies roughly below 200 cm^{-1}, typical of low frequency phonons. In these cases, the charge "sees" the lattice in sort of averaged vibrational state. The thermal effects are accounted for following the "thermalized" method, i.e., by including into the Marcus-Levich-Jortner rate of each jump the corresponding $\langle V_{el}^2 \rangle$ [37]. On the contrary, for faster vibrations, it is less straightforward: in this case each jump occurs at a rate extracted from the distribution of V_{el} implying the necessity to run several KMC trajectories on several MD snapshots and mediate the resulting mobilities.

1.6 Integrated QM-KMC-MD approach

The studies carried out on the molecular systems described in Chapters 3-5, employed an integrated computational approach in order to compute all the parameters described above. A scheme of the methodology is available in Fig.(1.6).

The starting point in all cases is the experimental crystal structure of the molecular system under investigation, employed for the experimental measure of charge mobility. The crystal is analyzed in order to identify the single molecule structure, for the calculations of intramolecular parameters, and the dimers, namely the pairs of nearest neighbors molecules for the calculation of the intramolecular parameters. The possible dimers are identified by evaluating the distances between the centers of mass of the molecules surrounding a central reference molecule in the crystal.

As a first step the single molecule geometry is optimized on the neutral and charged states and the nature of the stationary point is assessed by evaluating vibrational frequencies at the optimized geometry.

Then the site energies and electron couplings of the selected dimers (Section 1.2) are computed with the direct method. It requires a preliminary single point quantum-mechanical (**QM**) standard calculation on the two isolated monomers and on the molecular dimer, run with *Gaussian09* program [31]. The matrices of molecular and dimer eigenvalues and eigenvectors are collected and further elaborated by a program available in the group, that performs the necessary matrix multiplications, Eq.(1.20) and (1.21), along with the orthogonalization procedures, Eq.(1.2), providing the effective quantities to be used for the evaluation of the charge transport properties. The QM calculations are usually run at the B3LYP/6-31G* level of theory, that has been demonstrated to provide reliable results.

The reorganization energy (Section 1.3) is computed with both the adiabatic potential and the Huang-Rhys factors methods. The first one requires the calculations of the single points on the neutral and charged potential surfaces, see Fig.(1.3), computed through a standard QM calculation with the *Gaussian09* program [31]. The second

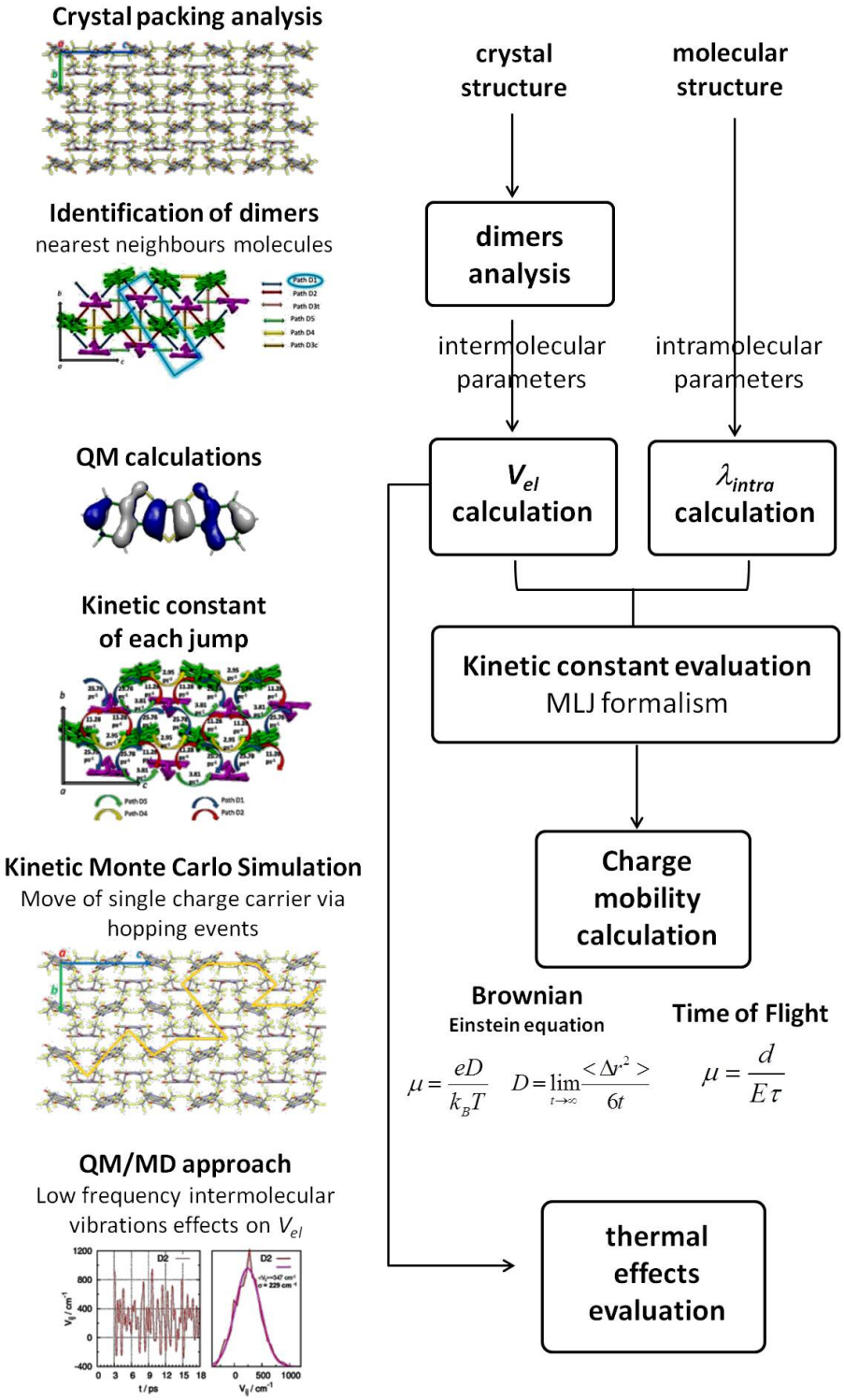

Figure 1.6: Scheme of the practical computational QM-KMC-MD approach employed for charge transport studies.

methods requires the equilibrium structures, in Cartesian coordinates, and the molecular vibrations, computed for both the ground and the charged states with *Gaussian09* [31]. Then, with a code available in the group, the geometry differences are projected on the normal modes, Eq.(1.31), and the Huang-Rhys factors are evaluated, Eq.(1.33), along with the intramolecular reorganization energy for higher frequency modes (> 250 cm^{-1}), Eq.(1.32). The lower frequency ones are collected in a "classical term", along with the external (intermolecular) reorganization energy, taken from estimates available in literature of about 0.01 eV. Finally the effective frequencies and Huang-Rhys factor to be inserted in the Marcus-Levich-Jortner equation are computed. Also in this case the B3LYP/6-31G* level of theory has been validated as a reliable method, through the comparison with UPS spectra [5].

Then the intra and inter molecular parameters obtained so far are employed in the Kinetic Monte Carlo (**KMC**) method for the propagation of the charge carrier in the crystal, to provide estimates of the charge mobility and its anisotropic character. With the KMC code available in the group, 20000 Brownian trajectories are run and divided in ten subgroups: this amount of simulations is proven to ensure a converged D coefficient, namely a linear relation between the square of the diffusion distance and time. The charge mobilities are computed for each subgroup and then mediated to provide the final value. Each trajectory consists typically of 10^6 moves and the temperature is set to 300 K. The final TOF mobility is computed by averaging over 100 trajectories. The magnitude of the electric field E is set to 10^{-5} Vcm^{-1} and the device thickness d is 50 μm, according to typical TOF experimental values. Electric field of that magnitude are not expected to influence significantly the electron distribution of the molecular orbitals nor their interactions; hence also in TOF simulations the quantum parameters employed (V_{el}, λ_{intra} and the site energies) are those computed for the unperturbed molecule as explained in the previous sections.

To assess eventual effects of thermally induced dynamical disorder, Molecular Dynamics (**MD**) simulations are run in combination with a quantum-mechanical evaluations of the electron coupling fluctuations. The MD simulation is run on a supercell of suitable dimension, built from the experimental unit cell. The dynamics is run by employing periodic boundary conditions (PBC) with the MM3 force field [47], suitable for conjugated systems, and the *Tinker* code [48]. The intramolecular degrees of freedom are kept frozen (rigid body dynamics) allowing only intermolecular motions. The simulations are run in the NVT ensemble (Berendsen's thermostat [49]) at room temperature ($T = 300$ K) to mimic the real crystal conditions. The dynamics lasts 100 ps and the integration step is 1 fs. A snapshot is picked every 30 fs, collecting 500 snapshots in total, and for each of them the V_{el} couplings are quantum-mechanically computed, in order to build the time evolution and the Gaussian distribution. Then, based on the relevance of V_{el} fluctuations, eventually KMC simulations in the thermalized limit (when suitable) are run.

This protocol available in the research group has been already successfully applied

to investigate the combined effect of intra- and inter- molecular properties on the charge transport of some fluorinated and chlorinated perylene-diimide (PDI) derivatives [50, 51]. In the following it will be shown its application to a naphtalene-diimide derivative, a *n*-type semiconductor (Chapter 2), and to some members of the thienoacene family (Chapter 3 and 4), providing a rationalization of their mobility anisotropy as well as a deeper insight of the underlying transport mechanism. Finally it has been applied to two pentacene polymorphs (Chapter 5) along with the cluster approach for the evaluation of the electron couplings, to assess the impact of the different crystalline environment on the charge transport properties.

CHAPTER 2

FNDI: Anisotropy of the *n*-type charge transport and thermal effects in crystal of a fluoro-alkylated naphtalene diimide

The content of this chapter is reproduced in part from Ref.[40]:
Canola S., Negri F. *Phys. Chem. Chem. Phys.*, **2014**, *16*, 21550-21558
with permission from the PCCP Owner Societies.

2.1 Introduction

Naphthalene diimide (NDI) derivatives are promising *n*-channel organic semiconductors [52, 53, 54], due to their easy synthesis from commercially available precursors combined with their high electron affinity and the tenability of their optoelectronic properties. Core-substituted NDIs are emerging as a class of conducting and functional materials [55, 56, 57]. On the other hand, chemical substitution at the imide nitrogens influences molecular packing in the solid state and therefore their charge transport properties and mobility [58, 59]. NDI derivatives without core substitution have shown remarkable high field effect mobilities (6 cm^2/Vs [60]) although suffering by lack of stability under ambient conditions. Ambient stability can be improved by introducing strongly electron-withdrawing groups such as fluoroalkyl groups [61, 62, 63]. Fluoro-alkylated and non-fluorinated analogues were synthesized and used to fabricate solution cast *n*-channel field effect transistors (FETs). Recently core-chlorinated NDI derivatives with different fluorinated side chains [62, 63] have shown electron mobilities up to 1.43 cm^2/Vs in thin film transistors prepared by vacuum deposition or solution shearing deposition. More recently, remarkably high mobilities up to 8.6 cm^2/Vs have been measured on ribbon-shaped crystals [61] of one of the three core-chlorinated NDI derivatives previously studied in thin films. Computational investigations on electron transport in NDI derivatives have been reported [64] and have shown an interplay between intermolecular

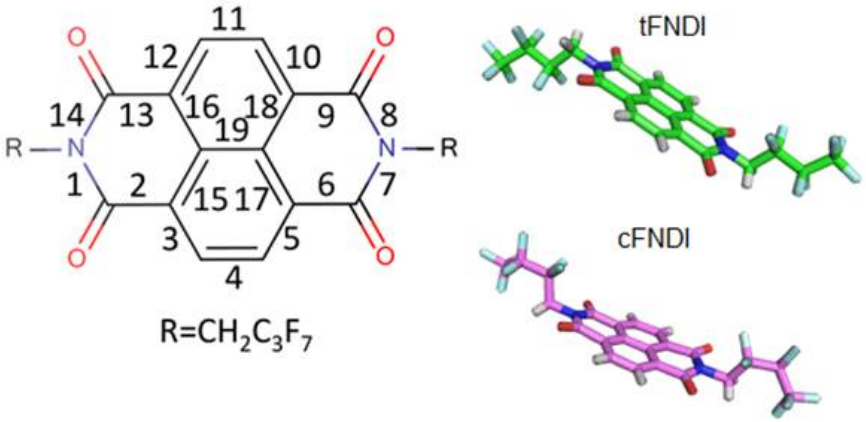

Figure 2.1: (left) Structural formula of the NDI derivative considered in this work and (right) the two conformers tFNDI and cFNDI that form the crystal.

interactions and molecular packing. A single crystal of a π-conjugated molecule represents a superior substrate for the study of its electric properties since the trap density originating from structural defects and hopping barriers among grains are minimized. This enables the evaluation of charge carrier mobilities close to the intrinsic values of the molecular material that can be compared with those determined by appropriate modeling. Recently, the n-type charge transport of the fluoro-alkylated NDI derivative shown in Fig.(2.1), previously investigated in thin film transistors [58], has been investigated in single-crystal devices fabricated with the "organic ribbon mask" technique [65, 66]. The two dimensional hexagonal shape of the crystals grown allowed the measurement of charge transport anisotropy which resulted in a factor of 1.6. The highest mobility of 0.7 cm^2/Vs was measured along the c axis, while mobility along the b axis did not exceed 0.45 cm^2/Vs [65]. Prompted by the availability of measurements in single crystals, here it is investigated the charge transport properties of the fluoro-alkyl NDI derivative of Fig.(2.1), hereafter labeled FNDI. Because the crystal of FNDI includes two conformers, one in which the imide fluoroalkyl substituents are on the opposite side with respect to the molecular plane (substituents in *trans* hereafter labeled tFNDI) and one in which the imide substituents are on the same side with respect to the molecular plane (substituents in *cis* hereafter labeled cFNDI), as shown in the bottom part of Fig.(2.1), both were considered in the calculations. The aim is to explore the effect of intra-molecular and inter-molecular parameters paying also attention to the possible role of thermally induced dynamical effects. To this end the previously introduced multi-scale protocol (Section 1.6) is employed: QM methods are used to evaluate of inter and intra-molecular charge transport parameters required to estimate charge transfer rate constants to be injected in a KMC scheme. Finally, based on the previously reported strong effects of thermally induced dynamical disorder for PDI derivatives, MD simulations combined with QM evaluation of electronic couplings, were employed to investigate the extent of fluctuations and the inter-molecular motions responsible for them.

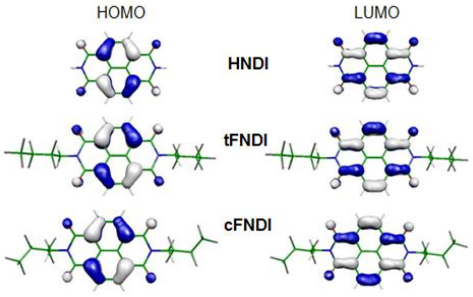

	geo. neutral [eV]			geo. anion [eV]
	E_H	E_L	ΔE_{HL}	ΔE_{HL}
tFNDI	-7.73	-4.15	3.57	3.24
cFNDI	-7.72	-4.15	3.57	3.24
HNDI	-7.51	3.93	3.59	3.25

Figure 2.2: (left) Frontier orbital energies of tFNDI, cFNDI and model compound HNDI computed at the B3LYP/6-31+G* optimized structures of the neutral species. (right) Transport gaps computed at the optimized structures of the neutral and anionic species.

Table 2.1: VEAs, AEAs and intramolecular reorganization energies λ_{intra} for tFNDI, cFNDI and HNDI computed at the B3LYP/6-31+G* level of theory.

	VEAn [eV]	VEAc [eV]	AEA [eV]	λ_{intra}=(VEAc-VEAn) [eV]
tFNDI	2.72	3.11	2.92	0.382
cFNDI	2.72	3.11	2.92	0.388
HNDI	2.46	2.79	2.63	0.332

2.2 Intramolecular properties

Beside FNDI also a model system featuring hydrogen atoms at the core and imide positions, hereafter labeled HNDI, was considered for comparison. From the equilibrium structures of neutral and charged species of both tFNDI and cFNDI both electron affinities and intramolecular reorganization energies are estimated: vertical electron affinities (VEA) of NDI derivatives were directly estimated as energy differences between neutral and charged species both computed at the geometries optimized for the neutral (VEAn) or the charged (VEAc) species. Fluorine substitution at the imide positions lowers the energy of the LUMO level, see Fig.(2.2), and increases the electronic affinity, thereby strengthening the n-type character of the semiconductor. This effect can be appreciated by comparing the energies of the LUMO levels of tFNDI and cFNDI reported in Fig.(2.2) and the correspondingly computed vertical and adiabatic EAs in Table 2.1 with those of the model compound HNDI. The computed LUMO energies of these NDI derivatives are in good agreement with those estimated from experimental reduction potentials [65]. Energetic disorder [37, 8] was neglected and it should be noted that in the one-electron approximation adopted to model electronic couplings, the site energy difference between tFNDI and cFNDI molecules is zero (see the LUMO energies in the Table of Fig.(2.2)) and therefore ΔG_0 was kept to zero.

The intramolecular reorganization energies of FNDI, Table 2.2 estimated from the adiabatic potential method [5, 9], fall in the region of about 0.380 eV and are very close to those determined from the Huang-Rhys factors. These computed values are relatively large compared with those of bay unsubstituted PDI derivatives (of the order of 0.260

Table 2.2: Reorganization energies computed with AP and HR method; Average of the parameters computed for the two conformers employed in the KMC simulations.

	Huang-Rhys				AP		
	λ_{intra} [eV]	λ_{class}intramol [eV]	S^{eff}	ω^{eff} [cm^{-1}]	λ_{intra} [eV]	λ^{n}_{intra} [eV]	λ^{a}_{intra} [eV]
tFNDI	0.013	0.012	3.058	975	0.382	0.192	0.190
cFNDI	0.011	0.010	3.152	967	0.388	0.194	0.194
KMC	0.012	0.011	3.105	971	-	-	

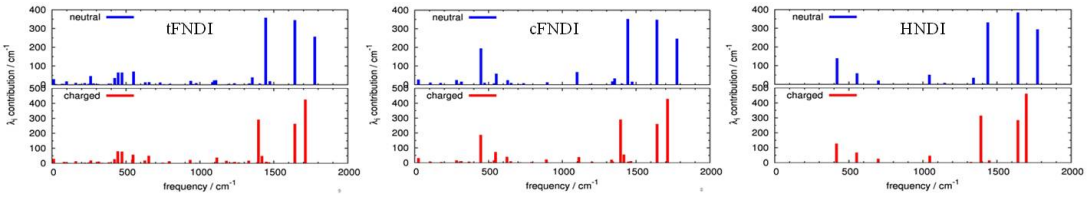

Figure 2.3: Huang-Rhys factors of tFNDI, cFNDI and HNDI.

eV), and in line with those of other NDI derivatives [66]. The outer sphere contribution to the reorganization energy was assumed to be 0.001 eV, in keeping with recent studies [34]. The computed vibrational contributions to the intramolecular reorganization energies are collected in Fig.(2.3) from which it is seen that the active modes are very similar for neutral and anionic states. The contributions from frequencies above 250 cm^{-1}, namely the frequencies that cannot be considered classical, were employed to estimate the effective parameters of the single quantum mode to be introduced in the Marcus-Levich-Jortner equation, ω_{eff} and S_{eff}. The remaining contributions were included into the λ_{class} parameter [32, 67, 68] together with the outer-sphere term (Table 2.2). These parameters were employed to estimate the charge transfer rate constants according to Eq.(1.6). Owing to the small difference between the intra-molecular parameters of tFNDI and cFNDI, a common set obtained as the average of the two, was used to evaluate the rate constants for the KMC simulations. A summary of geom-

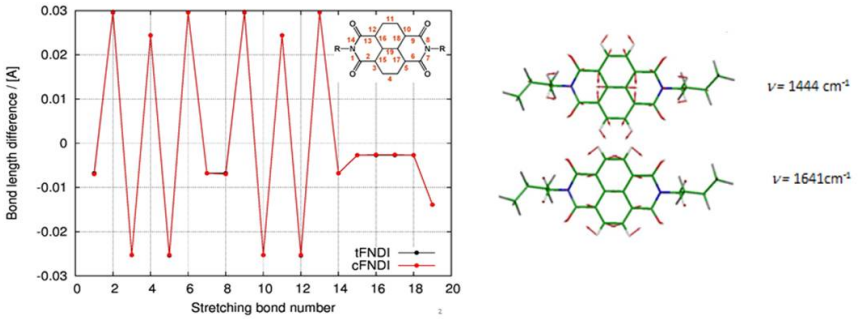

Figure 2.4: (left) Computed bond length changes upon charging (neutral-anion) for tFNDI (black) and cFNDI (red); bond numbering as depicted in the inset. (right) Two of the most active vibrational modes (neutral species) to the intramolecular reorganization energy.

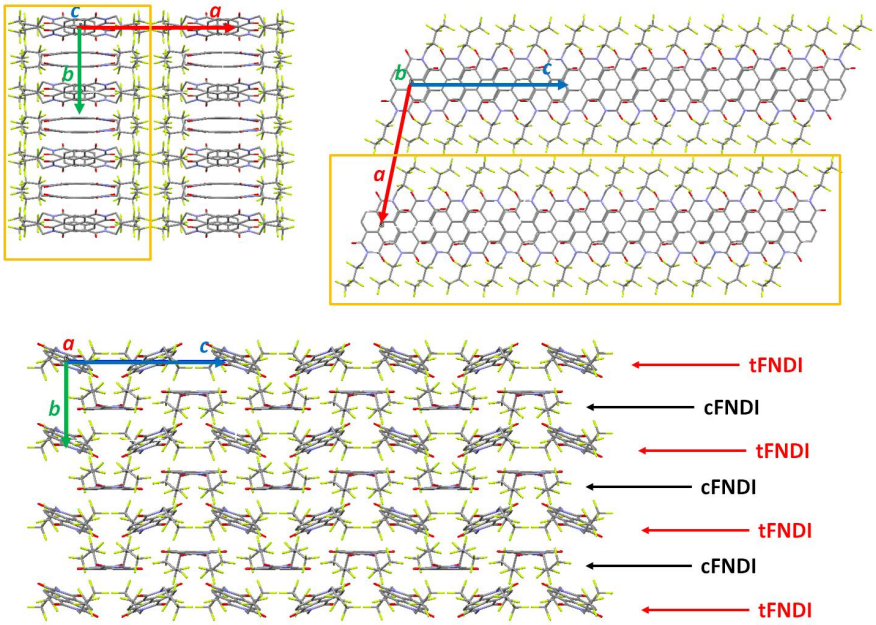

Figure 2.5: Molecular crystal of FNDI: views along crystallographic axes showing the presence of layer (in orange) of π-stacked NDI derivatives and alternating rows of tFNDI and cFNDI molecules in each plane.

etry changes upon doping is depicted in Fig.(2.4), from which it can be seen that the geometry change is almost identical for the tFNDI and cFNDI. The largest bond length variations occur for the peripheral bonds 2, 4, 6, 9, 11 and 13, whose length decreases upon doping and for bond 3, 5, 10 and 12, whose length increases upon doping, while the C-C bonds internal to the conjugated chromophore display modest changes with the exception of the central bond 19. The charge transfer is assisted by vibrational modes displaying a not negligible projection over this geometry change, as confirmed by the inspection of modes exhibiting the largest contributions to the reorganization energy and depicted in Fig.(2.4).

2.3 Intermolecular properties

The crystal of FNDI belongs to the monoclinic P/2c group [50]. The molecules assemble in well separated planes along the a axis and, within a plane laying parallel to the bc crystallographic plane, alternating rows of tFNDI and cFNDI molecules assemble to form a layer, as depicted Fig.(2.5). Accordingly, the charge transport is discussed in terms of intra-layer and inter-layer jumps for FNDI.

To investigate the possible charge hopping paths, from a portion of the crystal, all the possible neighbors of a given molecule are extracted. The distribution of distances between centers of mass at the crystal structure (along with the radial distribution function extracted from the MD simulations that will be discussed in the following) are collected in Fig.(2.10): it shows also that there are a number of charge jumps associated with distances lower than 10 Å. The most important paths for charge-propagation,

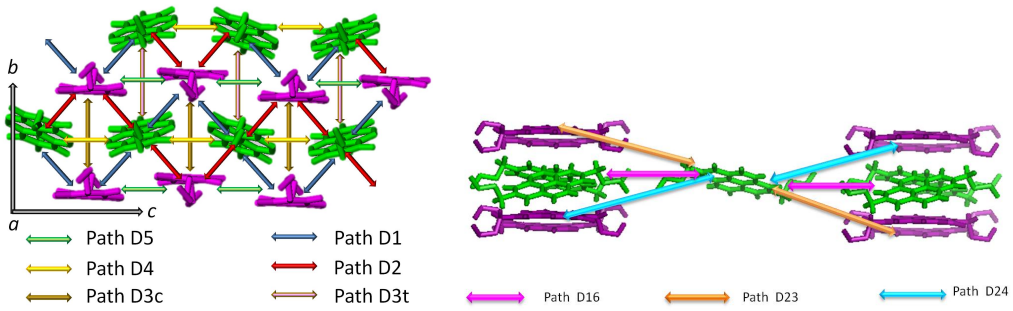

Figure 2.6: (left) Intra-layer and (right) inter-layer charge paths for the crystal of FNDI, green molecules are tFNDIs while purple cFNDIs (F and H atoms not shown for clarity).

Table 2.3: Electronic couplings V_{el} and charge transfer rate constants k_{eT} computed for the different intra-layer charge hopping paths in the crystal of FNDI.

dimer	d [Å]	V_{el}^{L} [cm^{-1}]	k_{eT}^{a} [ps^{-1}]	k_{eT}^{b} [ps^{-1}]	k_{eT}^{c} [ps^{-1}]
			tFNDI		
D1	5.6568	522	25.78	23.67-27.43	27.56-23.45
D2	5.7460	346	11.28	10.32-12.03	10.26-12.06
D3t	7.7605	1	-	-	-
D4	8.3540	175	2.953	2.95-2.95	3.28-2.37
			cFNDI		
D1	5.6568	522	25.78	27.43-23.67	23.45-27.56
D2	5.7460	346	11.28	10.32-12.03	10.26-12.06
D3c	7.7605	1	-	-	-
D5	8.3550	199	3.814	3.80-3.82	3.07-4.24

Kinetic constants [a]without electric field and with electric field applied along [b]b axis and [c]c axis.

depicted in Fig.(2.6), were selected on the basis of their computed electronic couplings V_{el} collected in Table 2.3. Only charge jumps associated with not negligible electronic couplings were included in the KMC simulations and the only active channels for charge propagation are intra-layer; indeed significant electronic couplings are not available for inter-layer paths, some of which (displaying the shortest distances between monomers) are depicted in Fig.(2.6) right. The most efficient intra-layer paths, shown by arrows in Fig.(2.6) left, correspond to jumps from tFNDI to cFNDI molecules (paths D1 and D2) or between molecules of the same type (paths D4 and D5). The two intra-layer jumps D1 and D2 originate from the presence of two different reciprocal orientations of cFNDI and tFNDI molecular sites in the crystal. Molecular orientation governs the magnitude of the corresponding electronic coupling which is indeed larger for path D2 compared to D1, owing to a better overlap between conjugated cores of the two interacting chromophores. Path D4 and D5 are associated with very similar distances between the centers of mass which are, however, considerably larger than those of paths D1 and D2. This explains their reduced magnitude compared with the couplings associated with paths D1 and D2. In between these two pairs of charge hops there is another path labeled D3t and

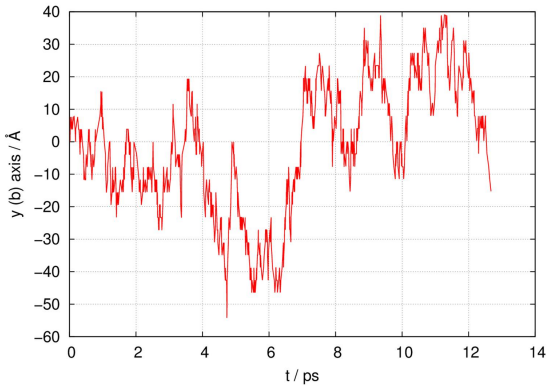

Figure 2.7: Short Brownian trajectory along the b crystallographic axis showing (inside rectangular areas) some traces of dimer trapping effects.

D3c Fig.(2.6) left which is associated with a distance between centers of mass smaller than that of paths D4 and D5. Nevertheless the coupling is computed to be negligible (1 cm^{-1}) because in this case the center of mass distance coincides with the separation between molecular planes which is much larger than for dimers D4 or D5. In the latter case a better overlap is reached for dimer D5 between cFNDI molecules than for dimer D4 between tFNDI conformers.

2.4 Charge transport anisotropy

The couplings discussed above were used to generate, together with the intra-molecular parameters, the set of rate constants, see table in Fig.(2.6) required by the KMC simulations. When the electric field is applied, backward and forward rate constants for the same dimer can differ, as shown in the Table 2.3. The hopping approach is justified here since the largest coupling (522 cm^{-1}) is considerably smaller than the polaron binding energy ($2\lambda_{intra}/2$) which is about 1540 cm^{-1} [10].

As a result of the above pattern of possible charge jumps, the KMC charge propagation in crystals of FNDI occurs in the crystallographic bc plane with a more marked tendency along the crystallographic c direction, Fig.(1.5), where a number of KMC trajectories are displayed). The preferential motion along the c direction is due to the fact that, as seen in Fig.(2.6), the yellow (D4) and green (D5) pathways follow the c direction. In addition the red (D2) and blue (D1) most efficient channels follow a zig-zag pathway also along the c direction. In contrast, along the b direction the charge carrier must follow a sequence of alternating red and blue pathways, having different efficiencies and therefore giving rise to a mechanism of dimer trapping similar to that occurring in core-twisted chlorinated PDI derivatives [32, 67]. This mechanism is expected to depress the charge mobility, as evidenced by inspecting a short portion of a KMC trajectory in Fig.(2.7), showing the propagation of the charge along the b direction as a function of time, in which several traces of the dimer trapping effect (namely several sequential oscillations back and forth inside the same dimer) can be seen.

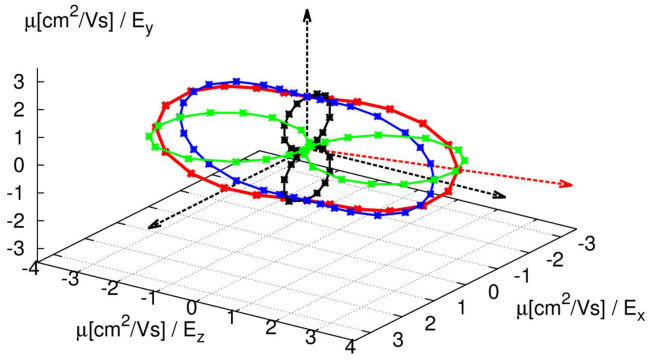

Figure 2.8: Charge transport anisotropy for TOF mobility ($|\boldsymbol{E}| \neq 0$) in the bc crystallographic plane (red), in the $y(\equiv b)$,z plane (blue), in the $y(\equiv b)x(\equiv a)$ plane (black) and in the $x(\equiv a)z$ plane (green).

Table 2.4: Computed electron mobilities μ, Brownian and TOF, and comparison with experimental data.

compound	mobilities [$\mathrm{cm^2V^{-1}s^{-1}}$] Brownian	TOF	exp.
FNDI	1.77		
	0.63 (b axis)[c]	1.87 (b axis)	0.45 (b axis)[d]
	1.14 (c axis)[c]	3.34 (c axis)	0.70 (c axis)[d]
Anisotropy c/b	1.8	1.8	1.6

[a] charge mobility in the absence of applied electric fields. [b] charge mobility for an electric field of 10^5 V/cm directed as indicated in parenthesis. [c]The two largest eigenvalues and eigenvectors (in parenthesis) of the mobility tensor. [d]From [50].

The computed Brownian mobility, according to Eq.(1.46), is 1.77 $\mathrm{cm^2/Vs}$. Note that this value is substantially different from the value 0.42 $\mathrm{cm^2/Vs}$ obtained from the more approximate isotropic formulation where the diffusion coefficient is estimated using Eq.(1.48) [69]. From the diagonalization of the mobility tensor, the largest eigenvalue is associated with the c direction and the second largest with the b directions (Table 2.4), in agreement with the above discussion pointing to a more efficient transport along c.

An additional approach to investigate anisotropy is based on the application of an electric field in various directions followed by the calculation of the corresponding charge mobility [70]. Application of an electric field along the intra-layer directions b and c increases both computed mobilities by a factor of 3 (Table (2.4)) but does not change the magnitude of the anisotropy ratio (1.8) which is equal to that computed in the absence of electric field and also very close to the observed value (1.6). A complete study of the anisotropy was carried out in the bc, ab, bz and az planes, by rotating the direction of the field in steps of 15°. A graphical summary is shown in Fig.(2.8). Finally it can be noticed that the computed mobilities are of the same order of magnitude of the observed ones. Although the model contains a number of approximations that may account for discrepancies, often observed values smaller than computed ones may be ascribed to the presence of impurities in the crystals compared with the ideal perfect nature of the simulated crystals.

Dimer	σ [cm^{-1}]	V_{el} [cm^{-1}]
D1	111	548
D2	229	347
D4	28	152
D5	65	206

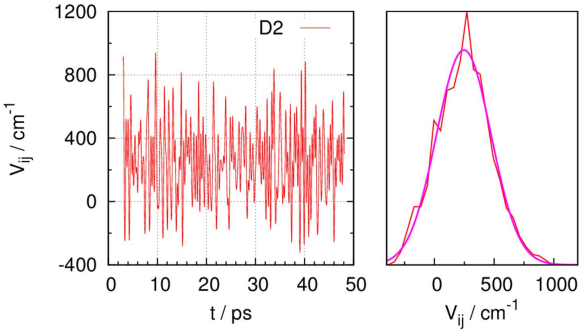

Figure 2.9: (left) Analysis of the electronic coupling fluctuations in terms of Gaussian distribution parameters. (right) Thermally induced disorder effects (300 K) on the distribution of the electronic coupling associated with the D2 pathway: fluctuation of the computed V_{el} as a function of time and Gaussian fitting (magenta) of the dispersion of V_{el} (red).

2.5 Non-local electron-phonon interactions and their intermolecular representation

To assess the role of thermally induced dynamical effects, namely the electronic coupling fluctuations related to the magnitude of non-local electron-phonon couplings, an analysis based on an integrated classical MD/QM approach (Section 1.6) is carried out. Molecular dynamics simulations were run on a supercell $3 \times 3 \times 3$ of the crystal unit cell of FNDI. The V_{el} fluctuations were computed for the four electronic couplings D1, D2, D4 and D5 as a function of time and they are fitted with a Gaussian function.

The D4 and D5 couplings show modest standard deviations (σ=28 and 68 cm^{-1}, respectively, see the table in Fig.(2.9)(left), while the σ of the D1 coupling (111 cm^{-1}) is considerably larger and that of the D2 coupling (230 cm^{-1}) is close to the size of the coupling itself, ca. 350 cm^{-1}. Note that, from the computed radial distribution function, see Fig.(2.10) top, the extent of inter-molecular displacements is similar for all the dimers of FNDI investigated. Therefore, the reduced electronic coupling fluctuations for dimers D4 and D5 compared to those of dimers D1 and D2, must be ascribed to a reduced efficiency of π-stacking and orbital overlap rather than to reduced intermolecular motions. Inspection of Fig.(2.10) bottom shows that while for couplings D1, D4 and D5 a good correlation is found between the center of mass (CoM) distance variation and the modulation of the electronic couplings, this is not equally clear for coupling D2. This suggests that not only the distance but also molecular reorientation plays a role in the modulation of D2 electronic couplings.

A suitable way to monitor molecular orientation when intra-molecular degrees of freedom are frozen, as in this case, is to evaluate Euler angles. The Euler angles are three angles that describe the orientation of a rigid body and represent a sequence of three elemental rotations. In the specific case, these rotations start from the principal inertial axes centered on each molecule and lead to the final coordinate system corresponding to the orientation of the molecules in the crystal [50]. Angles ϕ, θ and ψ correspond

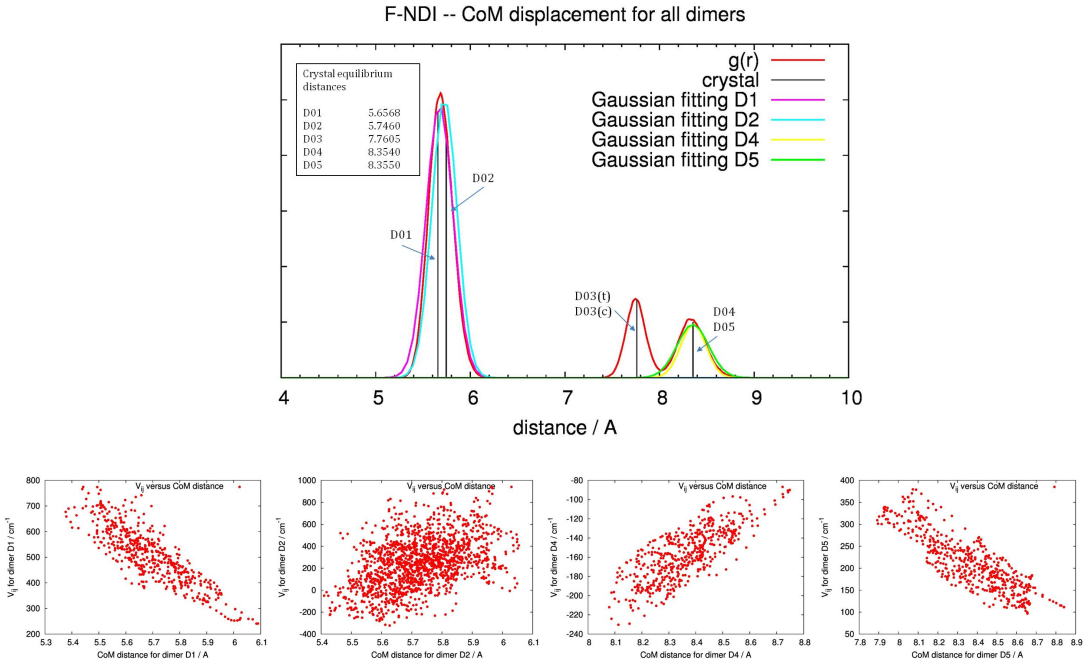

Figure 2.10: (top) Radial distribution function of intermolecular distances between centers of mass, computed from MD simulations at 300 K (red); center of mass distances computed for the crystal structure (black). The cyan, magenta, green and yellow curves are Gaussian fittings of the distribution of displacements extracted from MD simulations. (bottom) Correlation between CoM distance variations and the electronic coupling V_{el} associated respectively with dimer D1, D2, D4 and D5.

to rotations around Z, Y and X principal axes, respectively. Since the orientation of each molecule can change during the dynamics, the fluctuations of Euler angles provide a measure of molecular reorientation. To gain further insight on the molecular motions that favor non-local electron-phonon couplings, examined the Euler angles for each snapshot of the MD trajectory are examined and it is found that one of the three Euler angles, ψ, is subject to larger oscillations (see their Gaussian distributions and σ collected in Fig.(2.11) top) and is therefore more likely to contribute to electron-phonon coupling. Inspection of Fig.(2.11) bottom shows indeed that the ψ angle oscillations with respect to the crystal geometry, for the two monomers forming the D2 dimer, display a good linear correlation with electronic coupling fluctuations. This is even more clear when considering the out of phase combination of the two angles, Fig.(2.11) right.

To further explore the nature of these inter-molecular motions, the frequencies of the lattice vibrations governing electronic-coupling fluctuations are determined from the Fourier transforms of the autocorrelation function of the intra-layer electronic coupling D2, see Fig.(2.12), and found that they fall in the 15-80 cm^{-1} region. Inspection of the rigid-body lattice vibrations computed for super-cells of FNDI shows a number of modes with frequencies falling in the active region, see the bottom part of Fig.(2.12), in which pairs of adjacent FNDIs (in particular those forming D2 dimers) undergo an

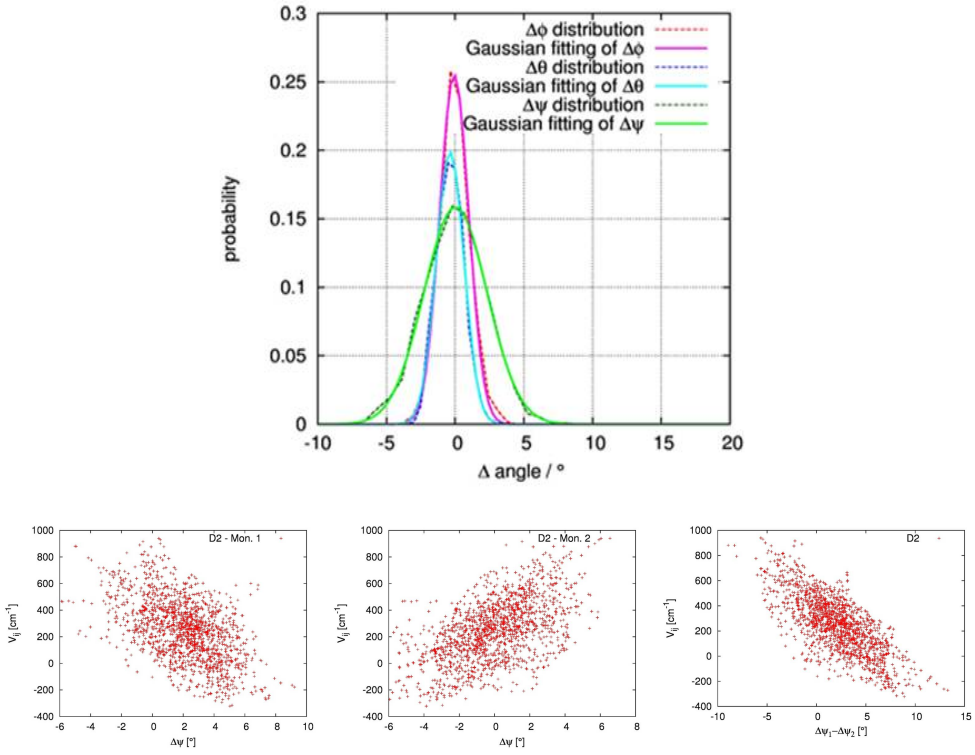

Figure 2.11: (top) Fluctuations and Gaussian fitting of the three Euler angles computed for one of the two molecules forming the D2 dimer: σ associated with the three angles ϕ, θ and ψ are, respectively, 1.06, 1.01, 2.30°. (bottom) Correlation between the fluctuations $\Delta\psi$ of the Euler angle ψ for (left) monomer 1 and (middle) monomer 2 forming the dimer D2 and V_{el} associated with D2 and (right) correlation between the out of phase combination ($\Delta\psi_1$ - $\Delta\psi_2$) of the fluctuations of ψ for monomer 1 and 2, and V_{el}.

out of phase molecular twist, namely a marked molecular reorientation and not simply a molecular translation, in close agreement with the results from the analysis of Euler angles. Owing to the overall modest role of thermal fluctuations for FNDI it can be concluded that the impact of lattice vibrations will be weak except for the D2 coupling. In this latter case it should be considered that, because of its large coupling at the crystal geometry, the rate constant for jump D2 is ca. 11.3 ps^{-1} (see Table 2.3). This implies that frequencies lower than 400 cm^{-1} are slower than the rate of jump. Therefore, the thermalized approach used for instance for some PDI derivatives [67] cannot be used here. A correct approach to include thermal effects in the charge propagation within the non-adiabatic hopping model would be to run KMC simulations on MD snapshots as described in [37, 71, 72] or following the two-step approach of [73]. These extensions, that will be considered in future investigations, are not expected, however, to change the major conclusions of this work.

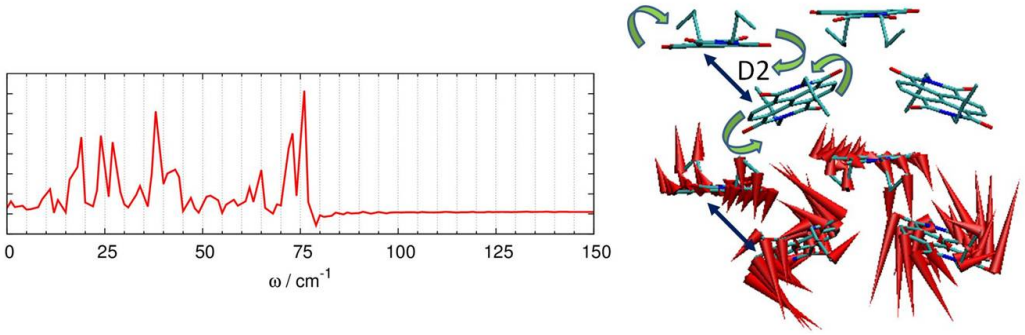

Figure 2.12: (left) Fourier transform of the autocorrelation function of the computed V_{el} and (right) graphical representation of one lattice vibrations (ω = 67 cm^{-1}) governing the modulation of D2 V_{el} (blue arrows). In the top part of the crystal portion only molecules with a schematic representation of their reorentation motion (green arrows) are shown to facilitate the visualization of the nuclear motion (by red cones) in the bottom part.

2.6 Conclusions

The electron transport properties in the crystal phase of a fluoro-alkyl NDI derivative are investigated and the results are compared with those of the corresponding experimental study in single crystal devices. Quantum-chemical calculations show that fluorinated substituents at the imide position enhances the n-type character by lowering the LUMO levels and increasing the computed electronic affinities. Calculations of charge transfer rate constants, according to the non-adiabatic hopping approach, and propagation of the charge carriers within a KMC scheme, lead to predicted charge mobilities of FNDI that compare very well with the experimental measurements in single-crystal devices fabricated with the organic-ribbon mask technique. The marked anisotropy in the bc plane is nicely reproduced by the calculations and rationalized in terms of the available charge pathways displaying not negligible electronic couplings. More specifically, charge transport is enhanced along the c direction by the presence of two pathways (D4 and D5) along this axis to which a contribution from two efficient zig-zag pathways (D1 and D2) also directed along the c axis is summed up. In contrast, for charge transport along b, a mechanism of dimer trapping is envisaged, similar to what has previously been shown to depress mobility in some core twisted chlorinated PDI derivatives [67]. The effect of thermal motion on the modulation of electronic couplings has been investigated with an integrated classical mechanics / quantum-mechanics approach and it has been shown that while for modest electron-phonon couplings a linear relationship between electronic-coupling fluctuations and molecular distance is obeyed, for the largest electron-phonon couplings characterizing the D2 pathway, also molecular reorientation plays a relevant role. This was confirmed by identifying the frequencies of active lattice vibrations via the Fourier transform of the autocorrelation functions of the electronic couplings and combining this information with the inspection of lattice vibration eigenvectors falling in the active frequency region which is located in the 20-80 cm^{-1} range. The study reveals a less relevant role of electronic coupling fluctuations (non-local electron-

phonon couplings) compared to PDI derivatives, possibly as a result of the less expanded conjugated core and associated π-π stacking. On the other hand the close agreement between observed and computed charge transport properties demonstrates the reliability of the model in this case, for the interpretation of data obtained from single crystal devices of FNDI.

CHAPTER 3

The role of the HOMO-1 orbital on the *p*-type charge transport of the fused-ring thienoacene DBTDT

3.1 Introduction

Hetero-annulation has recently become an effective route to enhance the charge transporting character in organic semiconductors [75]. Among others, sulphur decorated organic semiconductors have been proved to be valuable semiconductors for use in OFETs [76, 77]. Compared to the corresponding all-carbon based materials, the sulphur-analogue species benefit from stronger donating ability and less aromatic character than benzene, which results in a higher oxidation barrier and larger band gap. In addition, intermolecular interactions via highly polarizable sulphur atoms help tuning the packing in such systems [78]. Recently, two thienopentacene isomers, i.e., *anti*- and *syn*-dibenzothienodithiophene (DBTDT) were reported by Hu [79]. The thin film transistor fabricated with the anti-isomer afforded a mobility of up to 0.51 cm^2/Vs [80]. On the other hand, by applying the "two-dimensional organic ribbon mask" technique to micro and nanometer-size crystals of DBTDT grown by the horizontal physical vapor transport method, Li and Hu demonstrated marked mobility anisotropy [81]. The crystals of DBTDT [82] grown in ref. [81] display hexagonal shapes corresponding to the *ac* crystallographic plane and their configuration was the best for studying the anisotropic transport along the *c* and *a* directions. The measured mobility of DBTDT was found to be as high as 1.8 cm^2/Vs, along the *c* axis, while it did not exceed 0.8 cm^2/Vs along the *a* axis with a mobility anisotropy μ_c/μ_a ratio of ca. $2-2.5$. Organic single crystals,

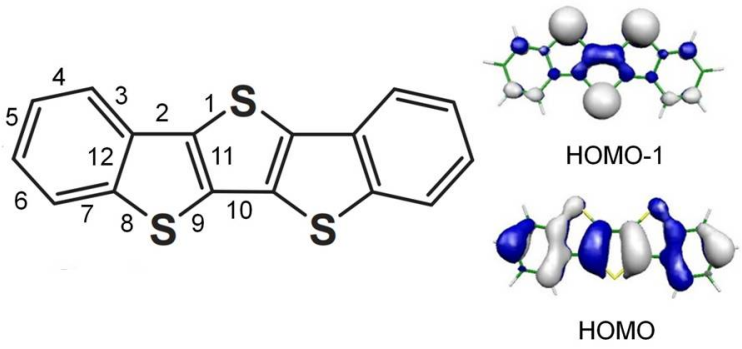

Figure 3.1: (left) Structural formula, bond numbering; (right) orbital shape of the HOMO-1 and HOMO of DBTDT.

because of their purity, few defects, long-range order, are ideal for analyzing the intrinsic properties of the semiconductor as a function of molecular arrangement. Computational investigations on the charge transport properties of DBTDT have been reported and included the evaluation of the most relevant electron transfer integrals [83, 84] and the determination of charge mobility [85]. However none of the reported investigations was concerned in detail with the large mobility anisotropy and its predominance along the c crystallographic axis. Motivated by the still unclear origin of the anisotropic charge mobility of DBTDT, here the intra-molecular and inter-molecular parameters of DBTDT governing charge transport are investigated, paying also attention to the possible role of thermally induced dynamical effects. In addition, not only the charge carriers generated by the highest occupied molecular orbital (HOMO) but also those originated by the nearby HOMO-1 [86] are taken into account and their relevant role is demonstrated. To this end embedding effects, due to the large size of the clusters investigated, were determined at B3LYP/6-31G* and M06L/6-31G* levels of theory. The latter functional was chosen, in particular, because it is well suited to describe π-π stacking interactions.

3.2 The proximity of HOMO and HOMO-1 orbitals

Electronic structure calculations on isolated molecules at the geometry of the crystal reveal that DBTDT has two energetically close occupied molecular orbitals, with the HOMO-1 located a fraction of eV below the HOMO (from 0.32 eV at B3LYP/6-31+G* to 0.16 eV at M06L/6-311G** level of theory, see also Table 3.1). To further explore the origin of the HOMO-1, HOMO proximity in DBTDT, a series of homologues is considered, namely dibenzo-thieno-N-thiophenes (DBTNT, N=0-5) and in Fig.(3.2) the computed energies and shapes of the HOMO and HOMO-1 orbitals are collected. It is shown that for the series of DBTNT the two highest occupied molecular orbitals can be describes as carbon-dominated (CD) or sulphur-dominated (SD) to schematically indicate that in the former most electron density is localized on the carbon skeleton

Table 3.1: Molecular orbital energies of DBTDT from different calculations at the crystal structure geometry of the neutral species.

	HOMO-1 [eV]	HOMO [eV]	Δ E(H-1/H) [eV]
B3LYP/6-31G*	-5.79	-5.51	0.28
B3LYP/6-31+G*	-6.07	-5.75	0.32
B3LYP/6-311G**	-5.73	-5.97	0.24
CAM-B3LYP/6-31+G*	-7.31	-7.01	0.31
ωB97X/6-31+G*	-8.22	-7.90	0.32
M062X/6-31+G*	-7.19	-6.94	0.26
M06L/6-31G*	-5.25	-5.03	0.22
M06L/6-31+G*	-5.35	-5.15	0.20
M06L/6-311G**	-5.33	-5.17	0.16

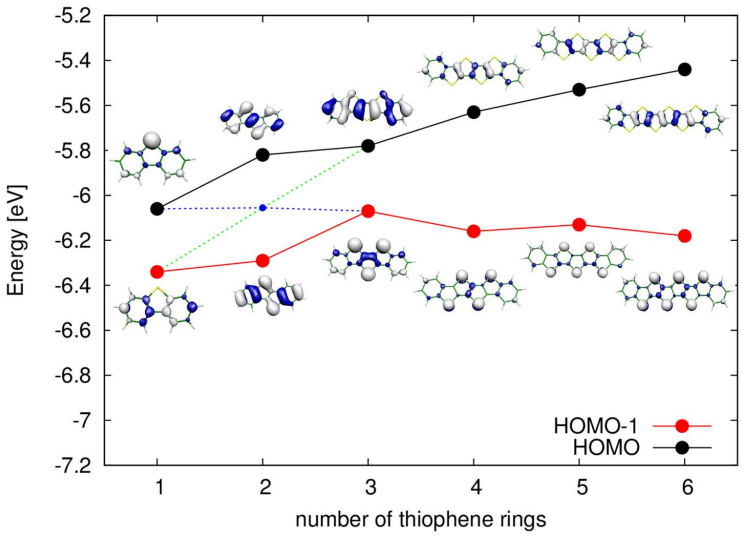

Figure 3.2: Computed energies of the HOMO and HOMO-1 orbitals of DBTNT. The blue and green dashed lines show the crossing between CD and SD orbitals occurring for the second member of the homologue series, BTBT; the crossing is avoided by symmetry rules.

while in the latter electron density is large on sulphur atoms. Notably, there is an inversion between the two highest occupied molecular orbitals along the series, with the SD orbital that lowers slightly its energy for an increasing number of fused thiophenes and becomes the HOMO-1 owing to the concomitant energy increase of the CD orbital. As a result, the SD orbital is slightly below the HOMO for DBTDT while its energetic separation from the HOMO increases for the longer members. It has been suggested that the shape of the orbital and especially the electronic density on sulphur atoms governs intermolecular interactions and electronic couplings in thiophene containing molecules [83, 87]. Since the SD orbital shows the largest sulphur density, it is expected that in the series, the potential for charge conduction is larger for the first few members. In fact DBT1T, better known as benzothieno-benzothiophene (BTBT) shows high performance charge transport properties. Additionally for the members in the series holding an even number of fused thiophenes, the HOMO and HOMO-1 have the same symmetry and

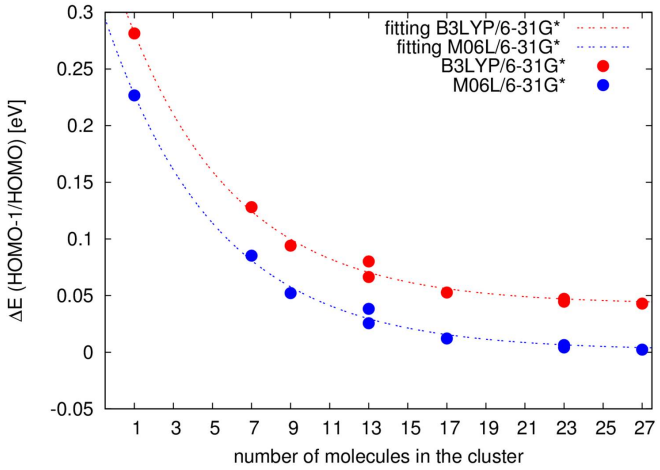

Figure 3.3: Embedding effects on the HOMO-1/HOMO energy difference estimated at B3LYP/6-31G* and M06L/6-31G* levels of theory with the cluster approach, as a function of the cluster size.

therefore their interaction can be not-negligible when they come close in energy. This is the origin of the mixed nature of the two orbitals for BTBT, see Fig.(3.2), in which both orbitals display large contributions on sulphur atoms. Evidence of the orbital interaction is clearly demonstrated by the unusually large HOMO-1/HOMO energy separation for BTBT compared with the adjacent left and right members DBT and DBTDT. The ideal trace of the crossing between the CD and SD orbitals is shown in the figure by blue and green dashed lines. In contrast to BTBT, the two orbitals cannot interact (for symmetry reasons) for DBTNT holding an odd number of thiophene units. DBTDT is one such example and because it follows BTBT in the series, (where the CD/SD crossing occurs), it displays two quite close occupied orbitals of different symmetry and nature (SD and CD).

The energy difference between these two orbitals is expected to be reduced in the solid phase, due to polarization effects that should preferentially affect the HOMO-1 orbital, owing to the larger polarizability of sulphur. The energy difference between the HOMO-1 and HOMO orbitals can be estimated by computing the polarization effects on a central molecular site embedded in the crystal. Several approaches to include polarization effects have appeared in the literature. Possible routes consist in the use of micro-electrostatic methods [88] or QM/MM approaches combined with polarizable force fields [89]. However, for the present work, the interest is in the energy difference between different molecular orbitals on the same molecule. Thus, to obtain realistic values, increasingly larger clusters are built centered on a molecular site by employing the cluster approach (Section 1.2.1) developed from the generalization of thef fragment orbital (Section 1.2 and [90, 29]). An Hamiltonian is built for a cluster made up of a DBTDT molecule with the full set of its orbitals, and its coordination sphere formed by and increasing number of molecules and the embedding effects on both HOMO-1 and HOMO orbitals are evaluated. Clusters of DBTDT including up to 27 molecules in the *ac* crystallographic plane (see Fig.(1.2), were considered at B3LYP/6-31G* and

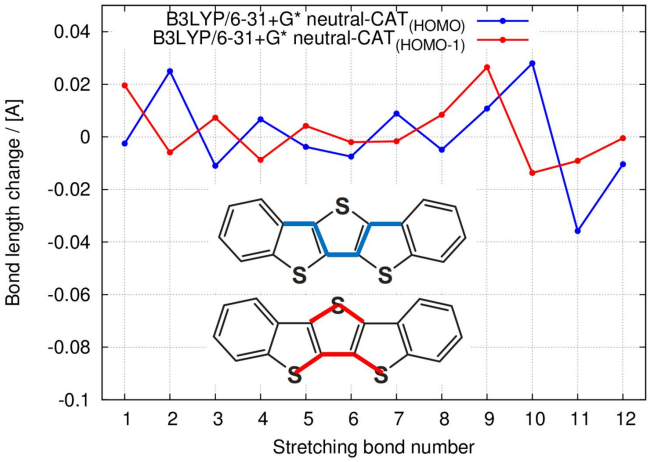

Figure 3.4: Geometry changes of the two cationic states CAT(HOMO) (blue) and CAT(HOMO-1) (red) with respect to the neutral DBTDT molecule (numbering as in Fig.(3.1)). The largest bond lengths changes are indicated on the DBTDT structure with the same colour label.

M06L/6-31G* levels of theory. The energy difference between the two occupied orbitals decreases, as a result of polarization, as shown in Fig.(3.3), and reaches the value of ca 0.05 eV for the B3LYP functional and even smaller for the M06L functional, thereby suggesting that the role of the HOMO-1 cannot be neglected in the discussion of solid state properties of DBTDT, such as charge transport.

3.3 Intramolecular properties of the two cations

In agreement with the observation above, it must be considered the possibility that charge carriers, generated either from injection of holes to the HOMO or the HOMO-1 orbitals, may contribute to charge transport. Assuming a charge hopping approach (Section 1.1 and [8]), intra- and inter-molecular parameters (reorganization energies and electronic couplings, Sections 1.2, 1.3 and [5, 9]) govern the charge transport and were therefore determined for both cationic species, hereafter labeled as CAT(HOMO) and CAT(HOMO-1).

The computed skeleton bond lengths for the neutral and cationic species have little dependence on the level of theory, and the bond length changes upon generation of CAT(HOMO) and CAT(HOMO-1) at the B3LYP/6-31G* level of theory are collected in Fig.(3.4). Bonds 2, 10 (shortened in the cation) and 11 (elongated in the cation) which are central C-C bonds, are subject to the largest changes upon formation of CAT(HOMO), in agreement with the CD character and the bonding and antibonding nature of the electron depleted HOMO orbital. In contrast, bonds 1 and 9 (C-S bonds) are shortened and bond 11 (C-C bond) is elongated upon formation of CAT(HOMO-1), in agreement with the SD character and bonding and antibonding nature of the HOMO-1 orbital. The intra- and inter-molecular parameters governing charge transport were previously investigated for CAT(HOMO) [83, 84, 85] and our results agree with available

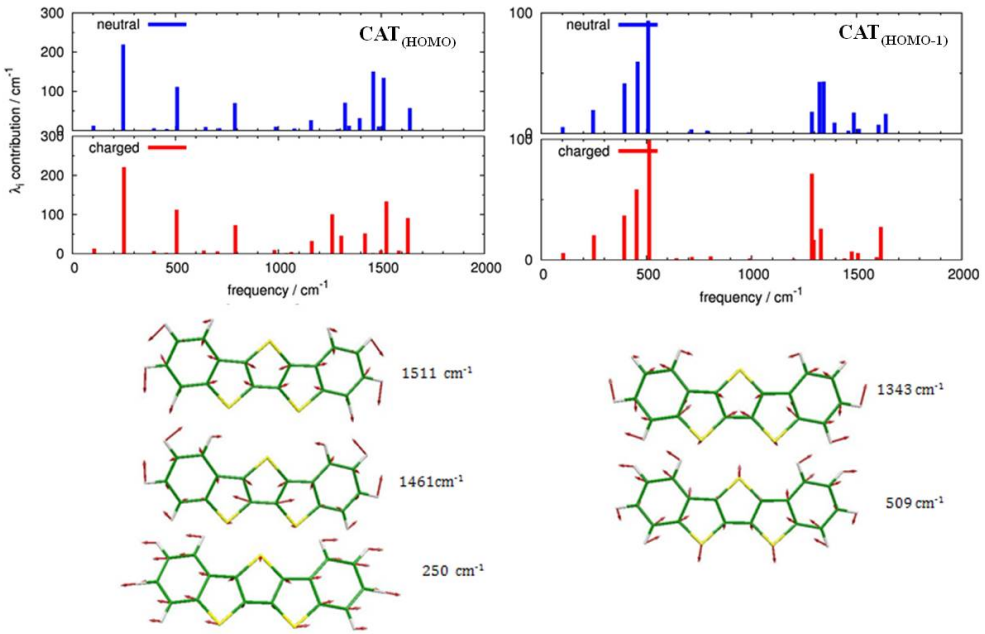

Figure 3.5: (top) Huang-Rhys factors of the HOMO (left) and HOMO-1 (right) cation; (bottom) most active vibrational frequencies of HOMO (left) and HOMO-1 (right) cation.

Table 3.2: Effective frequency ω_{eff}, associated Huang-Rhys factor S_{eff} and λ_{class} for charge transfer rate constants of CAT(HOMO) and CAT(HOMO-1).

	CAT(HOMO)	CAT(HOMO-1)
ω_{eff} [a] [cm^{-1}]	710	661
S_{eff} [a]	2.295	1.084
λ_{intra} [a] [eV]	0.202	0.090
λ_{class} intramol. [b] [eV]	0.031	0.006
λ_{class} total [c] [eV]	0.041	0.016

[a] Only frequencies above 250 cm^{-1} were considered. [b]Contribution from intra-molecular classical vibrations. [c] A value of outer sphere λ_o of 0.01 eV was assumed as in recent estimates [34].

literature data: the cationic state is associated with a relatively large reorganization energy of ca. 0.233 eV (see Table 3.2) compared to pentacene. For the first time it is reported the reorganization energy associated with the formation of CAT(HOMO-1) which, in contrast, is considerably smaller, in line with that of pentacene and amounts to 0.096 eV. Owing to the different geometries of the two cations, different vibrational coordinates contribute to their reorganization energies as shown in Fig.(3.5). These, in turn, influence the charge transfer rate constants.

3.4 Intermolecular properties of the two cations

In the one-electron approximation the electronic couplings for hole transfer are computed between occupied orbitals. In this case couplings were computed between HOMO, between HOMO-1 and also crossed couplings between HOMO and HOMO-1 orbitals

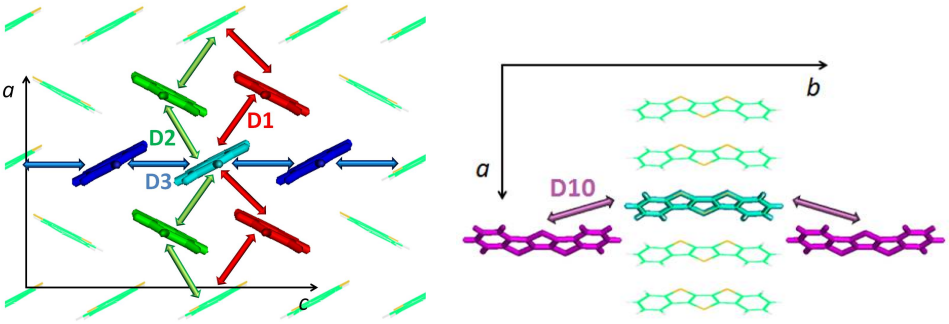

Figure 3.6: Charge pathways in the crystal of DBTDT from the central cyan molecule to the nearest neighbor molecules in the (left) *ac* crystallographic plane and (right) *ab* plane.

Table 3.3: Electronic couplings V_{el} (B3LYP/6-31G* level of theory) and charge transfer rate constants k_{eT} computed for the different charge hopping paths in the crystal of DBTDT.

dimer	d [Å]	V_{el}^{H} [meV]	V_{el}^{H-1} [meV]	k_{eT} [a] [ps^{-1}]
D1	4.8730	17	48	1.7^b/ 88.7^c / 6.2^d
D2	5.0190	45	32	12.1^b/ 39.4^c / 13.5^d
D3	5.9060	11	100	0.7^b/ 385.1^c / 20.7^d
D10	13.6687	11	1	0.7^b/ 0.0^c / 0.7^d

[a]Without applied electric field. [b]Rate constants for CAT(HOMO). [c]Rate constants for CAT(HOMO-1). [d]Rate constants as Boltzmann weighted contributions from CAT(HOMO) and CAT(HOMO-1), assuming a ΔE(HOMO/HOMO-1) of 0.075 eV.

were considered. The crystal of DBTDT is orthorhombic and belongs to the *Pnma* space group [82]. Molecules assemble, with herringbone packing, in planes parallel to the *ac* crystallographic plane, see Fig.(3.6) left. Accordingly, the largest interactions, either between HOMO or HOMO-1 orbitals, are expected between molecules in the *ac* plane, although at least one non-negligible interaction is computed (see Table 3.3) for the inter-planar charge pathway D10, Fig.(3.6) right. The computed electronic couplings for the HOMO orbitals, collected in Table 3.3, are in agreement with previous computations [83, 84, 85]. The possible and most efficient paths, shown by red, green and blue arrows in Fig.(3.6), are D1, D2 and D3. For CAT(HOMO) the couplings associated with D1 and D3 are modest and only for D2 is remarkable. D1 and D2 form zig-zag pathways directed along the *a* axis. One may consider also the possible zig-zag sequence of D1-D2 jumps along the *c* direction but, because their associated couplings are rather different, charge transport along this pathway is expected to be strongly hindered due to the alternation of fast (D2) and slow (D1) jumps, giving rise to a mechanism of dimer trapping (namely several sequential oscillations back and forth inside the same dimer) that was previously demonstrated to reduce charge transport efficiency in most core-twisted chlorinated PBI derivatives [32, 67, 70] and in fluoro-alkylated NDI, thereby determining a marked charge transport anisotropy [91]. The molecular orientation and the shape of molecular orbitals govern the magnitude of the electronic coupling: owing to the large

Table 3.4: Computed hole mobilities μ for the crystals of DBTDT and comparison with experimental data.

	mobilities [cm^2/Vs]					
	CAT(HOMO)		CAT(HOMO-1)		model[c]	Exp[d]
	μ Brown.	μ TOF	μ Brown.	μ TOF	μ TOF	μ
a axis	0.28	0.96	2.57	7.89	1.38	0.8
c axis	0.11	0.36	18.21	55.74	3.83	1.8
aniso. μ_c/μ_a	0.4	0.4	7.0	7.1	2.8	2-2.5

[a]Charge mobility in the absence of applied electric fields. [b]Charge mobility for an electric field of 10^5 V/cm directed as indicated in parenthesis. [c]See the discussion in the text. [d]From [81].

electron density on sulphur, the couplings in the ac plane for the CAT(HOMO-1) are all quite large, in contrast with CAT(HOMO). The striking difference is the magnitude of the D3 coupling which is about ten times larger for CAT(HOMO-1) compared to CAT(HOMO). The computed electronic couplings therefore suggest that the D3 coupling, owing to its directionality along the c axis, plays a key role in determining the anisotropy of charge transport. For CAT(HOMO) charge carriers, a modest charge transport efficiency is expected along c, in contrast to CAT(HOMO-1) charge carriers.

3.5 Anisotropy of charge mobility

To provide more quantitative evidence on the anisotropic charge transport of DBTDT, KMC simulations of charge transport for both charge carriers are carried out. To this end the multi-scale protocol introduced in Section 1.6 was employed. While the computed parameters are consistent with a non-adiabatic hopping approach for CAT(HOMO) charge carriers, the conditions are not fulfilled for CAT(HOMO-1) owing to its much larger couplings and reduced reorganization energy. Therefore, the results of KMC simulations on CAT(HOMO-1) are intended to provide only qualitative insights as regard charge mobility predictions. Nevertheless these results are expected to give correct indications on the anisotropy of the charge transport, which is our major concern here. This was the case, for instance, for the prediction of the charge transport anisotropy of pentacene [70].

As expected from the discussion above, the KMC charge propagation of CAT(HOMO) charge carriers, in the ac crystallographic plane of DBTDT crystals, occurs more efficiently along the crystallographic a direction see Fig.(3.8) left and (3.7) left where a number of KMC trajectories are displayed). The preferential motion along the a direction is due to above discussed efficient zig-zag pathway involving D2 dimers. The role of D3 jumps is modest, owing to its small electronic coupling. As a result the predicted μ_c/μ_a anisotropy ratio (0.4) is in marked disagreement with the experimental results (2-2.5, see Table 3.4). Application of an electric field does not change the results of the simulations. In contrast to CAT(HOMO), the KMC charge propagation of CAT(HOMO-1) charge carriers, occurs in the crystallographic ac plane more efficiently

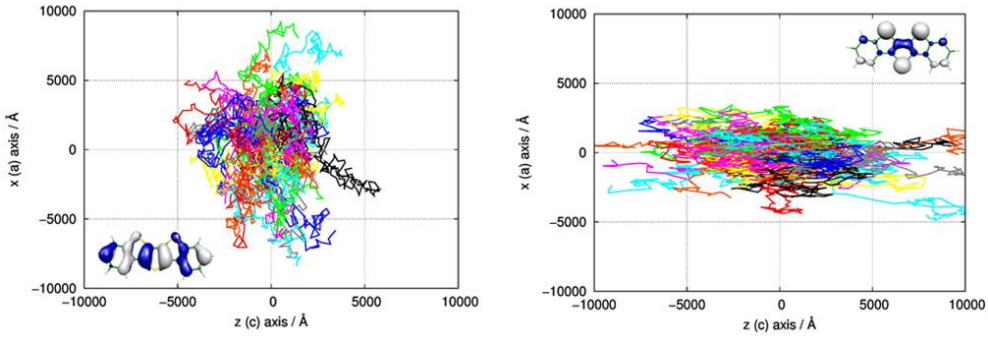

Figure 3.7: Plot of a number of Brownian trajectories involving (left) CAT(HOMO) and (right) CAT(HOMO-1) as charge carrier in the $x(\equiv a)z(\equiv c)$ plane.

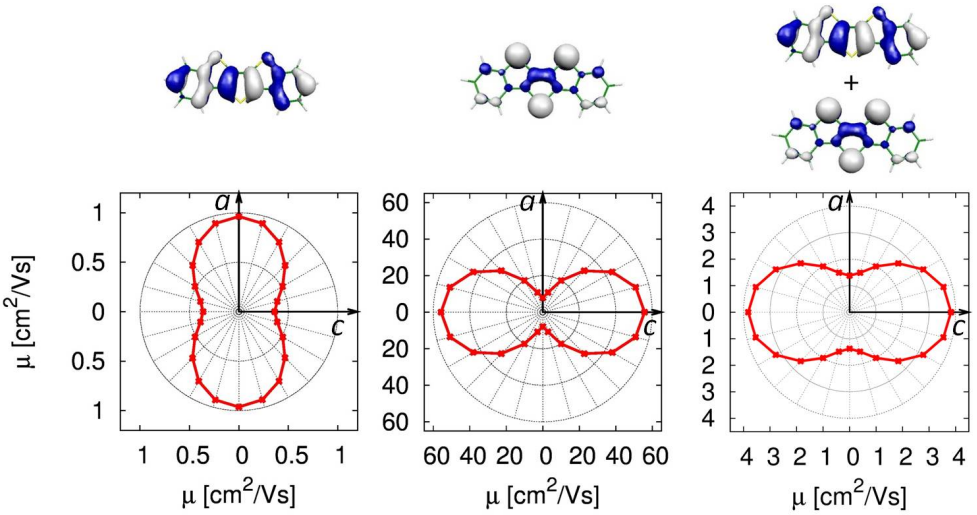

Figure 3.8: Charge transport anisotropy for the crystal of DBTDT. Anisotropy in the ac crystallographic plane from KMC TOF simulations involving CAT(HOMO) as charge carrier (left), CAT(HOMO-1) as charge carrier (center) and with Boltzmann weighted contributions from CAT(HOMO) and CAT(HOMO-1) (right).

along the c direction (see Fig.(3.8), center and (3.7) right), as a result of the large electronic coupling for the D3 path. However, the predicted charge transport anisotropy ratio, 7.0-7.1, computed for the CAT(HOMO-1) charge carriers is too large compared to the experimental value, Table 3.4. The availability of a second, competitive charge carrier CAT(HOMO-1) quite close in energy to CAT(HOMO) and its concomitant large coupling for the D3 path along c, suggests that, although it is a higher energy species, it may show a determinant role in the charge transport of DBTDT. This role can be accounted for in a simplistic way by considering its Boltzmann population in a charge localized hopping approach: as discussed above, computations of embedding effects (see Fig.(3.3)) predict an energy difference between the two orbitals of the order of 0.05 eV. Assuming an energy difference of about 0.075 eV between the two charge carriers, slightly above the computed limiting value, the population of CAT(HOMO-1) results to be about 5%; to include its contribution to the KMC scheme, an effective charge

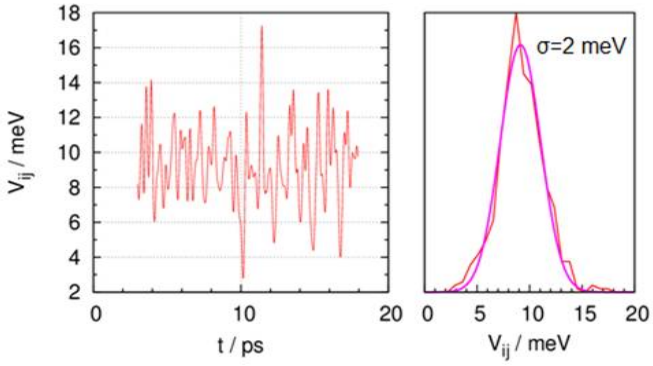

Figure 3.9: Thermally induced disorder effects (300 K) on the distribution of the HOMO electronic coupling of the D3 pathway of DBTDT. (left) Fluctuation of the computed (B3LYP/3-21G) electronic couplings in time and (right) Gaussian fitting (magenta) of the dispersion of computed couplings (red).

transfer rate constant is defined for each available path, by summing the Boltzmann weighted contributions of the two charge carriers. The resulting effective rate constants are collected in the last column of Table 3.3 from which it is evident how the contribution of the second charge carrier CAT(HOMO-1) increases the efficiency of the D3 path in the Boltzmann weighted model. Injecting the weighted rate constants in the KMC protocol allows to obtain a considerably larger mobility along c (see Table 3.4 and Fig.(3.8), right) giving rise to an anisotropy ratio μ_c/μ_a of 2.8 which is in much better agreement with the observed ratio of 2-2.5. The reproduction of exact numerical values of charge mobility is not the objective of this work, whose goal is to propose a convincing explanation for the larger observed mobility along c, as due to the non-negligible role of the HOMO-1 orbital for DBTDT.

To further support the role of the HOMO-1 orbital and related charge carriers in the charge conduction of DBTDT it is considered the bandwidth associated to path D3, in a simple one-dimensional tight-binding model, which is $4V_{el}^{H}(D3)$, namely ca. 0.4 eV for the HOMO-1, sufficient to overlap and overcome the bandwidth of the HOMO along the same direction, which is only 0.04 eV. Therefore, also within the tight-binding scheme it is clear that the HOMO-1 contributes to charge transport along c.

However, before ruling out a major role of CAT(HOMO) to account for the large mobility along c, one additional factor should be considered, namely the effect of thermally induced disorder on electronic couplings. MD simulations (run on a $5 \times 1 \times 3$ supercell of the crystal unit cell), combined with QM evaluation of electronic couplings, were employed to investigate the extent of electronic coupling fluctuations related to the magnitude of non-local electron-phonon couplings (Section 1.4). The electronic coupling fluctuations, computed for the D3 path are shown in Fig.(3.9) as a function of time and with their fitting with a Gaussian function. The strength of the non-local electron–phonon coupling can be evaluated by the standard deviation σ of thermal fluctuations and the modest electronic coupling fluctuations (see Fig.(3.9), σ =2 meV) for CAT(HOMO) confirm its negligible role to account for the large charge mobility along

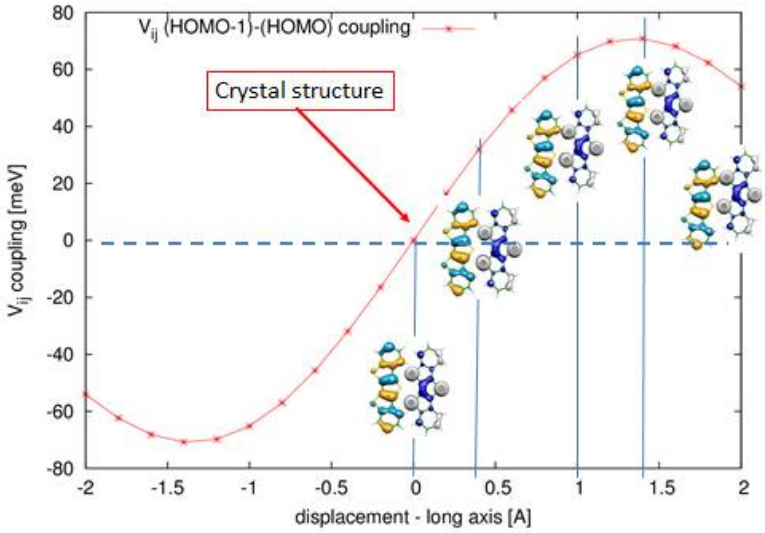

Figure 3.10: Activation of the HOMO-1/HOMO electronic couplings upon displacement of the two molecules (forming the D3 dimer) along the long molecular axis. The displacement leads to a symmetry breaking that switches on the coupling.

c. While the role of fluctuations is modest, the disorder induced by thermal motion is however important since it switches on (see Fig.(3.10)) the interaction between HOMO and HOMO-1 orbitals located on two different molecules, a coupling which is zero by symmetry at the crystal structure, and which is required to account for the generation of both charge carriers during charge propagation.

3.6 Conclusions

In conclusion, it has been shown the peculiar proximity of the HOMO-1 orbital to the HOMO, in DBTDT, results from the peculiar position of the crossing between the highest two occupied orbitals in the series of DBTNT molecules. Embedding effects reduce further their energy difference thereby indicating that charge carriers generated by the HOMO-1 orbital can become competitive with those generated by the HOMO and point to a relevant role of the second highest occupied orbital to explain the marked charge mobility anisotropy and more specifically the large mobility along *c*. While thermally induced fluctuations of the V_{el}^{H} couplings cannot explain such large mobility along *c*, thermally induced disorder is responsible for the activation of crossed $V_{el}^{H-1/H}$ couplings (otherwise zero by symmetry) that justify the generation of both charge carriers during charge propagation in the crystal. To the best of our knowledge, excluding high symmetry molecules for which degenerate pairs of orbitals are available, this is the first clear example of a non-degenerate HOMO-1 contribution to charge transport that has been recognized by simulation.

CHAPTER 4

Modeling *p*-type charge transport in thienoacene analogs of pentacene

The content of this chapter is reproduced in part with permission from Ref.[92]:
Canola S., Pecoraro C., Negri F. *Theor. Chem. Acc.*, **2016**, *135(2)*, 33.

4.1 Introduction

Hetero-substituted organic conjugated semiconductors have received considerable attention in recent years. The introduction of heteroatoms is a suitable way to create new non-covalent interactions which become effective in tailoring the solid-state packing and maximize the π-π contacts thereby leading to a better efficiency of charge transport [75]. In particular, sulfur substituted semiconductors have been proved to be very interesting systems [93, 83, 77]. Compared to the all-carbon based materials, sulfur influences both the intramolecular and the intermolecular properties: sulfur-substituted acene derivatives show less aromaticity, larger band gaps and higher oxidative stability while the introduction of new non-covalent interactions, like S-S or S-π due to the high polarizability of sulfur, contribute to tuning the packing in these systems [75, 78].

A number of thienoacene derivatives have been recently synthesized and several showed promising *p*-type charge transport properties [75, 83, 77]. Among these, two thienopentacene isomers, *anti*- and *syn*- dibenzo-thieno-dithiophene (DBTDT) were reported [93, 79] (see Fig.(4.1)). Measurements on micro and nanometer size crystals of the anti- isomer showed a marked anisotropy of charge transport, with a large mobility (1.8 cm^2Vs^{-1}) mainly along the *c* crystallographic axis [81]. As for the *syn* isomer, also known as bis-benzo-thieno-thiophene (BBTT), it shows a characteristic sickle-like shape. At variance with the *anti* isomer, and other linear fused-ring thienoacenes with herringbone packing motif, the sickle-like thienoacene exhibits a π-π molecular packing

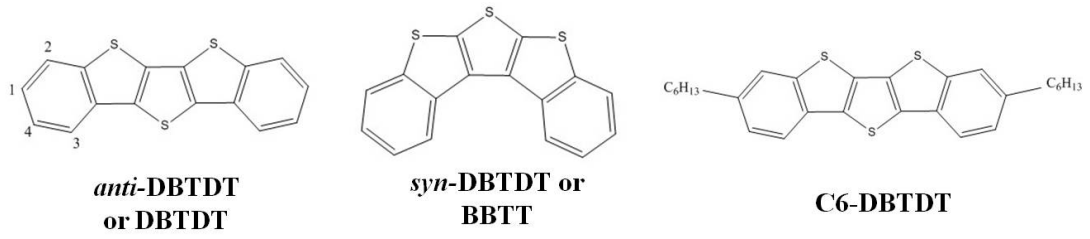

Figure 4.1: Molecular structure of (left) *anti*-DBTDT or simply DBTDT of Chapter 3 and [74] (the positions of possible substituents are indicated by numbers); (middle) *syn*-DBTDT or BBTT and (right) alkyl-substituted C6-DBTDT.

motif and could self-assemble into one dimensional single crystalline ribbons. Mobilities for thin film transistors were reported and showed a modest value of about 10^{-5} cm^2Vs^{-1} [84], while single crystal transistors fabricated with the "organic ribbon mask" technique showed a more relevant value of about 0.6 cm^2Vs^{-1} [79]. Beside unsubstituted DBTDT, substituted derivatives were reported, with alkyl chains of six carbon atoms on the peripheral phenyl rings (C6-DBTDT, see Fig.(4.1)). Mobilities for thin film FETs, obtained varying the substrate deposition temperature, spanned from 1.8 to 8.8 cm^2Vs^{-1} [94]. In addition, controllable solution self-assembly of two different crystal phases of C6-DBTDT was reported [86]. The α-phase crystals displayed an average hole mobility value of 5.0 cm^2Vs^{-1} with peaks of 8.8 cm^2Vs^{-1} [86], whereas the microribbon-shaped β-phase crystals showed a hole mobility up to 18.9 cm^2Vs^{-1}, which is among the highest values for p-type organic semiconductors [86]. Single crystals of π-conjugated molecules are an ideal substrate for the study of their charge transport properties because of their purity, long range order and absence of grain boundaries. As a consequence, the measured charge carrier mobilities should be close to the intrinsic values of the molecular material, and are more suitable for a comparison with those determined by appropriate modeling.

It has been applied the same computational approach (Section 1.6) to investigate the p-type charge transport properties and anisotropy of DBTDT (Chapter 3 and [74]): in this latter case the large anisotropy of charge mobility could be explained in terms of the role of a second occupied molecular orbital lying very close to the HOMO orbital and displaying remarkable electronic couplings for charge transport along the c crystallographic axis. Additionally for DBTDT a rationale for the origin of the HOMO/HOMO-1 proximity was provided by considering a series of dibenzo-thieno-N-thiophenes homologues: due to the peculiar energy proximity of the two orbitals, the charge carriers generated by the second highest occupied orbital become competitive with those generated by the HOMO in DBTDT and account for the observed anisotropy. In the light of the above considerations and owing to the availability of experimental investigations, it is therefore interesting to extend the study of p-type charge transport to the *syn* isomer of DBTDT (BBTT) and its alkylated derivative C6-DBTDT. To this end the integrated approach of Section 1.6 has been employed, involving quantum-mechanical (QM) calculations of intra- and inter-molecular parameters coupled with kinetic Monte

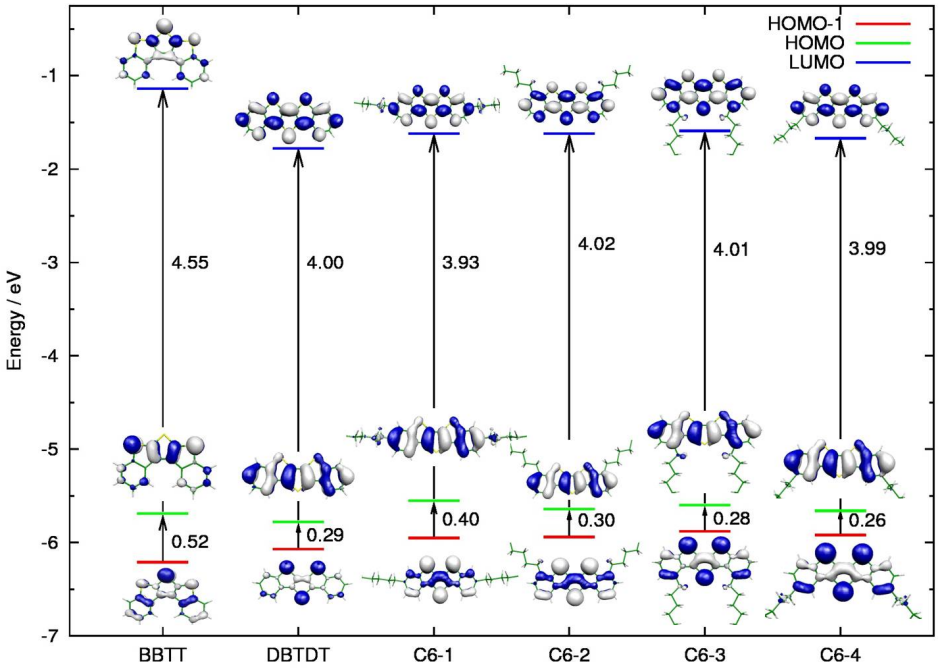

Figure 4.2: Frontier orbital energies and shape of the orbitals computed at B3LYP/6-31+G* level of theory, for BBTT, DBTDT, and the four substituted C6-DBTDT (C6-n) featuring -C_6H_{13} substituents in different positions (n=1-4, see Fig.(4.1) for numbering).

Carlo (KMC) simulations to propagate the charge across the molecular material.

4.2 Electronic structure: effect of substituent and isomerism

The results of electronic structure calculations and, more specifically, energy levels and shape of molecular orbitals at the B3LYP/6-31G* level of theory, are collected in Table 4.1 and Fig.(4.2). Beside the frontier orbitals HOMO and LUMO it is also included the HOMO-1 level to evaluate its energetic position with respect to HOMO and hence its eventual contribution to charge transport. In addition, to explore the positional effect of substituents, four C6-substituted DBTDTs were included in the calculations in which the alkyl substituents are bound (symmetrically) at the 1-4 positions of the two peripheral benzene rings (see Fig.(4.1) left for numbering). Comparison between *anti* and *syn* DBTDT shows that the transport gap is considerably larger for the latter, also in agreement with previous calculations [75], which indicates that the effect of stabilization generally induced in hetero-substituted oligoacenes is more substantial for BBTT than for DBTDT.

Compared with DBTDT, the transport gap is almost unchanged for most of the alkylated derivatives and it is only slightly reduced for the experimentally investigated derivative (substituents in position 1). As for the role of the HOMO-1 orbital, inspection

Table 4.1: Frontier orbital energies and transport gaps for BBTT, C6-DBTDT and unsubstituted DBTDT computed at the B3LYP/6-31G* optimized structures of the neutral systems.

	HOMO-1 [eV]	HOMO [eV]	LUMO [eV]	ΔE(H-1/H) [eV] [eV]	ΔE(H/L) [eV]
BBTT	-6.21	-5.69	-1.14	0.52	4.55
C6-DBTDT	-5.95	-5.55	-1.62	0.40	3.93
DBTDT[a]	-6.07	-5.78	-1.78	0.29	4.00

[a]From Chapter 3 and [74].

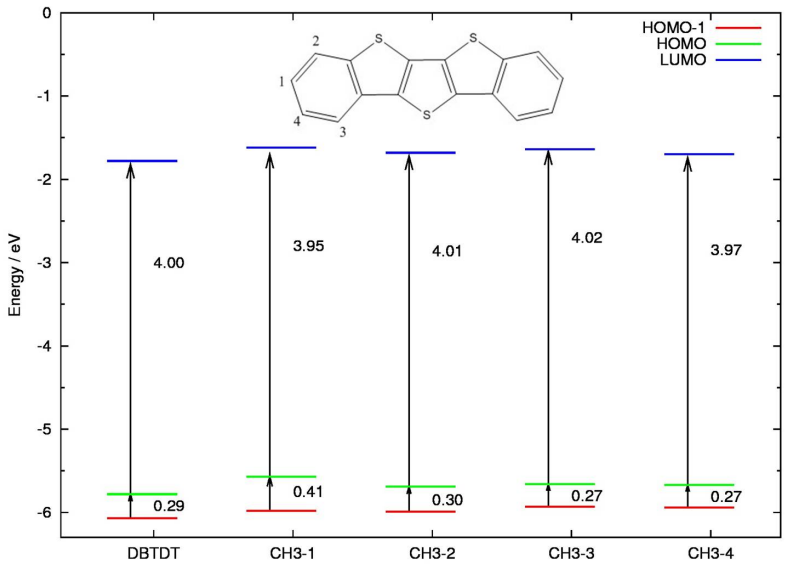

Figure 4.3: Frontier orbital energies computed at B3LYP/6-31+G* level of theory, for DBTDT Chapter 3, and the four substituted CH3-DBTDT (CH3-n) featuring -CH_3 substituents in different positions, (n=1-4, see the inset for numbering).

of Fig.(4.2) shows that it is quite well separated (0.52 eV) from the HOMO of BBTT, in contrast with the *anti* isomer (0.29 eV, Chaptr 3). On the other hand the nature of the two orbitals has changed in BBTT compared with DBTDT, with both HOMO and HOMO-1 of the former displaying large sulfur contributions. The gap between HOMO and HOMO-1 is almost unchanged for most C6-DBTDT derivatives except for the system experimentally investigated which displays a larger gap of ca 0.40 eV compared with DBTDT.

The peculiar increase of the gap for C6-DBTDT (C6-1) compared with DBTDT and with the remaining C6-DBTDT (C6-2; C6-3; C6-4) can be rationalized by inspecting the respective HOMO and HOMO-1 orbitals in Fig.(4.2): in positions 2-4 of the peripheral benzene, both the HOMO and the HOMO-1 display a large electronic density. Substitution in these positions, therefore, induces a hyper-conjugation effect which extends delocalization of both the HOMO and the HOMO-1 on the side chains. As a consequence, both orbitals rearrange their shape and energies compared to DBTDT in a similar way and the gap is substantially preserved. In contrast to the HOMO, how-

Table 4.2: Intramolecular reorganization energy computed with adiabatic potential (AP) method at B3LYP/6-31+G* level of theory: $\lambda_{intra}^{n(AP)}$ and $\lambda_{intra}^{c(AP)}$ are the contributions from the neutral and the cationic states, respectively, to the total AP reorganization energy $\lambda_{intra}^{(AP)}$.

	$\lambda_{intra}^{(AP)}$ [eV]	$\lambda_{intra}^{n(AP)}$ [eV]	$\lambda_{intra}^{c(AP)}$ [eV]
BBTT	0.239	0.123	0.117
C6-DBTDT	0.248	0.124	0.124
DBTDT[a]	0.233	0.116	0.117

[a]From Chapter 3.

ever, the HOMO-1 orbital has negligible electron density in position 1 and therefore for C6-DBTDT (C6-1) hyper-conjugation is effective only for the HOMO. The effect of substituents therefore operates differently for the two orbitals and the final effect is the observed increase of the HOMO/HOMO-1 gap up to 0.40 eV. Very similar results are also obtained from calculations on model systems featuring a methyl substituent instead of the longer alkyl chain (see Fig.(4.3)).

In Chapter 3 it has been shown that condensed phase effects reduce further the HOMO/HOMO-1 gap of DBTDT owing to the different nature of the two occupied orbitals. Since, in contrast to DBTDT, BBTT shows sulfur contributions in both orbitals, a remarkable energy gap reduction is not expected in this case, and therefore the role of the HOMO-1 for the charge transport properties of BBTT can be safely ruled out. For C6-DBTDT the parentage of the occupied orbitals with those of DBTDT is much stronger and a reduction of the gap in the condensed phase can be expected. Owing to the larger gap in C6-DBTDT, the role of the HOMO-1 is expected to remain minor in this case, compared with DBTDT. Nevertheless, in the following discussion also the electronic couplings mediated by HOMO-1 orbitals are included. The shape of C6-DBTDT HOMO closely resembles that of DBTDT, except for a less evident electronic density on the two lateral sulfur atoms while BBTT shows a much larger electronic density on them. For thiophene containing molecules, electronic density on sulfur atoms has, generally, an important role in governing the intermolecular interactions and electronic couplings in the solid state [78]. This is reflected, for instance, in the different solid state packing of the two systems: C6-DBTDT shows a typical oligoacene herring-bone packing while BBTT shows π-π stacking. Therefore the different sulfur contributions to the HOMOs of the two systems could be expected to lead to different electronic couplings and charge transport properties that should favor the molecule displaying larger sulfur contributions (BBTT). As it will be shown below, the calculations predict, in contrast with this general observation, but in agreement with measured charge mobilities, that the best performing system is C6-DBTDT.

4.3 Intra and intermolecular parameters

The computed intramolecular reorganization energies of BBTT and C6-DBTDT are quite close each other and also close to the reference DBTDT (see Table 4.2) while they are quite large in magnitude with respect to the oligoacene analogue, pentacene, whose typical value is about 0.1 eV [95]. The most active intramolecular vibrational modes involved in the molecular reorganization from the neutral to the charged state are provided by the Huang-Rhys analysis, Fig.(4.4), top.

Inspection of bond length variations from the neutral to the cationic state, Fig.(4.5), shows that for both BBTT and C6-DBTDT the major changes occur for the C-C bonds belonging to the central tiophenic unit. As a consequence, we expect that the most active vibrations in assisting charge transfer will also show considerable amplitudes on these C-C bonds. This is indeed the case, as it can be seen from Fig.(4.4), bottom, where the most active vibration (in the region of C-C stretching) is depicted for both BBTT and C6-DBTDT. In agreement with geometry changes (see Fig.(4.5)) the central thiophene ring undergoes the largest changes which lead to equalization and also reversal of the C-C bond lengths.

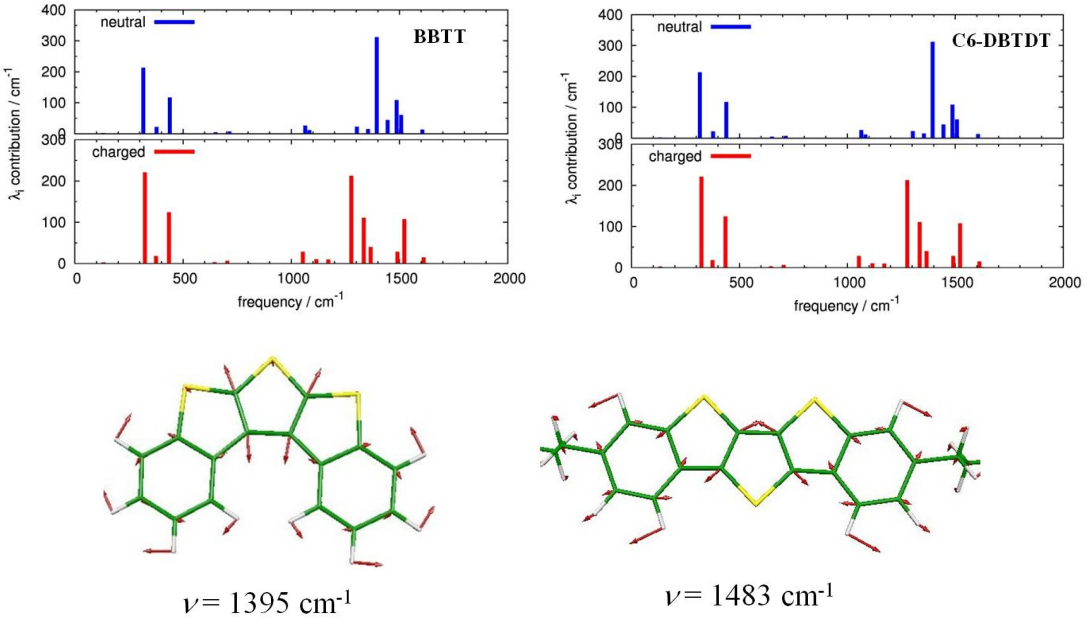

Figure 4.4: (top) The vibrational frequencies contributions to the computed intramolecular reorganization energies of BBTT (left) and DBTDT (right), both from neutral and cationic species, computed at B3LYP/6-31+G* level of theory. (bottom) The most active vibration for BBTT (left) and C6-DBTDT (right).

To estimate the inter-molecular interactions, we considered the available crystalline structures. Unfortunately the β-phase single crystal of C6-DBTDT was unsuitable for the X-ray structure analysis and only the cell parameters were obtained [84]. For this reason we restricted our investigation to the α polymorph of C6-DBTDT. The crystal of BBTT [79] belongs to the $P2_12_12_1$ space group and the molecules are arranged with π-π

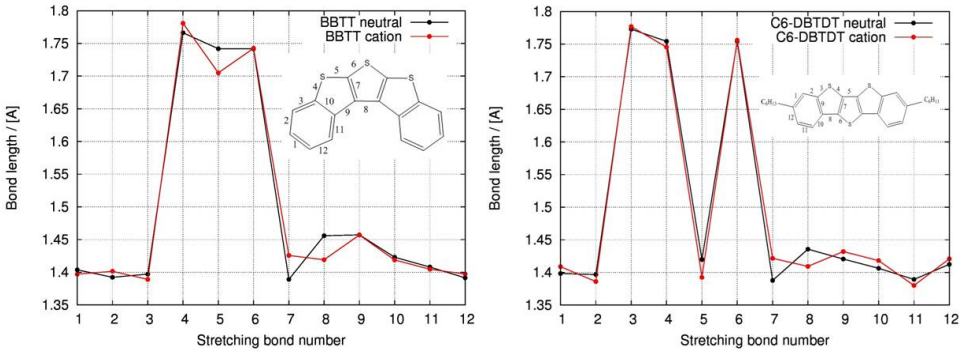

Figure 4.5: B3LYP/6-31+G* computed bond lengths of BBTT (left) and C6-DBTDT (right) neutral structure in black, and cationic structure in red (bond numbering as depicted in the inset).

stacking, Fig.(4.6) left. This is indeed the first example of a fused-ring thienoacene in which molecules are not arranged with herringbone packing [79]. The crystalline α-phase of C6-DBTDT [94] contains molecules with a highly planar π-conjugated skeleton with tilted alkyl chains, Fig.(4.6) right. Both alkyl chains do not lie in the same plane as the π-conjugated framework such that the structure of the molecule becomes bowl-shaped. The crystal belongs to the orthorombic *Pbcm* space group. Both systems present the molecules arranged in planes parallel to the crystallographic *ab* plane. For BBTT, each molecule is surrounded, in the *ab* plane, by eight molecules while the herring-bone arrangement of C6-DBTDT leads to six surrounding molecules. The hopping paths to these neighbors are indicated by arrows of different colors and different labels, in Fig.(4.6). Interactions between molecules belonging to two different planes are expected to be negligible owing to their large distances.

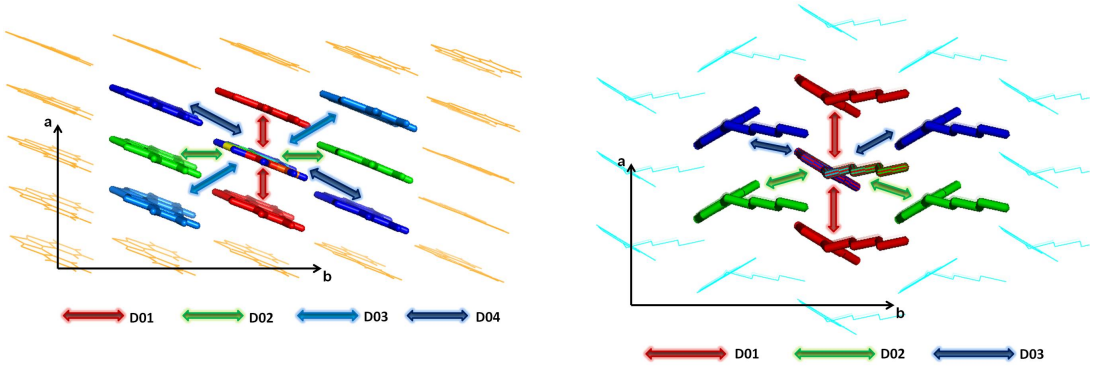

Figure 4.6: Portion of the BBTT crystal (left) and of the α-phase of C6-DBTDT (right) with a schematic view of the hopping pathways from the central molecule to the nearest neighbors in the *ab* crystallographic plane. The available pathways are labeled with increasing numbers (1 to 4) for increasingly larger intermolecular distances between constituent molecules.

Quantum-chemical calculations of electronic interactions between HOMO orbitals (see Table 4.3) agree closely with previous calculations [84, 94, 86] and show that the only efficient path is by far the D01 for both systems: this path is associated with

Table 4.3: Electronic couplings computed with standard 2×2 orthogonalization method (B3LYP/6-31G* level of theory) and charge rate constants for the selected hops in the crystals.

			Literature data		Computed data			
Compound	dimer	dist. [Å]	V_{el}^{H} [a] [meV]	V_{el}^{H-1} [b] [meV]	V_{el}^{H} [b] [meV]	V_{el}^{H-1} [a] [meV]	k_{eT}^{brown} [c] [ps^{-1}]	k_{eT}^{TOF} [d] [ps^{-1}]
BBTT	D01	3.8834	73	-	74	40	7.76	8.49-7.08
	D02	7.5943	9	-	9	20	0.12	0.12-0.12
	D03	8.5296	2	-	2	1	0.01	0.00-0.01
	D04	8.5296	0	-	0	0	0.00	0.00-0.00
C6-DBTDT	D01	4.1200	103	77	109	100	81.48	88.36-74.76
	D02	5.8390	3	47	2	39	0.04	0.04-0.04
	D03	5.9994	1	55	2	51	0.03	0.03-0.03

[a]Computed electron couplings from literature: BBTT computed at PW91/QZ4P level of theory [84]; C6-DBTDT computed at B3LYP/6-31G** level of theory [77]. [b] V_{el} computed with the standard 2×2 orthogonalization (Section 1.2 and [16]). [c]Kinetic constants computed for charge hopping between HOMO orbitals without external electric field. [d]Kinetic constants computed for charge hopping between HOMO orbitals with an external electric field applied along a axis: forward and backward rates.

the dimer displaying the shortest intermolecular distance and oriented along the a axis for both molecules. In both cases indeed this is the most favorable direction for π-π stacking. The magnitude of the coupling associated with this path is particularly relevant for C6-DBTDT and this is apparently in contrast with the generally accepted expectation, recalled in the previous section, of larger interactions for orbitals displaying large densities on sulfur atoms. Clearly, in this case, the solid state packing plays a determining role in tuning the magnitude of the electron couplings: compared with DBTDT, either isomerism or side chains strongly affect the packing and intermolecular interactions. Moving to the computed interactions between HOMO-1 orbitals, we note that for BBTT the couplings are slightly less anisotropic but also reduced in magnitude, compared with those of the HOMOs. Since we have already shown that the HOMO-1 is quite well separated from the HOMO, these results give additional support to the expectation of a negligible role of the HOMO-1 orbitals for the charge transport properties of BBTT. Similarly to BBTT, the computed results for the HOMO-1 of C6-DBTDT also point to a more balanced distribution of electronic couplings for the three available paths (see Table 4.3), with a coupling of 51 meV for path D3, although our computed electronic couplings are slightly different from previous calculations [86], possibly because the position of molecules inside the crystal were re-optimized in previous studies [86] and not taken directly from the experimental crystal structure as in this work. As in previous studies, we confirm that the HOMO-1 orbital displays couplings comparable to those of the HOMO. This, combined with the expected decrease of the HOMO/HOMO-1 energy gap in the condensed phase, might lead to some non-negligible contribution of the HOMO-1 orbital to the charge transport properties of C6-DBTDT. The electronic couplings are also computed including a Löwdin orthogonalization on

Table 4.4: Electronic couplings (B3LYP/6-31G* level of theory) computed with full orthogonalization and charge rate constants for the selected hops in the crystal.

	dimer	dist. [Å]	$V_{el}^{H\ b}$ [meV]	$k_{eT}^{brown\ c}$ [ps^{-1}]	$k_{eT}^{TOF\ d}$ [ps^{-1}]
BBTT	D01	3.8834	91	11.68	12.78-10.65
	D02	7.5943	15	0.30	0.30-0.30
	D03	8.5296	1	0.00	0.00-0.00
	D04	8.5296	0	0.00	0.00-0.00
C6-DBTDT	D01	4.1200	132	118.7	128.7-108.9
	D02	5.8390	4	0.13	0.13-0.13
	D03	5.9994	2	0.02	0.02-0.02

[a]Kinetic constants in the absence of an external electric field. [b]Kinetic constants in the presence of an external electric field applied along a axis: forward and backward rates.

Table 4.5: Effective frequency ω_{eff} and associated Huang-Rhys factor S_{eff} employed in the KMC simulations.

	ω^{eff} [cm^{-1}] [a]	S^{eff} [a]	λ_{intra} [eV] [a]	λ_{class} [eV] [b]	λ_{class}^{tot} [eV] [c]
BBTT	660	2.930	0.240	0.001	0.011
C6-DBTDT	901	1.778	0.199	0.049	0.059

[a] Refined values, considering only frequencies above 250 cm^{-1}. [b] Contributions to classical reorganization energy from intramolecular classical vibrations. [c] Total classical reorganization energy, adding 0.01 eV to λ_{class}, the contribution of external reorganization energy according to recent estimates [34].

the complete basis set of the two monomers forming the dimers (Section 1.2.1). The pattern of these couplings follows closely those discussed here, except that they are ca. 20% larger (see Table 4.4).

Finally, concerning the suitability of the hopping model, we note that we are within the limits for BBTT since the largest coupling (0.074 eV) is considerably smaller than one-half of the reorganization energy [10], while we are just at the limits of validity for C6-DBTDT. As a consequence, the numerical values of computed charge mobilities of C6-DBTDT have a more qualitative significance.

4.4 Charge transport anisotropy

To gain a more quantitative insight into charge transport properties of BBTT and C6-DBTDT, we performed KMC simulations, with the multiscale protocol in Section 1.6: the parameters determined by QM calculations (see Table 4.5) were employed to estimate the kinetic rate constants for each charge jump (Eq.(1.6)) and then were used by the KMC code to propagate the charge carrier in the crystal. KMC simulations were limited to the propagation of charges via hopping between HOMO orbitals.

For BBTT the computed Brownian mobility is relatively small and amounts to 0.07 cm^{2}Vs^{-1}, while for C6-DBTDT it reaches the considerably larger value of 1.77 cm^{2}Vs^{-1}. For both systems, as expected by the discussion of electronic couplings, the

Table 4.6: Diagonalized Brownian mobility tensors: associated eigenvalues and eigenvectors from KMC simulation employing V_{el} from (left) the standard 2×2 and (right) the complete orthogonalization procedure.

	2×2 partial orthogonalization				Complete orthogonalization			
	Eigenval. [cm^2Vs^{-1}]	Eigenvect. x	y	z	Eigenval. [cm^2Vs^{-1}]	Eigenvect. x	y	z
BBTT	0.00	0.00	0.00	1.00	0.00	0.00	0.00	-1.00
	0.01	0.00	1.00	0.00	0.02	0.00	1.00	0.00
	0.15	-1.00	0.00	0.00	0.22	-1.00	0.00	0.00
C6-DBTDT	0.00	0.00	0.00	1.00	0.00	0.00	0.00	1.00
	0.01	0.00	1.00	0.00	0.01	0.00	1.00	0.00
	1.76	1.00	0.00	0.00	2.60	1.00	0.00	0.00

charge transport takes place mainly along the a axis as it is shown by the diagonalization of the mobility tensor (see Table 4.6) with an almost negligible component along the b axis.

With respect to the Brownian case, the presence of an external electric field increases more than three times the charge mobility components (see Table 4.7) and enhances the already marked anisotropy of charge transport along a, leading to an almost one-dimensional character. To explore in detail the anisotropy [70] we applied the electric field in the ab plane and varied its orientation by small angular steps. TOF mobilities were computed for each direction of the applied field and a plot of the angular dependence of the mobility was collected in Fig.(4.7) for both BBTT and C6-DBTDT. KMC simulations were carried out also using the electronic couplings obtained from the complete basis set orthogonalization (Section 1.2 and 1.2.1). Owing to the larger values of the corresponding couplings, also computed mobilities are larger and increase by a factor of ca. 1.5 either for Brownian and TOF mobilities, while conserving the same strongly anisotropic character, see Table 4.6 and 4.7. For both systems our computed values show a good agreement with the experimental values of mean mobilities obtained for single crystal devices. Unfortunately, anisotropy measurements have not been reported. In the case of BBTT the single crystals assemble in long wires and are therefore 1D materials ideal to study the intrinsic properties in the longitudinal direction, namely the a axis. This means that our computed TOF mobility along the a axis (0.55 cm^2Vs^{-1}) can be compared with the observed mobility (0.6 cm^2Vs^{-1}) but we lack the experimental counterpart for the b direction. The agreement with the calculated results is however very good and, interestingly, the comparison with DBTDT (Chapter 3) is also in nice agreement with the observation that computed mobilities are considerably larger for the *anti*-DBTDT isomer than for the *syn* isomer, in keeping with the experimental results [81, 84]. This good agreement confirms that the role of the HOMO-1 for BBTT is negligible. For C6-DBTDT some measurements were carried out on thin films and it was found that the molecules are stacked perpendicular to the substrate [94]. More recent measurements were carried out on single crystals with

Table 4.7: TOF mobilities for BBTT and C6-DBTDT computed from KMC simulations employing V_{el} from the (left) standard 2×2 and (right) complete orthogonalization procedure with electric field directed along the a (μ_a) and b (μ_b) crystallographic axes.

	2×2 orthogonalization			Complete orthogonalization			
	μ_a [cm^2Vs^{-1}]	μ_b [cm^2Vs^{-1}]	μ_a/μ_b [a]	μ_a [cm^2Vs^{-1}]	μ_b [cm^2Vs^{-1}]	μ_a/μ_b [a]	μ_{exp} [cm^2Vs^{-1}]
BBTT	0.55	0.04	16	0.82	0.08	10	0.2-0.6[b]
C6-DBTDT	5.61	0.01	560	8.17	0.02	408	1.8-8.8[c]

[a]Anisotropy ratio between the mobility along a and the mobility along b. [b]Experimental values for BBTT from refs. [79, 84]. [c]Experimental values for C6-DBTDT from refs. [94, 86].

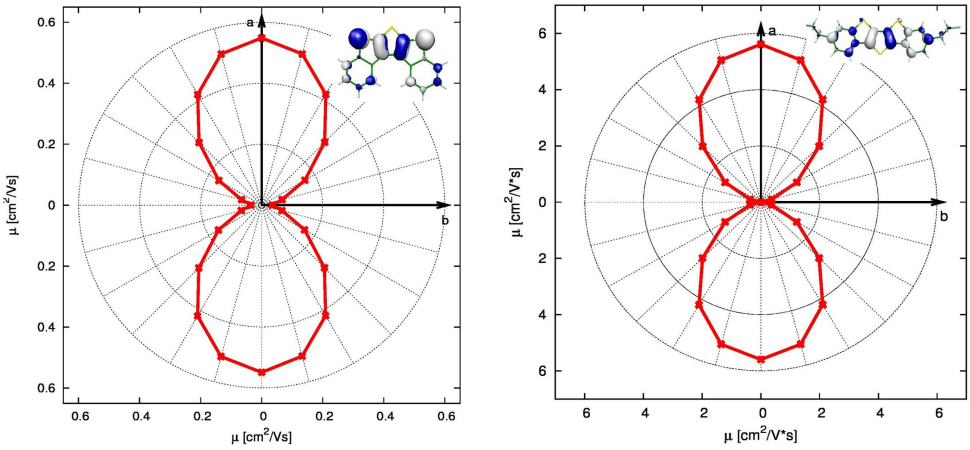

Figure 4.7: Computed TOF mobility anisotropy on the crystallographic ab plane for BBTT (left) and C6-DBTDT (right).

the "organic ribbon mask" technique but different directions of charge transport were not explored [86]. Therefore, also in this case, we can compare our computed result (5.61 cm^2Vs^{-1}) with the best result reported from single crystals [86] (8.5 cm^2Vs^{-1}). By comparing computed and observed mobilities, we must recall that, in this case, the validity of the hopping approach is at its limit. In addition we have pointed out, in the previous section, that the role of the HOMO-1 could be non-negligible in this case and might contribute to increase the charge mobility of C6-DBTDT. Nevertheless the agreement is good and in particular the comparison with the considerably lower mobility of unsubstituted DBTDT [84] is successfully reproduced by all the simulations.

Based on the KMC simulations that propagate charges via hopping between HOMO orbitals, we conclude that an almost 1D charge transport for both BBTT and C6-DBTDT (in its α-phase) can be expected. However the contribution of the HOMO-1 for C6-DBTDT might switch the one-dimensional character toward a slightly more marked 2D character, owing to the presence of non-negligible couplings for pathways D02 and D03. Their role in modulating charge transport is strictly related to the HOMO-1/HOMO energy difference in the condensed phase. In this sense, future measurements of anisotropy on the α-phase might shed light on the importance of the

HOMO-1 for C6-DBTDT.

4.5 Conclusions

The investigation on *anti*-DBTDT (Chapter 3) has been extended to the charge transport properties of the *syn* isomer, BBTT, whose crystal structure is one of the few examples of a π-π stacking arrangement for thienoacene derivatives and C6-DBTDT, an alkylated derivative, packing in the more conventional herringbone arrangement.

In contrast with *anti*-DBTDT, the energy difference between the HOMO-1 and HOMO orbitals is relatively large for BBTT and is not expected to decrease much in the condensed phase, owing to the similar sulfur dominated nature of the two orbitals. C6-DBTDT has frontier orbitals very similar to those of DBTDT but the HOMO-1/HOMO energy gap has increased compared with the unsubstituted compound and compared with other symmetrically substituted C6-DBTDT derivatives, because of an unbalanced hyperconjugation effect which affects only the HOMO and not the HOMO-1. As a consequence, the role of the HOMO-1 orbital is considered to be negligible for the charge transport properties of BBTT while it might still contribute, to a minor extent, to the charge transport of C6-DBTDT.

Charge mobilities simulated taking into account only the role of the HOMO charge carriers, compare very well with the measured mobilities in single-crystal devices. Both systems show an almost 1D charge transport with C6-DBTDT displaying a ten times larger mobility value in agreement with experiment. The role of the HOMO-1 orbital might reveal in a more marked 2D charge transport character for C6-DBTDT.

Taking together the simulated mobilities for the two thienoacene derivatives investigated here and *anti*-DBTDT (Chapter 3), a very nice agreement has been found concerning the order (and magnitude) of predicted and observed mobilities in that C6-DBTDT showed the largest mobility, followed by *anti*-DBTDT and finally BBTT. Interestingly, the computed (and measured) charge mobilities do not follow the generally accepted expectation that large sulfur contributions on orbitals involved in charge transport should favor high mobilities thereby showing that packing has a relevant role. The good agreement between computed and observed data supports the quality of the proposed model of charge transport.

CHAPTER 5

Dimer and cluster approach for the evaluation of electronic couplings governing charge transport : application to two pentacene polymorphs

The content of this chapter is reproduced in part with permission from Ref.[30]:
Canola S., Pecoraro C., Negri F. *Chem. Phys.*, **2016**, *478*, 130-138.

5.1 Introduction

The electronic structure of organic semiconducting materials has received considerable attention from the viewpoint of both fundamental research and device fabrication and performance. Pentacene, in particular, has become an important reference in organic-semiconductor material, with potential applications in thin-film transistors and single crystals, due to its high mobility.

The intrinsic charge transport properties of organic crystals depend strongly on the molecular packing and arrangement in the crystal. In this regard, pentacene, that shows one of the highest charge carrier mobilities among organic semiconductors, is known to crystallize in at least four polymorphs, which can be distinguished by their layer periodicity d [96, 97]. Various structure determinations on single crystals grown in different ways have revealed different triclinic structures for pentacene [98]. Polymorphism in pentacene, on the other hand, has been observed also in thin-film growth experiments. In all of these phases, pentacene molecules align their long axis approximately perpendicular to the film surface but different interlayer spacings (d-spacing) perpendicular to the thin-film surface have been observed, with values of 14.1, 14.5, 15.0, and 15.4 Å, sometimes used to label the different polymorphs. The shortest d-spacing of 14.1 Å is consistent with the recent room-temperature single-crystal structure of pentacene, and

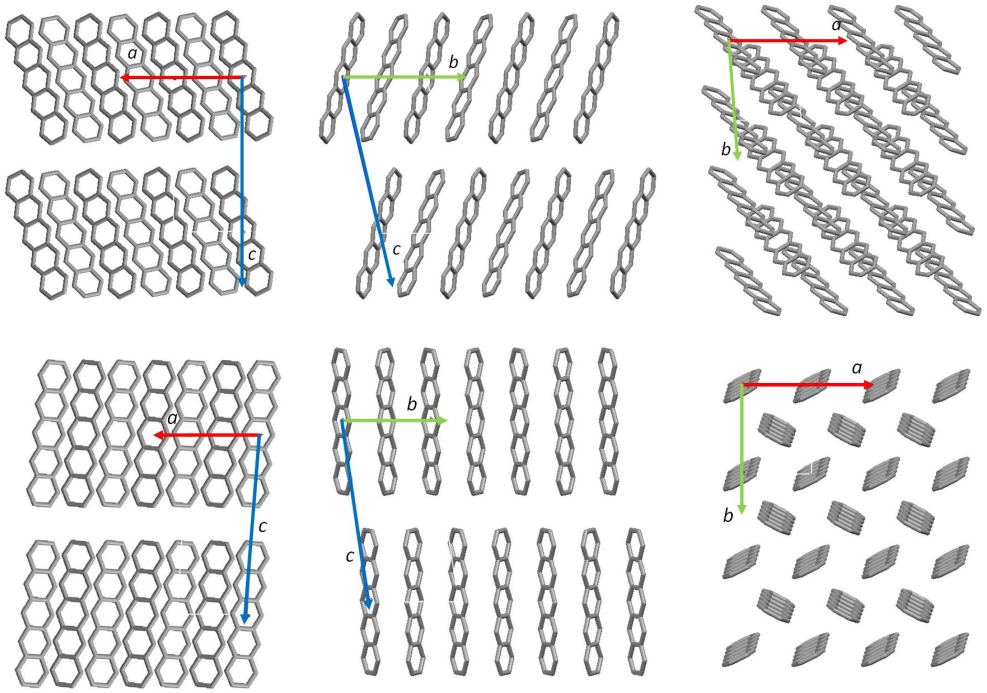

Figure 5.1: Portion of the two polymorphs of pentacene investigated in this work: (top) single crystal polymorph, (bottom) thin film polymorph. Views along the b axis (left), a axis (center) and c axis (right). Hydrogens are not shown.

the 14.5 Å d-spacing is consistent with the initial structure reported by Campbell [99] and with the high-temperature polymorph stable above 463 K [98]. Thin films fabricated on insulating layers often show a unique structure called the "thin film" phase that is characterized by an interlayer spacing of $d = 15.4$ Å. The substrate-induced 15.4 Å polymorph is the most relevant for organic thin-film transistor (OTFT) applications [100] because this polymorph is usually present in the working layers of pentacene OFETs [101]. The complete lattice parameters for the thin film phase of pentacene have been determined for various substrates [100, 101]. Recently the angle resolved photoemission spectroscopy measurements of thin film phase pentacene, (identical to that of the thin film phase grown on SiO_2) have been reported [102] and used to fit a tight-binding model from which effective masses have been derived. The effective masses indicated a less marked charge transport anisotropy compared to that reported for the single crystal phase of pentacene, from field effect mobility measurements [103].

Charge mobility calculations have been reported for pentacene, encompassing band theory and hopping approaches and computed electronic couplings have been discussed by several groups [104, 105, 106, 107, 108, 70, 109]. The band structure for different polymorphs of pentacene and their hole mobilities were determined in recent computational investigations [105, 106]. Charge mobility and mobility anisotropy has been predicted also in the framework of the hopping approach, but only for the single crystal structure of pentacene [107, 108, 70, 109] and generally using the classical Marcus equation to estimate charge transfer rate constants.

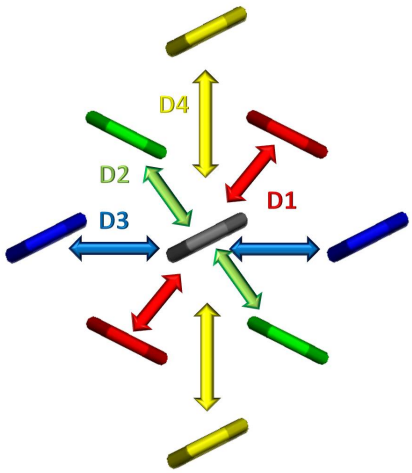

Figure 5.2: Schematic view of the hopping pathways from the central gray molecule to the nearest neighbors in the *ab* crystallographic plane of both polymorphs of pentacene. The available pathways are labeled with increasing numbers (D1 to D4) for increasingly larger intermolecular distances between the centers of mass of the molecules forming the dimers.

Here the single crystal polymorph [96] has been reconsidered, also including the thin film polymorph, whose structure and molecular orientation on SiO_2 has become available [100], see Fig.(5.1). The electronic couplings for the two different polymorphs have been determined and used to model charge transport. Usually the electronic couplings are estimated with the common dimer approach (Section 1.2 and [16]). Nonetheless, in the case of DBTDT (Chapter 3 and [74]), a cluster approach was employed to estimate the solid phase embedding effects on the small HOMO/HOMO-1 energy difference which influences charge transport. Here it is explored the use, for the first time, of the cluster approach (beside the dimer approach) also for estimating electronic couplings between the central molecule and surrounding molecules in the cluster.

5.2 Intramolecular reorganization energy

The intra-molecular reorganization energy, one of the parameters governing charge transport, was previously determined for pentacene and our results agree with available literature data [70]: the cationic state is associated with a small reorganization energy of ca. 0.092 eV from B3LYP/6-31G* calculations. From the analysis of Huang-Rhys factors, it is derived the effective quantum frequency of 1423 cm^{-1} used for the evaluation of charge transfer rate constants according to Marcus-Levich-Jortner equation, Eq.(1.6).

Table 5.1: Electronic couplings V_{el} (B3LYP/6-31G* level of theory) for the selected charge hopping paths of the single crystal and thin film polymorphs of pentacene.

		Dimer approach		Cluster approach	
dimer	intermol. dist. [Å]	$V_{el}^{H\ a}$ [meV]	$V_{el}^{H\ b}$ [meV]	$V_{el}^{H\ c}$ [meV]	$V_{el}^{H\ b}$ [meV]
Single crystal polymorph					
D1	4.7615	85	83	88	8
D2	5.2139	52	51	54	21
D3	6.2660	33	44	31	66
D4	7.7750	0	0	1	22
D3'	6.2660	36	47	34	85
D4'	7.7750	0	0	1	30
Thin film polymorph					
D1	4.8187	70	65	73	26
D2	4.8351	67	62	69	41
D3	5.9580	50	60	48	75
D4	7.5960	0	0	3	19
D3'	5.9580	49	59	47	84
D4'	7.5960	0	0	3	31

[a]From the usual 2×2 orthogonalization procedure. [b]From the full orthogonalization procedure. [c] From the orthogonalization procedure involving only HOMO orbitals.

5.3 Dimer approach: 2×2 orthogonalization

Electronic interactions computed from the dimer approach have been reported in several studies for the single crystal polymorph, and our computed values, collected in column three, in the top part of Table 5.1, agree with previous investigations at the same [107] or similar [108, 70] level of theory. In Table 5.1 four couplings corresponding to the pathways depicted in Fig.(5.2) are collected. Of these pathways, D1 and D2 involve two molecules belonging to different sites while D3 and D4 correspond to interactions between molecules belonging to the same site type. Owing to the presence of two different sites in the crystal, there are two types of D3 pathways, indicated as D3 and D3' and similarly for pathway D4.

In addition to the single crystal polymorph the computed electronic interactions for the thin film polymorph in the bottom part of the same table are reported. The distances between centers of masses are very similar for the first two dimers D1 and D2 in Table 5.1, a fact which is reflected in the similar values of the two associated electronic couplings (70 and 67 meV). The two different molecular sites, in contrast with the case of the single crystal structure, display less marked differences as indicated by the small difference between the couplings D3 and D3'.

These couplings, combined with the intra-molecular parameters, were employed to evaluate rate constants according to the Marcus-Levich-Jortner formulation and these were used to propagate the charge carrier in the two polymorphs. To explore in detail the hole transport anisotropy the electric field was applied in the *ab* plane and its

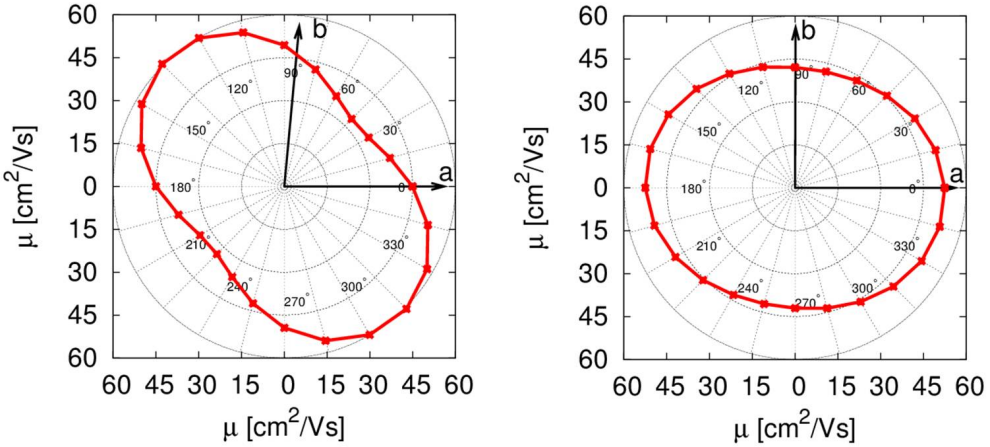

Figure 5.3: Polar plots of charge mobilities for (right) the thin film polymorph and (left) the single crystal polymorph employing electronic couplings computed from the usual dimer approach and 2×2 orthogonalization.

orientation varied by small angular steps. TOF mobilities were computed for each direction of the applied field and a plot of the angular dependence of the mobility was collected in Fig.(5.3). Both polymorphs show anisotropic hole mobilities, however the anisotropy is different for the two. More specifically the thin film polymorph, Fig.(5.3) right, shows less marked anisotropy compared to the single crystal polymorph, see Fig.(5.3) left, in agreement with the results inferred from experimental studies [102]. The anisotropy of the single crystal polymorph agrees with previous computational investigations [107, 108, 70] but the computed mobilities here reported, making use of the Marcus-Levich-Jortner formulation, are larger than those computed employing the classical Marcus equation for rate constants [70].It must be noticed that absolute values of the rate constants, and therefore of charge mobilities, can be strongly influenced by the chosen parameters and that lower mobilities can be obtained with larger outer sphere reorganization energies [33]. Although large experimental mobilities up to 35 $cm^2V^{-1}s^{-1}$ have been measured for ultrapure pentacene [110], the computed values should be taken with caution in the case of pentacene because of the small value of the intra-molecular polaron binding energy compared to the electronic interactions, which weakens the validity of the non-adiabatic hopping approach.

5.4 Dimer approach: full orthogonalization

As a second approach for determining the electronic couplings in the two polymorphs, the dimer approach is considered but with the full orthogonalization scheme described in the computational methods section. The couplings for the two polymorphs are also collected in Table 5.1, column four, from which it is seen that they are similar to those obtained in the 2×2 scheme. A slightly larger value is obtained for pathways D3 and D3' of the single crystal polymorph. A similar trend for thienoacene derivatives was already noticed (Chapter 4 and [92]) and these variations were attributed to the fact that the

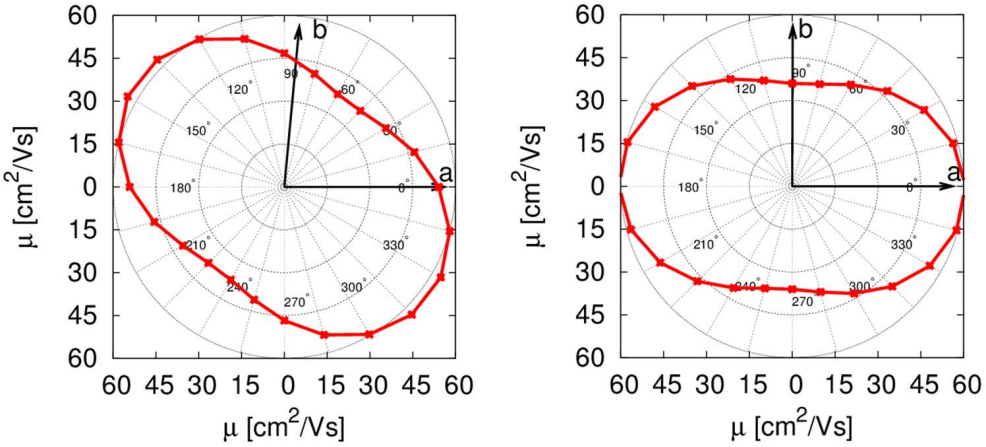

Figure 5.4: Polar plots of charge mobilities for (right) the thin film polymorph and (left) the single crystal polymorph. Electronic coupling computed from the usual dimer approach followed by orthogonalization over the full molecular orbital basis.

full orthogonalization scheme provides couplings that are suitable for a modified tight-binding model in which each molecular site is described with the entire set of molecular orbitals (the previously defined one molecule $\breve{}$ many states model). In this context it should be noted that the adopted KMC approach assumes a single type of charge carrier traveling through the material and therefore it is consistent with the usual tight-binding model in which each molecular site is described by a single charge carrier (represented by a single orbital, HOMO in this case, namely the one molecule – one state model defined in Section 1.2.1). Nevertheless the inclusion of additional charge carriers states (namely orbitals) as it results from the full orthogonalization procedure is not essential in the KMC simulation, to a good approximation, since the formation of higher energy charge carriers associated with these additional orbitals would be an unlikely event, being associated with very small charge transfer rate constants. For this reason the charge mobility and mobility anisotropy were simulated within the same KMC scheme also in the case of full orthogonalization. The resulting mobility anisotropies for the two polymorphs, shown in Fig.(5.4), are similar to those of Fig.(5.3) except for a slightly more marked anisotropy for the thin film polymorph that results from the slight change of some of the couplings.

5.5 Cluster approach

To investigate the effects of embedding on the central molecule and to explore whether the full orthogonalization approach may disclose couplings between non neighboring sites, a cluster approach, including not only the near neighbors but also molecules that are relatively far away from the central were considered. To this end 2D clusters composed by 9, 17, 31 molecules in the *ab* plane and 3D clusters that included either 9 or 17 molecules in the *ab* plane and two additional layers of 9 molecules above and

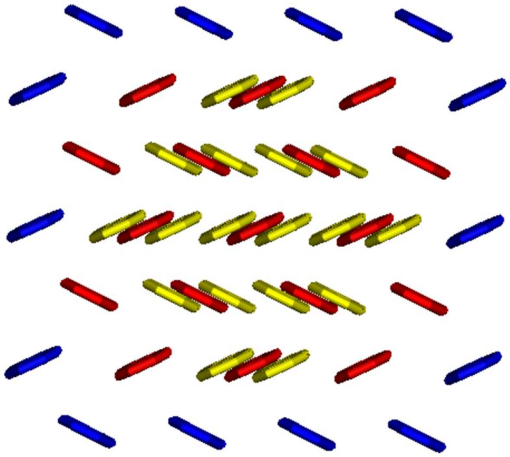

Figure 5.5: Schematic representation of the three most significant clusters considered in this work: (red) cluster formed by 17 molecules in the *ab* plane; (red and blue) cluster formed by 31 molecules in the *ab* plane; (yellow and red) cluster formed by 35 molecules of which 17 lie in the *ab* plane and the remaining yellow molecules lie above and below the layer of red molecules.

below the plane were taken into account.

The electronic couplings were determined either by orthogonalization of the HOMO orbitals (namely an extension of the dimer 2×2 approach to the cluster) or by full orthogonalization of the complete set of molecular orbitals of each molecule forming the cluster. The couplings corresponding to the first case are listed in the fifth column of Table 5.1. These are still very similar to those obtained from the dimer 2×2 approach but the couplings D3, D3' are slightly smaller while D4, D4' have become non zero and the diagonal couplings D1 and D2 have increased to a small extent. These changes, due to embedding effects, affect slightly the computed mobilities and anisotropies, as seen from Fig.(5.6), and confirm that the dimer approach (in the framework of the 2×2 orthogonalization) provides generally reliable couplings as long as embedding effects play a modest role as in this case. Interestingly at this level, the mobility anisotropy of the thin film polymorph, see Fig.(5.6) right has further decreased, as a result of embedding, in agreement with the experimental observation.

Larger changes occur instead when the full orthogonalization is considered (see column 6 in Table 5.1 and Fig.(5.7)). In this latter case the couplings for pathways D1-D4 undergo non negligible changes and in particular those for pathways D4, D4' have increased considerably. These changes are accompanied by the appearance of other couplings between molecules that are not near neighbors and that therefore are not listed in Table 5.1. These couplings are collected in the schematic representation of Fig.(5.7). The spread of computed couplings following the full-orthogonalization procedure for the cluster can be ascribed to the role of the basis set. Indeed it has been verified that with smaller basis sets the spread of couplings is less marked while for larger basis sets, including additional basis functions, the spread of couplings increases further. To rationalize this behavior, the overlap of each orbital on one molecule with each orbital on a

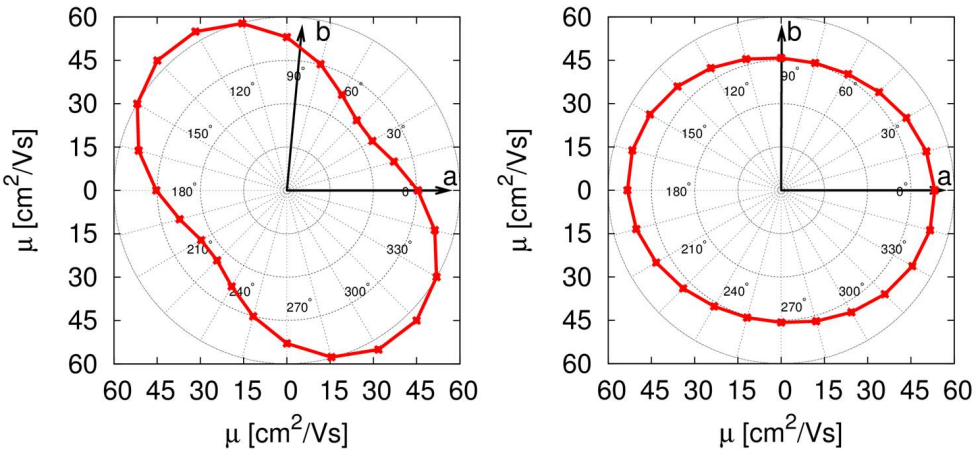

Figure 5.6: Polar plots of charge mobilities for (right) the thin film polymorph and (left) the single crystal polymorph. Electronic couplings computed from the orthogonalization restricted to the HOMO orbitals of the 31 molecules forming the cluster.

nearby molecule was examined and it was observed that, among others, large overlaps are computed between the HOMO orbital of one molecule and some non-valence orbital of the second molecule. These large overlaps between pairs of molecules extend all over the cluster and drive the large changes in the couplings couplings from the full orthogonalization. Indeed, including only valence orbitals in the orthogonalization procedure, the computed couplings remain similar to those obtained from the orthogonalization limited to HOMO orbitals. Because the underlying Hamiltonian for the full orthogonalization procedure is a tight-binding approach where each molecular site is associated with the full set of its molecular orbitals, (the one molecule ˘ many states model) it is not surprising that the couplings depend on the basis set, since the number of molecular orbitals depends on it.

Interestingly, the pattern of couplings, once introduced in the KMC charge propagation scheme, leads to predicted mobility anisotropies, see Fig.(5.8), that do not differ much from those of the previous cases. The anisotropies are similar for the different clusters considered, although the absolute values of computed hole mobilities has increased considerably compared to either the dimer approach or the cluster approach with orthogonalization limited to the HOMO orbitals. The reason for the increased mobilities is the large distance associated to some of the coupled molecules. Although the qualitative result is similar to those previously discussed, it can be concluded that the combination of full orthogonalization applied to the cluster, followed by KMC propagation of charge carriers is not suitable to obtain reliable predictions of charge mobilities. This can be ascribed to the fact that the two procedures (the first used to compute couplings and the second used to propagate the charge carrier) correspond to different model representations of the system. It should be recalled, indeed that the KMC propagation includes only one charge carrier type, namely it corresponds to a "one molecule ˘ one state" approach. In contrast, couplings are computed according to a "one molecule

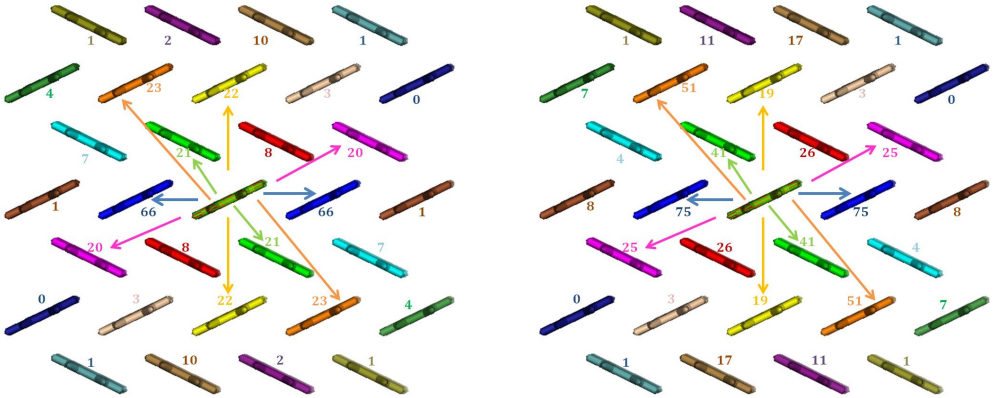

Figure 5.7: Map of couplings for one of the two sites of single crystal polymorph (left) and thin film polymorph (right) of pentacene, from full orthogonalization (B3LYP/6-31G*) calculations on the cluster formed by 31 molecules. The colored numbers in the figure are the electronic couplings (meV) between the central molecule and the molecule with the same color code of the number.

˘ many states" approach. A summary of the computed charge mobilities, from all the models discussed in the previous sections, is collected in Table 5.2.

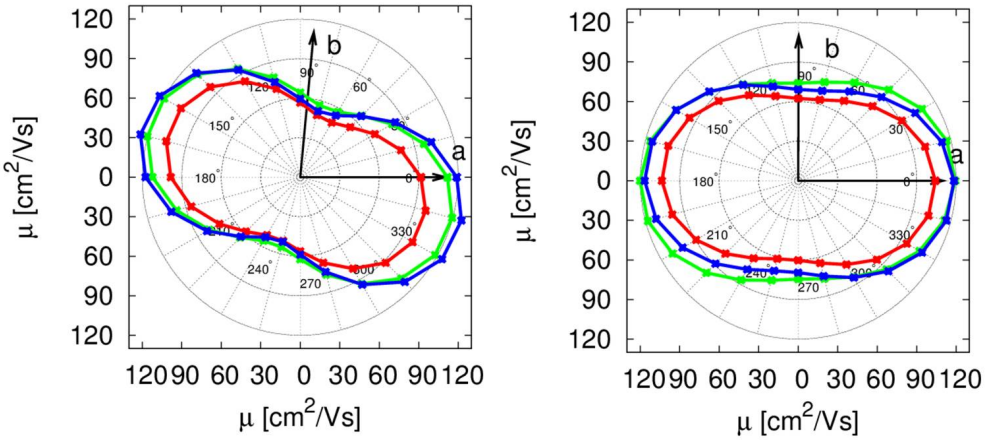

Figure 5.8: Polar plots of charge mobilities for (right) the thin film polymorph and (left) the single crystal polymorph computed using electronic couplings from the full orthogonalization procedure. (red) 2D cluster made by 17 molecules; (green) 2D cluster composed by 31 molecules; (blue) 3D cluster composed by 35 molecules. From 6-31G* calculations.

5.6 Embedding effects on energy sites

Using the clusters discussed in the previous sections it has been also considered the effect of embedding on the site energies. In the one-electron approximation adopted to discuss charge transport, the site energies correspond to the HOMO energies of the two different molecules in the cluster. Several approaches to include polarization effects have appeared in the literature. Possible routes consist in the use of micro-electrostatic

Table 5.2: Computed TOF hole charge mobilities for the two polymorphs of pentacene.

	Single crystal polymorph			Thin film polymorph		
	μ_{max} [cm^2/Vs]	μ_{min} [cm^2/Vs]	μ_{max}/μ_{min}	μ_{max} [cm^2/Vs]	μ_{min} [cm^2/Vs]	μ_{max}/μ_{min}
Dimer[a]	60.5	33.4	1.8	52.5	42.1	1.3
Dimer[b]	63.3	37.6	1.7	60.6	36.0	1.7
Cluster 31[c]	63.5	34.3	1.8	53.0	46.1	1.1
Cluster 31[b]	120.0	54.8	2.2	120.1	73.9	1.6
Cluster 35[b]	126.7	51.9	2.4	118.2	69.1	1.7

[a]From the usual 2×2 orthogonalization procedure. [b]From the full orthogonalization procedure. [c] From the orthogonalization procedure involving only HOMO orbitals.

Table 5.3: HOMO energies and their difference (B3LYP/6-31G* level of theory) for the two sites in the unit cell of pentacene computed as isolated molecules or embedded in clusters made by 17 and 31 molecules quantum-chemically described.

	ΔE [eV]	*HOMO* (site1) [eV]	*HOMO* (site 2) [eV]
Single crystal polymorph			
Isolated molecule	0.058	-4.503	-4.561
Cluster 17	0.077	-4.090	-4.167
Cluster 31	0.081	-3.997	-4.078
Thin film polymorph			
Isolated molecule	-0.001	-4.833	-4.832
Cluster 17	0.002	-4.137	-4.139
Cluster 31	0.001	-4.034	-4.035

(ME) methods [25] or QM/MM approaches combined with polarizable force fields [23]. The cluster approach described in Section 1.2.1 and previously employed for the electron couplings, is now exploited to determine the effect of embedding on the HOMO orbital energy of the central molecule. In this regard it must be noted that the two sites are substantially different for the single crystal polymorph, with the two molecules displaying remarkably different bond lengths, while they have very similar molecular structures in the case of the thin film polymorph. These geometry differences are reflected in a notable energy difference of the HOMO orbitals computed for isolated molecules at the geometries of the single crystal polymorph compared to those obtained for the thin film polymorph (see Table 5.3). The energy difference between the two orbitals is negligible for the latter and amounts to 58 meV for the former.

The embedded site energies are estimated by applying the orthogonalization limited to the HOMO orbitals since in this case the reference model is the usual tight-binding, in which each molecule is described by its HOMO orbital only. Accordingly, for the thin film polymorph, the site energies difference remains almost negligible (1 meV for the largest cluster) while it increases from 58 meV to 81 meV for the single crystal polymorph with an increase of 23 meV. A site energy difference of 24 meV has been derived by fitting a tight-binding model based on band structure measurements [111].

In other studies based on the tight-binding model site energy differences of 33-42 meV were derived for the single crystal polymorph [106, 112]. In a recent computational study based on intramolecular charge redistribution and induced dipoles it was shown that the energy site differences for pentacene are in the range 30-50 meV [113]. These values are close to the embedding effect predicted by our calculations if it is neglected the initial (isolated molecule) energy difference which is strongly related with the remarkable geometry difference of the two molecular sites.

5.7 Conclusions

The hole transport properties of two polymorphs of pentacene have been modeled, namely the single crystal polymorph, which has been considered in previous computational investigations, and the thin film polymorph, which is relevant for organic thin-film transistor applications but which has been seldom considered in computational studies. Electronic couplings have been evaluated following the standard dimer approach but also considering a cluster approach in which the central molecule is surrounded by a large number of molecules quantum-chemically described. Computed electronic couplings were orthogonalized and the effective electronic couplings, suitable for the parametrization of a tight-binding model, are derived either from the orthogonalization scheme limited to HOMO orbitals and from the orthogonalization of the full basis of molecular orbitals. These couplings were used to model charge transfer rate constants in the framework of the non-adiabatic hopping model and the angular dependent mobilities were computed via Kinetic Monte Carlo simulations. Couplings obtained from the dimer approach or from the cluster approach, with orthogonalization limited to HOMO orbitals are relatively similar and lead to similar predicted charge mobilities and anisotropies. It is interesting to note, however, that these couplings are similar but not identical as a result of embedding effects. It can be concluded therefore that the cluster approach with the orthogonalization limited to HOMO orbitals may be preferable to the dimer approach when embedding effects are not negligible. The couplings obtained in the framework of the full orthogonalization procedure applied to the cluster approach are remarkably different: they extend to pairs of molecules that are considerably far each other and they depend on the basis set. This behavior results from not negligible overlaps between valence and non-valence orbitals centered on two different molecules. The underlying effective Hamiltonian for the full orthogonalization procedure is the "one molecule – many states" while in the KMC simulations only one charge carrier ("one molecule ˘ one state") is considered; therefore the injection of the couplings from the first approach into the second is less appropriate being the two based on contrasting models. On the other hand a more complex KMC procedure corresponding to the "one molecule ˘ many states" model would be difficult to implement and of limited practical use. Therefore it can be concluded that the orthogonalization limited to frontier or at most few valence orbitals is recommended either within the dimer or

the cluster approach. However, all the considered approaches provide similar results as regard the anisotropy of the two polymorphs and show that the anisotropy of the thin film polymorph is different from that of the single crystal polymorph, in agreement with experimental data. Energy site differences cannot be predicted from the usual dimer approach. Here they have been estimated with the cluster approach limited to the orthogonalization of the HOMO orbitals and the predictions are shown to be in good agreement with previously reported fitted parameters for tight binding models and from microelectrostatic calculations.

Part II

Energy transport

CHAPTER 6

Introduction to energy transport

6.1 Energy transfer regimes

Energy transport is a physical process happening into molecular aggregates and involving the movement of excitation energy among the molecules. This corresponds to the transfer of an exciton, i.e., a "quasi-particle" made by a hole and an electron bound together through Coulomb attraction and treated as a single entity. It is assumed that such a bond is strong and so each exciton spreads in the aggregate moving among the molecules (Frenkel exciton). The formation of a Frenkel exciton generally follows the absorption of light of appropriate energy and the creation of an excitation, that might be localized on a single molecule (molecular excited state) or delocalized on several units. The exciton creation is a very fast process (on the order of sub fs) involving a "vertical" transition to the excited state S_e in a non equilibrium condition. Soon after, the exciton exchange occurs at the first excited state. If the vertical excitation leads to excited states high in energy (S_e, $e > 1$), intramolecular relaxation processes toward the first one are more efficient than intermolecular energy transfer, that therefore occurs only for the lowest excited state (S_1). In the absence of other perturbations, the exciton exchange typically occurs on a time scale t_{trans} of the order of several fs. In particular, t_{trans} depends on the entity of the intermolecular interaction between the molecules involved in the exchange, which is directly responsible for energy transfer. This interaction is represented by the exciton coupling V_{exc} and the larger V_{exc}, the shorter the time scale t_{trans}: the inverse of V_{exc} is directly related to the transfer time t_{trans} [11]. However generally in molecular systems, the exciton transfer is accompanied by a relaxation of the nuclear degrees of freedom through vibrational modes, usually on the sub ps time scale. This is related to the exciton-vibration coupling λ, describing the geometry variation in the transition between ground and excited electronic states;

in fact it is the analogous for energy transfer of the reorganization energy included in Marcus-Levich-Jortner equation for charge transfer (Section 1.1.2). The exceeding energy is dissipated through a coupling to the environment degrees of freedom (indeed λ is also named "system-bath coupling"). The inverse of λ is related to t_{rel}, the characteristic time necessary to the molecules for returning to thermal equilibrium once the electronic degree of freedom has been deexcited.
The two processes (transfer and relaxation) can occur in similar time scales, depending on the particular molecular aggregate under investigation. This aspect is very important for the choice of a proper dynamical model correctly describing the energy transfer behavior in each case: in other words, the transfer process has to be described with different dynamical regimes depending on the system under investigation, based on the relation between t_{trans} and t_{rel} (and so ultimately between λ and V_{exc}) [11, 114].

I. $\boldsymbol{t_{trans} \gg t_{rel} \quad \rightarrow \quad V_{exc} \ll \lambda}$. The exciton moves with a hopping between weakly electronically coupled molecules (small V_{exc}), since the fast vibrational dynamics causes a dephasing not allowing the definition of a unique delocalized wave function over different molecules. V_{exc} can be treated as a perturbation of the system Hamiltonian leading to a kinetic constant expression developed from the Fermi Golden Rule. The dynamical regime is an *incoherent transfer*: exciton transfer happens after full molecular vibrational relaxation and the localized excitations hop from molecule to molecule with a random walk. Its description is obtained by a solution of classical rates equations, i.e., the Master Equations: they can provide the probability for the exciton energy to be "located" on a certain molecule of the aggregate. The first development of such a model was given by Förster in 1946 and it did not contain any quantum parameter [115]; later it has been theoretically derived through time-dependent perturbation theory in the framework of quantum mechanics and is still known as "Förster theory" [116, 11].

II. $\boldsymbol{t_{trans} \ll t_{rel} \rightarrow V_{exc} \gg \lambda}$. The transfer occurs on a very fast time scale, not allowing for relaxation of the vibrational degrees of freedom: the coupling with the environment is not large enough to allow an efficient vibrational dissipation and it is treated as a perturbation. The system Hamiltonian induces a coherent spread of the excitation that moves almost freely among the molecules as a quantum wave packet. This *coherent transfer* is described by the corresponding time-dependent Schrödinger equation, often written employing a density matrix formalism and usually with Redfield approach [117]; the dynamics is provided by the solution of quantum Pauli Master Equations [118, 114, 11].

III. $\boldsymbol{t_{rel} \simeq t_{trans} \quad \rightarrow \quad V_{exc} \simeq \lambda}$. Currently there is not a unifying theory comprising also intermediate regimes. In these cases there might be an interplay of coherent and incoherent motion, therefore each specific case must be considered independently [11, 114].

The above considerations upon V_{exc}, λ and the appropriate dynamical model are sum-

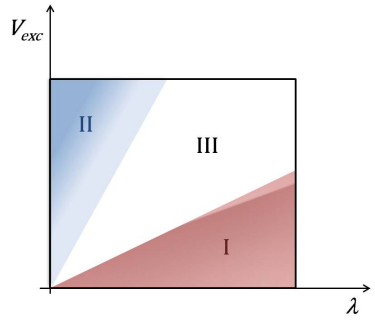

Figure 6.1: Scheme representing the validity range of the dynamical regimes of energy transfer, by varying the intermolecular (V_{exc}, in ordinate) and intramolecular (λ, in abscissa) parameters (adapted from [11]).

marized in Fig.(6.1). As mentioned, the description of energy transfer as an incoherent motion is successful when the assumption of a localized exciton holds: the intermolecular coupling V_{exc} is required to be very weak. This means that the molecules must retain their individuality in the aggregate, especially from a spectroscopic point of view: the electronic transition of the isolated single molecule must substantially coincide with that of the molecule in the aggregate. This assumption applies to systems with some degrees of disorder or at non-zero absolute temperature, since both conditions usually destroy any coherence effects (delocalized wave function) and to lead to incoherent transfer.
The choice of the suitable model, as said, depends on the kind of system to be investigated. For example there is a wide literature concerning the study of light harvesting complexes [119, 120]: the exciton couplings between the pigments have often a value comparable to the interaction with vibrational modes of the environment (represented, for example, by a protein). This is typically a case of an intermediate regime, that for a proper characterization might require a careful balance of coherent and incoherent description [120, 121, 114]. On the other hand, exciton diffusion in crystals of molecular semiconductors is usually modeled in the framework of Förster theory: in real systems lattice vibrations have an important role, destroying the long-range order and leading to a localization of excitons as for charge carriers [122, 123].

In the following the Förster theory is summarized, focusing on the calculation of the quantities and parameters included in the rate constant expression, related to the molecular properties of the aggregate. Its similarity with the Marcus-Levich-Jortner equation, and therefore with the charge hopping process, is also pointed out. In the derivation it is assumed a Frenkel exciton model: the excitation is always localized on one molecular unit and there is a sharp separation between electronic excitations and nuclear vibrations; the dynamics focuses on the electronic part (the electronic states, with their excitation energies and interactions).

6.2 Förster Equation

The energy transfer is described completely as an incoherent motion according to Förster equation. In the framework of weak coupling, the transfer of excitation happens between two independent molecules, a and b, each described by its vibronic state characterized by independent sets of Cartesian coordinates for nuclei $\boldsymbol{R}$ and electrons $\boldsymbol{r}$. The molecules

can change from the ground electronic state (S_0) with vibrational quantum number m to the excited e-th (S_e) electronic state with vibrational number n in excitation or deexcitation. As already pointed out, as an excited state, this process can involve only the first one ($e = 1$), that for simplicity from now on is indicated by the superscript *. In the Born-Oppenheimer framework, i.e., assuming the separation between nuclear and electronic motion, the molecular wave function Ψ for the a molecule is:

$$\begin{aligned} \Psi_a^{0,m} &= \psi^0(\boldsymbol{r}_a, \boldsymbol{R}_a)\chi^m(\boldsymbol{R}_a) \equiv \psi_a^0\chi_a^m \\ \Psi_a^{*,n} &= \psi^*(\boldsymbol{r}_a, \boldsymbol{R}_a)\chi^n(\boldsymbol{R}_a) \equiv \psi_a^*\chi_a^n \end{aligned} \tag{6.1}$$

where $\psi(\boldsymbol{r}, \boldsymbol{R})$ is the electronic wave function (parametrically dependent on the nuclear coordinates, due to the Born-Oppenheimer approximation) expressed by a Slater determinant on the molecular orbitals, and $\chi(\boldsymbol{R})$ is the vibrational state. $\Psi_a^{0,m}$ and $\Psi_a^{*,n}$ are the molecular vibronic states with related $E_a^{0,m}$ or $E_a^{*,n}$ energies. The wave function is analogous for the b molecule by replacing the subscripts with "b". The system Hamiltonian is:

$$\hat{H} = \hat{H}_a + \hat{H}_b + \hat{V} \tag{6.2}$$

comprising the single molecule Hamiltonians $\hat{H}_a$ and $\hat{H}_b$ plus the intermolecular interaction operator $\hat{V}$, representing the Coulomb term between all the couples of i-th electron belonging to a and j-th electron belonging to b:

$$\hat{V} = \sum_{i \in a, j \in b} \frac{1}{|\boldsymbol{r}_i - \boldsymbol{r}_j|} \tag{6.3}$$

expressed in atomic units.

Since we are in the framework of the weak coupling, the overall transfer process can be viewed as a "reaction" between the two independent molecular units. The excitation is "localized" on one molecule and it is exchanged with a hopping process from a donor a to the acceptor b, causing the deexcitation of the donor and simultaneous excitation of the acceptor [11, 124]:

$$a^* + b \rightarrow a + b^*. \tag{6.4}$$

The initial wave functions Ψ_i ("reactants" configuration, on the left of Eq.(6.4)) and final Ψ_f ("products" configuration, on the right of Eq.(6.4)) are the simple products of the two molecular wave functions in Eq.(6.1):

$$\begin{aligned} \Psi_i &= \Psi_a^{*,n}\Psi_b^{0,m} = \psi_a^*\chi_a^n\psi_b^0\chi_b^m \\ \Psi_f &= \Psi_a^{0,m}\Psi_b^{*,n} = \psi_a^0\chi_a^m\psi_b^*\chi_b^n. \end{aligned} \tag{6.5}$$

As mentioned, the excitation creation is a fast process, leading the molecule to an excited vibrational state. Then the energy transfer occurs after a complete vibrational relaxing of the excited donor molecule (a^*) to its equilibrium state, with respect to the excited electronic state (the first one). This means that its vibrational state population

in the excited states is arranged according to the Boltzmann distribution. As already mentioned in Section 6.1 the interaction between the electronic excited states V_{exc} must be small. Therefore when considering the total Hamiltonian of the system (explained in more detail in Section 6.3), it can be treated as a perturbation and the rate of the process can be derived from time-dependent perturbation theory, leading to the Fermi Golden Rule and represents the Förster equation [125]:

$$k_{ET} = \frac{2\pi}{\hbar} \sum_{m_a,n_a} \sum_{m_b,n_b} |\langle \Psi_i|\hat{V}|\Psi_f\rangle|^2 f_a^{*,n} f_b^{0,m} \delta(E_a^{*,n} - E_a^{0,m} + E_b^{0,m} - E_b^{*,n}). \quad (6.6)$$

The $\hat{V}$ operator in brackets is the interelectron interaction of Eq.(6.3). By substituting the configuration wave functions (6.5) and rearranging the integral, it is possible to factorize the vibrational wave function, since the $\hat{V}$ operator can be assumed (to a good approximation) as acting only on the electronic part:

$$\langle \Psi_i|\hat{V}|\Psi_f\rangle = \langle \psi_a^* \chi_a^n \psi_b^0 \chi_b^m|\hat{V}|\psi_a^0 \chi_a^m \psi_b^* \chi_b^n\rangle = \langle \chi_a^n|\chi_a^m\rangle \langle \chi_b^m|\chi_b^n\rangle \langle \psi_a^* \psi_b^0|\hat{V}|\psi_a^0 \psi_b^*\rangle . \quad (6.7)$$

The integral including $\hat{V}$ is the exciton coupling V_{exc}, the interaction between the excited states of the two molecular units, as mentioned in Section 6.1, and in Förster equation (6.6) is present with its squared value. The overlap integrals represent the superposition between the vibrational states pertaining to the ground and excited electronic state of each molecule; in their square form, as they appear in Eq.(6.6), they are named Franck Condon factors (FC) in the field of molecular spectroscopy. They describe the intensity of the vibronic progression underlying the bands of linear absorption and emission spectra of the isolated molecules a and b. The f and δ functions in Eq.(6.6) express the energy balance of excitation and dexcitation processes. In particular, $f_a^{*,n}$ and $f_b^{0,m}$ represent respectively the population distribution functions of the initial states of a, in its excited state, and b, in its ground state [11]. They weight the population of vibrational states in the "reactant configuration" (Ψ_i), which coincides with the Boltzmann distribution. The δ function with arguments $E_a^{*,n} - E_a^{0,m}$ and $E_b^{0,m} - E_b^{*,n}$ represents the total excitation/deexcitation energy. The latter corresponds to the acceptor absorption and donor emission energies, since it can be rewritten as [11]:

$$\delta(E_a^{*,n} - E_a^{0,m} + E_b^{0,m} - E_b^{*,n}) = \int_{-\infty}^{\infty} dE \quad \delta(E_a^{*,n} - E_a^{0,m} - E)\delta(E_b^{0,m} - E_b^{*,n} + E) \quad (6.8)$$

given the definition of Dirac delta function δ, according to which for any function $f(E)$:

$$f(E_0) = \int_{-\infty}^{\infty} dE\, f(E)\delta(E - E_0). \quad (6.9)$$

Now, the combination of FC integrals with the fs functions and the δ integrals in

Eq.(6.6) provides [11]:

$$\begin{aligned} Abs_b(E) &= \sum_{m_b,n_b} f_b^{0,m} |\langle \chi_b^m | \chi_b^n \rangle|^2 \delta(E_b^{0,m} - E_b^{*,n} + E) \\ Em_a(E) &= \sum_{m_a,n_a} f_a^{*,n} |\langle \chi_a^n | \chi_a^m \rangle|^2 \delta(E_a^{*,n} - E_a^{0,m} - E) \end{aligned} \tag{6.10}$$

that correspond to the lineshapes of absorption and emission spectra of, respectively, acceptor b and donor a. Therefore the rate constant expression, incorporating Eq.(6.10), requires the calculation of the spectral superposition integral between the electronic absorption and emission spectra of the molecules involved in the transfer [11]:

$$k_{ET} = \frac{2\pi}{\hbar}|V_{exc}|^2 \int_{-\infty}^{\infty} dE\, Abs_b(E) Em_a(E) = \frac{2\pi}{\hbar}|V_{exc}|^2 (FCWDoS). \tag{6.11}$$

The terms in the above equation are examined in more detail in the following paragraphs.

6.2.1 $FCWDoS$ - Franck Condon Weighted Density of States calculation

The spectral superposition in Eq.(6.11) is also called Franck Condon Weighted Density of states ($FCWDoS$) and, as mentioned, it is computed as the overlap between donor emission (Em_a) and acceptor absorption spectra (Abs_b) after a proper normalization [124, 125]:

$$FCWDoS \equiv \int_{-\infty}^{\infty} dE\, Abs_b(E) Em_a(E). \tag{6.12}$$

In other terms it corresponds to the product of the density of vibrational states in the initial and final states and their spectral overlap. This term accounts for the vibrations associated to the transfer process. The calculation of this quantity requires the simulation of the spectral lineshapes of the donor emission Em_a and acceptor absorption Abs_b spectra, including the underlying vibrational progression given by the Franck-Condon factors, as in Eq.(6.10). Then the integral (6.12) is estimated as the spectral superposition area. During the PhD, I have developed a code to calculate the vibronic progression from which the FCWDoS can be obtained and it is described in Chapter 7, along with some test calculations on perylene-bisimide molecule.

6.2.2 V_{exc} - Exciton coupling calculation

The exciton coupling is defined in Eq.(6.7) as the interaction between the electronic excited states localized on the molecular units:

$$V_{exc} = \langle \psi_a^* \psi_b^0 | \hat{V} | \psi_a^0 \psi_b^* \rangle \,. \tag{6.13}$$

where ψ_a and ψ_b are the electronic wave functions of, respectively, a and b molecular units in their ground state (with superscript 0) or excited state (with superscript *). The integral is expanded according to the Condon-Slater rules, employed for the calculation of bielectronic matrix elements between Slater determinants [126]. V_{exc} results to be given by two different integrals on the basis of the molecular orbitals of the isolated molecules involved in the excitation:

$$V_{exc} = 2\,\langle\varphi_i^a(\boldsymbol{r_1})\varphi_j^a(\boldsymbol{r}_1)|\hat{V}|\varphi_l^b(\boldsymbol{r}_2)\varphi_k^b(\boldsymbol{r}_2)\rangle - \langle\varphi_i^a(\boldsymbol{r}_1)\varphi_l^b(\boldsymbol{r}_1)|\hat{V}|\varphi_j^a(\boldsymbol{r}_2)\varphi_k^b(\boldsymbol{r}_2)\rangle \tag{6.14}$$

where φ_i^a, φ_j^a are the ith and jth molecular orbitals of molecule a and φ_k^b, φ_l^b are the kth and lth orbitals of molecule b directly involved in the excitation or deexcitation, assuming monoelectronic excitations and spin allowed. $\boldsymbol{r}_1$ and $\boldsymbol{r}_2$ are the electrons coordinates. The molecular orbital products on each side of brackets in Eq.(6.14) are termed "transition densities". The first term of Eq.(6.14) is the Coulomb integral between the transition densities localized on the molecular units; the second term is the exchange integral, given by an interaction between non classical transition densities. The magnitude of the exchange integral with respect to the Coulomb one decreases very fast with the intermolecular distance r_{ab}: the overlap between molecular orbitals belonging to different molecules decays exponentially with the distance making the exchange term very small or even negligible in many cases. Thus, it is sufficient in most cases to take into account only the Coulomb term:

$$V_{exc} \simeq V_{Coul} = 2\,\langle\varphi_i^a(\boldsymbol{r_1})\varphi_j^a(\boldsymbol{r}_1)|\hat{V}|\varphi_l^b(\boldsymbol{r}_2)\varphi_k^b(\boldsymbol{r}_2)\rangle\,. \tag{6.15}$$

This assumption is proven to be fulfilled in most cases and, as a consequence, several protocols for computing the exciton coupling, employed in the literature, are limited to the evaluation of the Coulomb integral as in Eq.(6.15). The simplest method is the so called *Point Dipole Approximation* (PDA), according to which the intermolecular interaction operator $\hat{V}$ is expressed through the multipolar expansion: [127]

$$\hat{V} = \hat{V}_{mono-mono} + \hat{V}_{mono-dip} + \hat{V}_{dip-dip} + \hat{V}_{dip-quad} + ... \tag{6.16}$$

In general by substituting the complete expansion of the operator $\hat{V}$ into the integral in Eq.(6.15), it develops as a sum of interactions between the transition moments of the expansion. Since the integral including the monopole term $\hat{V}_{mono-mono}$ vanishes due to the orthonormality of the wave functions, often $\hat{V}$ is conveniently cut off to the dipolar term, which is the most relevant one in case of a neutral molecule with a high spectral activity (high transition moment $\boldsymbol{\mu}$): then $\hat{V} \simeq \hat{V}_{dip-dip}$. Under this approximation, the integral (6.15) becomes equivalent to the equation [128]:

$$V_{exc} = \frac{\boldsymbol{\mu}_a \cdot \boldsymbol{\mu}_b}{r_{ab}^3} - \frac{(\boldsymbol{\mu}_a \cdot \boldsymbol{r}_{ab})(\boldsymbol{\mu}_b \cdot \boldsymbol{r}_{ab})}{r_{ab}^5}. \tag{6.17}$$

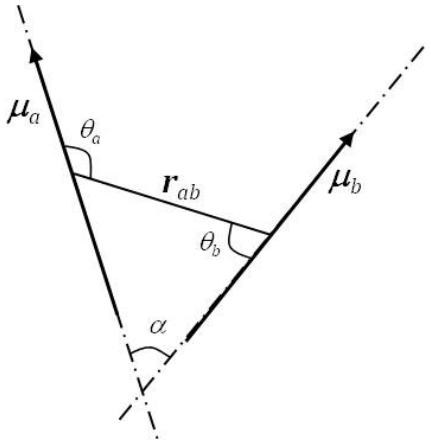

Figure 6.2: Transition moment vectors scheme.

where $\boldsymbol{\mu}_a, \boldsymbol{\mu}_b$ are the transition dipole moments of the isolated molecules, while $\boldsymbol{r}_{ab}$ represents the vector connecting the centers of $\boldsymbol{\mu}_a$ and $\boldsymbol{\mu}_b$, usually intended as the distance between the centers of mass of the two molecules. The scalar products among the vectors highlights the importance of the reciprocal orientation of $\boldsymbol{\mu}_a$, $\boldsymbol{\mu}_b$, $\boldsymbol{r}_{ab}$ vectors. Indeed, by rearranging Eq.(6.17) according to the definition of scalar product, it is obtained:

$$V_{exc} = \frac{|\boldsymbol{\mu}_a||\boldsymbol{\mu}_b|}{|\boldsymbol{r}_{ab}|^3}[\cos\alpha - 3\cos\theta_a\cos\theta_b] \tag{6.18}$$

where θ_a (θ_b) represents the angle between $\boldsymbol{\mu}_a$ ($\boldsymbol{\mu}_b$) and the distance vector $\boldsymbol{r}_{ab}$, while α is the angle between $\boldsymbol{\mu}_a$ and $\boldsymbol{\mu}_b$, see Fig. 6.2. The hypothesis which the expansion relies on, is that the intermolecular distance among the interacting electron distributions is much larger than the distribution itself and therefore there is no significant overlap between the electron densities. Under this condition the multipolar expansion holds, since it is ensured that each distribution "sees" the other more like a dipole and not as a continuous distribution of charge, and moreover the exchange contribution remains negligible. As a general rule, the multipolar expansion is considered valid for intermolecular distances $r_{ab} > 5$ Å [129], limit that may actually change depending on the system investigated. This methodology is quite simple and cheap, but in many cases not satisfactorily precise.

There are other more sophisticated methodologies for the calculation of the exciton interaction available in literature, involving the direct evaluation of the interaction between the transition densities, again limited to the Coulomb contribution. These methods employ a more detailed description with respect to the dipolar representation, which is often too poor and of a limited validity. One method, for example, defines the *transition atomic charges* located on the atoms of the molecule [130] while others involve a discretization in the space of the transition densities in the so called *Transition Density Cubes* [131, 132].

An "indirect" way of extracting V_{exc} is the so called *Supramolecular approach*. Assuming that the bright excited state is the first one, it requires the knowledge of its energy (E_a^1, E_b^1) and the lowest two dimer excited states (E_D^1, E_D^2) (see Fig.(6.3 in Chapter 8). V_{exc} is the interaction responsible of the energy splitting between the first two

excited states of the dimer and hence [129]:

$$V_{exc} = \sqrt{(E_D^2 - E_D^1)^2 - (E_a^1 - E_b^1)^2}. \tag{6.19}$$

This method is quite simple to be applied, since it requires only the knowledge of the dimer and monomers excited states energy, from standard calculations. In addition it is widely applicable, also outside the validity range for PDA and in case of strong coupling. It includes also the exchange contribution, allowing a reliable calculation also at shorter intermolecular distances. The method can be applied to get V_{exc}, provided that the dimer states do not have a relevant charge transfer character and are basically pure Frenkel states, i.e., there is no admixture between charge transfer and localized excitations (see Section 6.3 for a more detailed explanation). Otherwise, a coupling obtained this way will contain other contributions.

In addition in Chapter 8 we discuss a methodology for the calculation of the dimer electronic structure and related properties based on a CI approach. This method represents a direct way of obtaining V_{exc} by a simple transformation of the dimer Hamiltonian. This methodology is then applied to the study of perylene-bisimide molecular dimers.

6.3 Optical properties of molecular aggregates

The energy transfer properties of an aggregate are strictly related to its excited states properties (excitation energy and optical activity). It is known that they change with respect to the isolated molecule properties, to a greater or lesser extent depending on the interaction between the electronic wave functions of the molecular units (V_{exc}). This variation is usually described in terms of J- or H-aggregates , as it will be explained in the following.

6.3.1 Davydov splitting

The molecular exciton theory, developed by Davydov in 1962 [133], describes the main consequences of molecular aggregation on the energetic and optical properties of a molecular system. In the following it is considered the simplest possible aggregate, in which exciton transfer can take place: a dimer, composed by two identical molecules a and b, whose electronic states ψ_a^0, ψ_a^* and ψ_b^0, ψ_b^* interact.

The Hamiltonian operator of the dimer is given by:

$$\hat{H} = \hat{H}_a + \hat{H}_b + \hat{V} \tag{6.20}$$

where $\hat{H}_a$, $\hat{H}_a$ are the Hamiltonian operators of the isolated molecules and $\hat{V}$ represent the intermolecular interaction, as defined in Section 6.2. The ground state of the dimer Ψ_D^0 is given by the simple product of the single molecules ground state wave functions:

$$\Psi_D^0 = \psi_a^0 \psi_b^0 \tag{6.21}$$

and its energy results from the integral:

$$E_D^0 = \langle \psi_a^0 \psi_b^0 | \hat{H} | \psi_a^0 \psi_b^0 \rangle = E_a^0 + E_b^0 + \langle \psi_a^0 \psi_b^0 | \hat{V} | \psi_a^0 \psi_b^0 \rangle \,, \tag{6.22}$$

which is given by the sum of the single molecules ground state energies E_a^0, E_b^0 and an additional term representing a van der Waals stabilizing interaction between the molecules. The lowest two dimer excited states Ψ_D^1 and Ψ_D^2 are *"Frenkel states"*, linear combinations of localized transitions only:

$$\Psi_D^{1,2} = c_1 \psi_a^0 \psi_b^* \pm c_2 \psi_a^* \psi_b^0; \tag{6.23}$$

if the molecules are identical, as previously specified, the expansion coefficients take the same value $\frac{1}{\sqrt{2}}$ from normalization:

$$\Psi_D^{1,2} = \frac{1}{\sqrt{2}} (\psi_a^0 \psi_b^* \pm \psi_a^* \psi_b^0). \tag{6.24}$$

The basic assumption of the molecular exciton theory is that charge transfer (CT) states are much higher in energy and therefore neglected in the wave function expansion; the only excitations taken into account are localized on the molecular units. This assumption allows the development of a simple theory, able to explain the electronic and spectroscopic properties of a variety of cases. However it is known to fail for systems in which there is an appreciable mixing between CT and localized excitations, as it will be shown for perylene-bisimide in Chapter 8: in tis case a more comprehensive theory, including all kinds of excitations, is necessary. However, when the assumption holds, the eigenvalues of the dimer excited states are obtained through the diagonalization of the 2×2 matrix representing the Hamiltonian in the basis of the diabatic states, i.e., the localized excitations ($\psi_a^0 \psi_b^*$ and $\psi_a^* \psi_b^0$):

$$\begin{vmatrix} H_{11} - E & H_{12} \\ H_{21} & H_{22} - E \end{vmatrix} = 0 \tag{6.25}$$

whose terms are given by :

$$\begin{aligned} H_{11} &= \langle \psi_a^0 \psi_b^* | \hat{H}_a | \psi_a^0 \psi_b^* \rangle + \langle \psi_a^0 \psi_b^* | \hat{H}_b | \psi_a^0 \psi_b^* \rangle + \langle \psi_a^0 \psi_b^* | \hat{V} | \psi_a^0 \psi_b^* \rangle \\ &= E_a^0 + E_b^* + V_{11} \\ H_{22} &= \langle \psi_a^* \psi_b^0 | \hat{H}_a | \psi_a^* \psi_b^0 \rangle + \langle \psi_a^* \psi_b^0 | \hat{H}_b | \psi_a^* \psi_b^0 \rangle + \langle \psi_a^* \psi_b^0 | \hat{V} | \psi_a^* \psi_b^0 \rangle \\ &= E_a^* + E_b^0 + V_{22} \\ H_{12} &= \langle \psi_a^0 \psi_b^* | \hat{V} | \psi_a^* \psi_b^0 \rangle = V_{exc}. \end{aligned} \tag{6.26}$$

V_{11} e V_{22} are interactions between the configurations, representing again van der Waals stabilization; the off diagonal term H_{12} is the exciton interaction V_{exc}. The eigenvalues

come from the solution of the determinant in Eq.(6.25):

$$E_D^{1,2} = \frac{1}{2}(E_a^0 + E_b^0 + E_a^* + E_b^* + V_{11} + V_{22}) \tag{6.27}$$

$$\pm \frac{1}{2}\sqrt{((E_a^* - E_a^0) - (E_b^* - E_b^0) + (V_{22} - V_{11}))^2 + 4|V_{exc}|^2}. \tag{6.28}$$

Since the molecules are identical, their ground state energies are set as reference to 0 ($E_a^0 = E_b^0 = 0$) and their excited states energies are identical and set to $E_a^* = E_b^* = E^*$; due to the symmetry of the dimer, $V_{11} = V_{22}$ and consequently their difference goes to zero, while their sum is set as $V_{11} + V_{22} = V_{vdW}$. With these simplifications, the eigenvalues become:

$$E_D^{1,2} = \frac{1}{2}\left[E_a^* + E_b^* + V_{vdW}\right] \pm V_{exc} \tag{6.29}$$

$$\simeq E^* + V_{vdW} \pm V_{exc}. \tag{6.30}$$

and the eigenstates are Ψ_D^1 and Ψ_D^2 as expressed in Eq.(6.23). The equation simplified in this way, shows how the eigenvalues of the dimer excited states are given by the energy of the monomer excited state, plus a generally small interaction contribution and the exciton interaction. Hence the effect of the V_{exc} interaction between a and b is to mix the states and split the energy of the resulting dimer excited states of twice the entity of the interaction, the so called *"Davydov splitting"*:

$$\Delta E_D^{12} = \left|E_D^2 - E_D^1\right| = 2|V_{exc}|. \tag{6.31}$$

This is the development which the Supermolecular approach for the calculation of V_{exc} is based on, as previously reported in Section 6.2.

6.3.2 *H*- and *J*-aggregates

The transition dipoles $\boldsymbol{\mu}_D^1$ and $\boldsymbol{\mu}_D^2$, computed according to the definition as

$$\boldsymbol{\mu}_D^1 = \langle \Psi_D^1 | \hat{\mu} | \Psi_D^0 \rangle \qquad \boldsymbol{\mu}_D^2 = \langle \Psi_D^2 | \hat{\mu} | \Psi_D^0 \rangle \,. \tag{6.32}$$

are associated to each dimer excited state. In the framework of the molecular exciton theory they are simply given by the linear combination of the monomer moments $\boldsymbol{\mu_a}$ and $\boldsymbol{\mu_b}$:

$$\boldsymbol{\mu}_D^{1,2} = \frac{1}{\sqrt{2}}(\boldsymbol{\mu}_a \pm \boldsymbol{\mu}_b), \tag{6.33}$$

each provided by the integral with the dipole moment operator $\hat{\mu} = \sum_i^{N_e} e\boldsymbol{r}_i$, with e the electron charge and $\boldsymbol{r}_i$ the position of the i-th electron, on the molecular basis:

$$\boldsymbol{\mu}_a = \langle \psi_a^* | \hat{\boldsymbol{\mu}} | \psi_a^0 \rangle \qquad \boldsymbol{\mu}_b = \langle \psi_b^* | \hat{\boldsymbol{\mu}} | \psi_b^0 \rangle \,. \tag{6.34}$$

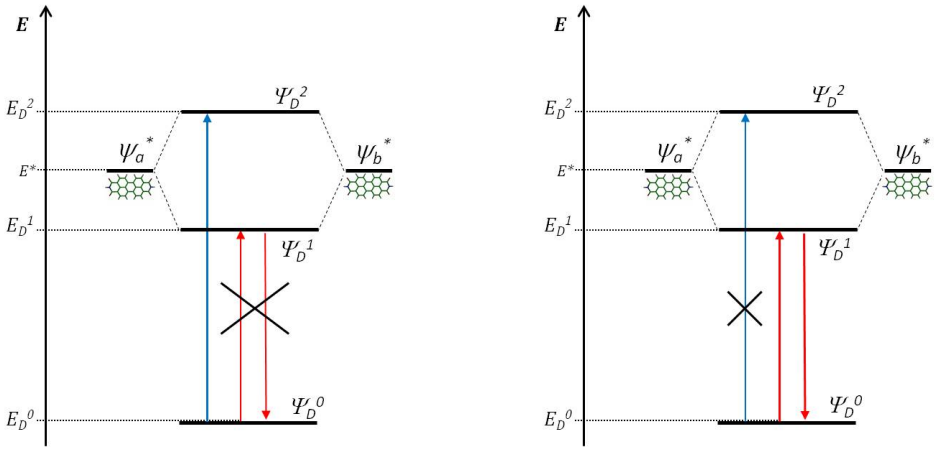

Figure 6.3: Scheme of dimer states energies for H- and J-aggregates.

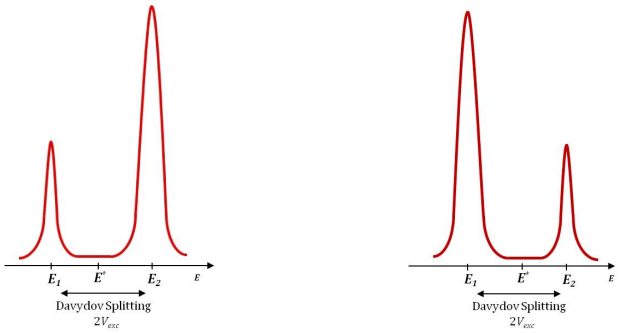

Figure 6.4: Spectral features of H- (left) and J- (right) aggregates.

In the system here discussed of identical monomers, also the transition moments are identical ($|\boldsymbol{\mu}_a| = |\boldsymbol{\mu}_b| = |\boldsymbol{\mu}|$). The square modulus of the transition dipole moment of a given dimer state is directly proportional to the intensity of the corresponding band in absorption or emission electronic spectra. The character of the aggregate is finally obtained by joining the information about energy and optical activity, as summarized in the scheme of Fig.(6.3). If the state with the most intense optical activity is the lowest (i.e., in this case $\left|\boldsymbol{\mu}_D^1\right| > \left|\boldsymbol{\mu}_D^2\right|$) the aggregate is said to be J and this corresponds to a red shift of the most intense peak in the spectrum with respect to the monomer. On the contrary, if the most active state is the highest ($\left|\boldsymbol{\mu}_D^1\right| < \left|\boldsymbol{\mu}_D^2\right|$), the dimer is a H-aggregate, which corresponds to a blue shift of the peak in the spectrum (Fig.(6.4)). In the extreme case in which only one state is spectroscopically active, the aggregates have a "pure" J- or H-character and in the electronic spectrum only one band is present, red or blue shifted with respect to the monomeric band: for J, $\left|\boldsymbol{\mu}_D^1\right| = 2\left|\boldsymbol{\mu}\right|$ and $\left|\boldsymbol{\mu}_D^2\right| = 0$ while for H, $\left|\boldsymbol{\mu}_D^1\right| = 0$ and $\left|\boldsymbol{\mu}_D^2\right| = 2\left|\boldsymbol{\mu}\right|$. This happens for example for the dimer geometries represented in Fig.(6.5).

A key point in defining the character of the aggregate is the sign of the exciton interaction V_{exc}, because it establishes, through Eq.(6.29), the reciprocal energetic order of the two linear combinations (6.24), since usually V_{vdW} is similar for the different excited states and it does not influence the energetic order significantly. A sign change of V_{exc} makes possible to switch from an aggregate character to the other. As shown in

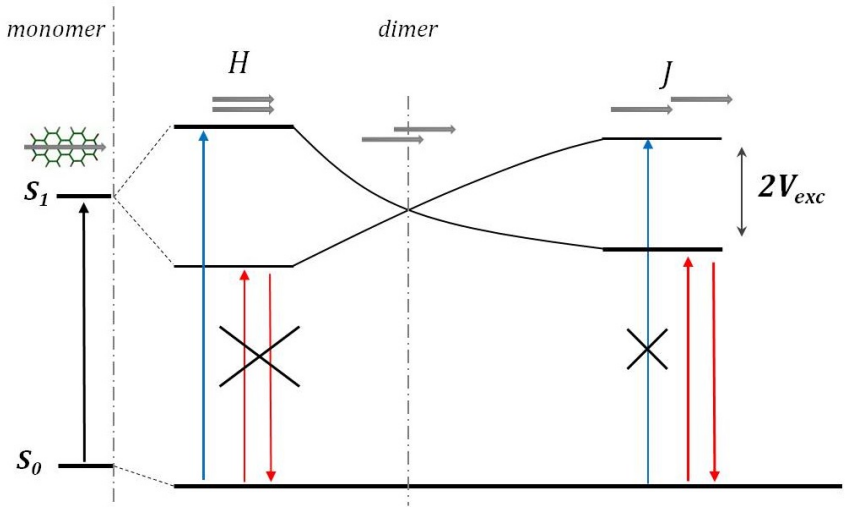

Figure 6.5: Switching from J- to H-aggregates upon dimer geometry variation (adapted from [134]).

Fig.(6.5), a modification of the dimer geometry is sufficient, for example by changing the intermolecular distance r_{ab} or the reciprocal orientation of the molecules, represented by the angle α, Fig.(6.2): those aspects has a strong influence on the integrals composing V_{exc}, see Eq.6.14, and this can be clearly visualized in the PDA expression of Eq.(6.18) where the orientation factor has a strong influence on the final value. There might be some cases in which the term V_{vdW} in Eq.(6.29) exceeds V_{exc}, making more difficult the attribution of the character, since in such a situation it is not directly determined by V_{exc} [135] (see below).

6.3.3 Aggregation and photophysical properties

The spectral features of an aggregate are different from that of a single molecule. In general, according to the Davydov model discussed above, the linear absorption band on a single molecule is generally split in two bands with an energy difference given by the Davydov splitting, which is twice V_{exc} (Eq.(6.31)) for identical molecular units. The relative intensity of the two bands defines the character: if the lower is the most intense it is a J-aggregate, otherwise it is H. In case of pure character, only one band for the dimer is visible: with respect to the monomer, H aggregation induces a hypsocromic (blue) shift of the band while J aggregates display bathocromic (red) shifts. As already discussed, this is related to the different sign of the exciton coupling and the strength of this interaction can be seen in the amount of the shift with respect to the monomer band position. In emission H aggregates have low radiative rate ("subradiant"), being the lowest energy excited state forbidden, while J aggregates have very intense emission ("superradiant") [134]. Aggregation induces also a distortion of the vibronic progression underlying the spectral bands, with different features for H- or J- aggregation. The spacings between the peaks become irregular and the peaks intensities deviate from

the Poisson distribution typical of the single molecule (more details in Chapter 7). In particular the ratio between the intensities of the first and the second vibronic peaks is changed: it decreases for H- aggregation and increases upon J. Therefore the spectrum of the formers shows a broader band with the maximum of intensity moving toward the center of the band, while J aggregates spectrum enhances its lower energy transition becoming very narrow [135]. The peculiar spectral features are an important way to define the character of the aggregate and to derive important information like for example the molecular arrangement and the exciton bandwidth. This is true particularly in the case in which the V_{vdW} contribution in Eq.(6.29) is relevant, not allowing a simple character attribution on the basis of V_{exc} only; in that case it is the peculiar shape of the vibronic progression that tells between H and J aggregation.

Aggregation and Energy transfer. J aggregates show favorable properties for energy transfer processes . The presence of an intense red shifted band (with respect to the monomeric one) with its peculiar shape is favorable for exciton transfer. Indeed as already discussed this process is possible only in the first excited state S_1, because for higher ones other deactivation paths are more efficient. The requirement for S_1 is to be spectroscopically allowed: it must be possible, upon excitation, to populate such a state and to create the superposition of localized excitations, Eq.(6.24). In H-aggregates the lowest excited state is optically dark (in case of a pure H, with transition dipole equal to zero) or anyway less active than the second excited state, and so there cannot be exciton transport in such systems but only in J. Indeed for example in nature, the arrangement of the Chlorophyll molecules in Light Harvesting complexes is such that they form J aggregates, favorable to the transport of energy in the system [136]. Therefore the possibility to tailor the aggregate character by modifying the geometry of the system is appealing, because it is a practical instrument in the hands of experimental chemists that are working in the synthesis of artificial systems displaying interesting energy transport properties. In Chapter 8 I will discuss a systematic theoretical study for the assessment of H or J character as a function of the displacement coordinate for a perylene-bisimide dimer.

CHAPTER 7

FCWDoS: the vibrational contribution

As discussed in Chapter 6, the Förster kinetic equation includes the calculation of the FCWDoS factor, Eq.(6.11). To this end, it is necessary to simulate the electronic emission and acceptor spectra of, respectively, donor and acceptor, starting from computed molecular properties. A code devoted to spectra simulation and FCWDoS calculation has been set up; in the following the theoretical foundation on which it relies (Section 7.1) will be described and then the main features of the code are summarized in Section 7.2 and finally test calculations on perylene-bisimide molecule are reported in Section 7.3.

7.1 Electronic spectra simulation

Vertical transitions between vibronic states. As a first step, it is necessary to simulate the electronic linear absorption and emission spectra of an isolated molecule. This kind of spectroscopy involves a transition from initial Ψ_i to final Ψ_f vibronic state. According to the *Franck Condon principle* the transition is vertical: the nuclear geometry remains basically unchanged during the transition (the nuclear coordinate $\boldsymbol{R}$ is conserved) and readjusts once the electrons have gained their final distribution. The absorption process is assumed to happen at the ground state equilibrium geometry and the excitation reaches the corresponding excited state configuration (Franck-Condon point); then the nuclear relaxation drives the reorganization of the molecular structure to the bottom of the excited state potential energy surface (PES), where the emission starts from, the ground state to reach through another vertical transition, Fig.(7.1) [126]. Within the framework of the Born-Oppenheimer approximation, the vibronic states can be factorized in the product of electronic and vibrational wave functions. The considered transition is $(0, m) \rightarrow (e, n)$: it moves from the ground ($g = 0$) electronic

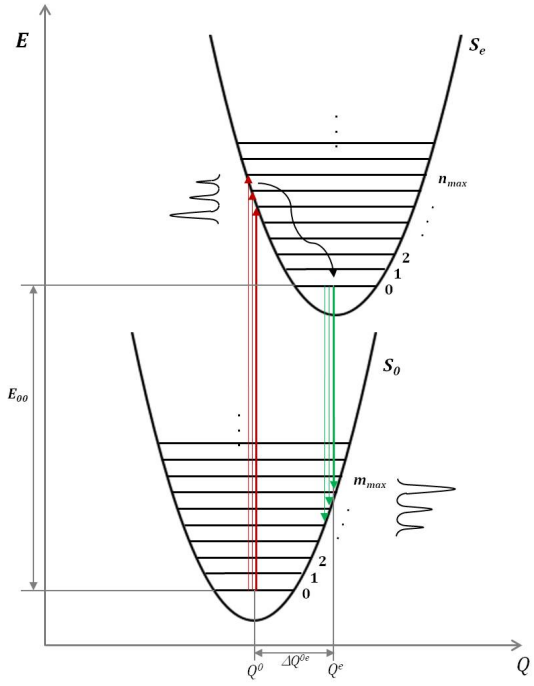

Figure 7.1: Schematic representation of vertical transition along a specific nuclear coordinate Q.

state with vibrational wavenumber m to the electronic excited state e with vibrational wavenumber n. The initial and final vibronic states are:

$$\begin{aligned} \Psi_i(\boldsymbol{r}, \boldsymbol{R}) &= \psi_0(\boldsymbol{r}, \boldsymbol{R})\, \chi_m(\boldsymbol{R}) \\ \Psi_f(\boldsymbol{r}, \boldsymbol{R}) &= \psi_e(\boldsymbol{r}, \boldsymbol{R})\, \chi_n(\boldsymbol{R})\ . \end{aligned} \tag{7.1}$$

(please note that here, in contrast to the previous chapter, the quantum numbers representing the state are indicated as a subscript). The electronic state ψ is described by a Slater determinant on the molecular orbitals and depends on the electrons coordinates $\boldsymbol{r}$ and parametrically on the nuclear coordinates $\boldsymbol{R}$, which are also the only variables of the vibrational wave function χ.

It is convenient to represent the Cartesian coordinates of the nuclei in terms of the $3N_a - 6$ normal coordinates $\boldsymbol{Q}$ (with N_a the number of atoms in the molecule). $\boldsymbol{Q}$ is defined as a linear combination of the mass weighted Cartesian displacements of each atom:

$$\boldsymbol{Q} = \boldsymbol{C}\boldsymbol{M}^{1/2}(\boldsymbol{R} - \boldsymbol{R}_e) \tag{7.2}$$

where $\boldsymbol{C}$ is the eigenvector of the mass weighted Hessian, $\boldsymbol{M}$ is the diagonal matrix of the atomic masses, $\boldsymbol{R}$ is the vector of the atomic Cartesian coordinates and $\boldsymbol{R}_e$ the equilibrium coordinates. This matrix has $3N_a \times 3N_a$ dimension, since it includes also the rotational and translational coordinates, not taken into account in the present discussion; thus, hereafter $\boldsymbol{Q}$ is intended only to include the $3N_a - 6$ vibrational coordinates. The combinations are built in such a way that the modes are orthonormal and independent one from another. To each vibrational coordinate k, it is associated the normal

mode vector Q_k and the frequency ω_k. A state of the k-th mode, represented by the quantum number v_k (correspondent to m or n in Eq.(7.1)), is represented by a wave function $\chi_v(\boldsymbol{Q}_k)$ modeled as an harmonic oscillator and its energy is accordingly:

$$E_v^k = \left(\frac{1}{2} + v_k\right)\hbar\omega_k. \tag{7.3}$$

The choice of such a model is usually appropriate for normal modes with medium high frequencies, as many of the molecular vibrations involved in spectroscopic transitions are. The favorable properties of the normal modes coordinate system allow the factorization of the total molecular vibrational wave function into the simple product of each k normal mode function χ_k in the relative quantum state v:

$$\chi_{\{v_k\}}(\boldsymbol{Q}) = \prod_{k=1}^{3N-6} \chi_k(\boldsymbol{Q}_k); \tag{7.4}$$

the subscript $\{v_k\}$ of χ indicates that it is computed for an ensemble of v values, each related to a k normal mode: $\chi_{(v_1,v_2,\ldots,v_{3N_a-6})}$.
The change of the electronic state in a spectroscopic transition is usually accompanied by a change in the normal modes of vibration, which are therefore no longer orthogonal when considering different electronic states. In general, in the framework of the harmonic approximation, modes belonging to different electronic states ($\boldsymbol{Q}^0$,$\boldsymbol{Q}^e$) are related by a linear transformation consisting of a multidimensional rotation and translation, known as Duschinsky mixing [137, 138, 139]:

$$\boldsymbol{Q}^e = \boldsymbol{J}\boldsymbol{Q}^0 + \Delta\boldsymbol{Q}^{e0}. \tag{7.5}$$

A general assumption is to neglect the Duschinsky rotation, i.e., $\boldsymbol{J} = 1$ (*parallel modes approximation*); the coordinates of ground and excited states are assumed to be basically equal $\boldsymbol{Q}^0 \simeq \boldsymbol{Q}^e \simeq \boldsymbol{Q}$ apart from a translational term represented by the geometric difference $\Delta\boldsymbol{Q}^{e0}$ between the ground and excited equilibrium structures. This assumption is generally reliable for molecules whose excited state equilibrium geometry is not that different from the ground state one (so also for small $\Delta\boldsymbol{Q}^{e0}$), i.e., for molecules that basically retain their shape, apart from small changes, in the excited state. That $\boldsymbol{Q}^0 \simeq \boldsymbol{Q}^e$, has been proven to be acceptably true for several molecules in their lower excited states, and it will be further discussed in Section 7.3. The normal modes of a molecule can be classified, according to the molecular symmetry, in totally symmetric (TS) and non-totally symmetric (NTS): the first ones preserve the symmetry of the molecule during the vibration, while the latter break it. Now, in general, for most organic dye molecules the symmetry of the ground and excited state is the same (consistently with the previous statement, according to which the molecules basically retain their shape upon excitation); this has proven to be true for most organic molecules, with few exceptions, as for example highly symmetric molecules. If considering a section of the ground and excited PES along a TS normal coordinate $Q_{k_{TS}}$, the two surfaces have

their minima displaced of a $\Delta \boldsymbol{Q}^{e0}_{k_{TS}}$: the TS vibration preserves the symmetry and the two PES minima show a neat displacement. On the contrary, a NTS vibration causes a symmetry breaking; however the excited states have the same symmetry, so along the $Q_{k_{NTS}}$ coordinate the only point that preserves the symmetry of the excited state during the vibration is $Q^{e}_{k_{NTS}} = Q^{0}_{k_{NTS}}$: the minima of the two curves coincide and $\Delta Q^{e0}_{k_{NTS}} = 0$. Therefore the NTS vibration modes, during the $g \to e$ transition, do not give a neat contribution in terms of geometry modification. As a consequence the $\Delta \boldsymbol{Q}^{e0}$ vector in Eq.(7.5) contains non zero contributions only for TS modes.

From the wave function to the transition dipole moment. The intensity of the electronic spectra is directly related to the square of the electric dipole transition moment between the ground and the upper vibronic state. The molecular electric dipole operator $\hat{\boldsymbol{\mu}}$ can be factorized into an electronic part $\hat{\boldsymbol{\mu}}_e$, including all the N_e electrons with charge e and position $\boldsymbol{r}$, and the nuclear contribution $\hat{\boldsymbol{\mu}}_N$, including all the N_N nuclei of eZ charge (Z is the protons number) and $\boldsymbol{R}$ Cartesian coordinates [126]:

$$\hat{\boldsymbol{\mu}} = \hat{\boldsymbol{\mu}}_e + \hat{\boldsymbol{\mu}}_N = -e \sum_{i=1}^{N_e} \boldsymbol{r}_i + e \sum_{j=1}^{N_N} Z_j \boldsymbol{R}_j. \tag{7.6}$$

The transition dipole moment $\boldsymbol{\mu}^{trs}_{if}$ between the ψ_i and ψ_f Eq.(7.1) is given by the integral:

$$\begin{aligned} \boldsymbol{\mu}^{trs}_{if} &= \langle \Psi_i(\boldsymbol{r},\boldsymbol{Q}) | \hat{\boldsymbol{\mu}}_e + \hat{\boldsymbol{\mu}}_N | \Psi_f(\boldsymbol{r},\boldsymbol{Q}) \rangle \\ &= \langle \chi_m(\boldsymbol{Q}) | \, \langle \psi_0(\boldsymbol{r},\boldsymbol{Q}) | \hat{\boldsymbol{\mu}}_e | \psi_e(\boldsymbol{r},\boldsymbol{Q}) \rangle \, | \chi_n(\boldsymbol{Q}) \rangle \\ &+ \langle \chi_m(\boldsymbol{Q}) | \hat{\boldsymbol{\mu}}_N \cancel{\langle \psi_0(\boldsymbol{r},\boldsymbol{Q}) | \psi_e(\boldsymbol{r},\boldsymbol{Q}) \rangle} | \chi_n(\boldsymbol{Q}) \rangle \, . \end{aligned} \tag{7.7}$$

$\hat{\boldsymbol{\mu}}_N$ acts only on the vibrational wave function and, as a consequence, in the second term of Eq.(7.7) the whole nuclear contribution cancels due to the orthogonality of the electronic states wave functions; only the term with $\hat{\boldsymbol{\mu}}_e$ survives and, since the operator acts only on ψ, it can be further simplified:

$$\begin{aligned} \boldsymbol{\mu}^{trs}_{if} &\simeq \langle \psi_0(\boldsymbol{r},\boldsymbol{Q}) | \hat{\boldsymbol{\mu}}_e | \psi_e(\boldsymbol{r},\boldsymbol{Q}) \rangle \; \langle \chi_m(\boldsymbol{Q}) | \chi_n(\boldsymbol{Q}) \rangle \\ &\simeq \boldsymbol{\mu}_{0e}(\boldsymbol{Q}) \; \langle \chi_m(\boldsymbol{Q}) | \chi_n(\boldsymbol{Q}) \rangle \, . \end{aligned} \tag{7.8}$$

The integral involving the electronic wave functions represents $\boldsymbol{\mu}^{trs}_{0e}$, the electronic transition dipole moment of the $0 \to e$ transition: when it is null, the transition is spectroscopically forbidden (the excited state is a dark state). In principle $\boldsymbol{\mu}^{trs}_{0e}$ would parametrically depend on the nuclear coordinate $\boldsymbol{Q}$ but the problem is simplified by adopting the *Condon approximation*, which means to assume the electronic transition dipole essentially independent on the nuclei position; the assumption retains as long as the nuclear geometry is not displaced too much from the equilibrium. The $\boldsymbol{\mu}^{trs}_{0e}(\bar{\boldsymbol{Q}})$ value is generally computed at the equilibrium geometry of the ground electronic state: $\boldsymbol{\mu}^{trs}_{0e}(\boldsymbol{Q}) = \boldsymbol{\mu}^{trs}_{0e}$. The vibrational part of the wave functions is collected into an over-

lap integral: the larger the overlap between $\chi_m(\boldsymbol{Q})$ and $\chi_n(\boldsymbol{Q})$, the more intense the vibronic transition [126, 140].

The spectral intensities. The intensity of the $(0,m) \rightarrow (e,n)$ transition for a single normal mode k is proportional to the square of the transition moment in Eq.(7.8) [140]:

$$\begin{aligned} I_k^{0,m\rightarrow e,n} \propto \left|\mu_{if}^{trs}\right|^2 &= \left|\mu_{0e}^{trs}\right|^2 |\, \langle \chi_m(\boldsymbol{Q}_k) | \chi_n(\boldsymbol{Q}_k) \rangle \,|^2 \\ &= \left|\mu_{0e}^{trs}\right|^2 FC_k(m,n)^2. \end{aligned} \tag{7.9}$$

The square of the overlap integral in Eq.(7.9) between the vibrational wave functions is the so called Franck-Condon factor $FC_k(m,n)^2$ and is the key term that determines the "vibronic progression" in the spectrum. Since the form of the harmonic oscillator wave functions are quite similar for states close in energy, there is generally not only a single n arrival state with favorable FC factor, but there is a progression of intensities, i.e., a series of active vibrational transitions $m \rightarrow n$ for several n close in energy. Moreover, if the thermal energy k_BT (with k_B the Boltzmann constant) is large enough to overcome the vibrational energy gap (so with a suitable absolute temperature $T \neq 0$ K), there might be several populated m states, which the transition can start from; in an equilibrium condition they are taken into account by including the Boltzmann distribution of the states populations. Therefore, for a normal mode k the total intensity of the $0 \rightarrow e$ electronic transition is the sum of all possible $m \rightarrow n$ transitions:

$$I_k^{0\rightarrow e} = \sum_{m=0}^{m_{max}} \sum_{n=0}^{n_{max}} I_k^{0,m\rightarrow e,n} \tag{7.10}$$

$$= \left|\mu_{0e}^{trs}\right|^2 \frac{1}{Z_k} \sum_{m=0}^{m_{max}} \left[\exp\left(-\frac{\hbar m \omega_k}{k_B T}\right) \sum_{n=0}^{n_{max}} FC_k(m,n)^2 \right], \tag{7.11}$$

with the sums over m and n vibrational states running to the limiting values m_{max} and n_{max} that have to be conveniently set (see Section 7.2); Z_k represents the vibrational partition function related to the electronic ground state (which the m states belong): $Z_k = \sum_{m=0}^{m_{max}} \exp(-\frac{\hbar m \omega_k}{k_B T})$. The favorable properties of the normal modes in the parallel mode approximation, on Eq.(7.5), allow the evaluation of the intensity for each k independently, making the Franck-Condon factors simply mono dimensional integrals independent one from the other. The total intensity of the electronic transition $I^{0\rightarrow e}$ is the product of all the $I_k^{0\rightarrow e}$, running over all the $3N_a - 6$ vibrational degrees of freedom:

$$\begin{aligned} I^{0\rightarrow e} &= \prod_{k=0}^{3N_a-6} I_k^{0\rightarrow e} \\ &= \left|\mu_{0e}^{trs}\right|^2 \prod_{k=0}^{3N_a-6} \frac{1}{Z_k} \sum_{m=0}^{m_{max}} \exp\left(-\frac{\hbar m \omega_k}{k_B T}\right) \sum_{n=0}^{n_{max}} FC_k(m,n)^2. \end{aligned} \tag{7.12}$$

Franck-Condon factors calculation. To compute the Franck-Condon factors, one needs to evaluate the overlap between the vibrational wave functions, which are the harmonic oscillator eigenfunctions, see Eq.(7.9). The derivation of a simple expression for the FC factors is possible due to the favorable properties of the Hermite polynomials, and by the additional assumption that $\omega_k^0 \simeq \omega_k^e$; this assumption points again to a similarity between the two electronic states energy surfaces (the same curvature of the harmonic PES), which is generally reasonable for many molecules similarly to the assumptions made for $\boldsymbol{Q}$, related to the parallel mode approximation. The harmonic oscillator wave functions for the m and n vibrational states are introduced in the overlap integral of Eq.(7.9) and reshuffling the terms exploiting the properties of the Hermite polynomials, the square of the overlap integrals turn out to be given by a Poisson distribution, that provides the vibronic progression [141]:

$$\begin{aligned} FC_k(m,n)^2 &= \langle \chi_m(\boldsymbol{Q}_k) | \chi_n(\boldsymbol{Q}_k) \rangle^2 \\ &= e^{-S_k}\, S_k^{(n-m)}\, \frac{m!}{n!}\, [L_m^{n-m}(S_k)]^2 \end{aligned} \tag{7.13}$$

computed with respect to S_k. This parameter is the Huang-Rhys factor related to the k-th normal mode, already described in Section 1.3 and here recalled [141, 140]:

$$S_k = \frac{\omega_k (\Delta Q_k^{0e})^2}{2\hbar} \tag{7.14}$$

where ΔQ_k^{0e} represents the displacements of the equilibrium positions of the two electronic states involved in the transition, projected on the k-th normal mode, as defined in Eq.(7.5). $L_m^{n-m}(S_k)$ is the generalized Laguerre polynomial of m degree defined through the general relation [141]:

$$L_n^{\alpha}(x) = \sum_{i=0}^{n} \binom{n+\alpha}{n-i} \frac{(-x)^i}{i!}. \tag{7.15}$$

The number of Franck-Condon factors to be computed increases steeply with the number of normal modes of the molecule, and so with the number of atoms, becoming computationally very demanding for larger molecules. However the Huang-Rhys factor (Eq.(7.14)) is zero for NTS normal modes because their $\Delta \boldsymbol{Q}_{k_{NTS}}^{e0} = 0$, as previously discussed. In this way the number of FC factors to be computed is limited to those related to TS modes, and also the product in Eq.(7.12) is restricted only to TS modes.

Absorption and Emission spectra. What has been obtained so far is the "stick" structure of the spectra, which means that the vibronic peaks are simulated with the correct intensity but infinitesimal width. Each peak given by Eq.(7.9) is located in the spectrum at the corresponding transition energy:

$$E_{\{n_k,m_k\}} = E_{00} + \sum_{k=0}^{3N-6} \left[n_k \hbar \omega_k^e - m_k \hbar \omega_k^g \right]. \tag{7.16}$$

where E_{00} is the energy difference between the equilibrium geometries of the ground and excited state. However, a realistic spectrum has a finite peak width, due to broadening processes. This aspect is included in the simulation by "dressing" the sticks with a proper function describing the lineshape. In the case of an isolated molecule in vacuum, the broadening is related to the excited state finite lifetime, and this can be described by a Lorentzian function $Lrtz(E)$; if there are other undergoing processes, as it is the case for molecules in condensed phase, as a lineshape function it is usually chosen a Gaussian $Gauss(E)$:

$$\begin{aligned} Lrtz(E) &= \frac{1}{\pi}\frac{hwhm}{hwhm^2 + E^2} \\ Gauss(E) &= \frac{\sqrt{\ln 2}}{hwhm\sqrt{\pi}} \exp\left(-\ln 2 \left(\frac{E}{hwhm}\right)^2\right) \end{aligned} \tag{7.17}$$

where $hwhm$ in both functions represents the half width of the curve corresponding to the point in the bell with half of the maximum height. The final spectrum is the result of a convolution operation between the stick intensities of Eq.(7.12) and one of the two shape functions ($lshp(E)$ in general, that can be $lshp(E) = Lrtz(E)$ or $lshp(E) = Gauss(E)$) of Eq.(7.17) [142]:

$$\begin{aligned} Abs(E) &= \sum_{\epsilon=0}^{E_{max}} lshp(\epsilon) I^{0\to e}(E-\epsilon) \\ Em(E) &= \sum_{\epsilon=0}^{E_{max}} lshp(\epsilon) I^{e\to 0}(E-\epsilon). \end{aligned} \tag{7.18}$$

All the derivations so far are made for absorption spectra but apply equally well for emission, by reversing the "direction" of the transition: $(e, n) \to (0, m)$, with $e = 1$ since emission almost always starts from the lowest excited state. As a consequence of the similarity between the frequencies ($\omega_k^0 \simeq \omega_k^e$) and the normal modes (parallel mode approximation) of the excited states, the absorption and emission spectra generally display a mirrored vibronic structure.

Spectral overlap. Once the spectra are available, for the Förster rate equation it is necessary to calculate the spectral overlap (SO), which is the superposition area of the absorption and emission spectra Eq.(7.18) here recalled:

$$FCWDoS = \int_{-\infty}^{\infty} dE\ SO(E) = \int_{-\infty}^{\infty} dE\ Abs(E) Em(E). \tag{7.19}$$

Since the simulated spectra are computed with a discrete domain in E (see Section 7.2 for more details), the integration is performed numerically using the extended trapezoidal rule [142]. According, given a general function $f(x)$ to be integrated in $[x_0, x_1]$

with $x_0 - x_1 = \Delta x$ small enough, the area under $f(x)$ is estimated as a trapezoid:

$$\int_{x_0}^{x_1} dx\ f(x) \simeq \tfrac{1}{2}\left[f(x_0) + f(x_1)\right]\ \Delta x. \tag{7.20}$$

If the domain function is more generally divided into x_N intervals of Δx extension, with $\Delta x = \frac{x_N - x_0}{x_N}$ small enough ($\Delta x \to 0$), the integral is approximated to a sum of trapezoids areas:

$$\int_{x_0}^{x_N} dx\ f(x) \simeq \left[\tfrac{1}{2}[f(x_0) + f(x_N)] + \sum_{i=1}^{N-1} f(x_i)\right]\ \Delta x. \tag{7.21}$$

Therefore the FCWDoS integral is estimated as a discrete summation between the spectral energy boundaries E_{min} and E_{max}:

$$FCWDoS \simeq\ \Delta E \sum_{E=E_{min}}^{E_{max}} Abs(E)Em(E) \tag{7.22}$$

where ΔE is the discrete step and the $\frac{1}{2}$ factor is neglected, since both the spectra at the spectral window boundaries decay to zero.

7.2 The code

- The spectra simulation code requires the knowledge of molecular informations as preliminary ingredients, i.e., the normal modes of the molecule $\boldsymbol{Q}$ (as vectors of Cartesian coordinates Eq.(7.2)) and the related frequencies ω, for both the ground and excited states: ω^g are employed for the emission simulation while ω^e for the absorption. As mentioned in Section 7.1, only the TS modes give a contribution. These informations allow the calculation of the Huang Rhys factors Eq.(7.14) with the program also employed for charge transport. The wavenumbers ω (cm^{-1}) and the Huang-Rhys factors S form the input of the simulation spectra program (*"input-freq-HR.dat"*, having the same structure as the Tables in Fig.(7.4) and (7.6)).

- With the input above and the absolute temperature additionally provided, as a first step the code sets the boundaries and the necessary parameters for the intensities evaluation. For each normal mode k, the maximum number of states involved in the vibronic transitions is determined: m_{max} is the vibrational level of ground electronic state with the highest m displaying a relevant population estimated through the related Boltzmann factor; n_{max} is the maximum vibrational level of the excited state with an appreciable $m \to n$ transition intensity, evaluated through an *on the fly* estimate of the related FC factors Eq.(7.13).

- Subsequently the parameters concerning the spectral window are set. The minimum E_{min} and maximum E_{max} energy values of the spectral range are given

in input (cm^{-1}). An energy step ΔE is set and the total energy range $E_{tot} = E_{max} - E_{min}$ is divided by ΔE into n_E discrete energy values E; each E point provides a possible peak position. In case $T > 0$ K, part of the spectral range is at $E < 0$, where peaks corresponding to transitions $m \to n$ with $m > n$ are located. The value of ΔE is set to 1 cm^{-1}, since it demonstrated to provide a good spectral resolution and to be a good integration step for the FCWDoS calculation (see below).

- The Franck-Condon factors $FC_k(m,n)^2$ are then accurately evaluated for each normal mode and for all the transitions $m \to n$, with $m : [0, m_{max}]$ and $n : [0, n_{max}]$. It is employed Eq.(7.13) and the Laguerre polynomial is calculated through the recursive expression [142]:

$$\begin{gathered} L_0^\alpha(S_k) = 1 \qquad L_1^\alpha(S_k) = -S_k + \alpha + 1 \\ L_{m+1}^\alpha(S_k) = \frac{(-S_k + 2m + \alpha + 1)L_m^\alpha(S_k) - (m+\alpha)L_{m-1}^\alpha(S_k)}{m+1}. \end{gathered} \tag{7.23}$$

- The peak spectrum is computed through the intensities equation Eq.(7.12), for both absorption and emission. The energetic position E of each peak is evaluated according to Eq.(7.16); since the spectral range is discrete, the peak is located to the closest E point available. The stick intensities are then convoluted with the chosen normalized shape function, Lorentzian or Gaussian Eq.(7.17), whose *hwhm* parameter (in cm^{-1}) is given as input. The spectra are normalized:

$$\int_{E_{min}}^{E_{max}} dE\ Abs(E) = 1 \qquad \int_{E_{min}}^{E_{max}} dE\ Em(E) = 1 \tag{7.24}$$

and the integral is numerically computed according to the trapezoidal rule Eq.(7.21). In particular the integral of the Lorentzian function has a slow convergence and, to be properly evaluated, requires a large enough E domain; this is due to the slow decay of the function tails. On the contrary, a Gaussian provides a much faster convergence due to its steeper decay.

- The spectral overlap SO is computed for each discrete energy point E according to Eq.(7.19). As a consequence, FCWDoS is evaluated with the numerical integration formula provided in Eq.(7.21), where ΔE is the chosen energy step that discretizes the energy window; the choice of an appropriate value is very important in order to obtain a good convergence of the integral value. The final FCWDoS is given both in $1/cm^{-1}$ and 1/eV.

7.3 Application to a molecular system: PBI

The code above presented was applied to perylene bisimide (PBI) molecule, Fig.(7.2). The molecular properties, i.e., normal modes and frequencies were computed with the

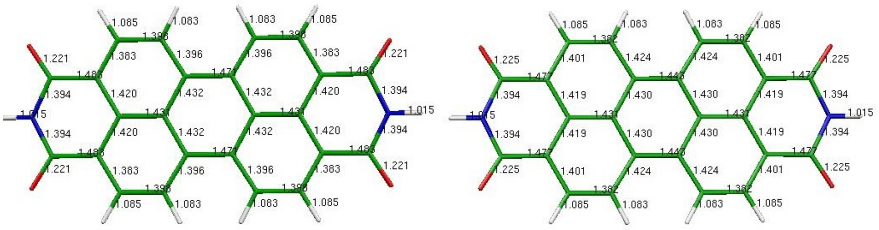

(a) ground (b) excited

Figure 7.2: Optimized geometries of ground (left) and first allowed excited (right) state of PBI in vacuo at B3LYP/6-31G*.

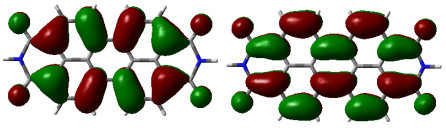

(a) HOMO (b) LUMO

	E [eV]	λ[nm]	f	wf.
S_1	2.4544	505	0.6108	0.70 $H \rightarrow L$

Figure 7.3: Excited state S_1 properties at the optimized geometry of PBI *in vacuo* at B3LYP/6-31G*: frontier orbitals involved in the transition (left) and table with excitation energy E, transition wavelength λ, oscillator strength f and wave function (right).

Gaussian09 program [31] at the B3LYP/6-31G* level of theory. The spectra and FCWDoS calculations were first reproduced *in vacuo*, also considering different values of the parameters required in the code, in order to assess their importance on the final FCWDoS. The same molecular properties have been also computed for the molecule solvated in dimethylformamide (DMF), for a better comparison with the available experimental absorption spectrum.

7.3.1 Molecular properties

PBI molecule has been optimized *in vacuo* in its ground state and its geometry is reported in Fig.(7.2). The calculation of the vertical excited state, at the ground state optimized geometry, confirmed that the first excited state (S_1) is strongly spectroscopically allowed and corresponds to the HOMO→LUMO excitation. S_1 state has been then optimized and its geometry is shown in Fig.(7.2) while the transition strength and molecular orbitals are reported in Fig.(7.3).

The normal modes and associated frequencies were computed for both states. PBI has 114 normal modes and 16 of them have non zero Huang-Rhys factor. These Huang-Rhys factors are computed for each mode according to Eq.(7.14) and are reported in Fig.(7.4) with the associated frequencies. The pattern of Huang Rhys factors for ground and excited states is similar. This is in agreement with the assumption made in the theoretical treatment, of similar frequencies and normal modes for ground and excited state. There are some slight differences among the frequencies of the most active modes and they are mainly due to a mixing between modes whose frequencies are relatively

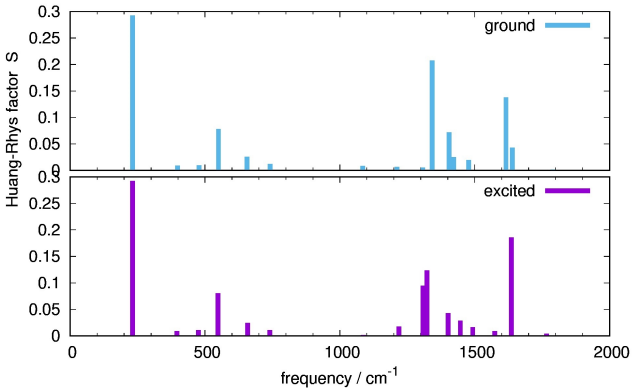

ground		excited	
ν [cm^{-1}]	S	ν [cm^{-1}]	S
231	0.2925	232	0.2921
398	0.0088	396	0.0090
478	0.0095	475	0.0109
550	0.0778	548	0.0805
656	0.0253	658	0.0247
742	0.0122	740	0.0109
1084	0.0082	1087	0.0016
1211	0.0066	1220	0.0179
1308	0.0052	1308	0.0944
1342	0.2077	1323	0.1235
1405	0.0720	1401	0.0427
1421	0.0252	1447	0.0283
1477	0.0194	1493	0.0163
1616	0.1379	1574	0.0086
1640	0.0427	1636	0.1856
1791	0.0014	1766	0.0038

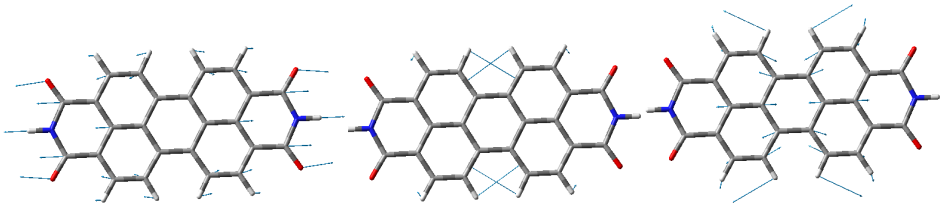

(a) ground 231 cm^{-1} (b) ground 1342 cm^{-1} (c) ground 1616 cm^{-1}

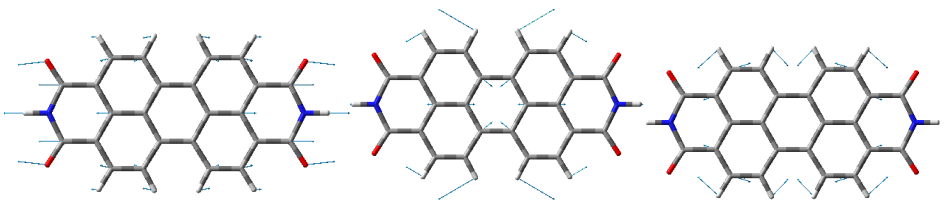

(d) excited 231 cm^{-1} (e) excited 1323 cm^{-1} (f) excited 1636 cm^{-1}

Figure 7.4: Frequencies and associated Huang-Rhys factors for ground and excited states and most active vibrations at B3LYP/6-31G* level of theory.

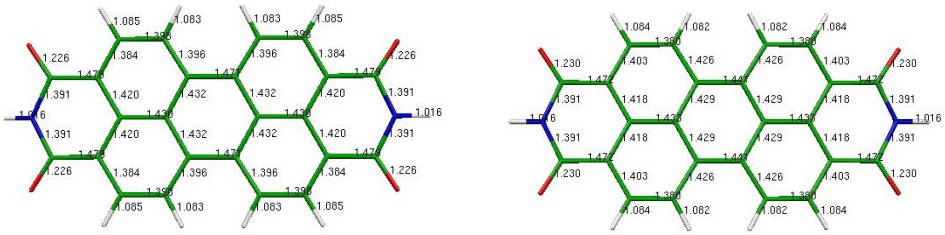

(a) ground (b) excited

Figure 7.5: Optimized geometries of ground (left) and first excited (right) state of PBI solvated in DMF at the B3LYP/6-31G* level of theory.

Table 7.1: Excited state S_1 properties for PBI solvated in DMF at the B3LYP/6-31G* level of theory.

	E [eV]	λ [nm]	f	wf.
S_1	2.4288	510	0.6416	0.71 $H \rightarrow L$

close. This happens in the spectral window $\sim 1300 - 1600$ cm^{-1}, where there are some differences between the active modes of ground and excited states, concerning both ν and S: indeed oscillators with similar frequencies can mix in the excited state compared with the ground state, owing to small couplings that may have significant effect because of the small energy difference between the frequencies of the two oscillators. Hence such modes can perturbatively mix together, slightly modifying the original frequencies and modes vectors. For both states, the mode at 230 cm^{-1} has the largest S factor. Then in the range of $\sim$ 1300 cm^{-1} there is an active mode involving a distortion of the central ring, accompanied by a bending of the central C-H bonds. Finally at $\sim$ 1600 cm^{-1} there is an active mode representing a stretching of the most external part of the aromatic core. These stretching vibrations mirror the geometric variations in moving from ground to excited state, that see an elongation of the bond lengths together with a deformation of the angles, especially around the central benzene ring, Fig.(7.2).

For a comparison with the experimental absorption spectrum, the optimized geometries and normal modes are computed for the solvated PBI in dimethylformamide (DMF), Fig.(7.5). The employed solvation model is PCM as implemented in *Gaussian09*. The solvated ground and excited state frequencies, at the equilibrium points, have been computed. The analogous Huang-Rhys factors are reported in Table 7.6. The geometries are quite similar to those computed in vacuum and also the vibrational modes involved in the Huang-Rhys factors. The are some small differences in the intensities of the S factors related to the stretching modes that are expected to reflect into slightly different spectral intensities.

7.3.2 Spectra simulations

The simulated absorption spectrum computed for solvated PBI in DMF is compared to the experimental spectra of a PBI derivative in dimethylformamide (DMF) provided

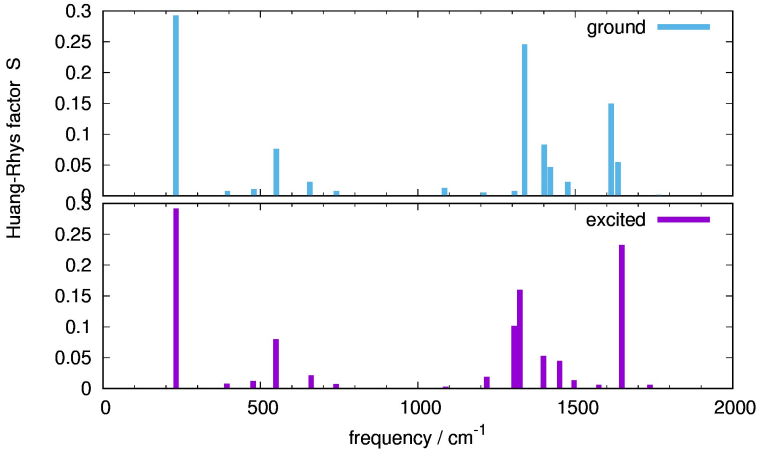

ground		excited	
ν [cm^{-1}]	S	ν [cm^{-1}]	S
231	0.2929	232	0.2917
395	0.0075	393	0.0078
479	0.0109	476	0.0124
550	0.0763	549	0.0799
657	0.0223	661	0.0214
742	0.0078	741	0.0069
837	0.0004	839	0.0001
1085	0.0126	1088	0.0029
1209	0.0054	1219	0.0186
1307	0.0079	1306	0.1012
1339	0.2458	1324	0.1600
1402	0.0831	1399	0.0525
1421	0.0467	1450	0.0448
1476	0.0224	1496	0.0131
1615	0.1495	1575	0.0058
1636	0.0547	1648	0.2326
1766	0.0015	1738	0.0056

Figure 7.6: Frequencies and associated Huang-Rhys factors for ground and excited states of PBI solvated in DMF at B3LYP/6-31G* level of theory.

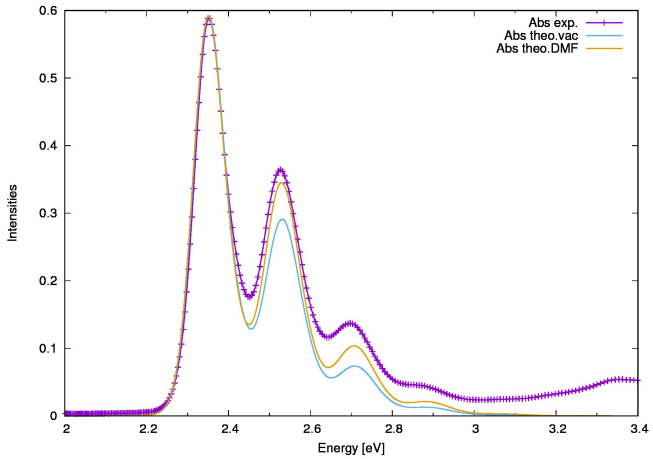

Figure 7.7: Experimental and computed absorption spectra of PBI; the computed spectra are obtained for PBI in vacuum and solvated in DMF (Gaussian lineshape, $T = 300$ K, $hwhm = 0.04$ eV).

by a collaborator [1], see Fig.(7.7) and [143]. More precisely, the experimental spectra belong to a molecule bearing phenyl rings on the imidic nitrogens but substitution in these positions does not influence significantly the photophysical properties of the first excited state, since the HOMO and LUMO orbitals directly involved in the transition do not have electron density on the N atoms, Fig.(7.3). In order to make the experimental and computed spectra comparable, their intensities have been rescaled in order to match the height of the first peak. In addition, since the computed transition energy, Table 7.3 and 7.1, does not perfectly match the experimental one, the maximum peak position of the computed spectrum is adjusted in order to match the experimental one, for the sake of comparison. The agreement between computed and experimental spectra is good. Both the peaks relative intensities and their positions are well reproduced, especially for the calculation in solvent, that reproduces more accurately the peaks relative intensities. The B3LYP functional provides therefore reliable geometry and frequency results.

7.3.3 FCWDoS

The spectral overlap is computed for spectra obtained through simulations employing different parameters values. The parameters that have been taken into account are those mentioned in Section 7.2:

- the lineshape: Lorentzian or Gaussian ;
- the temperature : $T = 0$ and $T = 300$ K ;
- the band width : $hwhm = 0.01, 0.02, 0.04, 0.05$ eV .

Based on the Huang-Rhys factors and frequencies computed in the previous section (both *in vacuo* and solvated), the spectra have been computed employing different

[1] Thanks to Dr. Marianna Marchini, University of Bologna

combinations of the parameters values listed above. As a further parameter, it has been also considered E_{00}, the possible mismatch between absorption and emission, Eq.(7.16). Since in our model the same type of molecule (PBI) represents both donor and acceptor, then $E_{00} = 0$. On the other hand, in realistic systems, the donor and acceptor molecules can have different environment or can be totally different molecules; in that case the E_{00} value is non zero. Also the relation between this factor and FCWDoS value is investigated, by "artificially" setting the PBI spectra mismatch of the following values: $E_{00} = \pm 0.1, \pm 0.2$ eV; the minus sign indicates a moving apart of the spectra while plus means an approach, and this latter way simulates realistic donor-acceptor systems in which the acceptor absorbs at lower energies than the donor.

It has already been pointed out that the HR factors and associated frequencies are quite similar for ground and excited state. In the following results the two sets of HR factors, for absorption and emission, are used. Here the numeric results are not explicitly reported, however it has been preliminary verified that using the same set of FC factors for both absorption and emission spectra (i.e., assuming that they are completely identical for ground and excited states) has a small influence on the FCWDoS results. This remark is interesting, since the excited state frequencies require a demanding calculation, that for larger molecules might become unfeasible. We can conclude that for the class of rylene-diimide chromophores one may consider only the evaluation of the ground state frequencies.

Spectra in vacuum with $E_{00} = 0$. As a first case, it has been assumed that $E_{00} = 0$ eV (Table 7.2). The PBI vibrational structure is characterized by the presence of modes with a large S factor. The overall vibronic progression is quite extended and determines the relatively low intensity of the first peak, being the spectra normalized; this fact generally keeps the FCWDoS integral quite small. More specifically the mode at low frequency also causes a certain shift among the maxima of the first peaks in absorption and emission, further contributing to a decrease of FCWDoS.

FCWDoS generally diminishes by increasing the temperature T. On one hand higher temperature populates some higher energy vibrational states of ground state, whose peaks are located at one side of the main transition and contributing to the overlap. On the other hand these bands "borrow" their intensities from the other bands that decrease, providing a lower overlap.

FCWDoS decreases by increasing the spectra width *hwhm*. Increasing the band width, the peak positions of absorption and emission spectra further increase their distances, since the vibronic progression associated with the 230 cm^{-1} mode is quite extended, and, as already discussed, this diminishes the optimal overlap. Such kind of behavior resembles the trend by increasing the temperature, and indeed spectra broadening and temperature are related.

FCWDoS from spectra with a Gaussian lineshape are larger than Lorentzian. In general the peak intensities of Lorentzian spectra are lower than Gaussian spectra. Recalling that all the spectra are normalized, this is due to the slower falling tails of the Lorentzian

Table 7.2: FCWDoS computed at $E_{00} = 0$.

		FCWDoS [eV^{-1}]			
		$E_{00} = 0$ eV			
lineshape	T [K]	*hwhm* [eV]			
		0.01	0.02	0.04	0.05
Gauss	0	4.359	2.828	2.200	1.837
	300	3.237	2.455	2.032	1.754
Lorentz	0	2.614	1.740	1.403	1.218
	300	2.198	1.616	1.351	1.351

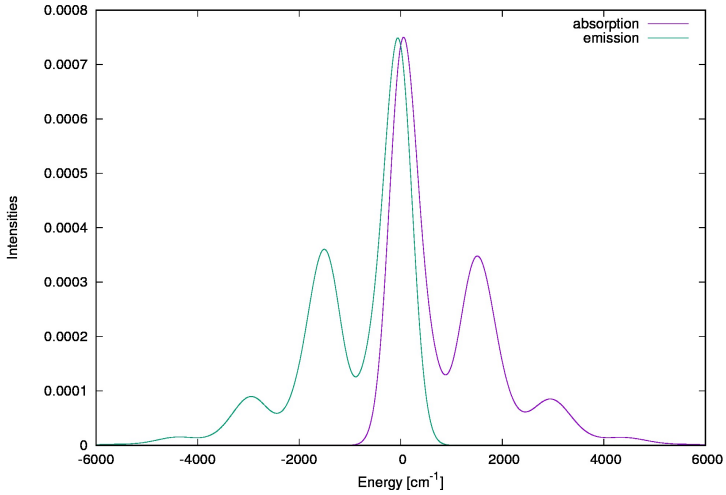

Figure 7.8: Spectral superposition example (Gaussian, $T = 300$ K, *hwhm* = 0.04 eV) for $E_{00c} = 0$ eV computed with B3LYP functional.

function that "subtract" part of the peak intensities; as a consequence the overlap, that is mainly due to the superposition of the first peaks, diminishes. However, by increasing the spectral width and the temperature, this effect has a much smaller influence and the difference decreases, the lineshape choice becoming less important.

Spectra in vacuum with variable E_{00}. Then as a further parameter also E_{00} influence on FCWDoS has been evaluated (Tables 7.3 and 7.4). Interestingly, by increasing the E_{00} value (so approaching the two spectra) the FCWDoS value has an oscillating behavior. For $E_{00} = 0.1$ eV, FCWDoS increases while for $E_{00} = 0.2$ eV it decreases. The value 0.1 eV ($\sim$800 cm^{-1}) is such that the main peak of emission lies between the two peaks of absorption, minimizing the overlap value, Fig.(7.9)a. Instead, $E_{00} = 0.2$ eV in this case roughly coincides with the energy spacing of the first two peaks ($\sim$ 1600 cm^{-1}, see Fig.(7.4)), and so the total overlap becomes more favorable and increases, Fig.(7.9)b, due to the "double" peaks superposition. So for $E_{00} = 0.1$ eV, an increase of both temperature and bandwidth contribute to a small increase of the spectral superposition, following the general trend as seen for $E_{00} = 0$ eV, while for

Table 7.3: FCWDoS B3LYP/6-31G* at variable E_{00}.

		FCWDoS [eV^{-1}]							
		$E_{00} \simeq 0.1$ eV				$E_{00} \simeq 0.2$ eV			
lineshape	T [K]	*hwhm* [eV]				*hwhm* [eV]			
		0.01	0.02	0.04	0.05	0.01	0.02	0.04	0.05
Gauss	0	0.949	1.123	1.502	1.781	3.608	2.981	2.496	2.186
	300	1.139	1.337	1.629	1.825	3.123	2.698	2.352	2.120
Lorentz	0	1.269	1.419	1.431	1.375	2.609	2.009	1.702	1.509
	300	1.390	1.480	1.455	1.381	2.383	1.917	1.659	1.486

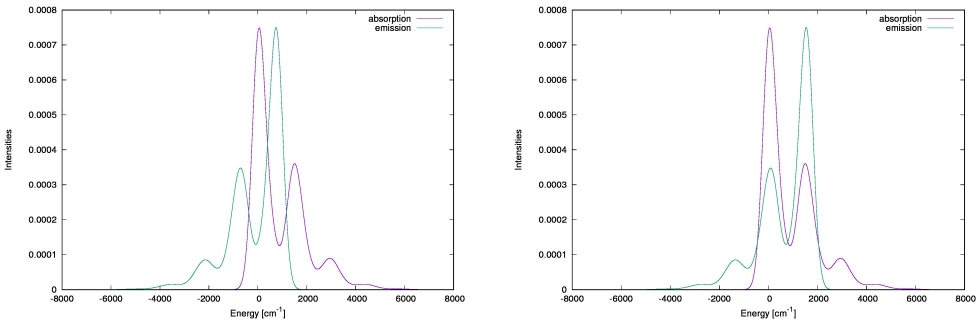

Figure 7.9: Spectral superposition example (Gaussian, $T = 300$ K, $hwhm = 0.04$ eV) for $E_{00} = 0.1$ eV (left) and $E_{00} = 0.2$ eV (right) computed with B3LYP functional.

Table 7.4: FCWDoS B3LYP/6-31G* at variable E_{00}.

		FCWDoS [eV^{-1}]							
		$E_{00} \simeq -0.1$ eV				$E_{00} \simeq -0.2$ eV			
lineshape	T [K]	*hwhm* [eV]				*hwhm* [eV]			
		0.01	0.02	0.04	0.05	0.01	0.02	0.04	0.05
Gauss	0	0.000	0.008	0.127	0.319	0.000	0.000	0.000	0.004
	300	0.032	0.078	0.212	0.377	0.002	0.002	0.003	0.013
Lorentz	0	0.219	0.391	0.504	0.267	0.077	0.149	0.213	0.504
	300	0.263	0.429	0.530	0.274	0.081	0.155	0.220	0.530

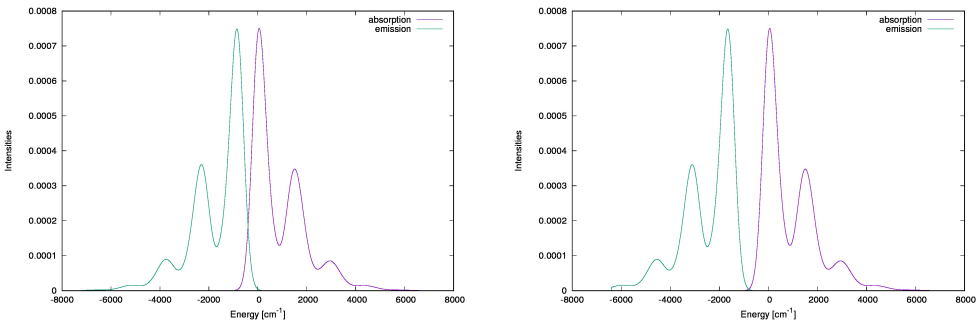

Figure 7.10: Spectral superposition example (Gaussian, $T = 300$ K, $hwhm = 0.04$ eV) for $E_{00} = -0.1$ eV (left) and $E_{00} = -0.2$ eV (right) computed with B3LYP functional.

$E_{00} = 0.2$ eV they have the opposite effect, even if to a quite small extent; furthermore, interestingly in this last case the Lorentzian lineshape provides a diminished superposition integral.

On the other hand, by increasing the distance between the spectra, the FCWDoS decreases continuously and quite steeply (Table 7.4 and Fig.(7.10)). For the spectra obtained by a convolution to Gaussian functions, FCWDoS decreases steeply, while also for the larger distance the Lorentzian spectra have a not negligible overlap. This is due to the longer tails typical of the Lorentzian function, that guarantee an overlap also for larger E_{00}. Moreover larger *hwhm* ensures a larger overlap also for larger E_{00} and the temperature gets less important modifying only slightly the resulting FCWDoS.

Table 7.5: FCWDoS computed at $E_{00} = 0$ for solvated PBI in DMF at the B3LYP/6-31G* level of theory.

		FCWDoS [eV^{-1}]			
		$E_{00} = 0$ eV			
lineshape	T [K]	*hwhm* [eV]			
		0.01	0.02	0.04	0.05
Gauss	0	3.588	2.326	1.807	1.508
	300	2.667	2.020	1.670	1.442
Lorentz	0	2.164	1.570	1.191	1.049
	300	1.823	1.356	1.150	1.029

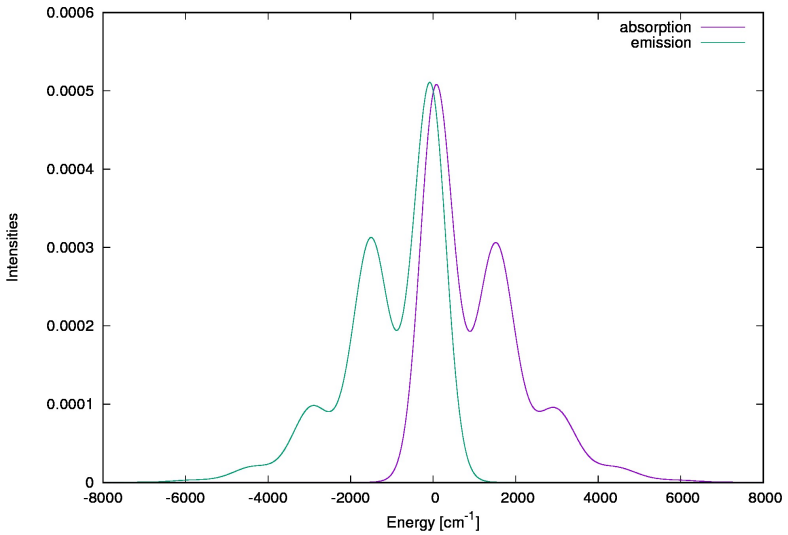

Figure 7.11: Spectral superposition example for solvated PBI in DMF (Gaussian, $T = 300$ K, *hwhm* $= 0.04$ eV) for $E_{00} = 0$ eV computed with B3LYP/6-31G*.

Spectra in solvent DMF. The spectral overlap has been calculated also for PBI spectra computed for the solvated molecule. Also in this case the parameters mentioned above have been taken into account, excepted E_{00} that in this case is kept equal to 0.

The FCWDoS of the solvated molecule show the same behavior of those computed in vacuum with respect to the increase of temperature, linewidth and lineshape. The values are generally smaller and this can be ascribed to the reduced intensity of the solvated spectral peaks with respect to those in vacuum. But on the other hand, increasing the linewidth the differences between the FCWDoS values get closer.

In conclusion, for PBI molecule the B3LYP/6-31G* method provides a good representation of the intensities of the vibrational structure underlying absorption and emission spectra. However simulations require several factors whose values need to be set up (temperature, linewidth, lineshape) and have an impact on the final FCWDoS. Apparently the most relevant factor is the linewidth and the broader the spectrum, the less relevant the other factors become. Therefore the availability of an experimental spectra as a reference for the linewidth choice is very important. Our computed values are in line with those computed with the same model for other molecular systems available in literature, as for example in [125].

CHAPTER 8

Dimer excited state analysis and exciton interaction

In the context of energy transport, the analysis of the excited states of a molecular aggregate provides important informations in order to evaluate its optoelectronic properties. As already discussed in Chapter 6, the aggregates are classified based on their optical properties into J- or H-aggregates, that display different efficiencies concerning energy transfer. The molecular exciton model takes into account only the excitations which are localized on the isolated molecules. However a more comprehensive description requires also charge transfer excitations that are possible owing to the presence of nearby molecules. The role of CT states is taken into account in the model employed in the following, that considers dimers of molecules. Their lowest energy excited states are analyzed in order to quantify to which amount they are represented by localized (LE) or charge transfer (CT) excitations. The dominant type of excitation determines also the optical properties of the state. This information, together with the excitation energy of the states, defines the aggregate character and hence the energy transfer properties. In addition it has recently been shown that CT states may play a relevant role in the application of organic materials in the field of optoelectronic, for instance in organic solar cells [7].

In the following, the role of CT states is elucidated by representing the electronic states of the dimer by means of a simple model described in Section 8.2. This model requires the calculation of the dimer Hamiltonian that can be obtained with different methodologies briefly introduced in Section 8.2 - 8.4. Finally the application to representative perylene-bisimide (PBI) molecule dimers is reported in Section 8.6.

8.1 Dimers excited states

Let's consider a molecular dimer composed by molecule a and b. The electronic excited states of the dimer (adiabatic wave functions) are multideterminantal wave functions, containing configurations of both localized (Ψ_i^{LE}) or charge transfer (Ψ_i^{CT}) excited state (diabatic) configurations:

$$\Psi = \sum_i c_i^{LE} \Psi_i^{LE} + \sum_i c_i^{CT} \Psi_i^{CT} \tag{8.1}$$

where c_i^{LE} and c_i^{LE} represent the relative weights of each configuration and i index runs over all the possible excitations that can be created, which depends on the chosen wave function (in other words on the truncation). In a locally excited configuration Ψ_i^{LE}, the excitation is localized on a molecular unit, so one electron is transferred from an occupied to an unoccupied orbital of the same molecule, Fig.(8.1) left (a) and (b). The charge transfer configurations Ψ_i^{CT} are characterized by the transfer of an electron from one monomer to the other and so each molecule achieves a net charge, see Fig.(8.1) left, (c) and (d). A characteristic property of states dominated by CT configurations is that they appear upon aggregation and they usually give rise to spectroscopically weak signals, because of their low transition dipole moment: this is related to the negligible orbital overlap, since the orbitals involved in the excitation belong to different molecular units. In the "molecular exciton theory", developed by Davydov and previously introduced in Chapter 6 for the definition of *J*- and *H*-aggregates, the dimer wave function by definition includes only the LE states and so the wave functions is the analogous of Eq.(8.1) but neglecting the second term; this choice is motivated by the fact that the CT configurations are expected to lie higher in energy than the LE. However it's not always the case, and therefore a more comprehensive theory must include both kinds of configurations; this is the choice of the model here presented in which the complete expansion in Eq.(8.1) is considered.

The relative weights of CT and LE configurations in the dimer eigenstates Ψ, Eq.(8.1), are represented by the coefficients $\{c_i^{CT}\}$, $\{c_i^{LE}\}$ that are necessary to identify the dominant character (LE or CT) in the dimer state Ψ. These coefficients are not generally obtained from standard calculations. Indeed Ψ is usually computed on the basis of the dimer orbitals, representing the Hamiltonian eigenstates built on configurations involving excitations among the dimer orbitals. In order to perform the CT or LE character analysis, it is necessary to recover the molecular orbitals localized on the two molecular moieties composing the dimer, and to identify which ones are directly involved in the excitations. This can be done for instance via orbital localization: it is a procedure that implies a rotation of the excited states Hamiltonian matrix and more specifically a transformation on a localized basis. The calculation of the dimer eigenstates relies on standard methodologies. In a first simple case one can employed the simplest possible wave function based QM method for electronic excited states, a CIS(4,4) considering four electrons in four (frontier) orbitals. The choice of such a

method is due to its cheapness and simplicity: on one hand it's not completely reliable from a quantitative point of view but on the other hand it allows to gain a deep insight into the model parameters and their physical meaning (see Section 8.2). Then the localized model has also been applied to a more sophisticated and more computationally demanding Coupled Cluster calculation, in its CC2 form, which is expected to give more reliable numerical results (Section 8.3); an attempt to obtain a fitting strategy between the two methodologies is also explained. The calculation on the dimer has also been made with density functional theory in the time dependent formulation for excited states calculations (TDDFT) reported in Section (8.4). And finally the application to perylene bisimide (PBI) dimers is reported in Section 8.6.

8.2 Model Hamiltonian from CIS(4,4) calculations

The wave function that describes the electronic states of the dimer, Eq.(8.1), is chosen to be the simplest configuration interaction singles wave function (CIS): four electrons are taken into account in four frontier orbitals. The dimer orbitals involved in the excitations are chosen to be limited to HOMO-1, HOMO, LUMO, LUMO+1. It can be seen that generally they are given by linear combinations of monomeric frontier orbitals: h_a, l_a localized on molecule a and h_b,l_b on molecule b which are also assumed orthogonalized, see Fig.(8.1)(a). As a consequence, in this localized picture only the $h \rightarrow l$ excitations of the monomer are explicitly considered. For a proper application of such a simple model, similarly as [144, 145], it's necessary that the chosen molecular systems have frontier orbitals well separated from the others, and this is the case of PBI molecule discussed below (Section 8.6).
Therefore in the following this model will be presented from the localized Hamiltonian on the basis of the isolated molecule orbitals toward its transformation into the dimer eigenstates. A schematic representation describing the transformation of the CIS(4,4) matrix is in Fig.(8.2).

Model Hamiltonian in the localized picture. The ground state wave function (Ψ_0) is represented by a Slater determinant on the Hartree-Fock localized orbitals:

$$|\Psi_0\rangle = |\psi_a\psi_b\rangle = |h_a\bar{h_a}h_b\bar{h_b}\rangle\,; \tag{8.2}$$

its energy E_0 is computed as the expectation value of the Hartree-Fock Hamiltonian [146]. The excited states configurations of the dimer (Ψ) are multideterminantal wave functions that in a localized basis are given as products of the electronic states ψ localized on each molecule, which are in turn Slater determinants built on the molecular orbitals. Among the resulting four excited configurations, two of them have a localized

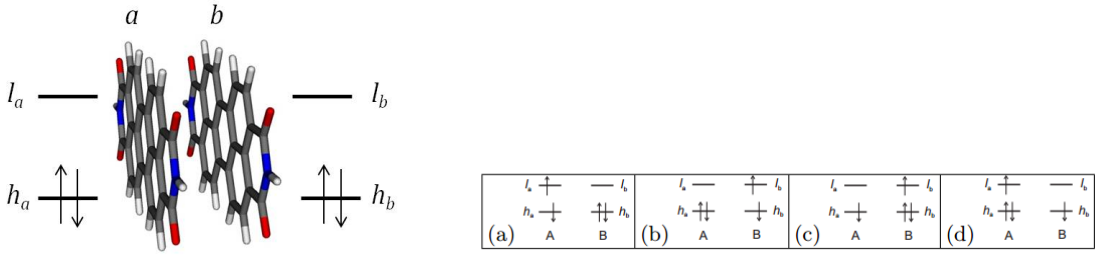

Figure 8.1: Dimer in the localized picture (left) and configurations (right).

excitation character (LE):

$$\begin{aligned} |\Psi_{a^*b}\rangle &= |\psi_a^*\psi_b\rangle = |h_a\bar{l_a}h_b\bar{h_b}\rangle \\ |\Psi_{ab^*}\rangle &= |\psi_a\psi_b^*\rangle = |h_a\bar{h_a}h_b\bar{l_b}\rangle \end{aligned} \tag{8.3}$$

with the excitation localized on one or the other monomer (Fig.(8.1)(b.a) and (b.b)), while the other two have a charge transfer (CT) character:

$$\begin{aligned} |\Psi_{a^+b^-}\rangle &= |\psi_a^+\psi_b^-\rangle = |h_a\bar{l_b}h_b\bar{h_b}\rangle \\ |\Psi_{a^-b^+}\rangle &= |\psi_a^-\psi_b^+\rangle = |h_a\bar{h_a}h_b\bar{l_a}\rangle \end{aligned} \tag{8.4}$$

since one electron is transferred from one molecule to the other (Fig.(8.1)(b.c) and (b.d)); the superscript bar represent the different electron spin. The complete excited state wave function (8.1) in this CIS(4,4) picture is the configurations vector:

$$|\Psi\rangle = \begin{pmatrix} |\Psi_{a^*b}\rangle \\ |\Psi_{ab^*}\rangle \\ |\Psi_{a^+b^-}\rangle \\ |\Psi_{a^+b^-}\rangle \end{pmatrix}. \tag{8.5}$$

If the two molecules are identical and equivalent by symmetry, the Hamiltonian on the localized basis set (8.5) is a simple 4×4 CIS matrix:

$$\mathbf{H} = \langle\Psi|\hat{H}|\Psi\rangle = \begin{bmatrix} E_{NE} & V_{exc} & D_e & D_h \\ V_{exc} & E_{NE} & D_h & D_e \\ D_e & D_h & E_{CT} & W \\ D_h & D_e & W & E_{CT} \end{bmatrix}. \tag{8.6}$$

Each element is evaluated by expanding on the molecular orbitals of the determinants, according to the Slater-Condon rules; being those integrals between single excitations of singlet multiplicity, the general formula states [146]:

$$\langle\Psi_a^r|\hat{H}|\Psi_b^s\rangle = E_0\langle\Psi_a^r|\Psi_b^s\rangle + (\epsilon_r - \epsilon_a)\delta_{rs}\delta_{ab} + \Big[2\langle\varphi_r\varphi_a|\varphi_b\varphi_s\rangle - \langle\varphi_r\varphi_s|\varphi_b\varphi_a\rangle\Big] \tag{8.7}$$

where φ_a,φ_b,φ_r,φ_s are the molecular orbitals directly involved in the excitations (in the model they coincide respectively with h_a, h_b, l_a, l_b), ϵ is their Hartree-Fock energy and Ψ_i^j describes the configuration with the $i \to j$ excitation (those in Eq.(8.3) and (8.4)). Therefore the parameters of the model Hamiltonian in Eq.(8.6) can be calculated from CIS(4,4) as:

$$E_{NE} = E_0 + \langle l_a|\hat{F}|l_a\rangle - \langle h_a|\hat{F}|h_a\rangle - \langle h_a h_a|l_a l_a\rangle + 2\langle h_a l_a|h_a l_a\rangle \tag{8.8}$$

$$E_{CT} = E_0 + \langle l_a|\hat{F}|l_a\rangle - \langle h_a|\hat{F}|h_a\rangle - \langle h_a h_a|l_b l_b\rangle + 2\langle h_a l_b|h_a l_b\rangle \tag{8.9}$$

$$V_{exc} = -\langle h_a h_b|l_a l_b\rangle + 2\langle h_a l_a|h_b l_b\rangle \tag{8.10}$$

$$W = -\langle h_a h_b|l_a l_b\rangle + 2\langle h_a l_b|h_b l_a\rangle \tag{8.11}$$

$$D_h = \langle h_b|\hat{F}|h_a\rangle - \langle h_a h_b|l_a l_a\rangle + 2\langle h_a l_a|l_a h_b\rangle \tag{8.12}$$

$$D_e = \langle l_b|\hat{F}|l_a\rangle - \langle l_a l_b|h_a h_a\rangle + 2\langle h_a l_a|l_b h_a\rangle \tag{8.13}$$

with $\hat{F}$ the Fock operator. The two electron integrals are given in the "chemists" notation [146]:

$$\langle ab|cd\rangle = \int\int d\mathbf{r}_1 d\mathbf{r}_2\; a(\mathbf{r}_1) b(\mathbf{r}_1) \frac{1}{\mathbf{r}_{12}} c(\mathbf{r}_2) d(\mathbf{r}_2).$$

If the dimer system has a lower symmetry, the corresponding matrix has a more general form:

$$\mathbf{H} = \langle\Psi|\hat{H}|\Psi\rangle = \begin{bmatrix} E_{NE} & V_{exc} & D_e & D'_h \\ V_{exc} & E'_{NE} & D_h & D'_e \\ D_e & D_h & E_{CT} & W \\ D'_h & D'_e & W & E'_{CT} \end{bmatrix}; \tag{8.14}$$

in this case, it is not possible to perform the block diagonalization discussed in the following.

Analysis of the model Hamiltonian matrix elements.

1. *Diagonal elements : E_{NE} and E_{CT}.*

$$E_{LE} = E_0 + \langle l_a|\hat{F}|l_a\rangle - \langle h_a|\hat{F}|h_a\rangle - \langle h_a h_a|l_a l_a\rangle + 2\langle h_a l_a|h_a l_a\rangle$$
$$E_{CT} = E_0 + \langle l_a|\hat{F}|l_a\rangle - \langle h_a|\hat{F}|h_a\rangle - \langle h_a h_a|l_b l_b\rangle + 2\langle h_a l_b|h_a l_b\rangle$$

Beside the energy of the ground state E_0, both terms contain the orbital energy difference between localized HOMOs and LUMOs. So to a first approximation the MOs energy difference might be an estimate of the excitation energy but actually it would be very imprecise because the other two electron integrals have comparable size of the orbital energies, since both of them comprise local densities on the same molecular moiety. More precisely the fourth term can be read as the Coulomb attraction between the electron in the LUMO and the hole in the HOMO; it is always negative, because of the minus sign, but the one in the LE configuration is larger and therefore more stabilizing than in CT, so the latter is

usually higher in energy than the former. The last term with the 2 factor is the exchange interaction between the electrons which is positive and much larger for LE than CT, since for LE it is a local property (the particles are on the same molecule); on the other hand this integral is usually smaller than the Coulomb but since it enters with the 2 factor it can achieve a certain importance specially for LE. Therefore the neat effect of the bielectron integrals is: E_{LE} is pushed down more than E_{CT} by the Coulomb integral but the opposite effect is due by the exchange term, which is in turn smaller than the Coulomb; generally the CT configurations lie higher in energy.

2. *Off diagonal elements (I) : V_{exc} and W.*

$$V_{exc} = -\langle h_a h_b | l_a l_b \rangle + 2\langle h_a l_a | h_b l_b \rangle$$
$$W = -\langle h_a h_b | l_a l_b \rangle + 2\langle h_a l_b | h_b l_a \rangle$$

V_{Exc} is the exciton coupling, the same quantity described in Section 6.2 and the same considerations exposed there apply equally well in this case. Indeed here V_{exc} represents the interaction between the two different locally excited configurations. Its second term (the Coulomb integral) is far more relevant than the first, because it is a local property: it represents the interaction between the "transition densities" of a local excitation on molecule a with identical excitation on molecule b. The first integral is positive but small because it contains two differential overlaps; therefore, unless the molecules are in close proximity, it is safe to neglect it. The W integral is, analogously, the interaction between the two CT configurations and contains only non local terms, so it is generally negligible ($W \simeq 0$).

3. *Off diagonal elements (II) : D_e and D_h.*

$$D_h = \langle h_b | \hat{F} | h_a \rangle - \langle h_a h_b | l_a l_a \rangle + 2\langle h_a l_a | l_a h_b \rangle$$
$$D_e = \langle l_b | \hat{F} | l_a \rangle - \langle l_a l_b | h_a h_a \rangle + 2\langle h_a l_a | l_b h_a \rangle$$

Both D_h and D_e contain, as a first integral, the non-diagonal Fock matrix elements, coincident to the electron couplings computed in the context of charge transfer (Section 1.2). The other two integrals are proportional to non local (differential) overlaps and are small; therefore D_e and D_h are mainly equivalent to charge transfer integrals and this also implies that they are proportional to the overlap of the two local HOMO and LUMO orbitals ($D_h \propto S_{HOMO} = \langle h_a | h_b \rangle$, $D_e \propto S_{LUMO} = \langle l_a | l_b \rangle$).

Model Hamiltonian in the partially delocalized picture: block matrix. The unitary matrix $\boldsymbol{U}$ is built over considerations based on the symmetry of the system

and is given by:

$$\boldsymbol{U} = \frac{1}{\sqrt{2}} \begin{bmatrix} 1 & 0 & 1 & 0 \\ 1 & 0 & -1 & 0 \\ 0 & 1 & 0 & 1 \\ 0 & 1 & 0 & -1 \end{bmatrix}. \tag{8.15}$$

It is employed to transform the original basis set in Eq.(8.5) into:

$$\boldsymbol{U}^{\dagger} \cdot \begin{pmatrix} \langle \Psi_{a^*b}| \\ \langle \Psi_{ab^*}| \\ \langle \Psi_{a^+b^-}| \\ \langle \Psi_{a^+b^-}| \end{pmatrix} = \frac{1}{\sqrt{2}} \begin{pmatrix} \langle \Psi_{a^*b}| + \langle \Psi_{ab^*}| \\ \langle \Psi_{a^+b^-}| + \langle \Psi_{a^+b^-}| \\ \langle \Psi_{a^*b}| - \langle \Psi_{ab^*}| \\ \langle \Psi_{a^+b^-}| - \langle \Psi_{a^+b^-}| \end{pmatrix} \tag{8.16}$$

which includes the linear combinations of the LE and CT degenerate configurations. In particular the states combinations of LE configurations coincide with the Frenkel exciton states of the molecular exciton theory discussed in Section 6.3. The first two elements of the new basis in Eq.(8.16) belong to the plus symmetry representation and the latter to the minus; the two groups are orthogonal with respect to each other. The CIS matrix in Eq.(8.6) (only in the symmetric case), is then transformed into the symmetry adapted basis (8.16) as:

$$\boldsymbol{U}^{\dagger} \cdot \boldsymbol{H} \cdot \boldsymbol{U} = \begin{bmatrix} E_{NE} + V_{exc} & D_e + D_h & 0 & 0 \\ D_e + D_h & E_{CT} + W & 0 & 0 \\ 0 & 0 & E_{NE} - V_{exc} & D_e - D_h \\ 0 & 0 & D_e - D_h & E_{CT} - W \end{bmatrix}. \tag{8.17}$$

In this form the Hamiltonian recovers the correspondence with the Frenkel states with their energies on the diagonal ($E_{LE} \pm V_{exc}$); it clearly emerges how the exciton coupling V_{exc} splits the energy of the E_{LE} configurations of an energy amount equal to the twice of its value as stated in the exciton model, Eq.(6.29). The same happens with the corresponding CT combinations and the W coupling, but since this interaction is much smaller, those states are essentially degenerate. The combinations of the electron coupling parameters $D_e + D_h$ (for plus states) and $D_e - D_h$ (for minus states) represent the off diagonal coupling terms and determine *the strength of the LE/CT mixing*: the larger this coupling, the stronger the character mixing between the combinations of the given symmetry. This information is very interesting for a deeper analysis of the eigenvectors dominant character; indeed it is expected that the eigenvalues (obtained by the diagonalization of each block of the matrix) show a "mirrored" behavior with an energy spacing given by the related combination of D_e and D_h.

Model Hamiltonian in the fully delocalized picture: Eigenvalues. Finally we consider the Hamiltonian matrix on the basis of its eigenvectors. They correspond to the four electronic excited states of the dimer (adiabatic states), involving the dimeric HOMO-1, HOMO, LUMO and LUMO+1 orbitals. The 4×4 CIS matrix

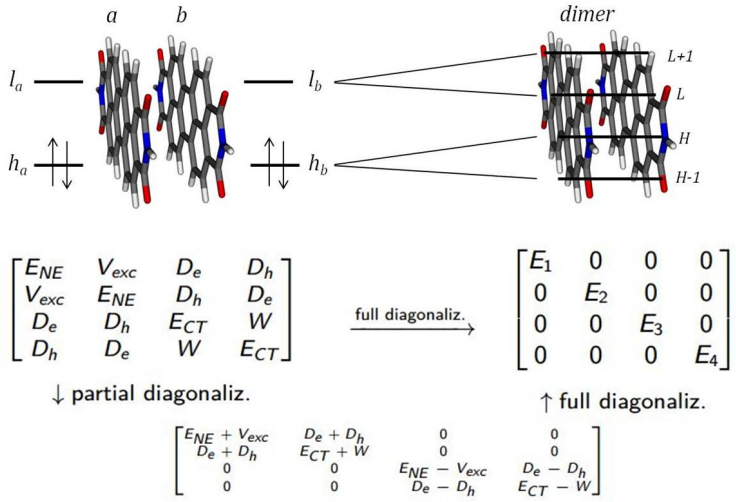

Figure 8.2: Scheme of the CIS matrix manipulation.

in Eq.(8.6) is fully diagonalized (operation which is equivalent to the diagonalization of the two blocks of the matrix in Eq.(8.17)) and the eigenvalues are the energies of the dimer excited states:

$$\begin{bmatrix} E_1 & 0 & 0 & 0 \\ 0 & E_2 & 0 & 0 \\ 0 & 0 & E_3 & 0 \\ 0 & 0 & 0 & E_4 \end{bmatrix} \tag{8.18}$$

whose analytical form reads:

$$E_{1,2} = \frac{1}{2}(E_{NE} + V_{exc} + E_{CT} + W) \pm \frac{1}{2}\sqrt{[(E_{NE} + V_{exc}) - (E_{CT} + W)]^2 + 4(D_e + D_h)^2} \tag{8.19}$$

$$E_{3,4} = \frac{1}{2}(E_{NE} - V_{exc} + E_{CT} - W) \pm \frac{1}{2}\sqrt{[(E_{NE} - V_{exc}) - (E_{CT} - W)]^2 + 4(D_e - D_h)^2}. \tag{8.20}$$

The eigenvectors are the CIS wave functions Ψ here given as linear combinations of the excited configurations built on the dimer orbitals. They are the states that can be decomposed into the linear combination Eq.(8.1) on the basis of the localized orbitals whose coefficients provide the dominant character (CT or LE) of each excited state. Such a character is reflected in the value of the transition dipole moment associated to each eigenstate $\boldsymbol{\mu}_{1-4}$: as mentioned, the CT configurations are spectroscopically weak and reduce the total $|\boldsymbol{\mu}|$ of the state of an amount proportional to their weight.

Running the calculations: *Wavels* program and the analysis tool. During my work in the laboratory of Prof. Reinhold Fink at the University of Tübingen, I used the *Wavels* code available in the group for the calculation of the dimer eigenstates and the localization procedure to obtain the Hamiltonian matrices in all the mentioned forms. As a first step, the coordinates of the dimer are generated, in *xyz*, *tmol* and

specific *Wavels* format. Then, using the *Turbomole* program "*define*", some necessary input files are generated, in particular the basis set (and eventual auxiliary basis set) and the guess of molecular orbitals of extended Hückel type; moreover also the input file of the RHF (*rhf.inp*) and CIS (*cas.inp*) calculations are necessary. The program *rhf* performs the single point HF calculation on the isolated monomers and on the dimer, providing the ground state molecular and dimer orbitals. In the first module of *casscf* program, the dimer excited states eigenvalues, eigenvectors and transition dipole moments are computed and then the HF dimer orbitals are localized on the two molecular fragments, according to Boys' localization procedure [147]. In this case the only dimer orbitals of interest, taken into account for the localization and the subsequent calculations are HOMO-1, HOMO, LUMO and LUMO+1, defining the space of the CIS(4,4) calculation. Then, the one and two electron integrals involving single excitations among those orbitals are computed. The Slater determinants of the system configurations are generated (Eq.(8.5)), comprising only the single excitations. There are 9 determinants: 1 determinant represent the ground state, while the other 8 represent the excited configurations, that mix among each other (as seen by the CI matrix) but not with the ground state (Brillouin theorem). The Slater determinants are not spin eigenfunction, therefore to have singlet and triplet states proper linear combinations are built, performing a linear transformation of the matrix (the singlets and triplets do not mix among each other, being spin orbit interaction absent). In this way the CI matrix in terms of configurations state functions is obtained; the external code "*geth.exe*" starts from the 8×8 excited configurations matrix, creates the singles and triplets configurations and splits the results into two 4×4 matrices, one for each multiplicity, providing the Hamiltonian matrices in the localized basis set, Eq.(8.6), with all the composing integrals, as in Eq.(8.8). The only element of uncertainty in this analysis is the sign of the out of diagonal elements in the Hamiltonian matrix, since the molecular orbital phases orientations are arbitrary.

8.3 CC2 calculations

Running the calculations: *Turbomole* and the analysis tool. Some basic aspects of Coupled Cluster methodology, especially in its CC2 formalism, are briefly reviewed in Appendix A. During my work in the group of Prof. Reinhold Fink at the University of Tübingen, I run CC2 calculations with the *Turbomole* package [148], in order to get excitation energies and amplitudes. To obtain results comparable to CIS, only the excited states showing a dominant character of single excitations between the dimer HOMO-1,HOMO, LUMO and LUMO+1 were taken into account. The total dimer system is divided into two domains, coincident with the two molecular moieties and the dimer orbitals are transformed, similarly as for CIS, by a localization procedure set up by Dr. Wenlan Liu of the University of Stuttgart [149]. From the localized orbitals and the cluster amplitudes, the dominant character of each excitation (CT

or LE) is computed. The localized states are determined, and through a similarity transformation of the model Hamiltonian 4×4 matrix analogous to the localized CIS, Eq.(8.6), is recovered.

8.4 TD-DFT calculations

Charge Transfer states. A brief description of DFT and TDDFT fundamentals is provided in Appendix A. However, for the purpose of the study presented here, it is necessary to point out some aspects concerning the performance of TDDFT method in relation to charge transfer (CT) excited states calculation. Indeed it is well known that TDDFT often fails in the description of CT states, especially when dealing with intermolecular charge transfer [150, 151, 152]. This failure arises from several issues. In first place, in general the potential curves of CT states do not show the correct $1/R$ decay with the charge separation distance R. This is related to the well known self interaction error. In the Kohn-Sham equations only the local interaction between electrons (Coulomb term, given by the second integral in Eq.(A.36)) is present, while the non-local electrostatic interaction is not explicitly accounted. As a consequence the hole-electron interaction in CT states appears as a short range interaction with an exponential decay. In contrast this term is present as the exchange term in Hartree-Fock (and hence also in CIS) that therefore provides the correct $1/R$ behavior. This lack in DFT theory can be at least partially recovered by including in the xc functional a non local contribution, for example as it is done in the hybrid functionals like B3LYP that include a certain amount of exact Hartree-Fock exchange. Another strategy to build a functional with a proper behavior is to split the Coulomb operator of the Hamiltonian into two parts: a short range part, treated with xc functionals from DFT, and a long range part, calculated with exact HF exchange or other functions. This is the way how long-range corrected functionals and CAM-B3LYP are built. In particular, the latter combines B3LYP at short range with an increasing amount of exact HF exchange at long range, providing in most cases good excitation energies also for CT states, even comparable to higher level wave function based methods as CC2 [153, 154]. As a second issue, the TDDFT excitation energies of intermolecular CT states are drastically underestimated because the terms in the expression of the $B_{ar,bs}$ integrals in Eq.(A.42) vanish: they include integrals which depend on the overlap between Kohn-Sham orbitals belonging to different molecules (donor and acceptor) which are close to zero. Consequently the only surviving terms is the first one in $A_{ar,bs}$, namely the orbital energy difference, which usually provides a drastic underestimation of the correct excitation energy. Good xc functionals, as the long range corrected CAM-B3LYP, allow to tackle at least partially also this weak aspect of TDDFT and, for this reason, it has been used for the calculations on PBI dimers (Section 8.6.4).

Running the calculation: *Gaussian09* and the wave function analysis. The dimer excited states calculations are run with the *Gaussian09* program [31]. They provide energies and wave functions, i.e., the excited configurations with the most relevant weights in terms of dimer molecular orbitals. In contrast with the calculations performed with *Wavels*, for TDDFT it is not available an automatized tool for the wave function analysis through the orbitals localization in order to determine the dominant character (CT or LE) of the transition. Thus, in this case, an analysis has been made, limited to the excited states dominated by transitions between the orbitals HOMO-1, HOMO, LUMO and LUMO+1. To briefly describe the analysis procedure, an example taken from the results of PBI in Section 8.6 is reported in the following. Note that the analysis is performed along the lines described in [155, 156].

As a preliminary aspect for a correct analysis, it is necessary to point out how *Gaussian09* builds the excited states wave functions. Here we are concerned only about singlet excited states. As already pointed out, the TDDFT wave function of a singlet electronic excited state Ψ (later also named S for simplicity) is expressed similarly to the CIS one as a linear combination of singly excited configurations state functions ψ:

$$\Psi = \sum_i c_i \psi_i. \tag{8.21}$$

Each configuration ψ_i is in turn given by a linear combination of two determinants D_1 and D_2. Each determinant is based on the same spatial orbitals but the excited electron has changed its spin. The two determinants corresponds to two different electron disposition ($\alpha\beta$ and $\beta\alpha$): the spin part is different and accounts for the possibility of exciting the α or the β spin:

$$\psi = \frac{1}{\sqrt{2}}(D_1 - D_2) = \frac{1}{\sqrt{2}}|\varphi_1^D ... \varphi_{N_{occ}}^D|(\alpha\beta - \beta\alpha). \tag{8.22}$$

It is the linear combination $(\alpha\beta - \beta\alpha)$ that determines the singlet character of the excitation. The combination coefficients ensure the normalization of ψ: $(\frac{1}{\sqrt{2}})^2 + (\frac{1}{\sqrt{2}})^2 = 1$, that reflects also in the normalization of Ψ in Eq.(8.21) ($\sum_i c_i^2 = 1$). Now, *Gaussian09* takes into account for each ψ function only "half" of the wave function, since both are based on the same spatial orbitals, and this affects the sum of the squared coefficients of Ψ which is in that case 0.5. In order to recover the proper normalization, in the following analysis all the configuration coefficients ($\{c_i\}$ in Eq.(8.21)) are therefore multiplied by a $\sqrt{2}$ factor ensuring the final sum of the squared coefficients to be 1.

- In *Gaussian09* output, for each wave function Ψ_n of the S_n excited state only the "dominant" ψ configurations are reported, i.e., those with coefficient c_i, Eq.(8.21), above a certain threshold. These configurations are identified by the dimer orbitals φ^D directly involved in the excitation.

  Example: S_1 excited state wave function of the dimer.

$$\Phi_1 \equiv S_1 = \sqrt{2}\Big[0.049\big[(H-1) \rightarrow (L+1)\big] + 0.703\big[H \rightarrow L\big]\Big]$$

- The dimer orbitals φ^D can be decomposed as the linear combinations of localized molecular orbitals: $\varphi^D = \sum_i a_i \varphi_i$. The localized orbitals φ and their coefficients in the combination a_i are identified by a "graphical inspection" of the shapes of the dimer orbitals: the comparison with the isolated molecule orbitals determines which ones are present in the combination (then which φ). Note that for the dimers investigated in this work, the graphical inspection is sufficiently precise, since for symmetry reasons the two local components must have the same weight, and hence it serves simply to state whether the linear combination has a plus or minus sign. In the following example it is shown how, as in the model Hamiltonian, the combinations of h_a,h_b give HOMO-1 and HOMO and of l_a,l_b give LUMO and LUMO+1.

Example: the dimer orbitals involved in S_1 are decomposed on the localized basis.

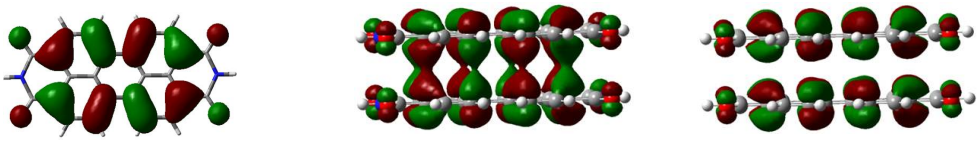

monomer h $\quad (H-1) = \frac{1}{\sqrt{2}}(h_a - h_b) \quad H = \frac{1}{\sqrt{2}}(h_a + h_b)$

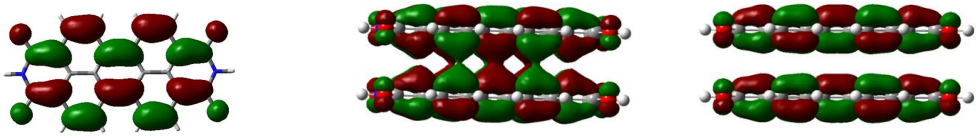

monomer l $\quad L = \frac{1}{\sqrt{2}}(l_a - l_b) \quad (L+1) = \frac{1}{\sqrt{2}}(l_a + l_b)$

- Each configuration included in the Ψ wave function is expanded on the localized orbital basis set, according to the dimer orbital decomposition of the previous step. The contributions of excitations between the localized orbitals are isolated, comprising their weight.

Example: expansion of S_1 wave function on the localized basis.

$$
\begin{aligned}
S_1 &= \sqrt{2}\Big[0.049[(H-1) \rightarrow (L+1)] + 0.703[H \rightarrow L]\Big] \\
&= \sqrt{2}\Big[0.049\ [\tfrac{1}{\sqrt{2}}(h_a - h_b) \rightarrow \tfrac{1}{\sqrt{2}}(l_a + l_b)] + 0.703\ [\tfrac{1}{\sqrt{2}}(h_a + h_b) \rightarrow \tfrac{1}{\sqrt{2}}(l_a - l_b)]\Big] \\
&= \sqrt{2}\Big[0.049\ \tfrac{1}{2}[(h_a \rightarrow l_a) + (h_a \rightarrow l_b) - (h_b \rightarrow l_a) - (h_b \rightarrow l_b)] \\
&\quad + 0.703\ \tfrac{1}{2}[(h_a \rightarrow l_a) - (h_a \rightarrow l_b) + (h_b \rightarrow l_a) - (h_b \rightarrow l_b)]\Big] \\
&= 0.532\ (h_a \rightarrow l_a) - 0.462\ (h_a \rightarrow l_b) + 0.462\ (h_b \rightarrow l_a) - 0.532\ (h_b \rightarrow l_b)
\end{aligned}
$$

- Among the excitations, it is distinguished between localized excitations (LE), centered on one molecular moiety ($h_a \rightarrow l_a$ and $h_b \rightarrow l_b$) and the charge transfer (CT) excitations, involving both molecules ($h_a \rightarrow l_b$ and $h_b \rightarrow l_a$), each with its weight that can be identified with the c_i^{LE} and c_i^{CT} coefficients of Eq.(8.1). The global LE and CT coefficients, given by the sum of each LE and CT transitions

resulting from the wave function expansion, allow to identify the dominant character of the excitation. The sum of the squared LE and CT character computed in this must be $\simeq 1$.

Example: the LE and CT transitions coefficients are gathered. In this case it can be concluded that S_1 has a mixed character, with a slightly predominant LE character.

$$\begin{aligned}\sqrt{0.532^2\ (h_a \rightarrow l_a) + \ (-0.532)^2\ (h_b \rightarrow l_b)} \quad &= \quad 0.752 \quad \text{LE character} \\ \sqrt{(-0.462)^2\ (h_a \rightarrow l_b) + \ 0.462^2\ (h_b \rightarrow l_a)} \quad &= \quad 0.654 \quad \text{CT character}\end{aligned}$$

8.5 Localized matrix fitting

A fitting procedure has been identified as a possible way to obtain the elements of the model Hamiltonian in its localized form of Eq.(8.6), starting from those obtained from low level calculations. In addition the fitting can serve to produce localized matrix elements of good quality when these are not directly available from high level calculations. The idea behind the fitting may also be to produce model Hamiltonian parameters of quality comparable to CC2 or other high level computations, by transferring the fitting parameters to CIS(4,4) calculations carried out on the same dimers.

In the case presented in Section 8.6, the fitting has been applied to recover a localized Hamiltonian in the form of Eq.(8.6) for CC2 and TDDFT. In the first case the application is instructive, since for CC2 that matrix is available also through a localization procedure and allows a comparison with the fitted one, to evaluate the validity of the procedure; in the second case, a fitting is a way to get the matrix elements. The CIS(4,4) matrix $\boldsymbol{H}_{CIS}$, Eq.(8.6), readily obtained by the localization procedure of *Wavels*, is rescaled with a suitable choice of parameters:

$$\boldsymbol{H}^{fit} = \boldsymbol{H}_{CIS} * f(a, \alpha, \beta, b, \gamma, \delta, c, d, e, f). \tag{8.23}$$

These parameters reflect the differences between the methodologies and in particular recover the failures of the simple CIS model employed. The off diagonal couplings are generally overestimated by CIS, due to the lack of the correlation effects and this is expected to be particularly relevant for the V_{exc} and W; therefore each element is rescaled with a different factor (c, d, e, f). For the diagonal terms the fitting is more complex: in general they are expected to be shifted downwards in both CC2 and CAM-B3LYP matrix due to the presence of the correlation energy that in CIS model is missing and this is included through a and b parameters. On the other hand, the amount of correlation is different for E_{LE} and E_{CT}: E_{CT} has a substantial polarization (orbital relaxation) that is lacking in CIS, while for the E_{LE} states one must consider also to add the dispersion interactions. In addition, those terms are variable with the dimer geometry, in particular with the intermolecular distance (in this analysis accounted by the sliding parameter x): it is expected to be larger for small distances. Therefore, the

parameter modifying the diagonal elements must include a term differentiating between short and long range distances, with some form of decay. To account for this effect a Gaussian function is added, characterized by different parameters for the two states (α and β for LE and γ and δ for CT). The final $\boldsymbol{H}^{fit}$ matrix takes the form:

$$\boldsymbol{H}^{fit} = \begin{bmatrix} E_{LE} - a + \alpha e^{-\beta x^2} & cV_{exc} & eD_e & fD_h \\ cV_{exc} & E_{LE} - a + \alpha e^{-\beta x^2} & fD_h & eD_e \\ eD_e & fD_h & E_{CT} - b + \gamma e^{-\delta x^2} & dW \\ fD_h & eD_e & dW & E_{CT} - b + \gamma e^{-\delta x^2} \end{bmatrix}. \tag{8.24}$$

The matrix is then diagonalized analytically to obtain the fitted eigenvalues E^{fit}_{1-4} that are function of the introduced parameters:

$$\begin{aligned} E^{fit}_{1,2} &= \tfrac{1}{2}(E_{LE} - a + \alpha e^{-\beta x^2} + cV_{exc} + E_{CT} - b + \gamma e^{-\delta x^2} + dW) \\ &\pm \tfrac{1}{2}\sqrt{[(E_{LE} - a + \alpha e^{-\beta x^2} + cV_{exc}) - (E_{CT} - b + \gamma e^{-\delta x^2} + dW)]^2 + 4(eD_e + fD_h)^2} \\ E^{fit}_{3,4} &= \tfrac{1}{2}(E_{LE} - a + \alpha e^{-\beta x^2} - cV_{exc} + E_{CT} - b + \gamma e^{-\delta x^2} - dW) \\ &\pm \tfrac{1}{2}\sqrt{[(E_{LE} - a + \alpha e^{-\beta x^2} - cV_{exc}) - (E_{CT} - b + \gamma e^{-\delta x^2} - dW)]^2 + 4(eD_e - fD_h)^2}. \end{aligned} \tag{8.25}$$

E^{fit}_{1-4} are then compared to E_{1-4} obtained from the complete standard CC2 and CAM-B3LYP calculations. With the *Solver* tool of *Microsoft Excel*, a nonlinear regression procedure provides the optimum values of the parameters that minimize the difference between the fitted and computed eigenvalues (least squares fitting). This procedure seems to be promising, because it allows to extract the localized Hamiltonian elements, for each level of theory and without a similarity transformation, requiring only the knowledge of the CIS(4,4) localized Hamiltonian and the eigenvalues of excited states computed with high level correlated methods.

8.6 PBI aggregates calculations

Perylene-Bisimide (PBI) is a well known molecular dye, with favorable photophisical and electronic properties. Indeed it is widely employed in the field of opto-electronic materials and for this reason it is a widely studied system. In particular, in solid state or solution its aggregation driving force is the π-stacking leading to the formation of *H*-aggregates with poor energy transport properties. It has been experimentally shown how in PBI crystals the exciton undergoes a fast relaxation toward a dimer trap state, drastically shortening the exciton diffusion length [157]. Theoretically [158] the presence of a conical intersection between the first two PBI dimers excited states has been demonstrated. This drives the trapping of the electronic excitation toward the dark S_1 state and hence it limits the exciton diffusion. The crystal packing geometry is a key aspect when dealing with these processes, since different aggregate geometries

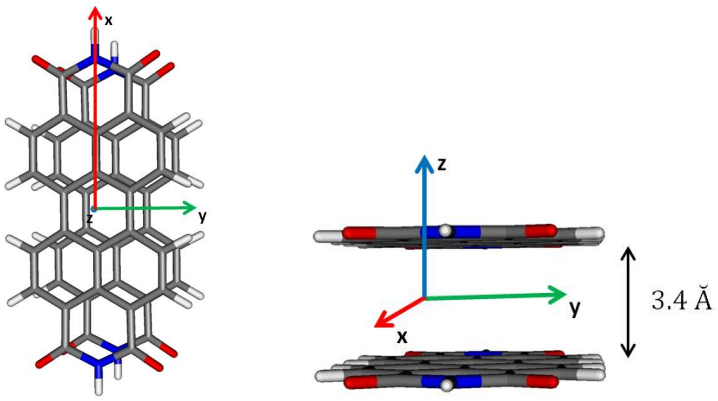

Figure 8.3: PBI dimers geometries.

can provide strongly different behaviors. In this regard, several attempts have been made, from a synthetic point of view, to obtain PBI *J*- aggregates [159, 160, 161, 135]. This goal is usually achieved by means of chemical substitution on the PBI molecule, in order to force the molecules toward a favorable packing with the inclusion of bulky substituents. Most of these systems, however, have been obtained only in solution or gel phase but measurements of exciton diffusion lengths have been reported in literature, with promising results [162]. In parallel, the role of charge transfer states (CT) in triggering this process is currently under discussion [163, 164]. The inclusion of CT states is necessary for the correct analysis of the excited state and photophysical properties of several π-stacked systems, since they can provide a relevant mixing with the locally excited (LE) states (Frenkel states). Recently, signatures of CT and LE mixing have been found also for PBI aggregates and the degree of LE/CT mixing depends also on the aggregate geometry, as it has been shown by Liu *et al.* in relation to the reciprocal orientation of PBI molecules [165, 166]. Additionally their strong impact on the photophysical properties has been theoretically valuated [164], especially in relation with the *H* or *J* dimer character, suggesting the necessity to go beyond the classical interpretation based on the molecular exciton theory [167].

The study here presented, similarly to that reported in [167], is aimed to compute the excited states properties for dimers of PBI molecules with various geometries, related by a translational shift. In each dimer geometry (Fig.(8.3)) the molecular plane is assumed parallel to the xy Cartesian plane; the interplanar distance along z is kept fixed to a certain distance, initially chosen to 3.4 Å as the typical distances of PBI crystals (but further z values are investigated in Section 8.6.2). A sliding is performed along the x and the y direction (the same of the molecular transition dipole moment, see below) and calculations are performed for values ranging from 0 to 12 Å for the first and from 0 to 6 Å for the latter, in both cases with steps of 0.5 Å. The dimer excited states energy and optical activity are computed, in order to define the aggregate character (*H* or *J*). Additional related properties, like the exciton coupling V_{exc} are also evaluated. The levels of theory employed are those described in Section 8.2-8.4: CIS(4,4)/SVP, CC2/TZVP and CAM-B3LYP/6-31G*.

8.6.1 PBI monomer

The geometry of the PBI molecule taken into account is depicted in Fig.(8.4).

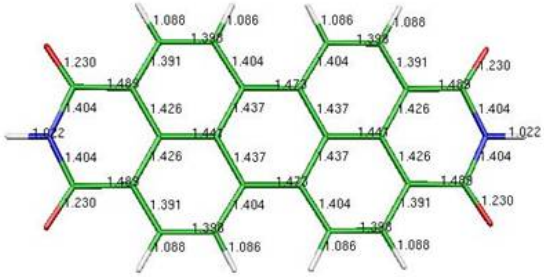

Figure 8.4: Geometry of PBI molecule.

The ground state electronic properties are computed, and in particular the molecular orbitals energies are reported in Table 8.1 at the Hartree-Fock and DFT level of theory. Interestingly in both cases the frontier orbitals are well separated from the other orbitals (like HOMO-1 and LUMO+1). This information is particularly relevant concerning the model assumptions, that take into account the frontier orbitals only, neglecting the others; it supports the expectation that the frontier orbitals of the dimer are provided by linear combinations of the monomer frontier orbitals only.

Table 8.1: PBI monomer energies and frontier orbitals energy.

	E [eV]				ΔE_{H-L} [eV]
	$HOMO-1$	$HOMO$	$LUMO$	$LUMO+1$	
HF	-9.94	-7.97	-1.18	1.22	6.79
CAM-B3LYP	-8.98	-7.21	-2.71	-0.81	4.50

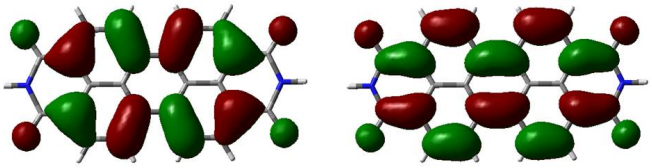

Figure 8.5: PBI monomer HOMO and LUMO orbitals.

Indeed the first excited state, for the level of theory, is a bright state dominated by the $HOMO \rightarrow LUMO$ transition (Table 8.2). It can be seen that CIS(4,4) overestimates very strongly the excitation energies. CAM-B3LYP and CC2 agree with their prediction, which is however overestimated compared to B3LYP and the experimental results (see Section 7.3); the general overestimate of CAM-B3LYP excitation energies with respect to B3LYP is well known. The oscillator strength is very high and the transition dipole moment is aligned along the long molecular axis, and hence along the Cartesian x direction, according to the orientation of Fig.(8.3). The second excited state is placed significantly higher in energy and is forbidden. These observations reinforce the suitability of the chosen model, since it appears reasonable to restrict the attention to the

Table 8.2: PBI monomer S_1 excitation energy E, oscillator strength f and dominant configurations of various levels of theory, compared to the experiment [143].

S_1	E [eV]	f	wf.
CIS(4,4)	3.98	-	$0.998(H \rightarrow L)$
CC2	2.85	0.815	$0.980(H \rightarrow L)$
CAM-B3LYP	2.70	0.766	$0.992(H \rightarrow L)$
exp.	2.36	-	-

excitations of the dimer arising from the frontier orbitals: they are expected to be the only orbitals involved in the dimer excited states of our interest.

8.6.2 PBI dimers: CIS(4,4)/SVP calculations

In Fig.(8.6) the matrix elements of the Hamiltonian in the localized basis, Eq.(8.6), computed at the CIS(4,4)/SVP level of theory are plotted as a function of the x sliding. The diagonal energy of the charge transfer configuration E_{CT} as expected lies higher in energy than the localized one E_{LE}, with values increasing with the sliding. However, for close molecules (close to 0 sliding) the energy difference between the configurations is very small ($\simeq$ 0.2 eV), Fig.(8.6) left. All the off diagonal coupling terms decrease for increasing x sliding, Fig.(8.6) right.

The exciton interaction V_{exc} decreases monotonically and changes sign around 6 Å sliding while the W coupling between the CT configurations, as expected, is close to 0. The electron couplings D_e and D_h both show a peculiar oscillating profile, with decreasing absolute values. Remarkably D_h changes sign several times and this behavior mirrors the overlap between the HOMOs of the two monomers (Fig.(8.1)) and its periodical variation in sign and magnitude while sliding, due to the typical π structure of the MOs with alternating phases of lobes. In contrast D_e oscillates without changing sign, accordingly to the orbital overlap.

The diagonal elements of the block diagonal matrix are depicted in Fig.(8.7) left. The blue and green lines represent the linear combinations between the localized configurations, i.e., the Frenkel states of the exciton model. Indeed they cross exactly at about 6 Å where $V_{exc} = 0$ and for each point their spacing is twice the coupling. The light-blue and magenta lines are the analogous combinations of CT configurations that are essentially degenerate ($W \simeq 0$). Interestingly, at small sliding distances they lie lower in energy than the plus combination of the Frenkel states (the one pushed higher in energy by the positive and large value of V_{exc}) and therefore they cross. The off diagonal terms, combination of the D_e and D_h terms, is represented in Fig.(8.7) right. Interestingly their combination display oscillations and in particular around $x = 0$ the plus combination is very large. Since it represents the extent of mixing between CT and LE configurations, in that area where these two configurations are very close in energy, the eigenvectors are expected to have a mixed character. Furthermore, since the CT state lies below the LE in this region, this implies that after mixing the largest

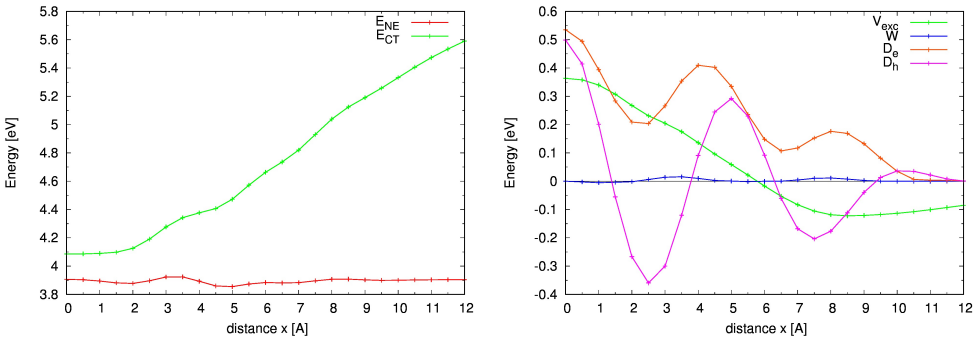

Figure 8.6: PBI dimer, elements of the localized matrix along x translation at the CIS(4,4)/SVP level of theory: diagonal (left) and off diagonal (right) elements.

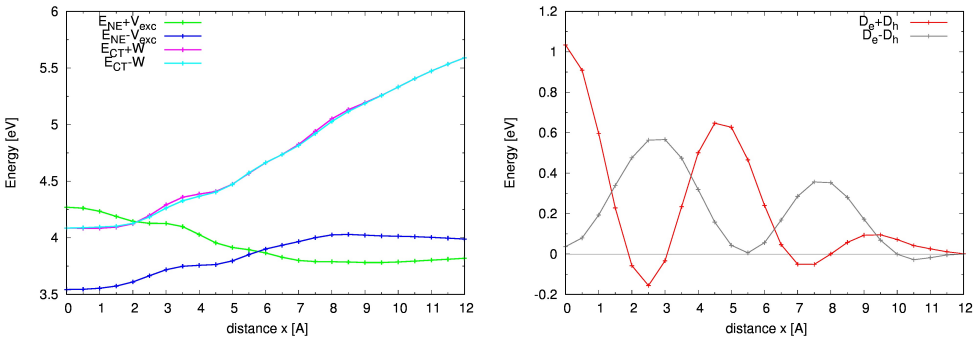

Figure 8.7: PBI dimer, elements of the block diagonal matrix along x translation at the CIS(4,4)/SVP level of theory: diagonal (left) and off diagonal (right) elements.

CT character will be found in the lowest energy state. This is a key point to be considered when comparing these results with those of high level CC2 calculations. The eigenvalues of the four eigenstates of the CIS matrix, i.e., the dimer excited states are reported in Fig.(8.8) top. The symmetry of the states, with respect to the inversion center that each dimer has, has been attributed on the basis of the spectroscopic activity: two of them have gerade g symmetry while the other two are ungerade u, and hence spectroscopically active, Fig.(8.8) bottom. States with different symmetry can cross and these crossings are due to the "mirrored" behavior of the states with analogous symmetry: the oscillatory trend of the state curves is due to "bounces" between the pair of states with the same symmetry and one of them, that in the region around 2 Å sliding, hides an avoided crossings. The combinations $D_e \pm D_h$ are the responsible interactions. Moreover the larger these terms the larger the mixing between CT and LE character, as it is pointed out by Fig.(8.8) middle. Therefore at small x values the two lowest states present a significant amount of mixing. Additionally, the larger the mixing, the smaller the transition moment of the state, since CT configuration have reduced spectroscopic activity. Merging these informations and focusing on the first two excited states, it is possible to assign the H or J character to the dimer, indicated in Fig.(8.8) top. The crossing of the curves determine an alternation of the characters. Interestingly, according to Kasha exciton model it would be expected a single character

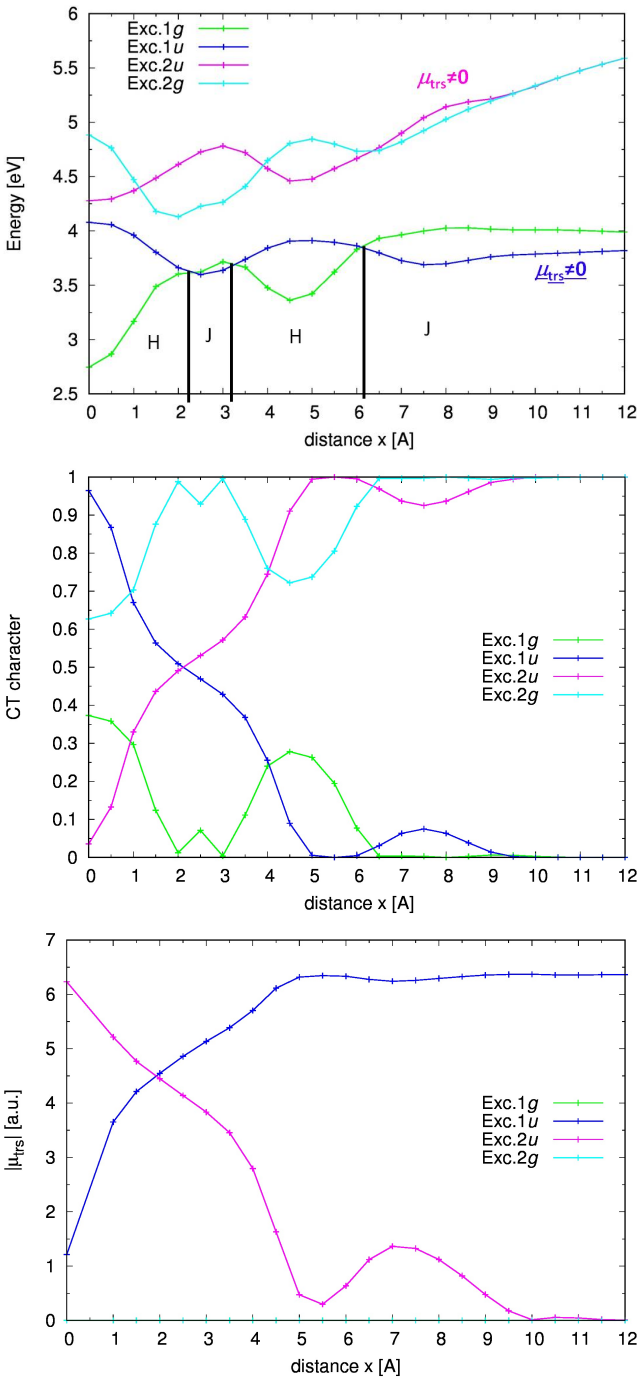

Figure 8.8: PBI dimer, fully diagonalized Hamiltonian along x translation at the CIS(4,4)/SVP level of theory: eigenvalues with H and J character (top), transition moments (middle) and CT character amount (bottom).

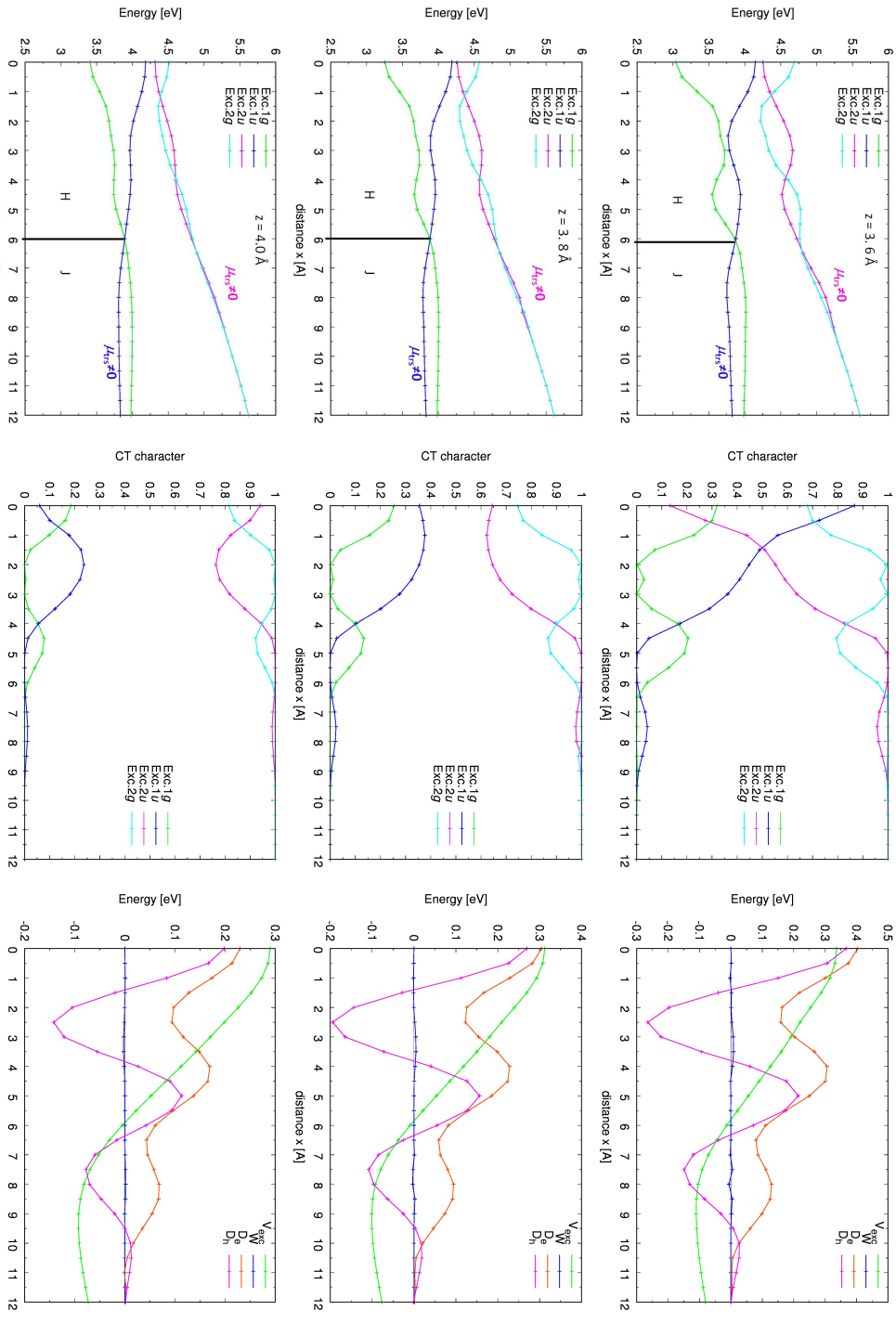

Figure 8.9: PBI dimer, eigenvalues along x translation, with different z inter planar distances (z=3.6 Å), at the CIS(4,4)/SVP level of theory.

change, at about 6 Å corresponding to the $V_{exc} = 0$ geometry. In contrast the presence of significant electron couplings, determines the presence of additional character switchings at smaller x. This determines the formation of a J character "area" in a region expected to be H-aggregates according to the simple exciton model.

In conclusion according to this simple CIS(4,4) methodology, the excited states of PBI dimers taken at different geometries varying along the x coordinate show an alternation of H and J character. This behavior is determined not only by the exciton coupling V_{exc}, as expected according to the molecular exciton theory, but also by and interplay of the electron couplings D_e and D_h, that drive the mixing of CT and LE configurations. These use of such a simple and cheap CIS(4,4) methodology allows a deep insight and of the interplay between the various integrals. The overall picture of the relation between dimer character and geometry is in accord with that reported in a recent investigation taking into account perylene aggregates [167], further supporting the reliability of the chosen model for this system.

PBI dimers with variable interplanar distances. The same calculations have been run with increasing interplanar distances, in order to verify the effect of the z coordinate on the J and H alternation of the character. Several distances have been taken into account but here we report the results for 3.6, 3.8 and 4.0 Å Fig.(8.9). The most remarkable effect concerns the number of crossings between the first two excited states, that already at 3.6 Å decrease from three to one. This can be easily understood by inspecting the plots of the off diagonal elements of the localized matrix of Eq.(8.6) in Fig.(8.9) right. By increasing the interplanar distance all of them decrease and this is particularly relevant for the electron coupling terms D_e,D_h, whose decay with intermolecular distance is exponential. As a consequence, the degree of character mixing between the LE and CT configurations is lower, see Fig.(8.9) middle, and the oscillations in the energies of the eigenstates are less prominent, Fig.(8.9) left. Notably, the CT states are placed higher in energy compared to LE, in contrast with the situation at the 3.4 Å distance, and as a consequence the lowest energy states have always a more marked Frenkel (LE) character (larger than 50 %) with one crossing in correspondence of the geometry at which $V_{exc} = 0$. Therefore, as expected, for more separated molecules, the picture is closer to the classical molecular exciton model, with negligible orbital overlap and hence less relevant contribution from charge transfer.

PBI dimers with sliding along y direction. For the sake of completeness the analogous investigation has been performed for PBI dimers geometries variable along y (Fig.(8.3)). The most relevant difference concerns the V_{exc} term of the localized Hamiltonian matrix, Fig.(8.10): in this case it never crosses 0. This can be understood by resorting to the simple PDA model: since the y direction is orthogonal to the molecular transition dipole vector, the translation does not vary the reciprocal orientation of $\boldsymbol{\mu}_a$ and $\boldsymbol{\mu}_b$ and hence it does not affect the interaction sign, but only the absolute value that decreases with the intermolecular distance. The CT states arising from the similarity

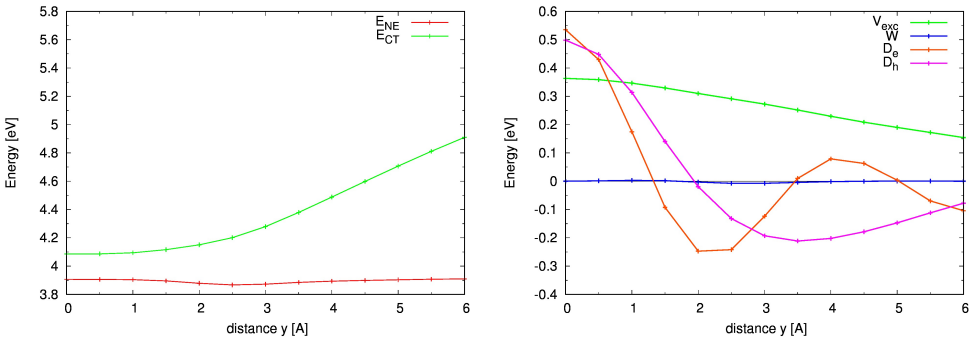

Figure 8.10: PBI dimer, elements of the localized matrix along y translation at the CIS(4,4)/SVP level of theory: diagonal (left) and off diagonal (right) elements.

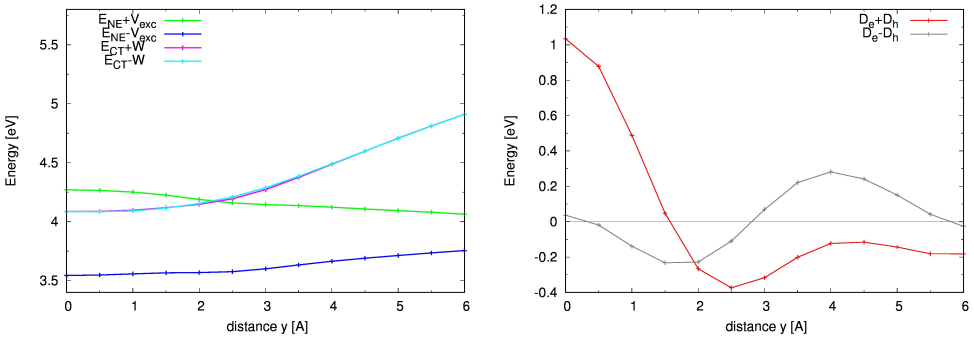

Figure 8.11: PBI dimer, elements of the block diagonalized matrix along y translation at the CIS(4,4)/SVP level of theory: diagonal (left) and off diagonal (right) elements.

transformation, see Fig.(8.11) left, also in this case are close in energy to the Frenkel states, even located below the highest LE state, at least for small y values. On the other hand, the off diagonal $D_e + D_h$ term (Fig.(8.11), right) takes a large value only around 0, while the minus combination keeps always smaller values. As a consequence, a couple of eigenvalues with the same symmetry (in this case the u, Fig.(8.12) top) remains close in energy due to the small $D_e - D_h$ coupling while the g are pushed far apart from the large $D_e + D_h$ coupling, especially around $y \simeq 0$. In particular the S_1 state (of g symmetry, green line) is much lower in energy than S_2 and, since V_{exc} is always different from zero, the overall result is that the first and the second excited states never cross, hence keeping for all the dimers H character despite the high degree of LE/CT mixing. In conclusion the excited state behavior along y does not show interesting properties as regard the switching from H to J. This property, in particular, is not expected to be sensitive to the methodology employed. For this reason y translation direction is not taken into account for further calculations. Nevertheless we note that the lowest energy of CT state, with respect to LE, can be again a key point to be considered when comparing CIS with higher level calculations.

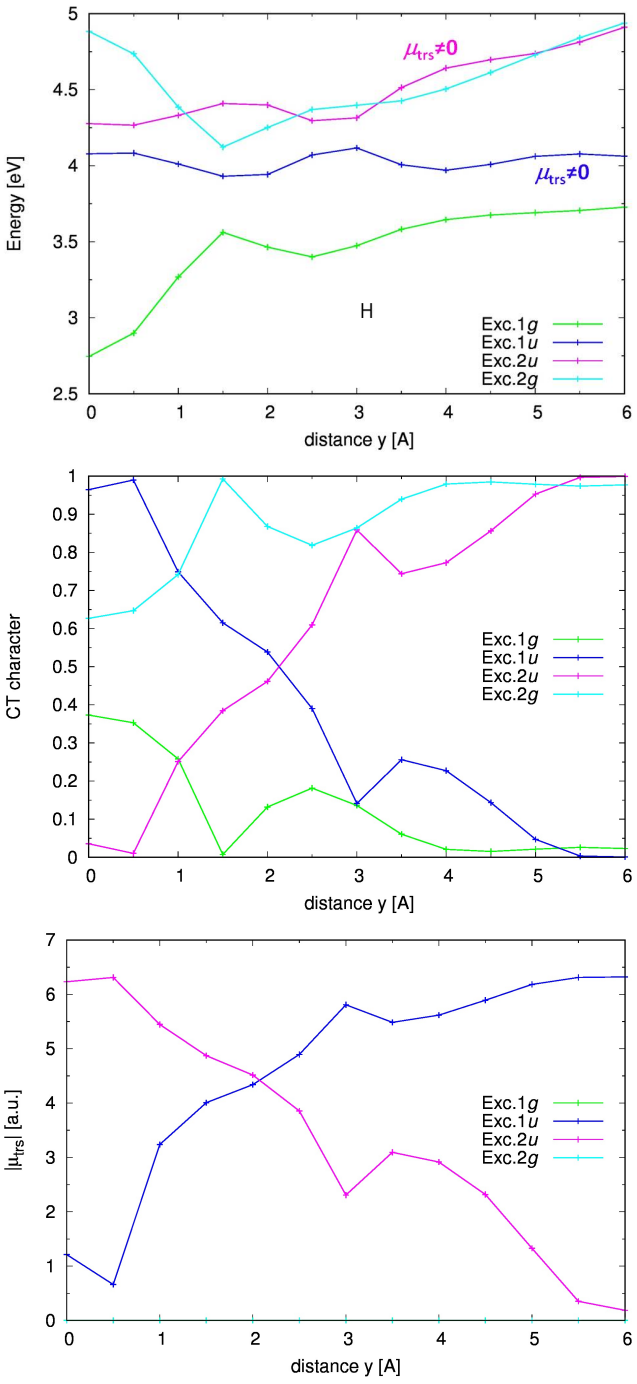

Figure 8.12: PBI dimer, fully diagonalized Hamiltonian along y translation at the CIS(4,4)/SVP level of theory: eigenvalues with H character (top), transition moments (middle) and CT character amount (bottom).

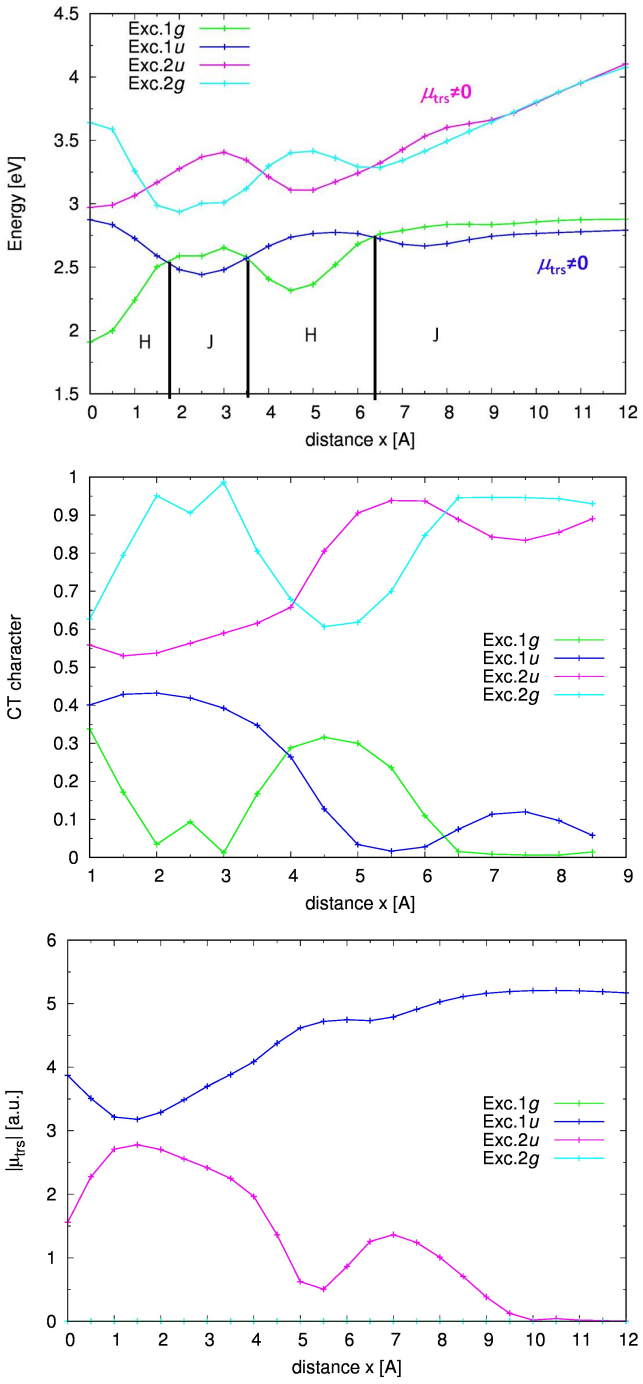

Figure 8.13: PBI dimer, fully diagonalized Hamiltonian along x translation at the CC2/TZVP level of theory: eigenvalues with H and J character (top), transition moments (middle) and CT character amount (bottom).

8.6.3 PBI dimers: CC2/TZVP calculations

The CIS(4,4) results have been validated with analogous calculations at a higher level of theory, namely CC2/TZVP. This method is expected to provide more reliable quantitative results and additionally, since it is a full electron methodology, allows to verify the reliability of the choice of including only the frontier orbitals in the CI expansion.

The excitation energy calculations for each dimer have been run with the *Turbomole* package, providing the energies, see Fig.(8.13) top, and the transition moments, see Fig.(8.13) bottom. The CT character is also obtained, Fig.(8.13) middle, by means of an analysis program set up by a collaborator [149].[1] The qualitative picture provided by CC2 is in very good agreement with CIS(4,4), cfr. Fig.(8.8): the three crossing points of the lowest energy states are recovered, along with a certain degree of character mixing. The only difference with respect to CIS(4,4) is represented by the missing crossing between the pink and blue lines in the CT character and transition moments plot. This means a lower degree of CT character in one of the lowest excited state (the blue one), never exceeding the 40% contribution to the wave function, and as a consequence a generally higher transition moment. The reasons behind these differences

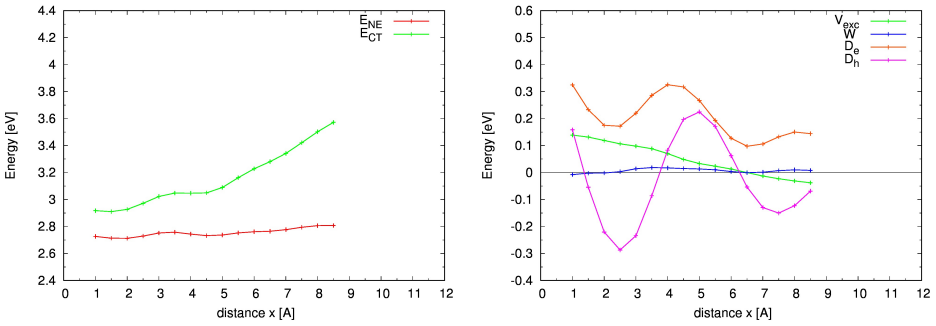

Figure 8.14: PBI dimer, elements of the localized matrix along x translation at the CC2/TZVP level of theory: diagonal (left) and off diagonal (right) elements.

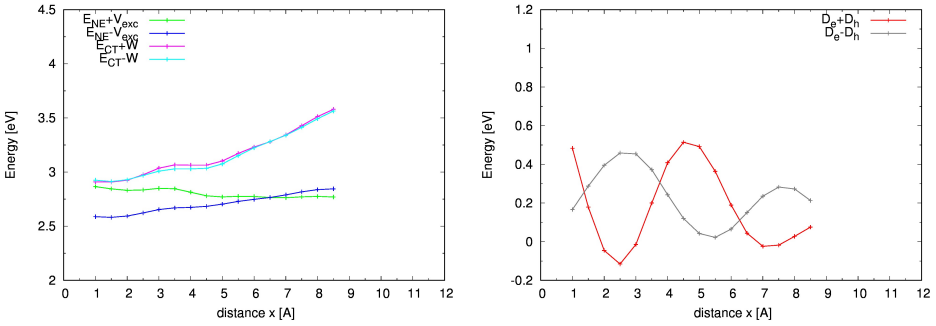

Figure 8.15: PBI dimer, elements of the partially localized (block) matrix along x translation at the CC2/TZVP: diagonal (left) and off diagonal (right) elements.

are evident from the inspection of the Hamiltonian matrix on the localized basis set. In fact the mentioned analysis program, starting from the transition amplitudes provided

[1] Thanks to Dr. Wenlan Liu, University of Stuttgart.

by the *Turbomole* standard calculations, builds a localized matrix analogous to the 4×4 CIS(4,4), Eq.(8.6). This analysis has been performed only for the central x sliding values, because of technical issues: the analysis program, is created to analyze only the first lowest energy excited states; however, for the smallest and biggest x sliding values, other eigenstates arising from the inclusion of double excitations appear at low energy, mixing up the analysis results. For this reason they have not been considered in the discussion. Interestingly, the curves of the diagonal elements E_{LE} and E_{CT}, see Fig.(8.14) left, do not cross, which is the most striking difference with CIS(4,4), Fig.(8.6). This implies a CT character mixing always lower than 50% and hence the absence of crossing in the curves of Fig.(8.13). CC2 calculation locates the CT configuration higher in energy than LE and this is due to the better description of the wave function and in particular to the inclusion of the correlation energy term. The Frenkel states (LE combinations in the block matrix, Fig.(8.15), left) lie lower in energy than the CT without crossing and the off diagonal $D_e \pm D_h$ couplings are generally smaller than the CIS ones (Fig.(8.15), right), but with an analogous profile. Consequently the lowest eigenvalues from the full orthogonalization retain a dominant Frenkel character, but still with some amount of CT mixing due to the non negligible $D_e \pm D_h$ coupling.

CIS(4,4) - CC2 Fitting. CIS(4,4) analytical eigenvalues are fitted to the CC2 excited states as described in Section 8.5. The resulting parameters are ($RMSD = 0.047$):

E_{LE}			E_{CT}			V_{exc}	W	D_e	D_h
a [eV]	α [eV]	β	b [eV]	γ [eV]	δ	c	d	e	f
1.088	-0.086	-0.045	1.548	0.409	-0.033	-0.417	-0.856	0.808	0.810

The fitted matrix elements of the localized Hamiltonian Eq.(8.23) are depicted in Fig.(8.17) superimposed to the CC2 parameters obtained by the *Turbomole* calculations, and already discussed. The values of the parameters help also to visualize the relation between the CIS(4,4) and CC2 results and the impact that the two different methodologies have on each term. In particular this highlights the extent of the CIS(4,4) energy overestimate. The downward shifts of the diagonal elements E_{LE} and E_{CT}, Fig.(8.17) left, are rather relevant (a, b > 1 eV), especially in relation to the CT state. The correcting Gaussian function for both states is very smooth (small β and δ) and particularly low in height for CT states (small γ), making the correlation effects for these configurations less sensitive to the distance dependence. Nevertheless, it is fundamental for a correct description of the states that would be way less accurate without it. The off-diagonal terms, see Fig.(8.17) right, are multiplied by factors having an absolute values less than 1. This is particularly true for V_{exc} which is reduced by more than 50% of its value (c $\simeq 0.4$), while the electron coupling terms D_e and D_h are much less sensitive to the lack of correlation (e, f $\simeq 0.8$).

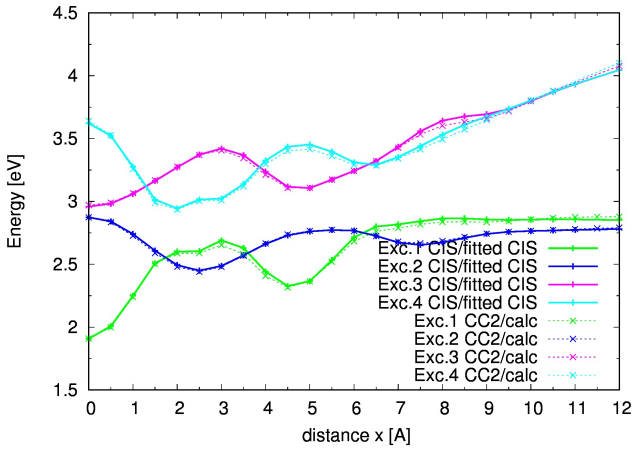

Figure 8.16: Fitted CIS(4,4) PBI dimer eigenvalues (solid line) to the computed CC2 ones (dashed lines).

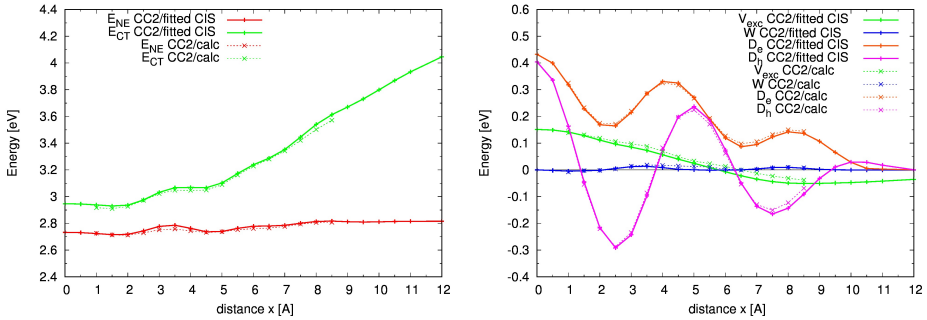

Figure 8.17: PBI dimer, fitted CIS(4,4) to the computed CC2 localized Hamiltonian matrix elements (solid line) to be compared to the computed CC2 ones (dashed lines).

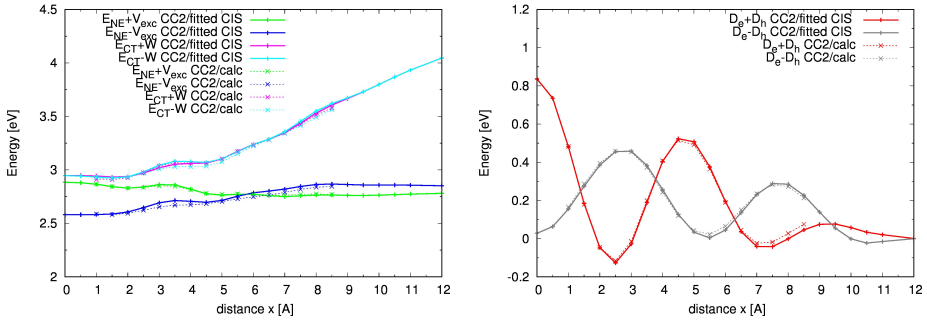

Figure 8.18: PBI dimer, fitted CIS(4,4) to the computed CC2 block Hamiltonian matrix elements (solid line) to be compared to the computed CC2 ones (dashed lines).

As a general conclusion, the CIS(4,4) calculation has a good agreement with the CC2, basically providing the same overall qualitative picture with alternating H and J dimer character along the x sliding. Quantitatively, the CC2 excitation energies and couplings are smaller, correcting the well known wrong tendency of CIS to overestimate the energies; this observation applies equally well to both the eigenvalues and the localized Hamiltonian elements. The availability of this latter matrix exactly computed through a localization procedure, allows to validate the fitting strategy, as an alternative way to extract the V_{exc}, W, D_e and D_h elements. The two methodologies provided results in good agreement, with a general difference of the order of $\simeq 0.01$ eV. Addi-

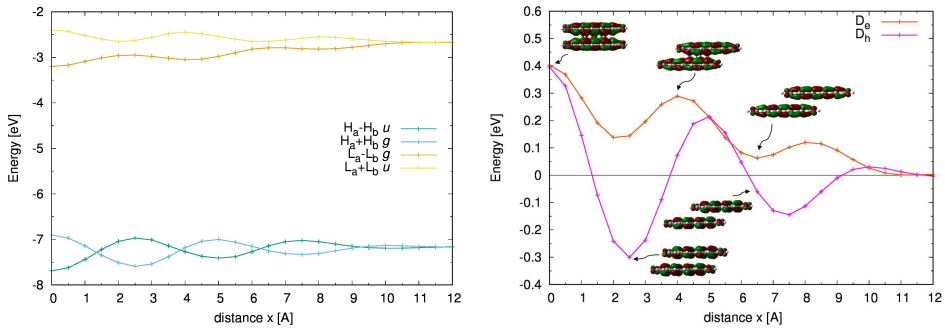

Figure 8.19: PBI dimers, energies of HOMO-1, HOMO, LUMO and LUMO+1 dimers orbitals, organized according to their linear combination (left) and D_e and D_h interactions (right).

tionally the fitting provides the missing values of Frenkel and CT states energies close to 0 sliding, see Fig.(8.18), showing the correct expected behavior according to which the Frenkel states lie lower in energy than the CTs.

8.6.4 PBI dimers: CAM-B3LYP/6-31G* calculations

As already discussed in Section 8.4, for TDDFT calculations we have not implemented the orbital localization available for CIS and CC2. Therefore the investigation is based on the excitation energies calculations and starts from the dimer orbitals analysis. By a graphical inspection it is verified that for all dimers geometries the dimer frontier orbitals are given by a linear combination of the monomers HOMOs (h_a,h_b) and LUMOs (l_a,l_b). The in phase combinations have the plus sign, while out of phase take the minus. Referring to the monomeric components of the dimer MOS, it is possible to assign the orbital symmetry. In particular the symmetry element taken into account is the inversion center i, since it is retained by the sliding operation and additionally it is related to the spectroscopic activity. The dimer orbitals symmetric with respect to i are labeled as g (gerade) while those antisymmetric are labeled u (ungerade). The energy of the dimer orbitals as a function of the x sliding, is collected in Fig.(8.19), left. For every geometry, the dimer LUMO and LUMO+1 are given by, respectively, the combination $l_a + l_b$ (g) and $l_a - l_b$ (u). In other words for every sliding value the combinations retain their relative energetic order and hence each orbital has the same symmetry for each x value. On the contrary, the combinations $h_a \pm h_b$ (of symmetry, respectively, g and u) vary their reciprocal energetic order along the x sliding. This is related to the intermolecular interactions between the molecular orbitals, identified by the D_h and D_e integrals, Fig.(8.19) right, and in particular to their sign, since the energy difference between the dimer orbitals provided by the same combination is roughly twice the integral:

$$\Delta E_{H/H-1} = |E_H - E_{H-1}| = 2D_h \qquad \Delta E_{L+1/L} = |E_{L+1} - E_L| = 2D_e.$$

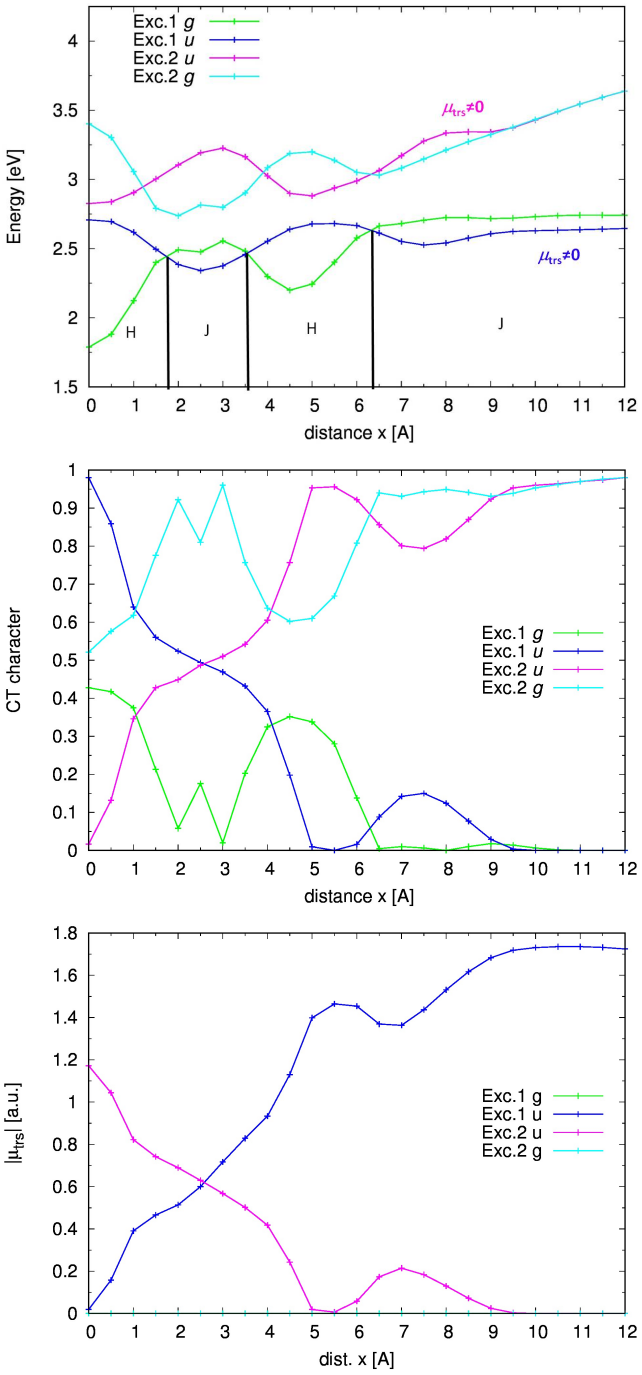

Figure 8.20: PBI dimers, fully diagonalized Hamiltonian eigenvalues with H and J character (top), transition moments (middle) and CT character amount (bottom) along x translation at the CAM-B3LYP/6-31G* level of theory.

As already pointed out, this interaction coincides with the electron coupling V_{el} employed for charge transfer studies, and hence it has been computed with the procedures described in Section 1.2; in this way it is also possible to visualize the dependence of the orbital overlap with the sliding along x. For $x = 0$ both molecular HOMOs and LUMOs orbitals have a favorable overlap. Increasing the sliding, the overlap is partially "dephased" decreases with an oscillating behavior, reflecting the dimer orbital oscillating energies, Fig.(8.19) left. However D_e always keeps its positive sign while D_h one changes several times. This effect is quite easy to be rationalized by inspecting the overlap geometries and the reciprocal phases orientation of the dimers orbitals. The effect of the D_h sign change is an inversion in the reciprocal order of the $h_a \pm h_b$ combinations, while this does not happen for LUMO and LUMO+1 since D_e remains positive.

The profile of the excitation energies, Fig.(8.20) top, reproduces with a close agreement the results of CC2 calculations, also quantitatively. The symmetry of the states is attributed by considering the symmetry of the orbitals involved in the transitions through the direct product: $g \times g = g$, $g \times u = u$. The symmetry of each transition, say for example $H \rightarrow L$, changes in correspondence to the symmetry changes of the $HOMO$ orbital, namely to the energy order exchange of the combinations. Therefore the excited state S_1 (the lowest state in energy), which is generally dominated by a $H \rightarrow L$ transition, undergoes a change in symmetry at every crossing with S_2. Indeed in Fig.(8.20) top, the states are organized according to the symmetry (as well as in the previous plots). A consequence concerns the transition probability to this state, since only the u state is bright (blue line): at every crossing the allowed state change the reciprocal order with the dark one and therefore the dimer character (H or J). The oscillator strength of the states, see Fig.(8.20) bottom, is not zero only for those of u symmetry and mirrors the amount CT character of each state, Fig.(8.20) middle. The CT character has been determined according to the procedure discussed in Section 8.6.4. Notably the CT character of the lowest u state is larger than 50% for small x displacements, similarly to CIS results and in sharp contrast with CC2 results.

CIS - CAM-B3LYP fitting. It is clear that the 4×4 model may be a good representation also for CAM-B3LYP results, since the lowest excited states of interest are dominated by transitions described by HOMO and LUMO molecular orbitals of the monomers. Therefore the fitting procedure has been applied, employing the $\boldsymbol{H}^{fit}$ of Eq.(8.23), namely we start from CIS model Hamiltonian parameters and change them to fit the eigenstates of CAM-B3LYP. The fitted eigenvalues resemble very closely the computed ones, Fig.(8.21), with the following choice of parameters ($RMSD = 0.023$):

E_{LE}			E_{CT}			V_{exc}	W	D_e	D_h
a [eV]	α [eV]	β	b [eV]	γ [eV]	δ	c	d	e	f
1.217	-0.039	-0.043	1.989	0.623	-0.020	-0.496	-1.324	0.732	0.781

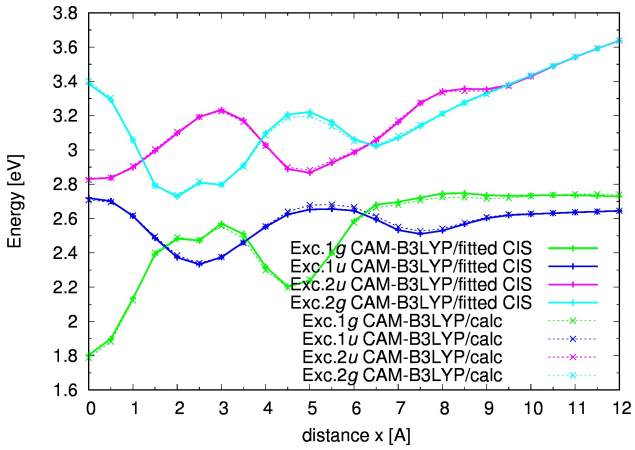

Figure 8.21: Fitted CIS(4,4) PBI dimer eigenvalues (solid line) to the computed CAM-B3LYP ones (dashed lines).

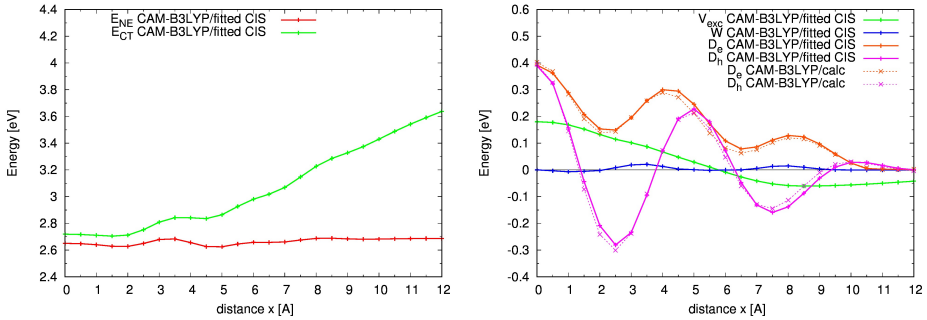

Figure 8.22: Fitted CIS(4,4) PBI dimer localized Hamiltonian matrix elements (solid line) to compared to the computed CAM-B3LYP ones (dashed lines).

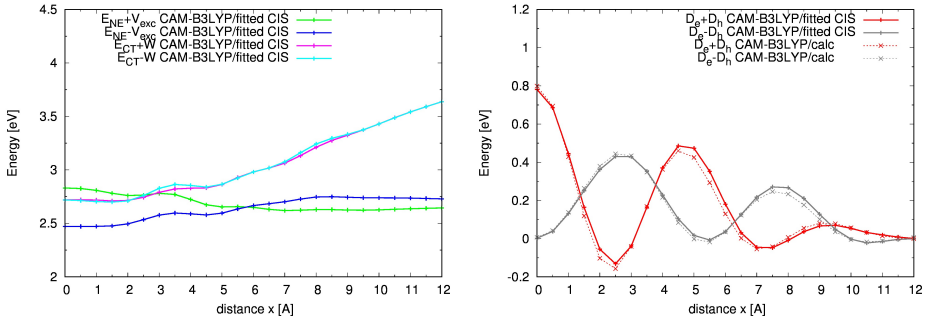

Figure 8.23: Fitted CIS(4,4) PBI dimer block Hamiltonian matrix elements (solid line) to compared to the computed CAM-B3LYP ones (dashed lines).

As a partial validation of the procedure, the fitted D_e and D_h couplings, Fig.(8.22) right, can be compared with the computed ones (already shown in Fig (8.19)) and they have a good agreement. Their values are quite close to the CC2 ones, see Fig.(8.17), as well as all the other parameters. Interestingly, the energies of the LE configurations are similar to the CC2 ones but CAM-B3LYP lowers significantly the energy of the CT configurations, keeping them closer to the LE energy than CC2 does, Fig.(8.23). As a consequence in the block matrix the CT combinations energies cross one of the Frenkel states, Fig.(8.23) left, creating a similar situation as for CIS, Fig.(8.7). This fact, together with the high values reached by the $D_e \pm D_h$ combinations, determines the strong CT/LE mixed character of the eigenstates, see Fig.(8.20) middle, observed

for CAM-B3LYP, rationalizing the difference from CC2, compare Fig.(8.13) middle.

In conclusion, CAM-B3LYP/6-31G* on the PBI dimers provides results in agreement with the higher level CC2 calculations, as far as energies are concerned. The global picture is similar to the CC2 one, with an alternation of H and J dimer character in correspondence of roughly the same geometries. However, similarly to CIS, CAM-B3LYP places the block diagonalized CT states below the LE, which implies a wrong description of the mixed CT-LE character in the final eigenstates. Additionally, the fitting procedure seems to be a reliable way to obtain the localized Hamiltonian elements otherwise not available and very useful for a more comprehensive rationalization of the eigenstates behavior. The only elements fo the localized matrix Hamiltonian available for CAM-B3LYP calculations are D_e and D_h, that can be computed as discussed in Section 1.2, a difference of the order of 0.01 eV, in line with the findings of the CC2 fitting.

Now, we plan to explore in the future the performance of additional functionals in order to see whether the problem of the inversion of CT/LE block diagonal states can be solved at TDDFT level.

Conclusions

My three years PhD activity was developed along two major lines of research: charge and energy transport, both based on the computational investigation of intramolecular properties and intermolecular interactions. In relation with energy transport, I also investigated the optical properties of condensed phase materials and how they evolve from those of isolated molecular components. To this end, on one side I developed some parts of software to compute specific properties, and on the other side I applied well established procedures and in house developed programs. The charge transport properties were investigated for several organic molecular crystals showing semiconducting properties, by computing microscopic parameters that govern these phenomena.

I have performed calculations of charge transport properties of several molecular organic semiconductors, whose experimental crystal structure and charge mobilities are available. I have modeled the electron transport properties in the crystal phase of a fluoro-alkyl NDI derivative (FNDI), a *n*-type semiconductor. Calculations of charge transfer rate constants according to the non-adiabatic hopping approach and propagation of the charge carriers within a KMC scheme lead to predicted charge mobilities of FNDI that compare very well with the experimental measurements in single-crystal devices. The marked anisotropy in the *bc* plane is nicely reproduced by the calculations and rationalized in terms of the available charge pathways displaying non-negligible electronic couplings.
As for *p*-type semiconductors, some members of the thienoacene family have been investigated. DBTDT molecule proved to be particularly interesting, due to the peculiar proximity of the HOMO-1 orbital to the HOMO, further enhanced by embedding effects, thereby indicating that charge carriers generated by the HOMO-1 orbital can become competitive with those generated by the HOMO. Indeed the inclusion of second highest occupied orbital was necessary to to explain the marked charge mobility anisotropy and more specifically the large mobility along *c* crystallographic axis. Additionally, I have shown that thermally induced disorder is responsible for the activation

of crossed electron couplings, justifying the generation of both charge carriers during charge propagation in the crystal. Interestingly, to the best of our knowledge, this is the first clear example of a non-degenerate HOMO-1 contribution to charge transport recognized by simulation. The investigation has been extended to the charge transport properties of other related thienoacenes, namely BBTT (the *syn* isomer of DBTDT) and C6-DBTDT (an alkylated derivative), that display however a larger energy difference between HOMO-1 and HOMO, in contrast with DBTDT: the role of the HOMO-1 orbital is considered to be negligible for the hole transport properties of BBTT while it might still contribute, to a minor extent, to the charge transport of C6-DBTDT. Charge mobilities simulated taking into account only the role of the HOMO charge carriers compare very well with the measured mobilities in single-crystal devices, pointing to an almost 1D charge transport especially larger for C6-DBTDT.
Finally the hole transport properties of two polymorphs of pentacene have been modeled, namely the single crystal and the thin film polymorph. Electronic couplings and site energies have been evaluated following the standard dimer approach but also considering the cluster approach, a scheme that I have implemented, in which the central molecule is surrounded by a large number of molecules quantum-chemically described and with an orthogonalization scheme limited to HOMO orbitals or employing the full basis of molecular orbitals. Couplings obtained both ways are relatively similar but not identical as a result of embedding effects and lead to similar predicted charge mobilities and anisotropies, in agreement with experimental data. The study allowed to conclude that the cluster approach with the orthogonalization limited to HOMO orbitals may be preferable to the dimer approach when embedding effects are not negligible.

In the framework of Förster theory, also energy transport is governed by intra and intermolecular properties of donor and acceptor molecules. In the Förster kinetic constant expression for energy transfer, the intramolecular properties are represented by the molecular spectral features, in particular by the overlap between the absorption and emission electronic spectra of, respectively, donor and acceptor molecules involved in the excitation transfer. In this regard, I have developed and successfully tested a code devoted to the simulation of linear absorption and emission spectra of a single molecule, comprising the underlying vibronic progression, starting from computed quantum mechanical properties. In particular, the resulting spectral overlap values are in line with those available in literature, and computed with the same model for different molecular systems.
As for the intermolecular interactions, they are represented by the electron and exciton couplings between donor and acceptor: the same interactions that drive the transport of charge are also involved in determining the energy transport and the optical properties in molecular aggregates. In this respect, I considered a simple molecular aggregate, namely a dimer formed by two perylene-bisimide (PBI) molecules, and I investigated the low lying electronic excited states for different configurations of the two molecules

in the dimer: according to a simple CIS(4,4) methodology, the excited states of PBI dimers, taken at different geometries varying along the x coordinate, show an alternation of H and J character. This behavior is determined not only by the exciton coupling V_{exc}, as expected according to the molecular exciton theory, but also by and interplay of the electron couplings D_e and D_h, that drive the mixing of charge transfer and locally excited configurations. A similar result is obtained with CC2 calculations and also with TDDFT employing long range corrected functionals. In this latter case the predicted energies are in very good agreement with CC2. Nevertheless we note that the lowest energy spectroscopically allowed excited state of the investigated dimers is dominated by a charge transfer character, according to CIS and TDDFT levels of theory. This results is in contrast with CC2 predictions and it is a crucial point that will have to be considered in future investigations.

APPENDIX A

Computational methods

A.1 CIS method

The Hartree-Fock (HF) is a method for the computation of electronic ground state based on a multideterminantal wave function. Its multielectron wave function, Ψ_0, is built as a Slater determinant over the Fock spinorbitals $\{\varphi\}$, determined by the Fock equations [146]. The ground state energy E_0 is computed as the expectation value of the system Hamiltonian $\hat{H}$:

$$E_0 = \langle\Psi_0|\hat{H}|\Psi_0\rangle = \sum_i \langle\varphi_i|\hat{h}|\varphi_i\rangle + \frac{1}{2}\sum_{i,j}\big[\langle\varphi_i\varphi_i|\varphi_j\varphi_j\rangle - \langle\varphi_i\varphi_j|\varphi_i\varphi_j\rangle\big] \tag{A.1}$$

where $\hat{h}$ is the monoelectronic operator as defined in Ref. [146] and the second and the third therm represent, respectively, the Coulomb and exchange integrals of the inter-electron interaction [146]. The Hartree-Fock method provides ground state energy and molecular orbitals in the approximation that the electron-electron interactions is described in an average fashion (mean-field approximation) [146, 168]. As a consequence, what is lacking is the correlation energy, accounting for the real electron-electron interaction.

To tackle this issue and hence improve the standard HF results, a multideterminantal wave function can be employed, as a linear combination of Slater determinants Ψ_i weighted on the $\{c_i\}$ coefficients:

$$\Psi = \sum_i c_i\Psi_i = c_0\Psi_0 + \sum_s c_s\Psi_s + \sum_d c_d\Psi_d + \sum_t c_t\Psi_t + ... \tag{A.2}$$

Each Slater determinant is built on the Hartree-Fock monoelectronic functions (namely the molecular orbitals $\{\varphi\}$) computed with the standard HF method, and kept fixed in

each excited determinant. One determinant coincides with the HF wave function (Ψ_0) and, by replacing occupied MOs with unoccupied ones, a set of excited determinants can be generated: they are singly (Ψ_s), doubly (Ψ_d), triply (Ψ_t), etc., excited determinants, classified on the number of empty MOs that substituted the occupied ones in Ψ_0.

The corresponding Schrödinger equation to be solved can be formulated in matrix form. The coefficients of the expansion in Eq.(A.2) can be collected in the $\boldsymbol{C}$ matrix and the system to be solved is a set of CI secular equations [146]:

$$(\boldsymbol{H} - E\boldsymbol{I})\boldsymbol{C} = 0. \tag{A.3}$$

where $\boldsymbol{H}$ is the Hamiltonian matrix, E the diagonal matrix of the eigenvalues and $\boldsymbol{I}$ the identity matrix. Solving this equation is equivalent to diagonalizing the Hamiltonian matrix. The lowest eigenvalue corresponds to the ground state energy, while the higher ones to the excited states, and the eigenvectors are the set of coefficients identifying each state.

The elements of the CI Hamiltonian matrix can be expanded in terms of integrals over the molecular orbitals, governed by the Slater-Condon rules [126]. These rules state that:

- if two determinants entering the integral are identical (in the diagonal matrix elements), that integral coincides with the expectation value of the single determinant wave function;
- determinants differing by more than two MOs have a null matrix element;
- the reference HF determinant (Ψ_0) does not mix with the singly excited ones, i.e., the corresponding elements are zero (*Brillouin theorem*). Consequently the singly excited determinants do not mix directly with the ground state, and hence have only a small indirect effect on its energy by mixing with the doubles that interact with Ψ_0. On the other hand, the singles play a very important role in the excited states.

As a consequence the CI matrix acquires a block diagonal form. A computationally feasible application of the CI method requires a truncation of the number of excited determinants included in the wave function expansion. The simplest approximation is the CIS truncation including only the singly excited determinants. This method does not provide any significant improvement in the ground state HF results, due to the Brillouin theorem, however it can be used for excited state calculations: the higher roots provide singly excited states. Additionally, also the space of the orbitals in which the excitations are generated can be limited, as it is done in the CIS(4,4) method presented in Section 8.2.

A.2 CC2 method

The Coupled Cluster theory (CC) is, similarly to CI, a method based on a multideterminantal wave function. The excited state determinants are generated by the action of the excitation operator $\hat{T}$:

$$\hat{T} = \hat{T}_1 + \hat{T}_2 + \hat{T}_3 + ... = \sum_i \hat{T}_i \tag{A.4}$$

and each term $\hat{T}_i$ acts on a Hartree-Fock reference Slater determinant Ψ_{HF}, generating the ith excited Slater configuration:

$$\begin{aligned} \hat{T}_1 \Psi_{HF} &= \sum_a^{occ} \sum_r^{virt} t_a^r \Psi_a^r \\ \hat{T}_2 \Psi_{HF} &= \frac{1}{2} \sum_{a,b}^{occ} \sum_{r,s}^{virt} t_{ab}^{rs} \Psi_{ab}^{rs}. \end{aligned} \tag{A.5}$$

The expansion coefficients t represent the weights of each configuration analogously to the coefficients of the CI expansion. The complete CC wave function is defined as:

$$\Psi_{CC} = e^{\hat{T}} \Psi_{HF} \tag{A.6}$$

where the exponential term can be expressed in terms of its Taylor expansion:

$$e^{\hat{T}} = 1 + \hat{T}_1 + (\hat{T}_2 + \tfrac{1}{2}\hat{T}_1^2) + (\hat{T}_3 + \hat{T}_2\hat{T}_1 + \tfrac{1}{6}\hat{T}_1^3) + ... \tag{A.7}$$

The first term of the expansion leaves the reference Ψ_{HF} ground state unchanged and the second generates the singly excited states. Each parenthesis in Eq. (A.7) collects the terms generating a given i excitation: the terms $\hat{T}_i$ represent the "connected excitations" corresponding to i electrons interacting simultaneously, while the other terms gathering into products or powers represent the "disconnected" excitations of non-interacting groups of interacting electrons. Therefore the CC wave function, compared to the CI, contains also additional terms given by the products of excitations. Eq.(A.6) is introduced into Schrödinger equation:

$$\hat{H} e^{\hat{T}} |\Psi_{HF}\rangle = E e^{\hat{T}} |\Psi_{HF}\rangle \,, \tag{A.8}$$

that has to be solved with respect to the energy and the amplitudes. A manifold of equations is set up, left projecting onto each excited state determinant Ψ_i:

$$\begin{aligned} E_{CC} &= \langle \Psi_{HF} | \hat{H} e^{\hat{T}} | \Psi_{HF} \rangle \\ E_{CC} \langle \Psi_i | e^{\hat{T}} | \Psi_{HF} \rangle &= \langle \Psi_i | \hat{H} e^{\hat{T}} | \Psi_{HF} \rangle \,. \end{aligned} \tag{A.9}$$

To simplify and decouple the equations, a similarity transformed Hamiltonian is defined as [169]:

$$\hat{H}^T = e^{-\hat{T}} \hat{H} e^{\hat{T}} \tag{A.10}$$

that inserted in Eq.(A.9) gives:

$$\begin{aligned} E_{CC} &= \langle \Psi_{HF} | \hat{H}^T | \Psi_{HF} \rangle \\ 0 &= \langle \Psi_i | \hat{H}^T | \Psi_{HF} \rangle \,. \end{aligned} \tag{A.11}$$

$\hat{H}^T$ can be Taylor expanded and, after a proper truncation, it is obtained the so called BCH (Baker-Campbell-Hausdorff) expansion [169]:

$$\hat{H}^T = \hat{H} + [\hat{H}, \hat{T}] + \tfrac{1}{2!}[[\hat{H}, \hat{T}], \hat{T}] + ... \tag{A.12}$$

The projected energy expression by substituting in Eq.(A.11) finally is:

$$E_{CC} = E_{HF} + \langle \Psi_{HF} | [\hat{H}, \hat{T}_2] | \Psi_{HF} \rangle + \tfrac{1}{2} \langle \Psi_{HF} | [[\hat{H}, \hat{T}_1], \hat{T}_1] | \Psi_{HF} \rangle \,; \tag{A.13}$$

the equation in this form highlights that only singles and doubles amplitudes contribute directly to the energy, but in turn they depend on all the other amplitudes. Analogously the BCH expansion is applied to the amplitude equations, giving a set of coupled non-linear equations, at most quartic in the amplitudes:

$$\begin{aligned} 0 &= \langle \boldsymbol{\Psi_i} | \hat{H}^T | \Psi_{HF} \rangle \\ &= \langle \boldsymbol{\Psi_i} | \hat{H} | \Psi_{HF} \rangle + \langle \boldsymbol{\Psi_i} | [\hat{H}, \hat{T}] | \Psi_{HF} \rangle + \tfrac{1}{2!} \langle \boldsymbol{\Psi_i} | [[\hat{H}, \hat{T}], \hat{T}] | \Psi_{HF} \rangle \\ &\quad + \tfrac{1}{3!} \langle \boldsymbol{\Psi_i} | [[[\hat{H}, \hat{T}], \hat{T}], \hat{T}] | \Psi_{HF} \rangle + \tfrac{1}{4!} \langle \boldsymbol{\Psi_i} | [[[[\hat{H}, \hat{T}], \hat{T}], \hat{T}], \hat{T}] | \Psi_{HF} \rangle \,. \end{aligned} \tag{A.14}$$

The solution of the set of CC wave function is self-consistent. It is introduced the vector of residuals of the amplitude equations $\boldsymbol{\Omega}$:

$$\Omega_i(\boldsymbol{t}) = \langle \Psi_i | e^{-\hat{T}} \hat{H} e^{\hat{T}} | \Psi_{HF} \rangle \tag{A.15}$$

and its Jacobian matrix details how it responds to change on the amplitudes. By minimizing the $\boldsymbol{\Omega}$ value, the optimum set of amplitudes is obtained. A truncation of $\hat{T}$ is necessary to solve the set of equations in Eq.(A.11). Each simplification represents a specific coupled cluster model.

Additionally the Hamiltonian is split into two parts, a zeroth order reference and a small perturbation:

$$\hat{H} = \hat{H}_0 + \hat{V} \tag{A.16}$$

and, in analogy with Møller Plesset (MP) development, $\hat{H}_0$ corresponds to the Fock operator $\hat{F}$ of the system and the perturbation represent the interelectron interaction. The Hamiltonian in Eq.(A.16) is substituted in the CC Eq.(A.11) which, after the

symmetry transformation in Eq.(A.10) becomes:

$$(\hat{F}^T + \hat{V}^T)\,|\Psi_{HF}\rangle = E\,|\Psi_{HF}\rangle \tag{A.17}$$

The terms in Eq.(A.17) are expanded in the order of the perturbation. The energy is:

$$E^{(n)} = \sum_{n}^{\infty} E^{(n)} \tag{A.18}$$

and also similarly the operator (A.16) is expanded. By collecting the terms of (n)th order in the perturbation and projecting on $|\Psi_{HF}\rangle$ and $|\Psi_i\rangle$, the CC perturbation expressions of energy and amplitudes are:

$$E^{(n)} = \langle\Psi_{HF}|\hat{V}^{T^{(n)}}|\Psi_{HF}\rangle \qquad t_i^{(n)} = -\frac{\langle\Psi_i|\hat{V}^{T^{(n)}}|\Psi_{HF}\rangle}{E_i}. \tag{A.19}$$

The excitations present at each order n of perturbation are determined by the amplitude expressions. In general the nth order excitations enter the order $n-1$, with the exception of the singles that enter at second order, because of the Brillouin theorem. Notice that this result is the same as for MP theory. The solution of the amplitude equations is obtained recursively up to a certain given order n.

One of the most widely employed CC methods is CCSD (Coupled Clustes Singles and Doubles). I this case T is truncated as $\hat{T} = \hat{T}_1 + \hat{T}_2$, which coincides to include the single and double excitations. In this case the energy of Eq.(A.13) in terms of the amplitudes and the MOs ϕ corresponds to:

$$E_{CC} = E_{HF} + \sum_{a,b}^{occ}\sum_{r,s}^{virt}\left[t_{ab}^{rs} + t_a^r t_b^s\right]\left[2\,\langle\phi_r\phi_a|\phi_s\phi_b\rangle - \langle\phi_s\phi_a|\phi_r\phi_b\rangle\right]. \tag{A.20}$$

The amplitudes equations (A.11) are developed in doubles and singles contributions. The Hamiltonian is once again simplified by a similarity transformation:

$$e^{-\hat{T}_2-\hat{T}_1}\hat{H}e^{\hat{T}_1+\hat{T}_2} = e^{-\hat{T}_2}\hat{\bar{H}}e^{\hat{T}_2} \tag{A.21}$$

and the resulting $\hat{\bar{H}}$ operator is in its "T_1-transformed" form. The CCSD amplitudes equations for singles and doubles are then:

$$\begin{aligned} \langle\Psi_1|\hat{\bar{H}}|\Psi_{HF}\rangle + \langle\Psi_1|[\hat{\bar{H}},\hat{T}_2]|\Psi_{HF}\rangle &= 0 \\ \langle\Psi_2|\hat{\bar{H}}|\Psi_{HF}\rangle + \langle\Psi_2|[\hat{\bar{H}},\hat{T}_2]|\Psi_{HF}\rangle + \tfrac{1}{2}\,\langle\Psi_2|[[\hat{\bar{H}},\hat{T}_2],\hat{T}_2]|\Psi_{HF}\rangle &= 0 \end{aligned} \tag{A.22}$$

The introduction of the perturbative development in CCSD leads to amplitude equations containing corrections to the singles and doubles to second order in $\hat{V}$, and so the resulting wave function is correct to first order. In particular, in the equations of the doubles amplitudes , there are terms corresponding to second order corrections.

The CC2 model is obtained by approximating the CCSD amplitude equations as

follows: the singles are retained in their original form, since they are assigned to be of zeroth order in $\hat{V}$; the doubles are approximated to be correct through first order only (the singles are treated as zeroth order parameters). Thus the equations become:

$$\begin{aligned} \langle \Psi_1 | \hat{\bar{H}} + [\hat{\bar{H}}, \hat{T}_2] | \Psi_{HF} \rangle = 0 \\ \langle \Psi_2 | \hat{\bar{H}} + [\hat{F}, \hat{T}_2] | \Psi_{HF} \rangle = 0 \end{aligned} . \tag{A.23}$$

The t_2 amplitudes may be expressed directly in terms of the t_1 amplitudes and MOs integrals. The iterative procedure therefore involves only the t_1 amplitudes. The operators are in their T_1-transformed forms, which is a convenient way to retain the singles in the equations. Indeed the singles, although they don't have a direct impact on the calculated energy of the system, provide approximate orbital relaxation to the correlation and to external perturbation. Indeed they are necessary to derive response functions, such that excitation energies and transition moments can be defined. So CC2 may be defined loosely as MP2, but including in addition the orbital relaxation arising from the singles. The energy is then correct to second order and has about the same quality as the MP2 energy because the singles do not give any direct contribution to the energy. The wave function has an intermediate quality between the CCS and CCSD. So with respect to CIS, this method is much more sophisticated, since it includes additionally the electron correlation and partially the double excitations. The inclusion of singles in the CC2 model improves the energy and makes it possible to determine the response functions, allowing the definition of excitation energies and transition moments. They are obtained by considering the system as perturbed by a time-dependent one electron perturbation:

$$\hat{H} = \hat{H}_0 + \hat{V}_t \tag{A.24}$$

where $\hat{H}_0$ is the 0th order time independent Hamiltonian and $\hat{V}_t$ the time dependent perturbation in the form of an oscillating wave [170]. The time evolution of the CC2 parameters in the presence of external perturbations are:

$$\begin{aligned} \langle \Psi_1 | \hat{\bar{H}} + [\hat{\bar{H}}, \hat{T}_2] | \Psi_{HF} \rangle = i \frac{\partial t_1}{\partial t} \\ \langle \Psi_2 | \hat{\bar{H}} + [\hat{F} + \hat{V}_t, \hat{T}_2] | \Psi_{HF} \rangle = i \frac{\partial t_2}{\partial t} . \end{aligned} \tag{A.25}$$

The solution of these time-dependent equations provides the excited state energies. Usually CC2 calculations are run with the resolution of the identity (RI) approximation, that applies an additional projection on an auxiliary basis set of functions. RI represents a computational simplification of the integral calculation, leading to important computational savings [168]. It is also introduced the spin-component-scaling (SCS), further improving the quality of the results without additional cost [168, 171, 172].

A.3 DFT methods

DFT. A system of N_e interacting electrons is described by the Hamiltonian [126]:

$$\begin{aligned}\hat{H} &= -\frac{1}{2}\sum_i \nabla^2 + \frac{1}{2}\sum_{i\neq j}\frac{1}{|\boldsymbol{r}_i - \boldsymbol{r}_j|} + \sum_i V(\boldsymbol{r}_i) \\ &= \hat{K}_e + \hat{V}_{ee} + \hat{V}_{eN}\end{aligned} \tag{A.26}$$

already assuming the Born-Oppenheimer approximation and neglecting the internuclear term. The $\hat{K}_e$ term represents the kinetic energy of the electrons, $\hat{V}_{eN}$ is the term responsible for the electron-nucleus interactions and $\hat{V}_{ee}$ the electron electron interaction. Due to this last term it is not possible an exact solution of the Schrödinger equation for a system of interacting electrons. Density Functional Theory (DFT) in order to simplify the problem, introduces the electron density distribution $\rho(\boldsymbol{r})$ defined as:

$$\rho(\boldsymbol{r}) = N_e \int |\Psi(\boldsymbol{r}, \boldsymbol{r}_2, ..., \boldsymbol{r}_{N_e})|^2 d\boldsymbol{r}_2 ... d\boldsymbol{r}_{N_e} \tag{A.27}$$

computed on the multielectron wave function Ψ and integrated on the electron coordinates $\boldsymbol{r}$. The energy of the system is the expectation value and represents a functional of the $V(\boldsymbol{r})$ potential, in terms of the electron density $\rho(\boldsymbol{r})$ [126]:

$$\begin{aligned}E[V] &= \langle\Psi|\hat{K}_e + \hat{V}_{ee} + \hat{V}|\Psi\rangle \\ &= \left[\langle\Psi|\hat{K}_e + \hat{V}_{ee}|\Psi\rangle + \int \rho(\boldsymbol{r})V(\boldsymbol{r})dr\right].\end{aligned} \tag{A.28}$$

The functional derivative of $E[V]$ with respect to $V(\boldsymbol{r})$ is computed by exploiting the Hellmann-Feynman theorem; it provides $\rho(\boldsymbol{r})$ and it is a monotonic function, which is an important property, also in relation to the definition of a variational principle (see below). As a consequence, a biunivocal mapping between the potential $V(\boldsymbol{r})$ and the charge density $\rho(\boldsymbol{r})$ holds [151]:

$$\rho(\boldsymbol{r}) = \frac{\partial E}{\partial V(\boldsymbol{r})} \leftrightarrow V(\boldsymbol{r}). \tag{A.29}$$

The above equation means that the density distributions of systems with different $V(\boldsymbol{r})$ potentials are also different and the ground state electronic properties can be determined through the electron density (first Hohenberg-Kohn theorem). The energy $E[V]$ of the system with $\rho(\boldsymbol{r})$ density can be obtained variationally (second Hohenberg-Kohn theorem) [173]:

$$\begin{aligned}E[V] &= \min\left[\langle\Psi|\hat{K}_e + \hat{V}_{ee}|\Psi\rangle + \int \rho(\boldsymbol{r})V(\boldsymbol{r})dr\right] \\ &= \min\left[F[\rho] + \int \rho(\boldsymbol{r})V(\boldsymbol{r})dr\right]\end{aligned} \tag{A.30}$$

through the minimization of the $F[\rho]$ term ("Hohenberg-Kohn functional"), collecting the electron kinetic energy and the interelectron interaction, plus the integral involving the potential $V(\boldsymbol{r})$.

So far the theory is exact, but the introduction of a number of assumptions is necessary in order to make the equations solvable. The most widely used method relies on the approximations introduced by Kohn and Sham [174]. The strategy is to consider an ansatz for which it is possible to compute the terms in $E[V]$: a reference system is chosen composed of non-interacting electrons having the same density as the investigated real system (and hence the same $V(\boldsymbol{r})$ potential). In this case $F[\rho]$ of Eq.(A.30) can be expanded into the sum of terms:

$$F[\rho] = T_{ref}[\rho] + \frac{e^2}{2}\int \frac{\rho(\boldsymbol{r}_1)\rho(\boldsymbol{r}_2)}{|\boldsymbol{r}_1 - \boldsymbol{r}_2|} d\boldsymbol{r}_1 d\boldsymbol{r}_2 + E_{xc}[\rho] \tag{A.31}$$

where T_{ref} represents the kinetic energy of the reference system, and the second integral the electrostatic self-interaction of a classical charge density distribution, i.e, the Coulombian interaction $J[\rho]$. The term E_{xc} includes the difference between kinetic energy and $e-e$ interaction computed for the real system and those of the non interacting reference one; in other words it represents everything that cannot be exactly computed:

$$E_{xc} = (T[\rho] - T_{ref}[\rho]) + (V_{ee}[\rho] - J[\rho]). \tag{A.32}$$

The solution of the variational problem proceeds using the Lagrange multipliers method, requiring the differentiation with respect to $\rho(\boldsymbol{r})$ and the equation to the λ multiplier:

$$\frac{\partial T_0}{\partial \rho(\boldsymbol{r})} + V(\boldsymbol{r}) + \int \frac{\rho(\boldsymbol{r'})}{|\boldsymbol{r} - \boldsymbol{r'}|} dr' + \frac{\partial E_{xc}}{\partial \rho(\boldsymbol{r})} = \lambda \quad \leftrightarrow \quad \frac{\partial T_0}{\partial \rho(\boldsymbol{r})} + V_{KS}(\boldsymbol{r}) = \lambda. \tag{A.33}$$

The equation represents the variational principle for the reference system of non interacting electrons with the *effective* potential V_{KS}. For such a system, the application of the variational principle leads to solve a set of N_e monoelectronic equations known as Kohn-Sham equations [174]:

$$\left(-\frac{1}{2}\nabla^2 + V_{KS}\right)\varphi_i(\boldsymbol{r}) = \epsilon_i \varphi_i(\boldsymbol{r}). \tag{A.34}$$

The equations provide the set of monoelectronic functions $\{\varphi_i(\boldsymbol{r})\}$ (Kohn-Sham orbitals) with eigenvalues ϵ. The reference density which was, by hypothesis, identical to the real system density $\rho(\boldsymbol{r})$ in this mono-electronic framework can be computed as:

$$\rho(\boldsymbol{r}) = \sum_i |\varphi_i(\boldsymbol{r})|^2. \tag{A.35}$$

Finally the energy of the system is given by:

$$E[V] = \sum_i \epsilon_i - \frac{1}{4}\int \frac{\rho(\boldsymbol{r})\rho(\boldsymbol{r'})}{|\boldsymbol{r} - \boldsymbol{r'}|} d\boldsymbol{r'} + E_{xc}[\rho] + \int \frac{\partial E_{xc}}{\partial \rho(\boldsymbol{r})}\rho(\boldsymbol{r}) d\boldsymbol{r} \tag{A.36}$$

with a similar expression to that of the Hartree-Fock method, beside the xc term. Then most of the deal is about a proper choice of the exchange-correlation functional E_{xc}. Since it cannot be exactly computed, it must be defined on the basis of some physical considerations. A wide variety of functionals are available in literature and in order to run a DFT calculation it must be carefully chosen, depending on the system under investigation and on the type of properties of interest.

TDDFT. Since DFT method is only suitable for ground state calculations, Time Dependent DFT (TDDFT) is the related density-based approach to the calculation of excited-state properties. The ground state DFT results represent the starting point for the excited state calculation and this methodology provides the excitation energies and oscillator strengths along with other related properties. The formalism of DFT described so far was developed for time independent wave functions and for TDDFT an analogous theoretical model is generalized to time dependent systems. The Runge-Gross theorem defines the correspondence between a time-dependent electron density and the functional, similarly to the first Hohenberg-Kohn theorem [175]:

$$\rho(\boldsymbol{r},t) \leftrightarrow V(\boldsymbol{r},t). \tag{A.37}$$

Additionally, also in this case, a variational principle is ensured, allowing to rewrite the Kohn Sham equations in a time dependent formalism (TD-KS) [150]:

$$i\frac{\partial}{\partial t}\varphi_i(\boldsymbol{r},t) = \left(-\frac{1}{2}\nabla_i^2 + V(\boldsymbol{r},t) + \int \frac{\rho(\boldsymbol{r'},t)}{|\boldsymbol{r}-\boldsymbol{r'}|}dr + \frac{\partial E_{xc}[\rho]}{\partial\rho(\boldsymbol{r},t)}\right)\varphi_i(\boldsymbol{r},t) \tag{A.38}$$

providing a single particle picture that allows to compute the density $\rho(\boldsymbol{r},t)$ as:

$$\rho(\boldsymbol{r},t) = \sum_i |\varphi_i(\boldsymbol{r},t)|^2. \tag{A.39}$$

Also the TD case requires the introduction of an exchange-correlation functional E_{xc}, collecting all the terms that cannot be exactly computed, in a similar philosophy as for DFT.

The most widely used technique employed in order to obtain the excitation energies and oscillator strengths from the solution of the TD-KS equations, is the Linear Response TDDFT. In this case it is considered an oscillatory time-dependent external field perturbing the system, represented by a monochromatic radiation with ω frequency and V_0 amplitude:

$$V_{PT} = V_0(\boldsymbol{r})e^{i\omega t}. \tag{A.40}$$

If the perturbation is weak compared to the internal electric fields caused by the ions, as it usually is in linear spectroscopy experiments, the induced change in the density can be described within perturbation theory considering only the first order (linear) response of the system; in other words, the response is linearly dependent on the applied perturbation. After some algebra and Fourier transformation from the time to the

energy domain one arrives to the Casida equation, that takes the form of a non-hermitian eigenvalue equation [150, 151]:

$$\begin{bmatrix} A & B \\ B^* & A^* \end{bmatrix} \begin{bmatrix} X \\ Y \end{bmatrix} = E \begin{bmatrix} 1 & 0 \\ 0 & -1 \end{bmatrix} \begin{bmatrix} X \\ Y \end{bmatrix}. \tag{A.41}$$

where

$$\begin{aligned} B_{ar,bs} &= \int \varphi_a(\boldsymbol{r}_1)\varphi_r(\boldsymbol{r}_1)\frac{1}{|\boldsymbol{r}_1 - \boldsymbol{r}_2|}\varphi_s(\boldsymbol{r}_2)\varphi_b(\boldsymbol{r}_2)d\boldsymbol{r}_1 d\boldsymbol{r}_2 \\ &\quad + \int \varphi_a(\boldsymbol{r}_1)\varphi_r(\boldsymbol{r}_1)\frac{\partial E_{xc}}{\partial\rho(\boldsymbol{r}_1)\partial\rho(\boldsymbol{r}_2)}\varphi_s(\boldsymbol{r}_2)\varphi_b(\boldsymbol{r}_2)d\boldsymbol{r}_1 d\boldsymbol{r}_2. \\ A_{ar,bs} &= \delta_{ab}\delta_{rs}(\epsilon_r - \epsilon_a) + B_{ar,sb} \end{aligned} \tag{A.42}$$

Similarly as for a CI wave function, the elements of the matrix require the calculation of integrals involving the KS orbitals in which the excitations happen: φ_a, φ_b represent ground state occupied KS orbitals while φ_r, φ_s virtual ones, each with its energy ϵ. $\boldsymbol{X}$ and $\boldsymbol{Y}$ represent the eigenvectors and are, respectively, excitations and deexcitations, mixed in the matrix equation by the B term; the final wave function is multideterminantal, given by a linear combination of excited configurations.

The iterative solution of Eq.(A.41) provides the excitation (and deexcitation) energies contained in the eigenvalues E matrix, along with the eigenvectors (the electronic states). In principle in TDDFT formalism, the E_{xc} functional depends on the perturbation frequency ω, making the Casida equation non linear. A common simplification is to neglect this dependency (adiabatic approximation), such that the Casida equations are linear and it is possible to employ the standard ground state xc functionals [151]. An additional consequence of the adiabatic approximation and the linearization of Casida equations is the neglect of the doubles and in general the multiple excitations in the wave functions. In this framework the structure of Casida equation is closely related to CIS and TDHF. In analogy with CIS only single excitations are described with TDDFT. States with a substantial double excitation character cannot be satisfactorily treated in linear response theory with the adiabatic approximation. With respect to CIS, that is based on a HF ground state wave function, in TDDFT the correlation is included already in the DFT ground state through the xc functional. Generally, the excitation energies of TDDFT are expected to be far more accurate than CIS: for the first the error is about 0.1-0.5 eV compared to 1 or more eV of the latter [150].

Bibliography

[1] Brédas, J.-L.; Norton, J. E.; Cornil, J.; Coropceanu, V. *Acc. Chem. Res.* **2009**, *42*(11), 1691–1699.

[2] Kippelen, B.; Bredas, J.-L. *Energy Environ. Sci.* **2009**, *2*, 251–261.

[3] Sundström, V.; Pullerits, T. o.; van Grondelle, R. *J. Phys. Chem. B* **1999**, *103*(13), 2327–2346.

[4] Romero, E.; Novoderezhkin, Vladimir I. ans van Grondelle, R. *Nature* **2017**, *543*, 355–365.

[5] Brédas, J.-L.; Beljonne, D.; Coropceanu, V.; Cornil, J. *Chem. Rev.* **2004**, *104*(11), 4971–5004.

[6] Ostroverkhova, O. *Chem. Rev.* **2016**, *116*(22), 13279–13412.

[7] Deibel, C.; Strobel, T.; Dyakonov, V. *Adv. Mater.* **2010**, *22*(37), 4097–4111.

[8] Barbara, P. F.; Meyer, T. J.; Ratner, M. A. *J. Phys. Chem.* **1996**, *100*(31), 13148–13168.

[9] Coropceanu, V.; Cornil, J.; da Silva Filho, D. A.; Olivier, Y.; Silbey, R.; Brédas, J.-L. *Chem. Rev.* **2007**, *107*(4), 926–952.

[10] Troisi, A. *Chem. Soc. Rev.* **2011**, *40*, 2347–2358.

[11] May, V.; Kühn, O. *Charge and Energy Transfer Dynamics in Molecular Systems;* Wiley-VCH, 2004.

[12] Jortner, J. *J. Chem. Phys.* **1976**, *64*(12), 4860–4867.

[13] Marcus, R. A. Jul **1993**, *65*, 599–610.

[14] Newton, M. D. *Chem. Rev.* **1991**, *91*(5), 767–792.

[15] Senthilkumar, K.; Grozema, F. C.; Bickelhaupt, F. M.; Siebbeles, L. D. A. *J. Chem. Phys.* **2003**, *119*(18), 9809–9817.

[16] Valeev, E. F.; Coropceanu, V.; da Silva Filho, D. A.; Salman, S.; Brédas, J.-L. *J. Am. Chem. Soc.* **2006**, *128*(30), 9882–9886.

[17] Koopmans, T. *Physica* **1934**, *1*(1), 104–113.

[18] Troisi, A.; Orlandi, G. *Chem. Phys. Lett.* **2001**, *344*(5–6), 509–518.

[19] Li, H.; Brédas, J.-L.; Lennartz, C. *J. Chem. Phys.* **2007**, *126*(16), 164704.

[20] Knowles, D. B.; Munn, R. W. *J. Mater. Sci. - Mater. Electron.* **1994**, *5*(2), 89–93.

[21] Ide, J.; Fazzi, D.; Casalegno, M.; Meille, S. V.; Raos, G. *J. Mater. Chem. C* **2014**, *2*, 7313–7325.

[22] Norton, J. E.; Brédas, J.-L. *J. Am. Chem. Soc.* **2008**, *130*(37), 12377–12384.

[23] Ryno, S. M.; Lee, S. R.; Sears, J. S.; Risko, C.; Brédas, J.-L. *J. Phys. Chem. C* **2013**, *117*(27), 13853–13860.

[24] Lipparini, F.; Mennucci, B. *J. Chem. Phys.* **2007**, *127*(14), 144706.

[25] D'Avino, G.; Mothy, S.; Muccioli, L.; Zannoni, C.; Wang, L.; Cornil, J.; Beljonne, D.; Castet, F. *J. Phys. Chem. C* **2013**, *117*(25), 12981–12990.

[26] Kitoh-Nishioka, H.; Ando, K. *Chem. Phys. Lett.* **2015**, *621*, 96–101.

[27] Löwdin, P. *J. Chem. Phys.* **1950**, *18*(3), 365–375.

[28] Löwdin, P.-O. Vol. 5 of *Advances in Quantum Chemistry;* Academic Press, 1970; pages 185–199.

[29] Baumeier, B.; Kirkpatrick, J.; Andrienko, D. *Phys. Chem. Chem. Phys.* **2010**, *12*, 11103–11113.

[30] Canola, S.; Pecoraro, C.; Negri, F. *Chem. Phys.* **2016**, *478*, 130–138.

[31] Gaussian 09 revision d.01. Frisch, M. J.; Trucks, G. W.; Schlegel, H. B.; Scuseria, G. E.; Robb, M. A.; Cheeseman, J. R.; Scalmani, G.; Barone, V.; Mennucci, B.; Petersson, G. A.; Nakatsuji, H.; Caricato, M.; Li, X.; Hratchian, H. P.; Izmaylov, A. F.; Bloino, J.; Zheng, G.; Sonnenberg, J. L.; Hada, M.; Ehara, M.; Toyota, K.; Fukuda, R.; Hasegawa, J.; Ishida, M.; Nakajima, T.; Honda, Y.; Kitao, O.; Nakai, H.; Vreven, T.; Montgomery Jr., J. A.; Peralta, J. E.; Ogliaro, F.; Bearpark, M.; Heyd, J. J.; Brothers, E.; Kudin, K. N.; Staroverov, V. N.; Kobayashi, R.; Normand, J.; Raghavachari, K.; Rendell, A.; Burant, J. C.; Iyengar, S. S.; Tomasi, J.; Cossi, M.; Rega, N.; Millam, J. M.; Klene, M.; Knox, J. E.; Cross, J. B.; Bakken, V.; Adamo, C.; Jaramillo, J.; Gomperts, R.; Stratmann, R. E.; Yazyev,

O.; Austin, A. J.; Cammi, R.; Pomelli, C.; Ochterski, W. J.; Martin, R. L.; Morokuma, K.; Zakrzewski, V. G.; Voth, G. A.; Salvador, P.; Dannenberg, J. J.; Dapprich, S.; Daniels, A. D.; Farkas, .; Foresman, J. B.; Ortiz, J. V.; Cioslowski, J.; Fox, D. J.

[32] Di Donato, E.; Fornari, R. P.; Di Motta, S.; Li, Y.; Wang, Z.; Negri, F. *J. Phys. Chem. B* **2010**, *114*(16), 5327–5334.

[33] Martinelli, N. G.; Savini, M.; Muccioli, L.; Olivier, Y.; Castet, F.; Zannoni, C.; Beljonne, D.; Cornil, J. *Adv. Funct. Mater.* **2009**, *19*(20), 3254–3261.

[34] McMahon, D. P.; Troisi, A. *J. Phys. Chem. Lett.* **2010**, *1*(6), 941–946.

[35] Negri, F.; Orlandi, G. In *Computational Photochemistry*; Olivucci, M., Ed., Vol. 16 of *Theoretical and Computational Chemistry;* Elsevier, 2005; pages 129–169.

[36] Troisi, A.; Orlandi, G. *J. Phys. Chem. A* **2006**, *110*(11), 4065–4070.

[37] Martinelli, N. G.; Olivier, Y.; Athanasopoulos, S.; Ruiz Delgado, M.-C.; Pigg, K. R.; da Silva Filho, D. A.; Sánchez-Carrera, R. S.; Venuti, E.; Della Valle, R. G.; Brédas, J.-L.; Beljonne, D.; Cornil, J. *ChemPhysChem* **2009**, *10*(13), 2265–2273.

[38] Coropceanu, V.; Sánchez-Carrera, R. S.; Paramonov, P.; Day, G. M.; Brédas, J.-L. *J. Phys. Chem. C* **2009**, *113*(11), 4679–4686.

[39] Zhao, Y.; Brown, D. W.; Lindenberg, K. *J. Chem. Phys.* **1997**, *106*(7), 2728–2740.

[40] Canola, S.; Negri, F. *Phys. Chem. Chem. Phys.* **2014**, *16*, 21550–21558.

[41] Cuppen, H. M.; Karssemeijer, L. J.; Lamberts, T. *Chem. Rev.* **2013**, *113*(12), 8840–8871.

[42] Voter, A. F. In *Radiation effects in solids;* Springer, 2007; pages 1–23.

[43] Fichthorn, K. A.; Weinberg, W. H. *J. Chem. Phys.* **1991**, *95*(2), 1090–1096.

[44] Van Kampen, N. *Stochastic Processes in Physics and Chemistry*, North-Holland Personal Library; Elsevier Science, 2011.

[45] Kwiatkowski, J. J.; Nelson, J.; Li, H.; Bredas, J. L.; Wenzel, W.; Lennartz, C. *Phys. Chem. Chem. Phys.* **2008**, *10*, 1852–1858.

[46] Deng, W.-Q.; Goddard, W. A. *J. Phys. Chem. B* **2004**, *108*(25), 8614–8621.

[47] Allinger, N. L.; Yuh, Y. H.; Lii, J. H. *J. Am. Chem. Soc.* **1989**, *111*(23), 8551–8566.

[48] TINKER - Software Tools for Molecular Design. Ponder, J. W.

[49] Berendsen, H. J. C.; Postma, J. P. M.; van Gunsteren, W. F.; DiNola, A.; Haak, J. R. *J. Chem. Phys.* **1984**, *81*(8), 3684–3690.

[50] Lv, A.; Li, Y.; Yue, W.; Jiang, L.; Dong, H.; Zhao, G.; Meng, Q.; Jiang, W.; He, Y.; Li, Z.; Wang, Z.; Hu, W. *Chem. Commun.* **2012**, *48*, 5154–5156.

[51] Jiang, L.; Gao, J.; Wang, E.; Li, H.; Wang, Z.; Hu, W.; Jiang, L. *Adv. Mater.* **2008**, *20*(14), 2735–2740.

[52] Anthony, J. E.; Facchetti, A.; Heeney, M.; Marder, S. R.; Zhan, X. *Adv. Mater.* **2010**, *22*(34), 3876–3892.

[53] Zhan, X.; Facchetti, A.; Barlow, S.; Marks, T. J.; Ratner, M. A.; Wasielewski, M. R.; Marder, S. R. *Adv. Mater.* **2011**, *23*(2), 268–284.

[54] Würthner, F.; Stolte, M. *Chem. Commun.* **2011**, *47*, 5109–5115.

[55] Bhosale, S. V.; Bhosale, S. V.; Bhargava, S. K. *Org. Biomol. Chem.* **2012**, *10*, 6455–6468.

[56] Li, Y.; Xu, W.; Di Motta, S.; Negri, F.; Zhu, D.; Wang, Z. *Chem. Commun.* **2012**, *48*, 8204–8206.

[57] Yue, W.; Lv, A.; Gao, J.; Jiang, W.; Hao, L.; Li, C.; Li, Y.; Polander, L. E.; Barlow, S.; Hu, W.; Di Motta, S.; Negri, F.; Marder, S. R.; Wang, Z. *J. Am. Chem. Soc.* **2012**, *134*(13), 5770–5773.

[58] Gsänger, M.; Oh, J.; Könemann, M.; Höffken, H.; Krause, A.-M.; Bao, Z.; Würthner, F. *Angew. Chem. Int. Ed.* **2010**, *49*(4), 740–743.

[59] Fabiano, S.; Wang, H.; Piliego, C.; Jaye, C.; Fischer, D. A.; Chen, Z.; Pignataro, B.; Facchetti, A.; Loo, Y.-L.; Loi, M. A. *Adv. Funct. Mater.* **2011**, *21*(23), 4479–4486.

[60] Katz, H. E.; Lovinger, A. J.; Johnson, J.; Kloc, C.; Siegrist, T.; Li, W.; Lin, Y. Y.; Dodabalapur, A. *Nature* **2000**, *404*(6777), 478–481.

[61] Katz, H. E.; Johnson, J.; Lovinger, A. J.; Li, W. *J. Am. Chem. Soc.* **2000**, *122*(32), 7787–7792.

[62] Shukla, D.; Nelson, S. F.; Freeman, D. C.; Rajeswaran, M.; Ahearn, W. G.; Meyer, D. M.; Carey, J. T. *Chem. Mater.* **2008**, *20*(24), 7486–7491.

[63] He, T.; Stolte, M.; Würthner, F. *Adv. Mater.* **2013**, *25*(48), 6951–6955.

[64] Lee, W.-Y.; Oh, J. H.; Suraru, S.-L.; Chen, W.-C.; Würthner, F.; Bao, Z. *Adv. Funct. Mater.* **2011**, *21*(21), 4173–4181.

[65] Oh, J. H.; Suraru, S.; Lee, W.-Y.; Könemann, M.; Höffken, H. W.; Röger, C.; Schmidt, R.; Chung, Y.; Chen, W.-C.; Würthner, F.; Bao, Z. *Adv. Funct. Mater.* **2010**, *20*(13), 2148–2156.

[66] Geng, Y.; Wu, S.-X.; Li, H.-B.; Tang, X.-D.; Wu, Y.; Su, Z.-M.; Liao, Y. *J. Mater. Chem.* **2011**, *21*, 15558–15566.

[67] Di Motta, S.; Siracusa, M.; Negri, F. *J. Phys. Chem. C* **2011**, *115*(42), 20754–20764.

[68] Fazzi, D.; Castiglioni, C.; Negri, F. *Phys. Chem. Chem. Phys.* **2010**, *12*, 1600–1609.

[69] Deng, W.-Q.; Goddard, W. A. *J. Phys. Chem. B* **2004**, *108*(25), 8614–8621.

[70] Stehr, V.; Pfister, J.; Fink, R. F.; Engels, B.; Deibel, C. *Phys. Rev. B* **2011**, *83*, 155208.

[71] Olivier, Y.; Muccioli, L.; Lemaur, V.; Geerts, Y. H.; Zannoni, C.; Cornil, J. *J. Phys. Chem. B* **2009**, *113*(43), 14102–14111.

[72] Nelson, J.; Kwiatkowski, J. J.; Kirkpatrick, J.; Frost, J. M. *Acc. Chem. Res.* **2009**, *42*(11), 1768–1778.

[73] Shuai, Z.; Geng, H.; Xu, W.; Liao, Y.; Andre, J.-M. *Chem. Soc. Rev.* **2014**, *43*, 2662–2679.

[74] Canola, S.; Negri, F. *J. Phys. Chem. C* **2015**, *119*(21), 11499–11505.

[75] Jiang, W.; Li, Y.; Wang, Z. *Chem. Soc. Rev.* **2013**, *42*, 6113–6127.

[76] Wang, C.; Dong, H.; Hu, W.; Liu, Y.; Zhu, D. *Chem. Rev.* **2012**, *112*(4), 2208–2267.

[77] Takimiya, K.; Osaka, I.; Mori, T.; Nakano, M. *Acc. Chem. Res.* **2014**, *47*(5), 1493–1502.

[78] Barbarella, G.; Zambianchi, M.; Bongini, A.; Antolini, L. *Adv. Mater.* **1993**, *5*(11), 834–838.

[79] Li, R.; Dong, H.; Zhan, X.; He, Y.; Li, H.; Hu, W. *J. Mater. Chem.* **2010**, *20*, 6014–6018.

[80] Gao, J.; Li, R.; Li, L.; Meng, Q.; Jiang, H.; Li, H.; Hu, W. *Adv. Mater.* **2007**, *19*(19), 3008–3011.

[81] Li, R.; Jiang, L.; Meng, Q.; Gao, J.; Li, H.; Tang, Q.; He, M.; Hu, W.; Liu, Y.; Zhu, D. *Adv. Mater.* **2009**, *21*(44), 4492–4495.

[82] Okamoto, T.; Kudoh, K.; Wakamiya, A.; Yamaguchi, S. *Org. Lett.* **2005**, *7*(23), 5301–5304.

[83] Takimiya, K.; Shinamura, S.; Osaka, I.; Miyazaki, E. *Adv. Mater.* **2011**, *23*(38), 4347–4370.

[84] Li, R.; Dong, H.; Zhan, X.; Li, H.; Wen, S.-H.; Deng, W.-Q.; Han, K.-L.; Hu, W. *J. Mater. Chem.* **2011**, *21*, 11335–11339.

[85] Zhang, S.-F.; Chen, X.-K.; Fan, J.-X.; Ren, A.-M. *Org. Electron.* **2013**, *14*(2), 607–620.

[86] He, P.; Tu, Z.; Zhao, G.; Zhen, Y.; Geng, H.; Yi, Y.; Wang, Z.; Zhang, H.; Xu, C.; Liu, J.; Lu, X.; Fu, X.; Zhao, Q.; Zhang, X.; Ji, D.; Jiang, L.; Dong, H.; Hu, W. *Adv. Mater.* **2015**, *27*(5), 825–830.

[87] Atahan-Evrenk, S.; Aspuru-Guzik, A. *Top. Curr. Chem.* **2014**, *345*, 95.

[88] D'Avino, G.; Mothy, S.; Muccioli, L.; Zannoni, C.; Wang, L. J.; Cornil, J.; Beljonne, D.; Castet, F. *J. Phys. Chem. C* **2013**, *117*, 12981.

[89] Ryno, S. M.; Lee, S. R.; Sears, J. S.; Risko, C.; Bredas, J. L. *J. Phys. Chem. C* **2013**, *117*, 13853.

[90] Ide, J.; Fazzi, D.; Casalegno, M.; Meille, S. V.; Raos, G. *J. Mater. Chem. C* **2014**, *2*, 7313.

[91] Canola, S.; Negri, F. *Phys. Chem. Chem. Phys.* **2014**, *16*, 21550–21558.

[92] Canola, S.; Pecoraro, C.; Negri, F. *Theor. Chem. Acc.* **2016**, *135*(2), 33.

[93] Li, R.; Hu, W.; Liu, Y.; Zhu, D. *Acc. Chem. Res.* **2010**, *43*(4), 529–540.

[94] Miyata, Y.; Yoshikawa, E.; Minari, T.; Tsukagoshi, K.; Yamaguchi, S. *J. Mater. Chem.* **2012**, *22*, 7715–7717.

[95] Di Motta, S.; Di Donato, E.; Negri, F.; Orlandi, G.; Fazzi, D.; Castiglioni, C. *J. Am. Chem. Soc.* **2009**, *131*(18), 6591–6598.

[96] Mattheus, C. C.; Dros, A. B.; Baas, J.; Meetsma, A.; Boer, J. L. d.; Palstra, T. T. M. *Acta Crystallogr., Sect. C* **2001**, *57*(8), 939–941.

[97] Mattheus, C. C.; Dros, A. B.; Baas, J.; Oostergetel, G. T.; Meetsma, A.; de Boer, J. L.; Palstra, T. T. *Synth. Met.* **2003**, *138*(3), 475–481.

[98] Siegrist, T.; Besnard, C.; Haas, S.; Schiltz, M.; Pattison, P.; Chernyshov, D.; Batlogg, B.; Kloc, C. *Adv. Mater.* **2007**, *19*(16), 2079–2082.

[99] Campbell, R. B.; Robertson, J. M.; Trotter, J. *Acta Crystallogr.* **1961**, *14*(7), 705–711.

[100] Schiefer, S.; Huth, M.; Dobrinevski, A.; Nickel, B. *J. Am. Chem. Soc.* **2007**, *129*(34), 10316–10317.

[101] Yoshida, H.; Inaba, K.; Sato, N. *Appl. Phys. Lett.* **2007**, *90*(18), 181930.

[102] Ohtomo, M.; Suzuki, T.; Shimada, T.; Hasegawa, T. *Appl. Phys. Lett.* **2009**, *95*(12), 123308.

[103] Lee, J. Y.; Roth, S.; Park, Y. W. *Appl. Phys. Lett.* **2006**, *88*(25), 252106.

[104] Deng, W.-Q.; Goddard, W. A. *J. Phys. Chem. B* **2004**, *108*(25), 8614–8621.

[105] Troisi, A.; Orlandi, G. *J. Phys. Chem. B* **2005**, *109*(5), 1849–1856.

[106] Yoshida, H.; Sato, N. *Phys. Rev. B* **2008**, *77*, 235205.

[107] Yin, S.; Lv, Y. *Org. Elec.* **2008**, *9*(5), 852–858.

[108] Wen, S.-H.; Li, A.; Song, J.; Deng, W.-Q.; Han, K.-L.; Goddard, W. A. *J. Phys. Chem. B* **2009**, *113*(26), 8813–8819.

[109] Nguyen, T. P.; Shim, J. H.; Lee, J. Y. *J. Phys. Chem. C* **2015**, *119*(21), 11301–11310.

[110] Jurchescu, O. D.; Baas, J.; Palstra, T. T. M. *Appl. Phys. Lett.* **2004**, *84*(16), 3061–3063.

[111] Hatch, R. C.; Huber, D. L.; Höchst, H. *Phys. Rev. B* **2009**, *80*, 081411.

[112] de Wijs, G. A.; Mattheus, C. C.; de Groot, R. A.; Palstra, T. T. *Synth. Met.* **2003**, *139*(1), 109–114.

[113] D'Avino, G.; Muccioli, L.; Zannoni, C.; Beljonne, D.; Soos, Z. G. *J. Chem. Theory Comput.* **2014**, *10*(11), 4959–4971.

[114] Levi, F.; Mostarda, S.; Rao, F.; Mintert, F. *Rep. Prog. Phys.* **2015**, *78*(8), 082001.

[115] Förster, T. *Naturwissenschaften* **1946**, *6*, 166–175.

[116] Förster, T. *Annalen der Physik* **1948**, *437*(1-2), 55–75.

[117] Redfield, A. In *Advances in Magnetic Resonance*; Waugh, J. S., Ed., Vol. 1 of *Advances in Magnetic and Optical Resonance;* Academic Press, 1965; pages 1–32.

[118] Yang, M.; Fleming, G. R. *Chem. Phys.* **2002**, *275*(1-3), 355–372.

[119] Curutchet, C.; Mennucci, B. *Chem. Rev.* **2017**, *117*(2), 294–343.

[120] van Grondelle, R.; Novoderezhkin, V. I. *Phys. Chem. Chem. Phys.* **2006**, *8*, 793–807.

[121] Renger, T. *Photosynth. Res.* **2009**, *102*(2), 471–485.

[122] Stehr, V.; Engels, B.; Deibel, C.; Fink, R. F. *J. Chem. Phys.* **2014**, *140*(2), 024503.

[123] Athanasopoulos, S.; Emelianova, E. V.; Walker, A. B.; Beljonne, D. *Phys. Rev. B* **2009**, *80*, 195209.

[124] Stehr, V. *Prediction of charge and energy transport in organic crystals with quantum chemical protocols employing the hopping model* PhD thesis, Julius-Maximilians-Universität Würzburg, **2015**.

[125] Hennebicq, E.; Pourtois, G.; Scholes, G. D.; Herz, L. M.; Russell, D. M.; Silva, C.; Setayesh, S.; Grimsdale, A. C.; Müllen, K.; Brédas, J.-L.; Beljonne, D. *J. Am. Chem. Soc.* **2005**, *127*(13), 4744–4762.

[126] Atkins, P.; Ronald, F. *Molecular Quantum Mechanics;* Oxford University Press, 2011.

[127] York, A. P. N., London., Eds.; *The Molecular Exciton Model*, **1963**.

[128] Kasha, M.; Rawls, H.; Ashraf El-Bayoumi, M. *Pure Appl. Chem.* **1965**, *11*, 371–392.

[129] Beljonne, D.; Cornil, J.; Silbey, R.; Millié, P.; Brédas, J. L. *J. Chem. Phys.* **2000**, *112*(10), 4749–4758.

[130] Chang, J. C. *J. Chem. Phys.* **1977**, *67*(9), 3901–3909.

[131] Krueger, B. P.; Scholes, G. D.; Fleming, G. R. *J. Phys. Chem. B* **1998**, *102*(27), 5378–5386.

[132] Czader, A.; Bittner, E. R. *J. Chem. Phys.* **2008**, *128*(3), 035101.

[133] Davydov, A. S. *Theory of Molecular Excitons;* Mc-Graw-Hill, New York, 1962.

[134] Gierschner, J.; Park, S. Y. *J. Mater. Chem. C* **2013**, *1*, 5818–5832.

[135] Spano, F. C. *Acc. Chem. Res.* **2010**, *43*(3), 429–439.

[136] Würthner, F.; Kaiser, T. E.; Saha-Möller, C. R. *Angew. Chem. Int. Ed.* **2011**, *50*(15), 3376–3410.

[137] Duschinsky, F. *Acta Physicochim. URSS* **1937**, *7*, 551.

[138] Sando, G.; Spears, K. *J. Phys. Chem. A* **2001**, *105*(22), 5326–5333.

[139] Reimers, J. R. *J. Chem. Phys.* **2001**, *115*(20), 9103–9109.

[140] Negri, F.; Orlandi, G. *Electronic and vibronic spectra of molecular systems: models and simulations based on quantum chemically computed molecular parameters;* M. Olivucci Ed., Elsevier, 2005.

[141] Ballhausen, C. *Molecular Electronic Structures of Transition Metal Complexes;* McGraw-Hill, 1979.

[142] Press, W.; Teukolsky, S.A.and Vetterling, W.; Flannery, B. *Numerical Recipes;* Cambridge University Press, 1992.

[143] Lee, S. K.; Zu, Y.; Herrmann, A.; Geerts, Y.; Müllen, K.; Bard, A. J. *J. Am. Chem. Soc.* **1999**, *121*(14), 3513–3520.

[144] Petelenz, P. *Chem. Phys. Lett.* **1977**, *47*(3), 603 – 605.

[145] Improta, R.; Santoro, F.; Barone, V.; Lami, A. *J. Phys. Chem. A* **2009**, *113*(52), 15346–15354.

[146] Szabo, A.; Ostlund, N. S. *Modern Quantum Chemistry: Introduction to Advanced Electronic Structure Theory;* Dover Publications, Inc.: Mineola, first ed., 1996.

[147] Pipek, J.; Mezey, P. G. *J. Chem. Phys.* **1989**, *90*(9), 4916–4926.

[148] TURBOMOLE V6.2 2010, a development of University of Karlsruhe and Forschungszentrum Karlsruhe GmbH, 1989-2007, TURBOMOLE GmbH, since 2007; available from `http://www.turbomole.com`.

[149] Liu, W.; Lunkenheimer, B.; Settels, V.; Engels, B.; Fink, R. F.; Köhn, A. *J. Chem. Phys.* **2015**, *143*(8).

[150] Dreuw, A.; Head-Gordon, M. *Chem. Rev.* **2005**, *105*(11), 4009–4037.

[151] Ullrich, C. A.; Yang, Z.-h. *ArXiv* **2013**.

[152] Dreuw, A.; Weisman, J. L.; Head-Gordon, M. *J. Chem. Phys.* **2003**, *119*(6), 2943–2946.

[153] Friese, D. H.; Hättig, C.; Ruud, K. *Phys. Chem. Chem. Phys.* **2012**, *14*, 1175–1184.

[154] Beerepoot, M. T. P.; Friese, D. H.; List, N. H.; Kongsted, J.; Ruud, K. *Phys. Chem. Chem. Phys.* **2015**, *17*, 19306–19314.

[155] Shirai, S.; Iwata, S.; Tani, T.; Inagaki, S. *J. Phys. Chem. A* **2011**, *115*(26), 7687–7699.

[156] Casanova, D. *Int. J. Quantum Chem.* **2015**, *115*(7), 442–452.

[157] Schubert, A.; Settels, V.; Liu, W.; Würthner, F.; Meier, C.; Fink, R. F.; Schindlbeck, S.; Lochbrunner, S.; Engels, B.; Engel, V. *J. Phys. Chem. Lett.* **2013**, *4*(5), 792–796.

[158] Settels, V.; Schubert, A.; Tafipolski, M.; Liu, W.; Stehr, V.; Topczak, A. K.; Pflaum, J.; Deibel, C.; Fink, R. F.; Engel, V.; Engels, B. *J. Am. Chem. Soc.* **2014**, *136*(26), 9327–9337.

[159] Würthner, F.; Kaiser, T. E.; Saha-Möller, C. R. *Angew. Chem. Int. Ed.* **2011**, *50*(15), 3376–3410.

[160] Kaiser, T.; Wang, H.; Stepanenko, V.; Würthner, F. *Angew. Chem. Int. Ed.* **2007**, *46*(29), 5541–5544.

[161] Li, X.-Q.; Zhang, X.; Ghosh, S.; Würthner, F. *Chem. Eur. J.* **2008**, *14*(27), 8074–8078.

[162] Marciniak, H.; Li, X.-Q.; Würthner, F.; Lochbrunner, S. *J. Phys. Chem. A* **2011**, *115*(5), 648–654.

[163] Hestand, N. J.; Spano, F. C. *J. Chem. Phys.* **2015**, *143*(24), 244707.

[164] Hestand, N. J.; Kazantsev, R. V.; Weingarten, A. S.; Palmer, L. C.; Stupp, S. I.; Spano, F. C. *J. Am. Chem. Soc.* **2016**, *138*(36), 11762–11774.

[165] Liu, W.; Settels, V.; Harbach, P. H. P.; Dreuw, A.; Fink, R. F.; Engels, B. *J. Comput. Chem.* **2011**, *32*(9), 1971–1981.

[166] Liu, W.; Lunkenheimer, B.; Settels, V.; Engels, B.; Fink, R. F.; Köhn, A. *J. Chem. Phys.* **2015**, *143*(8), 084106.

[167] Hestand, N. J.; Spano, F. C. *Acc. Chem. Res.* **2017**, *50*(2), 341–350.

[168] Jensen, F. *Introduction to Computational Chemistry;* John Wiley & Sons, 2006.

[169] Helgaker, T.; Jørgensen, P.; Olsen, J. *Molecule Electronic-Structure Theory;* John Wiley & Sons, 2012.

[170] Christiansen, O.; Koch, H.; Jørgensen, P. *Chem. Phys. Lett.* **1995**, *243*(5), 409 – 418.

[171] Hellweg, A.; Grun, S. A.; Hättig, C. *Phys. Chem. Chem. Phys.* **2008**, *10*, 4119–4127.

[172] Grimme, S.; Goerigk, L.; Fink, R. F. *Wiley Interdiscip. Rev. Comput. Mol. Sci.* **2012**, *2*(6), 886–906.

[173] Hohenberg, P.; Kohn, W. *Phys. Rev.* **1964**, *136*, B864–B871.

[174] Kohn, W.; Sham, L. J. *Phys. Rev.* **1965**, *140*, A1133–A1138.

[175] Runge, E.; Gross, E. K. U. *Phys. Rev. Lett.* **1984**, *52*, 997–1000.

List of Publications

Canola S., Pecoraro C. and Negri F. *Chem. Phys.*, **2016**, *478*, 130-138
"Dimer and cluster approach for the evaluation of electronic couplings governing charge transport: Application to two pentacene polymorphs"

Canola S., Pecoraro C. and Negri F. *Theor. Chem. Acc.*, **2016**, *135(2)*, 33
"Modelling p-type charge transport of thienoacene analogues of pentacene"

Canola S. and Negri F. *J. Phys. Chem. C*, **2015**, *119(21)*, 11499-11505
"Role of the HOMO-1 Orbital on the p-Type Charge Transport of the Fused-Ring Thienoacene DBTDT"

Canola S. and Negri F. *Phys. Chem. Chem. Phys.*, **2014**, *16*, 21550-21558
"Anisotropy of the n-type charge transport and thermal effects in crystals of a fluoro-alkylated naphthalene diimide: a computational investigation"

List of oral presentations

2016 *DCTC 2016* – Congresso della Divisione di Chimica Teorica e Computazionale della Società Chimica Italiana, Scuola Normale Superiore, Pisa.
Canola S., Negri F. and Fink R. F. *"Modeling excited state character and exciton couplings in J and H aggregates of perylene-bisimide"*

2016 *EnLight Workshop*, Pisa.
Canola S., Negri F. and Fink R. F. *"Modeling excited state character and exciton couplings in J and H aggregates of perylene-bisimide"*

2014 *SCI 2014* - XXV Congresso della Società Chimica Italiana, Università della Calabria, Arcavacata di Rende (CS).
Canola S. and Negri F. *"Anisotropy of the n-type charge transport and thermal effects in crystals of a fluoro-alkylated naphthalene diimide: a computational investigation"*

Other presentations

2015 Poster presentation to *XV GdC* – Giornata della Chimica della sezione SCI dell'Emilia Romagna, Università di Modena e Reggio Emilia, Modena.
Canola S., Pecoraro C. and Negri F. *"Modeling the Anisotropy of Charge Transport in Crystals of p-type Thienoacene Semiconductors"*

2015 Poster presentation to *DCTC 2015* – Congresso della Divisione di Chimica Teorica e Computazionale della Società Chimica Italiana, Roma.
Canola S., Pecoraro C. and Negri F. *"Modeling the Anisotropy of Charge Transport in Crystals of p-type Thienoacene Semiconductors"*

2015 Poster presentation to *MolSimEng 2015* – Molecular Simulation and Engineering, Politecnico di Milano, Milano.
Canola S. and Negri F. *"Modeling the Anisotropy of Charge Transport in Crystals of n-type and p-type Semiconductors"*

2015 Poster presentation to *CHITEL 2015* - Congress of Theoretical Chemists of Latin Expression , Torino.
Canola S. and Negri F. *"Modeling the Anisotropy of Charge Transport in Crystals of n-type and p-type Semiconductors"*

Acknowledgments

PhD is not just about science, it's about life, experience and growth... or at least this is what it represented to me. This has been made mostly possible by the many people that I met on this path three year long. For sure nothing of this work would have been possible without the constant and attentive supervision of Prof. Fabrizia Negri, that accompanied this shy and insecure student in moving the first steps toward the complex world of science. I felt really a lucky and privileged student in having the possibility in every moment to count on such a Mentor, capable of showing in every occasion what a real Scientist should be and how should behave. Another huge chance of growth has been represented by the time in Tübingen, my first incredible experience so far from Home, where Prof. Reinhold Fink gave me the warmest hospitality ever. The amount of things learned in those months dense of experiences and discoveries is invaluable and, for this reason, all the friendly people met there deserve a big Danke, mentioning in particular Stefan Behnle a patient and friendly support. These years have seen many new friendships creating and evolving, and even more old friendships strengthening, often regardless of space and time, becoming another successful project developed this years and maybe one of those I'm most proud of. A really special mention goes to Dr. Mario Prosa, a colleague and a friend, with whom it has been a real pleasure to share discussions and jokes, successes and delusions, time and space on a daily basis. Another essential part of these years has been the everyday routine in the laboratory with all the friendly people that here I had the luck to meet. In particular, the friendship and the support of the friends and colleagues Tainah Marforio and Francesco Segatta is one of most precious and lasting results that computational chemistry has delivered to me. And finally, it is here toward the conclusion af these acknowledgments that the deepest thought goes the Person, the Scientist and the Support that still keeps traveling at my side after all these years and places, always regardless of space and time. Infine come tutti i traguardi fin qui raggiunti, non sarebbe stato possibile senza il silenzioso supporto della mia famiglia nel momento delle scelte, delle delusioni e delle soddisfazioni. Gli anni passano ma il riferimento rimane sempre quel piccolo paese e quel burbero padre. Grazie a tutti. Thanks to everyone. Dank euch allen.